

Co-tutorial doctoral thesis

Characterization of the spatial distribution of lignins in plant cell walls using chemical reporters and Raman spectroscopy

submitted by

Oriane MOREL, MSc

in partial fulfilment of the requirements for the academic degree

Docteure en biologie structurale et moléculaire (Lille)

Doktorin der Bodenkultur (Dr.nat.techn.) (Vienna)

Lille and Vienna, 12th July 2023

Supervisors:

Pr Simon HAWKINS

UMR CNRS 8576—UGSF—Unité de
Glycobiologie Structurale et Fonctionnelle,

University of Lille

Lille, France

Dr Notburga GIERLINGER

Institute of Biophysics, Department of
Bionanosciences

University of Natural Resources and
Life Sciences Vienna (BOKU)

Vienna, Austria

Jury members:

Dr. Elisabeth Jamet - Research Director CNRS, University of Toulouse, Reporter

Dr. Annabelle Dejardin - Researcher HDR INRAE, Orléans, Reporter

Dr. Brigitte Chabbert - Researcher INRAE, Reims, Examiner

Pr. Godfrey Neutelings - Professor, University of Lille, Chair

Dr. Notburga Gierlinger – Assistant Professor, University of Vienna

Pr. Simon Hawkins – University of Lille

Thèse de doctorat en cotutelle

Caractérisation de la distribution spatiale de la lignine dans les parois cellulaires végétales à l'aide de rapporteurs chimiques et de la spectroscopie Raman

Soumis par :

Oriane MOREL,

Pour le grade de

Docteure en biologie structurale et moléculaire (Lille)

Doktorin der Bodenkultur (Dr.nat.techn.) (Vienna)

Lille et Vienne, 12 Juillet 2023

Directeurs de thèse:

Pr Simon HAWKINS

UMR CNRS 8576—UGSF—Unité de
Glycobiologie Structurale et Fonctionnelle,

University of Lille

Lille, France

Dr Notburga GIERLINGER

Institute of Biophysics, Department of
Bionanosciences

University of Natural Resources and
Life Sciences Vienna (BOKU)

Vienna, Austria

Membre du jury:

Dr. Elisabeth Jamet – Directrice de recherche CNRS, Université de Toulouse, Rapporteur

Dr. Annabelle Dejardin - Chercheuse HDR INRAE, Orléans, Rapporteur

Dr. Brigitte Chabbert - Chercheuse INRAE, Reims, Examineur

Pr. Godfrey Neutelings - Professor, University of Lille, Président

Dr. Notburga Gierlinger – Professeure associée, University of Vienna

Pr. Simon Hawkins – University of Lille

Affidavit

I hereby declare that I have authored this dissertation independently, and that I have not used any assistance other than that which is permitted. The work contained herein is my own except where explicitly stated otherwise. All ideas taken in wording or in basic content from unpublished sources or from published literature are duly identified and cited, and the precise references included. Any contribution from colleagues is explicitly stated in the authorship statement of the published papers.

I further declare that this dissertation has not been submitted, in whole or in part, in the same or a similar form, to any other educational institution as part of the requirements for an academic degree.

I hereby confirm that I am familiar with the standards of Scientific Integrity and with the guidelines of Good Scientific Practice, and that this work fully complies with these standards and guidelines.

City, date

First name SURNAME (*manu propria*)

Preface

This research was co-financed by the generous support of the Austrian Science Fund and the Hauts de France Region over the period October 2019 to September 2022, and by Lille University over the period October 2022 to August 2023



Der Wissenschaftsfonds.

Acknowledgements

Four years of exciting study on the study of the plant wall, this ends with this manuscript. This work could never have been completed without the help of many people to whom I would like to express my sincere thanks

I cannot thank enough my thesis supervisors, Simon HAWKINS and Notburga Gierlinger, for having proposed me this subject and for having accompanied me so well during these three years. I had the chance to carry out many experiments on various scientific equipments, at the interface between physics, chemistry and biology, and I am very grateful to them. I also want to thank Cédric LION and Godfrey NEUTELINGS, the “co-supervisors” of my thesis for their supervision of the chemical and biological aspects of the work.

I also thank Corentin SPRIET for guiding and advising me on fluorescence microscopy and plug-in creation, Christophe BIOT for their help on all chemical aspects of this thesis and Peter Bock for answering my questions on RAMAN spectroscopy. In general, I would like to thank all the members of my two host teams for their good mood, and for having welcomed me so well in the team.

I thank obviously the members of the jury, who made me the honour to examine this work with attention. Thanks therefore to Elisabeth JAMET, to Annabelle DEJARDIN and to Brigitte CHABBERT for having fulfilled the role of reporter, without forgetting. I also thank Vincent BURLAT and Gaël PAES for having officiated as members of my thesis monitoring committee, and for having advised me well during each of our exchanges.

I would also like to thank Fabien BALDACCI-CRESP, for having explained me the bases of my future works and Dmitry GALINOUSKY.

And finally, thanks to my colleagues of office, Anne Sophie BLERVACQ, Estelle GOULAS, Nannan XIAO, Max WILLINGER, Julia Bock and Suvajit MUKHERJEE for their sunny disposition, their dynamism, and their deep kindness. Finally, I would like to thank my family, without whom I would not be here today; thanks, to my partner, Raphaël, for his unshakeable faith in my success and my dog.

Table of contents

Preface.....	ii
Acknowledgements.....	iii
Table of contents.....	iv
List of publications.....	vii
Publications that comprise the main part of this cumulative dissertation	vii
Abstract.....	ix
Kurzfassung	x
Résumé.....	xi
1 Introductory overview	1
1.1. The Plant Cell Wall.....	1
1.1.1. Background	1
1.1.2. Cell wall organisation.....	2
1.1.3. Cell wall composition	3
1.1.3.1. Cellulose.....	3
1.1.3.2. Hemicelluloses	5
1.1.3.3. Pectins	7
1.1.3.4. Proteins.....	9
1.1.3.5. Lignins.....	11
1.1.3.6. Monolignols.....	15
1.1.3.7. Lignins Polymerisation	20
1.1.3.8. Polysaccharide and lignins interactions	23
1.2. Lignins analysis.....	25
1.2.1. Quantification of lignins	26
1.2.2. Composition and structural characterization.....	27
1.2.3. Lignins imaging.....	29
2 Bioorthogonal chemistry: biomolecule tagging with click chemistry	32

2.1	History	32
2.2	Principal bioorthogonal reactions.....	34
2.2.1	Staudinger reaction.....	34
2.2.2	CuAAC reaction.....	35
2.2.3	SPAAC reaction.....	35
2.2.4	DAinv reaction.....	36
2.3	Metabolic tagging in plants	37
3	Spectroscopy imaging technology	42
3.1	Raman Imaging.....	44
3.1.1	Introduction.....	44
3.1.2	Generalities	45
3.2	Infrared spectroscopy	47
4	Objectives.....	49
5	Results and discussion	51
5.1	Paper I: Development of a novel analytical technique to quantify monoglignol reporter incorporation into the cell wall	51
5.1.1	Supplemental Dataset S1 : Dataset supporting the manuscript dedicated to lignin precursor incorporation analysis, bioorthogonal labelling, parametric and AI based segmentation.	69
5.1.1.1	Cell Wall Segmentation Tutorial	70
5.1.1.2	Run.py.....	72
5.1.1.3	parametric_segmentation.ijm :.....	98
5.1.2	Supplemental Figure S1. Bioorthogonal lignin triple (H*, G*, and S*) labelling in WT Arabidopsis floral stems.	107
5.1.3	Supplemental Figure S2. UV lignin autofluorescence and bioorthogonal lignin triple (H*, G*, and S*) labelling in Arabidopsis WT and prx64 mutant floral stems	109

5.1.4	Supplemental Figure S3. Comparison of monolignol reporter incorporation profiles in WT and prx64 mutant Arabidopsis stem fiber cell walls.	110
5.1.5	Supplemental Figure S4. Automatic segmentation of cell wall zones in flax stem tissues showing relative distribution of lignin and NCP reporters.	111
5.2	Paper II : Application of plant cell wall segmentation to safranin-O staining	112
5.3	Paper III : Adaptation of Raman spectra analysis	123
5.3.1	SUPPLEMENTARY INFORMATION	134
5.4	Multimodal analysis of the impact of hemicellulose matrix modification on lignins polymers in the <i>Arabidopsis thaliana irx9-2</i> mutant.....	136
5.4.1	Introduction.....	136
5.4.2	Material and methods	138
5.4.3	Results	143
5.4.4	Discussion	153
5.4.5	Conclusion.....	155
6	Discussion and perspectives	156
	List of abbreviations	162
	List of figures.....	167
	Bibliography.....	169

List of publications

Publications that comprise the main part of this cumulative dissertation

- Morel, O., Lion, C., Neutelings, G., Stefanov, J., Baldacci-Cresp, F., Simon, C., Biot, C., Hawkins, S., & Spriet, C. (2022). REPRISAL: mapping lignification dynamics using chemistry, data segmentation, and ratiometric analysis. *Plant Physiology*, 188(2), 816–830. <https://doi.org/10.1093/PLPHYS/KIAB490> : published

Authors contributions:

- MOREL Oriane (Conceptualization; Data Curation, Formal Analysis, Investigation, Methodology, Resources, Software, Visualisation, Writing-Original Draft)
 - LION Cédric (Conceptualization, Resources, Validation, Visualization, Writing-Original Draft, Writing - Review & Editing)
 - NEUTELING Godfrey (Conceptualization, Resources, Validation, Visualization, Writing-Original Draft, Writing - Review & Editing)
 - STEFANOY Jonathan (Software)
 - BALDACCI-CRESP, Fabien (Methodology, Resources)
 - SIMON Clémence (Resources)
 - BIOT Christophe (Conceptualization, Resources, Validation, Visualization, Writing-Original Draft, Writing - Review & Editing)
 - HAWKINS Simon (Conceptualization, Funding Acquisition, Methodology, Resources, Supervision Validation, Visualization, Writing-Original Draft, Writing - Review & Editing)
 - SPRIET Corentin (Conceptualization, Project Administration, Resources, Software, Supervision, Validation, Visualization, Writing-Original Draft, Writing - Review & Editing)
-
- Morel, O., Spriet, C., Lion, C., Baldacci-Cresp, F., Pontier, G., Baucher, M., Biot, C., Hawkins, S., & Neutelings, G. (2023). Ratiometric fluorescent safranin-o staining allows the quantification of lignins contents in muro. *methods in molecular biology* (Clifton, N.J.), 2566, 261–268. https://doi.org/10.1007/978-1-0716-2675-7_21/COVER : published

Authors contributions :

- MOREL Oriane (Conceptualization; Data Curation, Formal Analysis, Investigation, Methodology, Resources, Software, Visualisation, Writing-Original Draft)
 - SPRIET Corentin (Conceptualization, Software, Resources, Validation, Visualization, Writing-Original Draft, Writing - Review & Editing)
 - LION Cédric (Conceptualization, Resources, Validation, Visualization, Writing-Original Draft, Writing - Review & Editing)
 - BALDACCI-CRESP, Fabien (Methodology, Resources)
 - PONTIER Garence (Investigation, Resources)
 - BAUCHER Marie (Conceptualization, Resources)
 - BIOT Christophe (Conceptualization, Resources, Validation, Visualization, Writing-Original Draft, Writing - Review & Editing)
 - HAWKINS Simon (Conceptualization, Funding Acquisition, Methodology, Resources, Supervision Validation, Visualization, Writing-Original Draft, Writing - Review & Editing)
 - NEUTELING Godfrey (Conceptualization, Project Administration, Resources, Supervision, Validation, Visualization, Writing-Original Draft, Writing - Review & Editing)
- Morel, O., & Gierlinger, N. (2023). Chemical tissue heterogeneity of young Arabidopsis stems revealed by Raman imaging combined with multivariate data analysis. *Microchemical Journal*. : published

Authors contributions :

- MOREL Oriane (Conceptualization ; Data Curation, Formal Analysis, Investigation, Methodology, Resources, Visualization, Writing-Original Draft)
- GIERLINGER Notburga (Conceptualization, Data Curation, Formal Analysis, Funding Acquisition, Investigation, Methodology, Project Administration, Resources, Supervision, Validation, Visualization, Writing-Original Draft, Writing - Review & Editing)

Abstract

Lignins is a polyphenolic polymer of the cell wall involved in many aspects of growth and development in higher plants. As a major component of lignocellulosic biomass, it is also of economic interest. Although the biosynthesis of the lignins polymer is relatively well understood, we need to know more about how changes (quantity/structure) to other cell wall polymers (e.g., cellulose, hemicelluloses, pectins) affect lignins production. To provide more information on this question we implemented a two-phase approach based on the use of biological imaging. The first phase involved the development/improvement of different high-resolution complementary imaging techniques. We firstly developed a novel quantitative ratiometric approach (REPRISAL) based on the parametric/artificial intelligence segmentation of confocal microscopy images obtained by lignins chemical reporter bio-orthogonal chemistry. This methodology allowed us to precisely map the lignification capacity of different cell wall layers (cell corner, compound middle lamella and secondary cell wall) in Arabidopsis WT plants and the *prx64* mutant. In a second development, we modified the REPRISAL segmentation algorithm thereby enabling it to be used to map relative cell wall lignins levels determined by the ratiometric safranin-O fluorescence technique. Finally, we used Raman imaging to compare the ability of three different multivariate analytical methods (unmixing, cluster analysis and orthogonal matching) to provide detailed spatial information about the distribution of different polymers in plant cell walls. In the second phase we used the developed/improved imaging techniques to analyse whether changes to cell wall hemicelluloses affect lignification in the Arabidopsis *irx9* mutant. Our results demonstrated that changes in the distribution of cell wall hemicelluloses do indeed modify the lignification process, particularly in the younger parts of the plant floral stem. Targeted transcriptomics of selected cell wall genes suggested that the observed changes could be related to the induction of a defence response. Overall, the techniques developed within the framework of this thesis should prove valuable for future studies of cell wall dynamics. The results obtained on the *irx9* mutant provide a novel insight into the dynamic relationships that exist between different polymers of the plant cell wall.

Kurzfassung

Lignins ist ein phenolisches Polymer der Zellwand, das an vielen Aspekten des Wachstums, der Entwicklung und der Widerstandsfähigkeit von höheren Pflanzen beteiligt ist. Als wesentlicher Bestandteil der pflanzlichen Biomasse ist Lignins auch von wirtschaftlichem Interesse. Obwohl die Biosynthese von Lignins relativ gut verstanden ist, wissen wir nicht, wie sich Veränderungen (Menge/Struktur) bei anderen Zellwandpolymeren (z. B. Cellulose, Hemicellulosen, Pektine) auf die Lignifizierung auswirken. Um diese Frage zu beantworten, haben wir mehrere Ansätze basierend auf biologischer Bildgebung verfolgt. In der ersten Phase ging es um die Entwicklung/Verbesserung verschiedener hochauflösender komplementärer Bildgebungsverfahren. Zunächst entwickelten wir einen neuartigen quantitativen ratiometrischen Ansatz (REPRISAL), der auf der parametrischen/künstlichen Intelligenz-Segmentierung von konfokalen Mikroskopie-Bildern basiert. Diese Bilder wurden mit Hilfe der biologisch-orthogonalen Chemie von Lignins-Reportern gewonnen und ermöglichten die Lignifizierungskapazität verschiedener Zellwandschichten (Zellecke, zusammengesetzte Mittellamelle und sekundäre Zellwand) in Arabidopsis Pflanzen und der prx64-Mutante präzise zu kartieren. Dann haben wir den REPRISAL-Segmentierungsalgorithmus so modifiziert, dass er zur Kartierung des relativen Zellwandligningehalts basierend auf ratiometrischen Safranin-O-Fluoreszenztechnik verwendet werden kann. Zusätzlich haben wir die Raman-Mikrospektroskopie eingesetzt und in Kombination mit drei verschiedenen multivariaten Analysemethoden (Unmixing, Clusteranalyse und orthogonales Matching) detaillierte räumliche Informationen über die Verteilung aller Polymere in Pflanzenzellwänden zu bekommen. Damit konnten wir nicht nur die Lignifizierung verfolgen, sondern auch ob Cellulose und Hemicellulosen die Lignifizierung in der Arabidopsis irx9-Mutante beeinflussen. Unsere Ergebnisse zeigten, dass Veränderungen in der Verteilung der Hemicellulosen tatsächlich den Lignifizierungsprozess modifizieren, insbesondere in den jüngeren Teilen des Blütenstamms der Pflanze. Die gezielte Transkriptomik ausgewählter Zellwandgene legt nahe, dass die beobachteten Veränderungen mit der Induktion einer Abwehrreaktion zusammenhängen könnten. Insgesamt werden die im Rahmen dieser Arbeit entwickelten Techniken wertvoll für künftige Untersuchungen der Zellwanddynamik sein. Die mit der irx9-Mutante erzielten Ergebnisse geben einen neuen Einblick in die dynamischen Beziehungen zwischen den verschiedenen Polymeren der Pflanzenzellwand

Résumé

La lignine est un polymère polyphénolique de la paroi cellulaire qui intervient dans de nombreux aspects de la croissance et du développement des plantes supérieures. En tant que composant majeur de la biomasse lignocellulosique, elle présente également un intérêt économique. Bien que la biosynthèse du polymère de la lignine soit relativement bien comprise, nous avons besoin d'en savoir plus sur la façon dont les changements (quantité/structure) des autres polymères de la paroi cellulaire (par exemple, la cellulose, les hémicelluloses, les pectines) affectent la production de lignine. Afin de fournir plus d'informations sur cette question, nous avons mis en œuvre une approche en deux phases basée sur l'utilisation de l'imagerie biologique. La première phase a consisté à développer/améliorer différentes techniques d'imagerie complémentaires à haute résolution. Nous avons tout d'abord développé une nouvelle approche ratiométrique quantitative (REPRISAL) basée sur la segmentation paramétrique/intelligence artificielle d'images de microscopie confocale obtenues par la chimie bio-orthogonale des rapporteurs chimiques de la lignine (click chemistry). Cette méthodologie nous a permis de cartographier précisément la capacité de lignification des différentes couches de la paroi cellulaire (coin cellulaire, lamelle moyenne composée et paroi cellulaire secondaire) chez les plantes *Arabidopsis* WT et le mutant *prx64*. Dans un deuxième temps, nous avons modifié l'algorithme de segmentation REPRISAL afin de pouvoir l'utiliser pour cartographier les niveaux relatifs de lignine de la paroi cellulaire déterminés par la technique de fluorescence ratiométrique de la safranine-O. Enfin, nous avons utilisé l'imagerie Raman pour comparer la capacité de trois méthodes analytiques multivariées différentes (non-mixage, analyse en grappes et correspondance orthogonale) à fournir des informations spatiales détaillées sur la distribution des différents polymères dans les parois cellulaires des plantes. Dans la deuxième phase, nous avons utilisé les techniques d'imagerie développées/améliorées pour analyser si les modifications des hémicelluloses de la paroi cellulaire affectent la lignification chez le mutant *irx9* d'*Arabidopsis*. Nos résultats ont démontré que les changements dans la distribution des hémicelluloses de la paroi cellulaire modifient effectivement le processus de lignification, en particulier dans les parties les plus jeunes de la tige florale de la plante. La transcriptomique ciblée de certains gènes de la paroi cellulaire suggère que les changements observés pourraient être liés à l'induction d'une réponse de défense. Globalement, les techniques développées dans le cadre de cette thèse devraient s'avérer précieuses pour les études futures de la dynamique des parois cellulaires. Les résultats

obtenus sur le mutant *irx9* donnent un nouvel aperçu des relations dynamiques qui existent entre les différents polymères de la paroi cellulaire des plantes

.

Introductory overview

1.1. The Plant Cell Wall

1.1.1. Background

In plant cells, unlike animal cells, the plasma membrane is surrounded by a semi-rigid wall with a complex structure. This wall, unlike fungi, has no chitin and contains cellulose. It is also different from the typical wall of prokaryotes, which is composed of a molecular mesh based on peptidoglycans. The wall contributes to the anisotropic growth of plant cells and, consequently, to their very high diversity of shapes and sizes. This cell wall plays various functions in the plant. It allows living cells to support high water potential values in their surrounding environment. The water is then accumulated in the vacuole which will swell and push the cytoplasm and plasma membrane against the wall that will prevent the cell from bursting. This structure combines both elasticity and plasticity properties allowing cell division, irreversible elongation and permeability to water and solutes. It allows the erect growth of the plant, i.e. it provides a structure that allows the plant to grow in height. offers protection against biotic (Vaahtera et al., 2019) and abiotic (Le Gall et al., 2015) stresses.

With regard to biotic stress, the plant cell wall serves as a passive barrier against microorganisms that can, however, bypass the wall to establish a connection with the host. In this case the defence barrier can be a major active player in the anti-microbial defence strategies developed by the plant. During infection and following lytic activities, oligosaccharide elicitors may be released from the cell wall of the host plant (Damage-Associated Molecular Patterns, DAMPs) or from the cell wall of the pathogen (Pathogen-Associated Molecular Patterns, PAMPs) (Boller & Felix, 2009). When the plant perceives these elicitors through membrane receptors, a signalling cascade is triggered by the numerous defence responses called DAMP- or PAMP-triggered immunity (Jones & Dangl, 2006). The plant will then, for example, strengthen its cell wall to create more resistance to physical pressure and enzymatic hydrolysis caused by pathogens.

The plant cell wall properties are also influenced by abiotic stresses. When the plants are under the influence of environmental modifications, the expression of many genes associated with

cell wall metabolism (e.g. cellulose) is modulated (Le Gall et al., 2015 ; Wang et al., 2016). In addition, it has recently been shown that the adaptive response of the cell wall also include osmosensitive induction of phytohormone production through the function of a cell wall integrity sensor (Bacete et al., 2022)

1.1.2. Cell wall organisation

The cell wall is a dynamic structure that can be modified during the life of the cell. It includes an assembly of biopolymers such as polysaccharides (cellulose, hemicelluloses, pectins) and phenolic polymers (e.g. lignins), as well as structural proteins and enzymes (Jamet & Dunand, 2020).

These molecules present in various proportions form the different layers of the wall that appear over time (example in Figure 1). Each layer has a unique structure and chemical composition that varies according to the plant species, tissue, and developmental stage of the plant. The middle lamella is first synthesized between two daughter-cells during cell division at the end of the telophase. It is mainly composed of pectins, which play a major role in the mechanical properties of plant tissues as it forms a link between the different cells. It can also be noted that the preferential attack of this layer by some fungi reduces mechanical resistance.

Then the primary cell wall is deposited against the middle lamella. It appears as a very thin structure and is characteristic of young growing or dividing plant cells. It mainly contains polysaccharides (cellulose, hemicelluloses and pectins) and proteins. It can also become lignified at the end of development in cells with secondary walls. It provides sufficient rigidity and mechanical support to withstand osmotic pressure, while being sufficiently elastic to allow cell growth and division.

And finally, only in certain cell types, a secondary cell wall can be deposited against the previous one, thus reducing the internal volume of the cell. It forms in cells that have completed their elongation and are in the process of differentiation. By its structure and volume, it plays a major role in the mechanical properties of the cell. It contains cellulose, hemicelluloses, lignins and glycoproteins, but their relative proportions vary according to the plant species and tissues.) The lignified secondary cell wall's impermeability facilitated the transport of water and nutrients and allowed plants to grow vertically. The secondary cell wall consists of 2 or 3

distinct layers which are named, from the outside to the inside, the layers S1, S2 and sometimes S3. These layers differ in the orientation of the cellulose microfibrils that make them up. In the tension wood fibres of some hardwoods, a gelatinous layer (G-layer) is added to or replaces the S3 layer and partially or totally replaces the S2 layer.

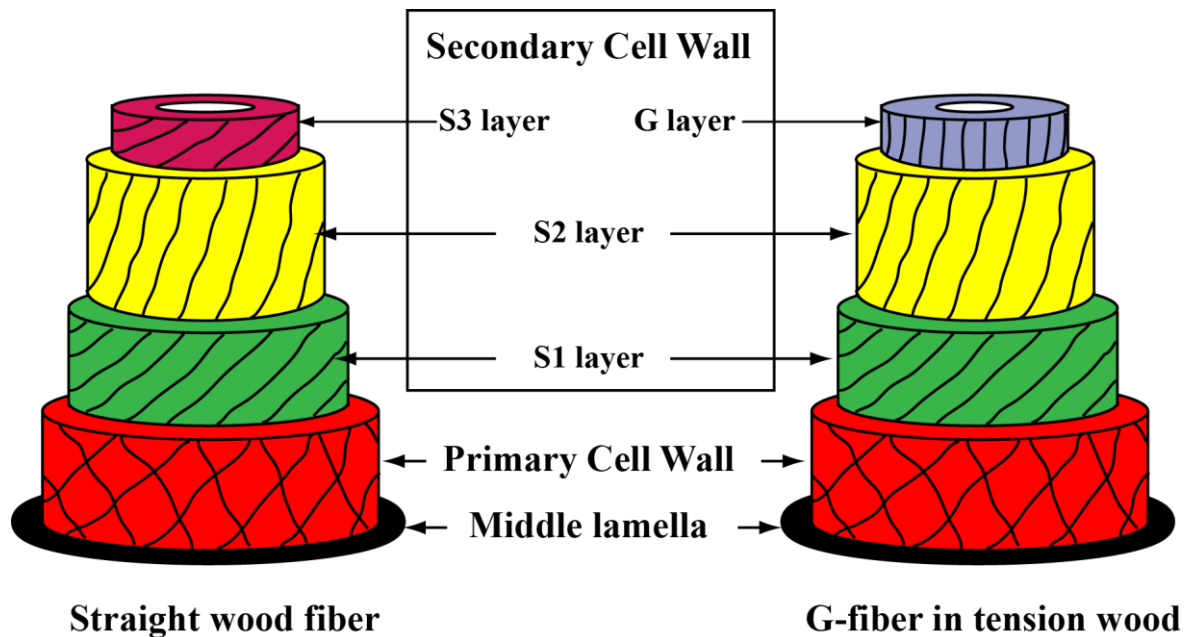


Figure 1 : Schematic representation of the different cell wall layers in tracheid cells (left) and gelatinous fibers from tension wood (right). The lines within the different layers represent the orientation of cellulose microfibrils. Adapted from (Jourez, 1997).

1.1.3. Cell wall composition

1.1.3.1. Cellulose

Cellulose (Figure 2) is quantitatively the most abundant component of plant biomass (40 to 45% of the dry mass). Cellulose is an unbranched biopolymer of D-glucose residues linked by β -(1-4) glycosidic bonds. Cellulose molecules are synthesized by a six-lobed plasma membrane spanning cellulose synthesis complex (CSC) rosettes (McFarlane & Persson, 2014) It was admitted for a long time that there are 36 molecules of cellulose synthases (CESAs) (Sommerville, 2006) included in the CSC but recent studies suggested that they may only be 18 (Nixon et al., 2016). The CESA enzymes are glycosyltransferases made up of eight

transmembrane domains and N- and C-terminal domains facing the cytoplasm. The CSC is linked to underlying

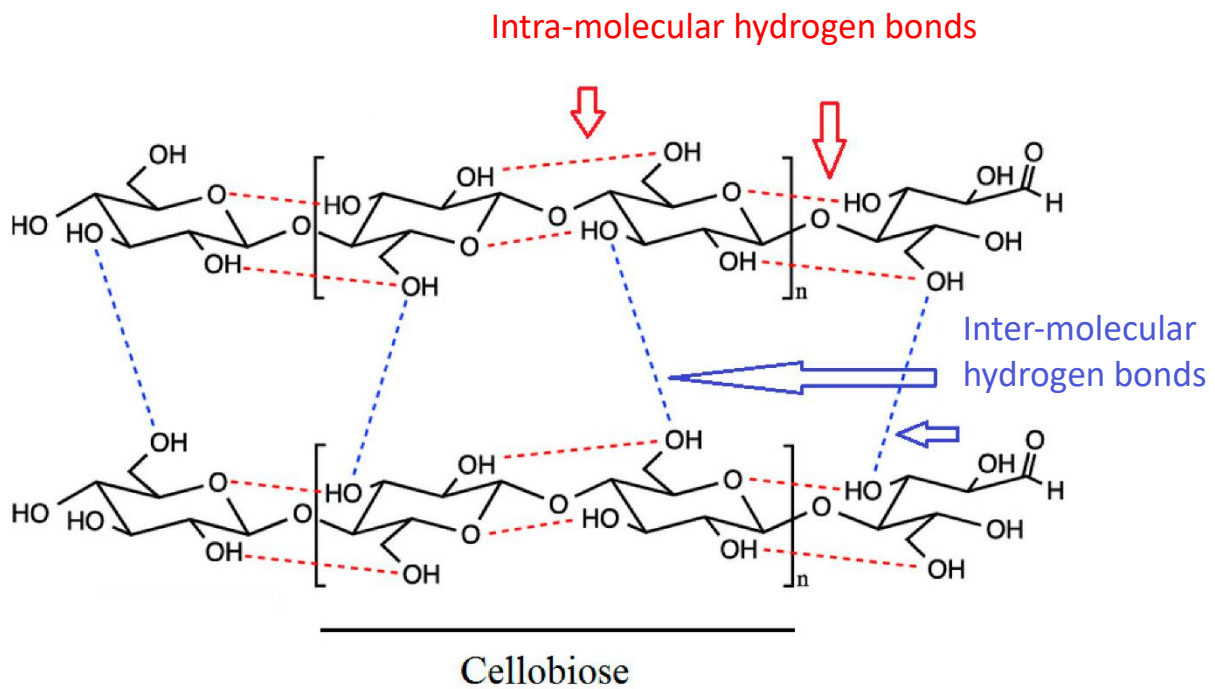


Figure 2 : Cellulose structure from (Baghaei & Skrifvars, 2020). Biopolymer of D-glucose residues linked by β -(1-4) glycosidic bonds that form cellulose. Intra-molecular hydrogen bonds are represented in red and inter-molecular hydrogen bonds in blue. Two D-glucose residues form cellobiose.

microtubules that serve as guiding tracks to determine the direction of cellulose microfibril alignment (Farquharson, 2009). The movement is propelled forward through the force generated by polymerization of monomers. After their synthesis, the cellulose molecules are arranged into microfibrils due to the presence of numerous OH groups that facilitate their organization in parallel by intra- and intermolecular hydrogen bonds. In the microfibrils, the cellulose chains are bound together in an orderly and periodic manner and then form a crystalline pattern. The crystalline regions are connected to each other by amorphous zones consisting of disordered cellulose chains which can form hydrogen bonds with water or other molecules (Rowland & Howley, 1988).

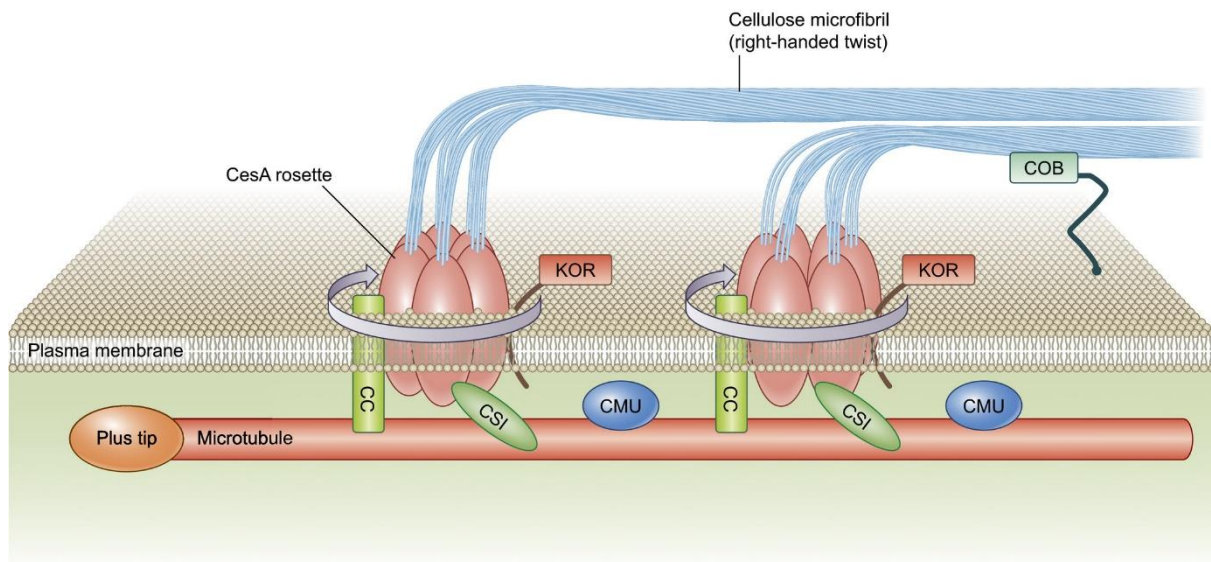


Figure 3 : Model for cellulose biosynthesis (Buschmann & Borchers, 2020). Cellulose (blue fibrils) is produced by CESA rosettes (light red) that move along microtubules (in red). Linker proteins such as CELLULOSE SYNTHASE INTERACTING (CSI) (green) and COMPANION OF CELLULOSE SYNTHASE-MICROTUBULE UNCOUPLINGS (CMU) (blue).

1.1.3.2. Hemicelluloses

Hemicelluloses are part of the non-cellulosic polysaccharides (NCPs) present in primary and secondary cell walls in all terrestrial plants in which they account for 20-30% of the dry mass of the wall. They interact with cellulose microfibrils through hydrogen bonds, but also with lignins through covalent bonds (Terrett & Dupree, 2019).

Hemicelluloses have a basic structure close to cellulose, but the main chains are shorter and most often branched by polyoses (Ebringerová et al., 2005). These ramifications prevent a crystalline arrangement as observed for cellulose. The fibrils are flexible and can settle around the cellulose rods. Their branched structure and quantity vary according to the plant species and according to the cell type. Hemicelluloses are synthesized from sugar nucleotides by glycosyltransferases located at the membranes of the Golgi apparatus. They include xylans, xyloglucans, mannans, glucomannans, arabinoxylans and mixed-linkage glucans (Scheller & Ulvskov, 2010) (Figure 4).

- **Xylans** are nature's most abundant non-cellulosic parietal polysaccharides, accounting for up to one third nature, accounting for up to a third of wood cell walls, or even half in the case of

annual plants. They consist of a backbone of β -1,4-linked D-xylopyranose units, with irregular branching. Xylans are classified according to their branching: glucuronoxylan (GX) have glucuronic acid and 4-O-methyl-glucuronic acid as their main substituents, glucuronoarabinoxylan (GAX) also have arabinose substituents and arabinoglucuronoxylan (AGX) are substituted by 4-O-methyl-glucuronic acid residues and to a lesser extent by arabinose (Curry et al., 2023).

- **Mannans** are widely distributed and the main hemicellulose in Charophytes (Scheller & Ulvskov, 2010); Voiniciuc, 2022). Their backbones may consist entirely of β -(1 \rightarrow 4)-linked mannose, as in mannans and galactomannans, or with additional glucose in a nonrepeating pattern as in glucomannans and galactoglucomannans.

- **Mixed-linkage glucan** are unbranched chains of D-glucoses linked in β -(1-4) or β -(1-3) Unlike other hemicelluloses, they are not present in all terrestrial plants and are notably absent from the dicotyledons.

- **Xyloglucans** are composed of glucose bound in β -1,4. They have ramifications of xylose α -1,6. Various sugars can then be attached to the xylose such as fucose, galactose etc. It is the most important hemicellulose in the primary walls of the dicotyledons. (Pauly et al., 2013)

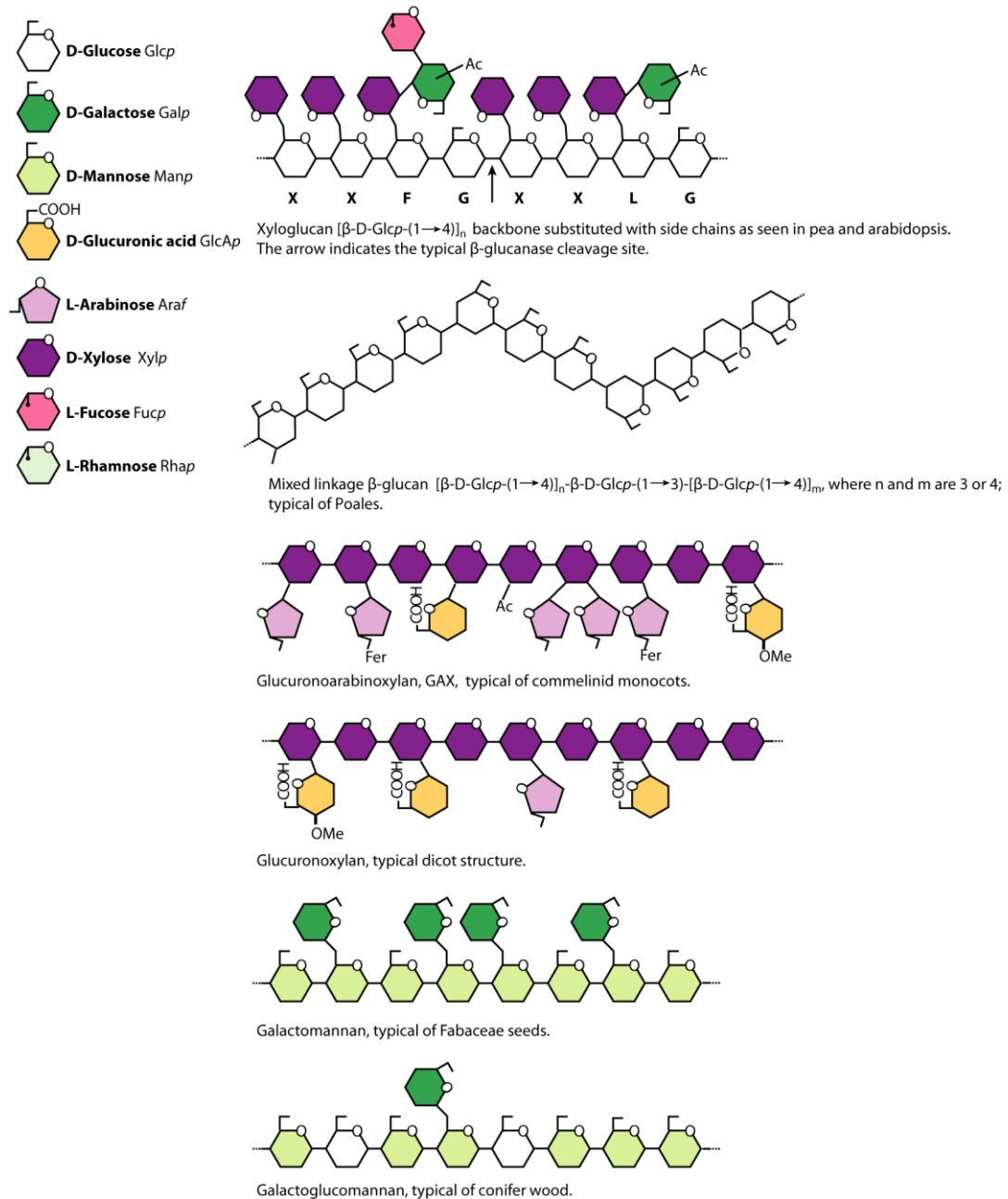


Figure 4 : Schematic representation of hemicelluloses. Adapted from (Scheller & Ulvskov, 2010)

1.1.3.3. Pectins

Pectins form a group of complex non-cellulosic polysaccharides (Figure 5). They have functions in plant growth, morphology, development, and defence. These polymers are predominant in the middle lamella and are also found in the primary cell wall of terrestrial plants. Pectins are usually composed of α (1 \rightarrow 4)- α -bound D-galacturonic acid residues

backbone interrupted by the insertion of (1→2)- α -linked L-rhamnose residues (Gawkowska et al., 2018). Other glycans, mainly L-arabinose, D-galactose, D-xylose, L-fucose are attached in the side chains. In general, there are considered to be four domains among pectins: homogalacturonan (HG), xylogalacturonan (XGA), rhamnogalacturonan I (RGI) and rhamnogalacturonan II (RGII) (Mohnen, 2008).

HG is a linear polymer of galacturonic acids bound in α -(1-4) that can be methylated on C6 and acetylated on O2 or O3. Two homogalacturonan chains can interact via Ca^{2+} bridges forming a so called “egg-box” structure (Mravec, Kračun, Rydahl, et al., 2017). This interaction is controlled by the degree of methyl-esterification of the galacturonate, which masks the carboxyl groups participating in these ionic bonds.

XGA is also a galacturonan, but residues of xylose connect in β -(1-3) to the galacturonic acids. In RGI, the main skeleton is composed of alternating galacturonic acid and L-rhamnose residues linked in α -(1-2), to which are grafted many side chains. Some galacturonic acid residues are also acetylated. Finally, the RGII motif consists of approximately nine galacturonan residues to which four complex carbohydrate side chains of 12 different sugars are linked. These side chains contain particular monosaccharides, such as D-apiose (Api), L-acerate (AceA), 2-O methyl, L-fucose, 2-O methyl D-xylose, L-galactose, 2-keto-3-deoxy-D-lyxo-2-heptulosaric acid (Dha), and 2-keto-3-deoxy-D-manno octulosonate (Kdo). The name RGII may be misleading as it suggests that this polysaccharide contains a rhamnose (Rha) backbone, which is not the case. In RGII, Rha is scarce and forms part of the side chains (Mohnen, 2008 ; Harholt et al., 2010 ; Barceló & Pomar, 2001).

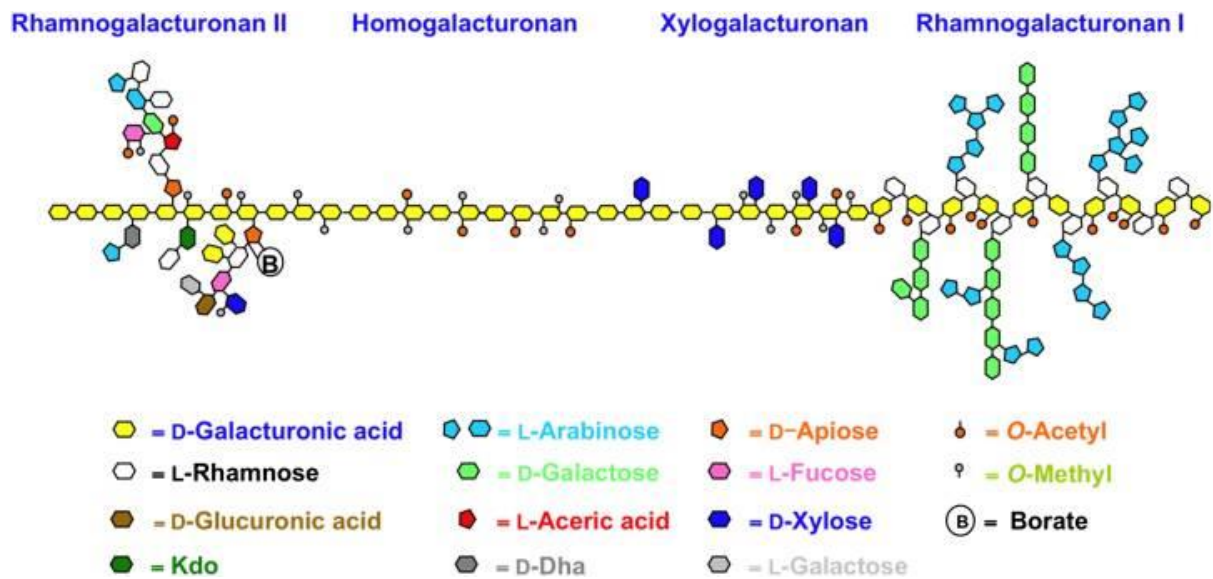


Figure 5 : Schematic representation of pectin (Harholt et al., 2010)

1.1.3.4. Proteins

The proteins present in the plant wall are important components. They are involved in numerous physiological processes such as polysaccharide organization and intercellular communication (Albenne et al., 2013). It is always rather difficult to clearly identify the proteins involved in the structure or function of the walls as they can be extremely numerous if we consider in particular the enzymes that participate in the synthesis of polymers during the vesicular secretion process (Cassab, 1998). In general, the proteins located within the cell wall (CWPrs) are first synthesized with a *bona fide* N-terminal signal peptide as predicted by several bioinformatics programs although the existence of CWPrs lacking this extension is still a matter of debate (Albenne et al., 2013). In total, these proteins represent 1 to 10% of the dry mass of the plant cell wall and are listed in several online databases such as WallProtDB (San Clemente & Jamet, 2015). They are classified as structural proteins or enzymes but some still have unknown functions and others, such as expansins have a specific loosening action within the cell wall. With the exception of glycine-rich proteins (GRPs), all the structural proteins are glycosylated (Cassab, 1998). A usual classification in 9 different groups is generally accepted, based on bioinformatics predictions of their functional domains (Jamet et al., 2008).

Proteins acting on polysaccharides are grouped in the most abundant class since they represent about 25% of the CWPrs. They include different enzymes belonging to the CAZy

classification namely glycoside hydrolases (GHs) (Minic & Jouanin, 2006) such as xyloglucan endotransglucosylases/ hydrolases (XTHs) (Eklöf & Brumer, 2010), carbohydrate esterases (CEs) such as pectin methylesterases (PMEs) (Giovane et al., 2004) or polysaccharide lyases (PLs) such as pectate lyases (Bai et al., 2017). The high abundance of these proteins is not surprising since polysaccharides constitute the most important fraction of cell walls and are constantly being remodelled during plant development or in response to environmental constraints.

Proteases include Asp-proteases, Cys-proteases, Ser-proteases and Ser-carboxypeptidases (about 12% of the CWPrs). These proteins could be involved in the maturation of cell wall proteins, their degradation or the release of signalling peptide (van der Hoorn, 2008).

Other smaller protein families are also present among the CWPrs such as **interaction domains** including lectins that interact with sugars, proteins that interact with other proteins through LRR (leucine-rich repeat) domains, and enzyme inhibitors.

Signalling proteins mainly include arabinogalactan proteins (AGPs), fasciclin-like AGPs (FLAs) (Seifert & Roberts, 2007) and lectin receptor kinases or LRR receptor kinases identified through their extracellular domain.

Lipid metabolism-related proteins include proteins homologous to GDSL-type lipases/acylhydrolases (Chepyshko et al., 2012) and lipid transfer proteins (LTPs). LTPs may play a role in transporting lipids through hydrophilic walls, while lipases/acylhydrolases may be involved in the formation of lipid bonds in the cuticle (Yeats & Rose, 2013). LTPs may also be involved in cell wall extension by interacting with the cellulose/xyloglucan network (Nieuwland et al., 2005).

Structural proteins include mainly hydroxyproline rich glycoproteins (HRGPs). They can themselves be classified into three categories according to their *O*-glycosylation: moderately glycosylated extensins (EXTs), highly glycosylated (AGPs) and low-glycosylated Pro-Rich Proteins (PRPs) (Showalter et al., 2010). They are believed to be involved in many physiological and developmental processes in plants (Cannon et al., 2008), in plant defence (protection against pathogenic attacks or mechanical injuries) (Deepak et al., 2010) and also participate in cell wall rigidity (D. Xie et al., 2011). AGPs are secreted in large quantities during the wounding process to form a gel that acts as a physical barrier against pathogenic invasions.

However, they have other functions that have not been fully elucidated. They are believed to be involved in the plant's development process and during stress. Glycine Rich Proteins (GRPs) contain up to 70% glycine. They participate in the development of vascular tissue and are involved in stress responses (healing, cold resistance).

Proteins of various families include all proteins that are not numerous enough to form a functional class and **proteins of unknown function** correspond to proteins without a predicted functional domain or with a predicted domain of unknown function (DUF).

Finally, **oxido-reductases** include peroxidases, multicopper oxidases, berberine-bridge oxido-reductases and blue copper binding proteins (between 15 and 20% of the parietal proteome). Peroxidases and laccases are described in detail in the following chapter about lignins.

1.1.3.5. Lignins

1.1.3.5.1. Generality

Lignins are an essential component of the cell wall in certain tissues (xylem, sclerenchyma) in higher vascular plants (Vanholme et al., 2019). Lignification is a process that begins in the middle lamella as the secondary wall thickens and then gradually extends to the primary wall and afterwards to the secondary wall. Lignins content changes according to the wall sublayer. The cell corners (CCs) are the most lignified parts, followed by the compound middle lamellae (CMLs) and then the secondary walls (Wilson & Hatfield, 1997), In *Caragana Korshinskii*, for example, the ratio of lignins concentration in the CML, ML and secondary cell wall S2 layer is 1.5:1.2:1.(Xu et al., 2006). As the secondary wall is very thick and constitutes the bulk of the biomass, lignins is extracted mainly from the secondary wall. At present, 35 monomers have been identified in lignins, of which the three main ones are derived from *p*-coumaryl alcohol, coniferyl alcohol and sinapyl alcohol. Once incorporated into the lignins, they give respectively hydroxyphenyl (H), guaiacyl (G), and syringyl (S) monomeric units (Figure 6). Given the aromatic nature of the monomers, lignins are considered an aromatic biopolymer. They are amorphous polymers, i.e. they do not take on any particular shape but fill the free spaces between the other constituents of the wall.

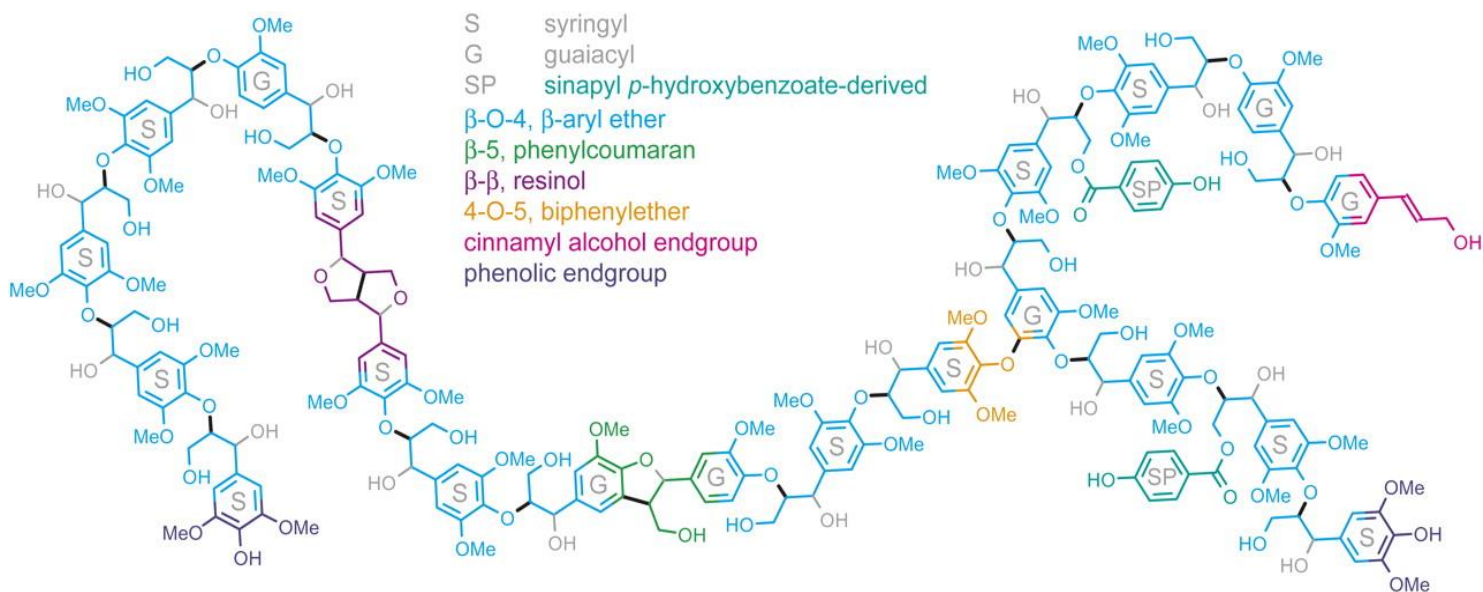


Figure 6 : Schematic representation of poplar lignins polymer predicted by NMR (Nuclear magnetic resonance) analysis (Vanholme et al, 2010).

1.1.3.5.2. Economic interest

As we have seen, the plant wall is composed of multiple polymers, each with a potential economic interest (Figure 7) (Anwar et al., 2014). For example, fibers containing cellulose can be extracted to produce paper pulp. Cellulose is a compound with various interests. It is the compound that will be degraded by herbivores during digestion or used to produce biofuels.

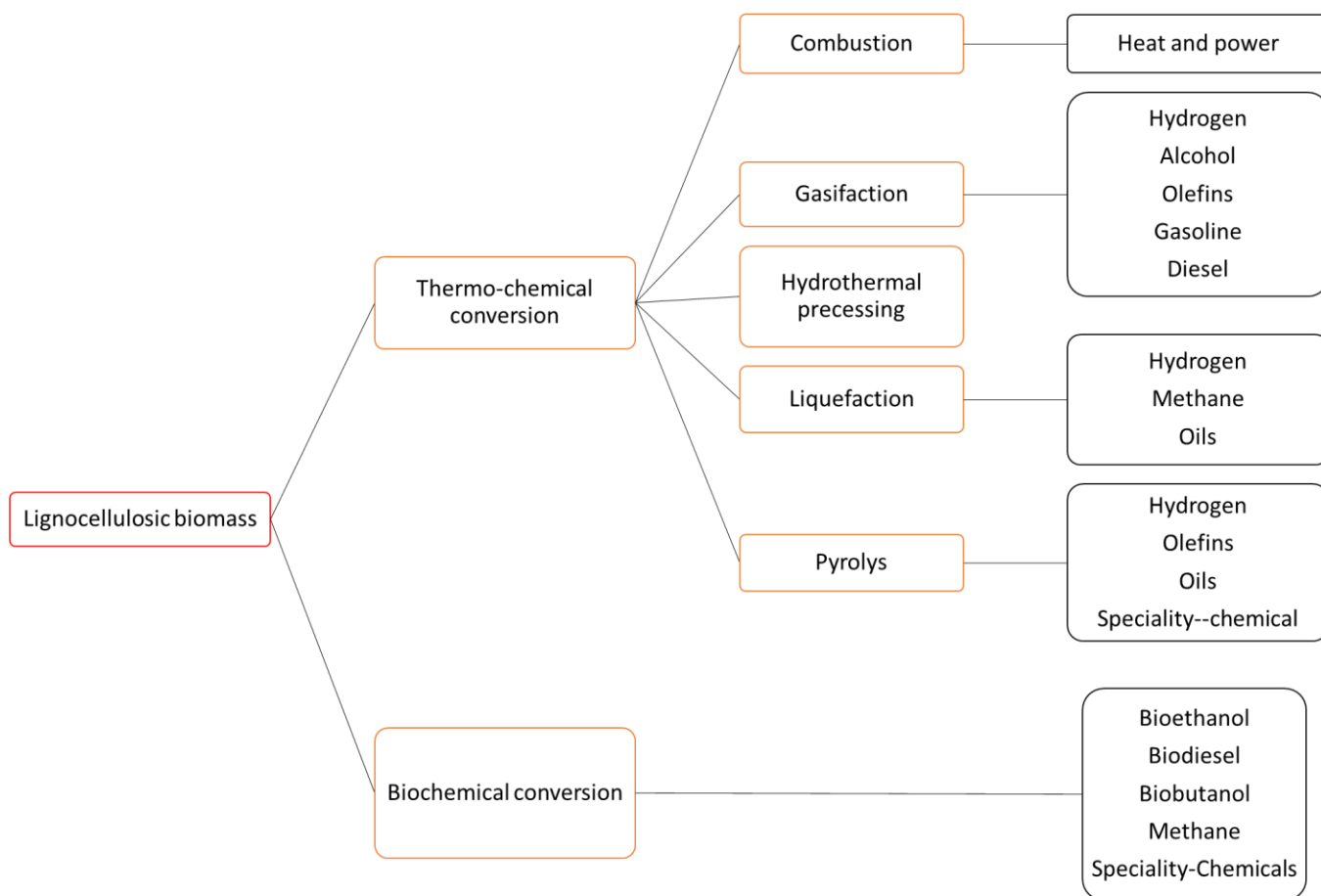


Figure 7 : Various transformation processes of lignocellulosic biomass adapted from (Anwar et al., 2014)

Lignins is an abundant aromatic resource. But for some of the industries using biomass, it's considered as a nuisance. For the paper industry, it's a waste, and for the cellulose extraction industry, its presence decreases the degradability of the biomass. Thus, it is certain that nature generates macromolecules very rich in chemically cleavable ether bonds (which allows high recovery rates of molecules of interest), on the other hand, during lignins-cellulose (or hemicellulose) separations, the treatment generates C-C bonds (sometimes very stable, interatomic) that are not easily cleavable (which reduces the recovery of these molecules of interest). This is the case of residual lignins from the paper industry for which the recovery rate of recoverable products is low, which explains why the residues are burned to generate heat.

These last years, with the problem of the future shortage of fuel, alternatives have been sought. One of them is to use plants to make biofuel. Biofuel can be produced in different ways, from sugars of plants rich in polysaccharides (sugarcane, beet ...), oils (rapeseed ...), but also from agricultural waste or fast growing trees (Saini et al., 2015 ; Pang, 2019). The production of biofuel, like the production of paper pulp, requires prior treatment, whether by chemical, thermal or enzymatic process, to be able to extract efficiently the molecules of interest. In this case, the lignins are an obstacle to the valorization because it entraps the polysaccharides. To increase the yield, a lignin-alteration step is necessary (Kumar & Sharma, 2017). Research, through lignins engineering, tries to decrease the recalcitrance to extraction by producing transgenic plants with less lignins or lignins with an modified structure (Umezawa, 2018).

However, lignins has other economic advantages, so the lignins can be either an asset or an obstacle to the industrial process. It is able to conduct electric current. It could also replace certain materials in batteries (Jung et al., 2022) or even be used as a reinforcing agent in the automotive or aeronautical industry (Vasile & Baican, 2023). Lignins are important in construction wood because they are responsible for the mechanical performance of this material. The phenolic property of lignins also makes it interesting for the synthesis of phenolic derivatives, even if for the moment, the exploitation of this property remains limited due to the cost of the different processes to be used (Wenger et al., 2020). Lignins is characterized by a variety of distinct and chemically different binding units, each requiring different cleavage conditions when selective depolymerization is targeted. Although structurally more complex, the higher carbon content and oxygen content of lignins, make it an attractive feedstock for biofuel and chemical production (Rinaldi et al., 2016).

The main problem here is that each of the cell wall polymers interact with the others, so it is important to understand how each influences the others to be able to access more easily, or even improve the targeted compound.

1.1.3.5.3. *Functions*

Lignins contribute to the rigidity of cell walls, the upright growth habit of terrestrial flowering plants, water transport and defence against pathogens. They are found in vessels, rays, and fibers, as well as in axial parenchyma in angiosperms, and tracheids and rays in gymnosperms. The vessels ensure the conduction of the sap; the rays control the lateral transport of nutrients between cells; the tracheid fibres provide both the conduction of the sap and mechanical support. Their hydrophobicity also contributes to better conduction of sap from the roots to the leaves. Lignins are also found, outside the vascular system, in the sclerenchyma tissue (involved in mechanical support), in the Casparian strip (structure of the root endodermis) and in some seed coats to protect the embryo (Barros et al., 2015).

Lignins are extremely resistant to degradation. By forming bonds with both cellulose (hydrogen bonding) and hemicelluloses (direct or indirect bonds via the ferulic esters of hemicelluloses), they create a hydrophobic barrier to all solutions or enzymes, thus limiting the penetration of lignocellulosic enzymes into the cell wall structure.

1.1.3.6. *Monolignols*

1.1.3.6.1. *Biosynthesis*

As indicated above, there are three main monomeric units constituting lignins, H, G and S. Other units can however be incorporated into lignins such as 5HG (5-hydroxyguaiacyl) or the catechyl unit (C) derived from caffeoyl alcohol (Dixon & Barros, 2019).

Monolignols are synthesised from phenylalanine and/or tyrosine (grasses). These amino acids are produced in the chloroplasts via the shikimate pathway. From these amino acids, various specific lignification steps take place in the cytosol of the cells undergoing lignification to produce the various monolignols. (Vanholme et al., 2010)(Y. Wang et al., 2013).

After the synthesis of phenylalanine, the first step in the synthesis of monolignols is described in Figure 8. It begins with the deamination of the phenylalanine side chain, or tyrosine for grasses, catalysed by the enzymes Phenylalanine/Tyrosine Ammonia Lyase (PAL/TAL). The aromatic ring is then hydroxylated by Cinnamate 4-hydroxylase (C4H), which is a cytochrome P450 monooxygenase. This is followed by Coenzyme A thio-esterification of the carboxyl

group, catalysed by 4-coumarate-CoA ligase (4CL) and leading to the formation of *p*-coumaroyl-CoA.

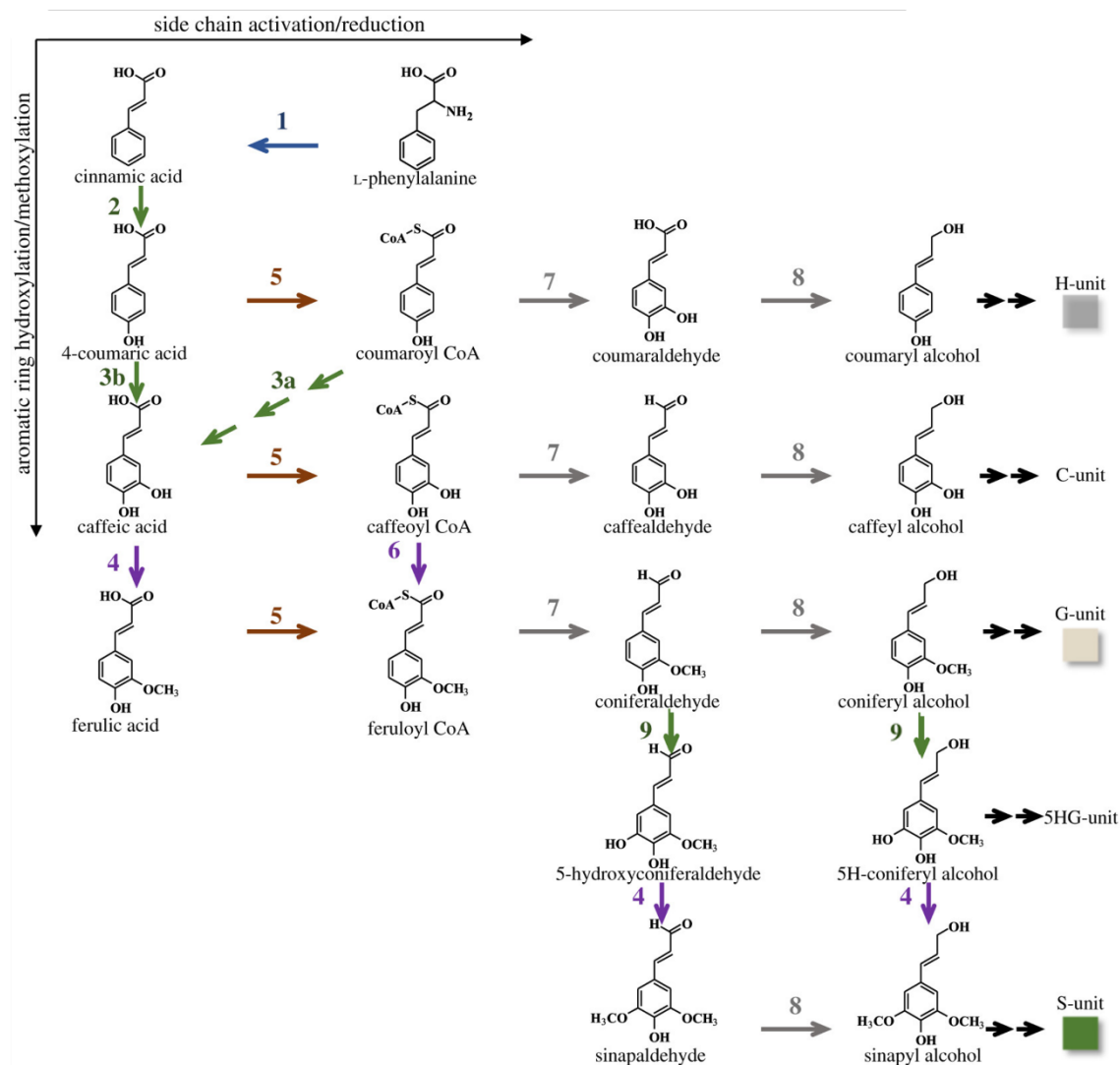


Figure 8 : biosynthesis pathway of monolignols from Dixon & Barros, 2019 : Schematic representation of the different enzymatic reactions involved in the biosynthesis of monolignol from l-phenylalanine. Deamination is represented in blue, hydroxylation in green, O-methylation in purple, CoA activation in brown and reduction in grey. The enzymes are: 1, phenylalanine ammonia lyase (PAL); 2, cinnamic acid 4-hydroxylase (C4H); 3a, hydroxycinnamoyl CoA : shikimate hydroxycinnamoyl transferase (HCT), coumaroyl shikimate 3'-hydroxylase (C3'H), and CSE; 3b, coumarate 3-hydroxylase (C3H); 4, caffeic acid/5-hydroxyconiferaldehyde 3/5-O-methyltransferase (COMT); 5, 4-hydroxycinnamate CoA ligase (4CL); 6, caffeoyl CoA 3-O-methyltransferase (CCoAMT); 7, cinnamoyl CoA reductase (CCR); 8, cinnamyl alcohol dehydrogenase (CAD); 9, ferulic acid/coniferaldehyde 5-hydroxylase (F5H).

1.1.3.6.2. Biosynthesis Regulation

The biogenesis of the cell wall requires precise coordination of the genes involved in its biosynthesis, transport and assembly of its constituents. Several transcription factors of the NAC family (for NO APICAL MERISTEM, *ARABIDOPSIS THALIANA* ACTIVATING FACTOR1/2 and CUP-SHAPED COTYLEDON) are involved in the regulation of secondary wall biosynthesis genes (Sulis & Wang, 2020), and in particular NST1 (NAC Secondary wall Thickening promoting factor) and VND1 and VND7 (Vascular-related Nac-Domain protein) in the vessels, occurs upstream of other transcription factor cascades (Yamaguchi et al., 2010). The latter factors include members of the LIM (LIN11, ISL-1 and MEC-3) and MYB (MY eloBlastosis) families, in particular MYB58, MYB63 and MYB85 (Zhong & Ye, 2009), which are expressed in the xylem where they bind to the AC sequences of the promoters of monolignol biosynthesis genes and regulate their expression. In *Arabidopsis*, the factors ZmMYB31 and ZmMYB42 have direct effects on the expression of *C4H*, *4CL*, *CCoAOMT*, *COMT* and *CAD* (Fornalé et al., 2006). Some other transcription factors can interact with factors known to regulate monolignol synthesis. This is the case, for example, of the KNOTTED ARABIDOPSIS THALIANA 3 (KNOT3) factor in *Arabidopsis* which interacts with NST1/2, the KNAT3-NST1/2 heteromorphism complex appears to regulate *F5H* to promote syringyl lignins synthesis (Qin et al., 2020). Another way to regulate monolignol biosynthesis is the phosphorylation of enzymes. However, it is difficult to detect this change due to the dynamics of this mechanism. Researchers nevertheless succeeded in identifying two phosphopeptides in 5-hydroxyconiferaldehyde O-methyltransferase (Wang et al., 2015).

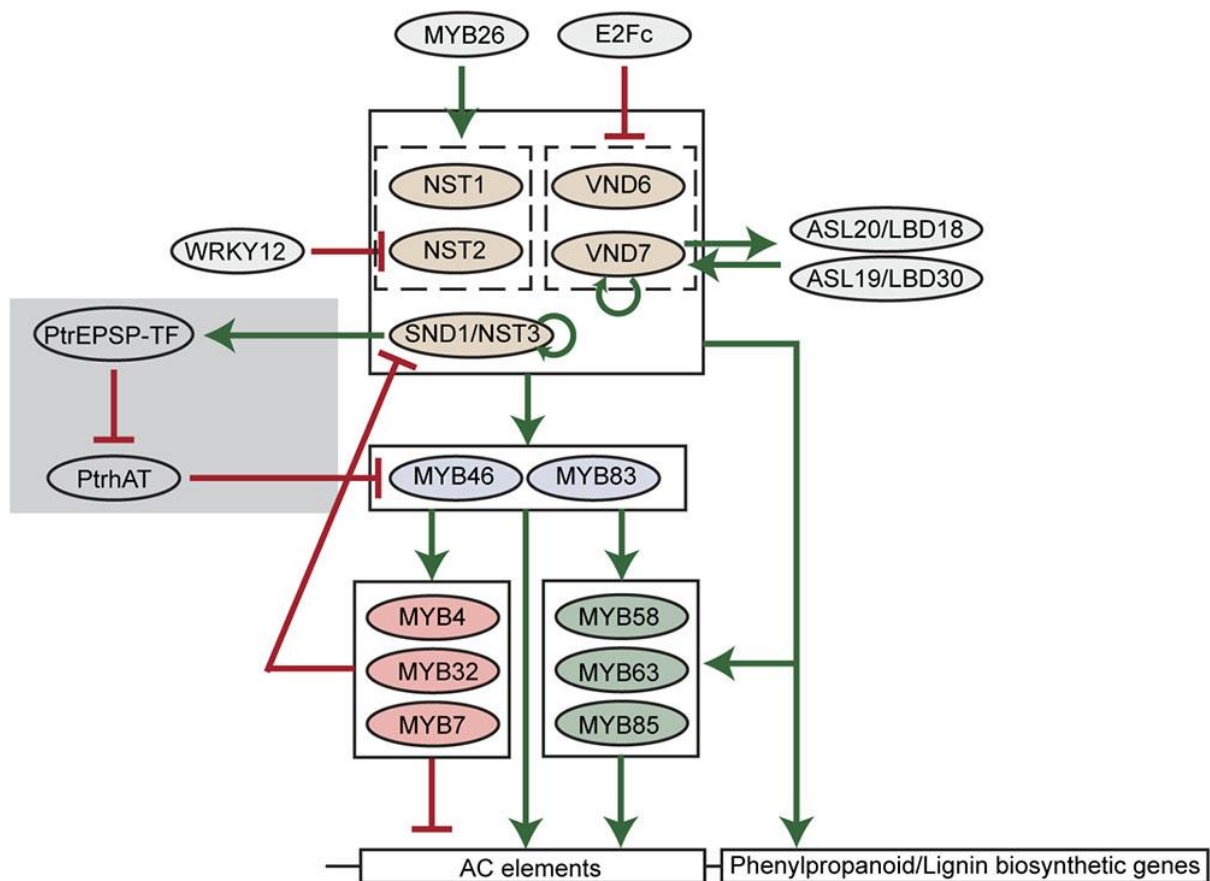


Figure 9 : A scheme of transcriptional regulation of lignin biosynthetic genes in plants from (Xie et al., 2018). Green arrows indicate transcriptional activation. Red blunt arrows indicate transcriptional repression. The gray shading indicates the woody plant-specific regulatory loop.

1.1.3.6.3. Mobility

In plants, lignins biosynthesis begins as a branch of the shikimate pathway to create monolignols and ends with their radical polymerization within the cell wall. The enzymes of the monolignol pathway are in the cytoplasm and endoplasmic reticulum, while the class III peroxidases and laccases that form the radicals necessary for lignins polymerization are located in the apoplastic space. Thus, monolignols must pass through the cell membrane before being incorporated into the growing lignins polymer.

There are currently three main hypotheses concerning this crossing. The first is that there are specific transporters, the second is that the monolignols cross the membrane passively (Vermaas et al., 2019) and the third is a Golgi-mediated transport (not seem probable) (Kaneda et al., 2008 ; Miao & Liu, 2010).

For the transporter hypothesis, it seems that monolignol glycosides are good candidates. This form reduces monolignol toxicity and reactivity. Moreover, they have been detected in gymnosperms (Terashima et al., 2016) and angiosperms (Tsuji et al., 2004). Glycosylation would be done by a Uridine-di-Phosphate Dependent Glycosyltransferase (UGT) (Lim, Jackson and Bowles, 2005). In plants, UGTs form a multigene family with more than 100 genes discovered (Le Roy et al., 2016). The monolignol then appears to be released from its sugar function by cell-wall-located beta-glucosidases to allow incorporation into lignins (Dharmawardhana et al., 1995). It also appears that the ABC (ATP-Binding Cassette) transporters can play a role in transport in Arabidopsis. AtABCG29 is a transporter that is thought to act as a *p*-coumaryl alcohol transporter at the plasma membrane (Alejandro et al., 2012). It seems that secondary active transporters such as MFS (Major Facilitator Superfamily) and MATE (Multidrug And Toxic Compound Extrusion) are also involved in membrane transport (Väisänen et al., 2020).

For the passive permeation mechanism, it appears to be accessible to monolignols. The permeability of the membrane to monolignols was shown by (Boija & Johansson, 2006) and (Vermaas et al., 2019). Only glycosylation or carboxylation of the lignins monomer significantly reduces permeability (Tsuyama et al., 2013), slowing passive diffusion and promoting transport and thus regulation by transporters.

For Golgi-mediated transport, early studies were mainly done by autoradiography. Results suggested that lignins precursors could be transported via an Endoplasmic Reticulum (ER) to Golgi pathway as for the secretion of polysaccharides to the wall. Vesicular trafficking between the cytosol and the plasmalemma could be observed in autoradiographic and ultrastructural studies in wheat (Pickett-Heaps, 1968). The developing xylem was labelled with labelled phenylalanine. The radiolabelling was then associated with the rough endoplasmic reticulum, the Golgi apparatus, and some vesicles fused with the plasma membrane or aggregated in the cytoplasm near the microtubule bands of the wall (Pickett-Heaps, 1968 ; Fujita & Harada, 1979). The ER-Golgi apparatus would thus appear to be involved in the synthesis and transport of monolignols to the cell wall. However, the radioactive precursors could be incorporated into both lignins and proteins thereby interfering with the interpretation of the autoradiography (Liu et al., 2011).

1.1.3.7. Lignins Polymerisation

The lignins polymer is formed by the oxidative polymerisation of monolignols. The three major forms are *p*-coumaryl alcohol (3-(4-hydroxyphenyl)-2-propen-1-ol), coniferyl alcohol (3-(3-methoxy-4-hydroxyphenyl)-2-propen-1-ol) and sinapyl alcohol (3-(3,5-dimethoxy-4-hydroxyphenyl)-2-propen-1-ol) that, once incorporated into the polymer are designated as H, G and S units, respectively. These monolignols differ from each other by the presence of methoxy groups in ortho and para to the phenol group.

The oxidative copolymerization of monolignols is carried out by enzymatic oxidation of the monolignols followed by radical coupling (Vanholme et al., 2010). In a first step, the monolignol is oxidized to form the radical monomer. Class III peroxidases and/or laccases could carry out this oxidation (Önnerud et al., 2002) (Figure 10). The electron of the formed radical is delocalized in the conjugated

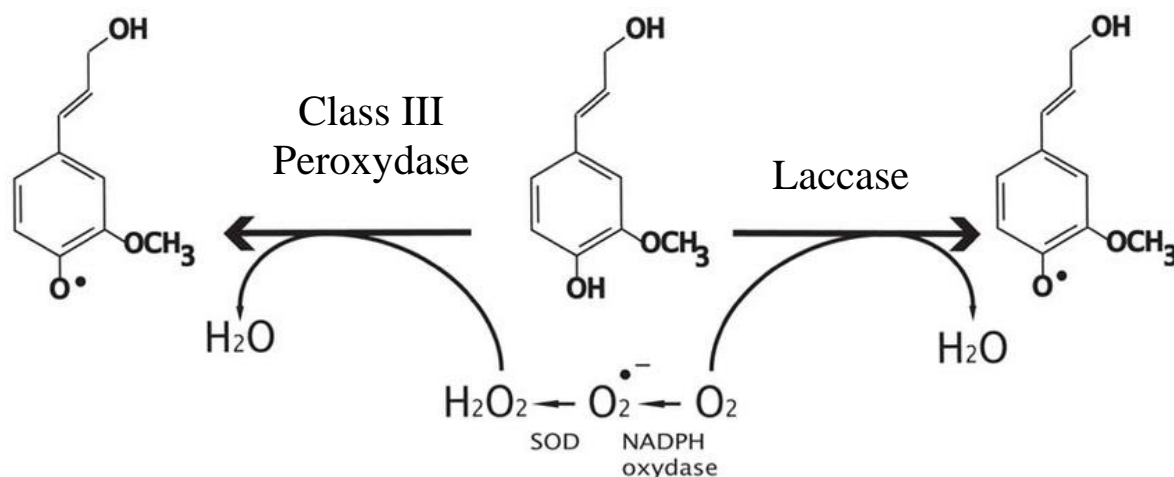


Figure 10 : Laccase- and peroxidase-mediated oxidation of coniferyl alcohol. SOD: Superoxide Dismutase.

system between the preferential positions 4, 5 and β . Two radical monomers can then couple together to form a dehydrodimer. The monomers can be linked by different types of bonds, carbon-carbon bonds (5-5 bonds, β -1, β -5, β - β), diaryl ether bonds (4-O-5 bonds), ester bonds (β -O-4), dibenzodioxocin bonds and spirodienone bonds (Figure 11) (Patil et al., 2016).

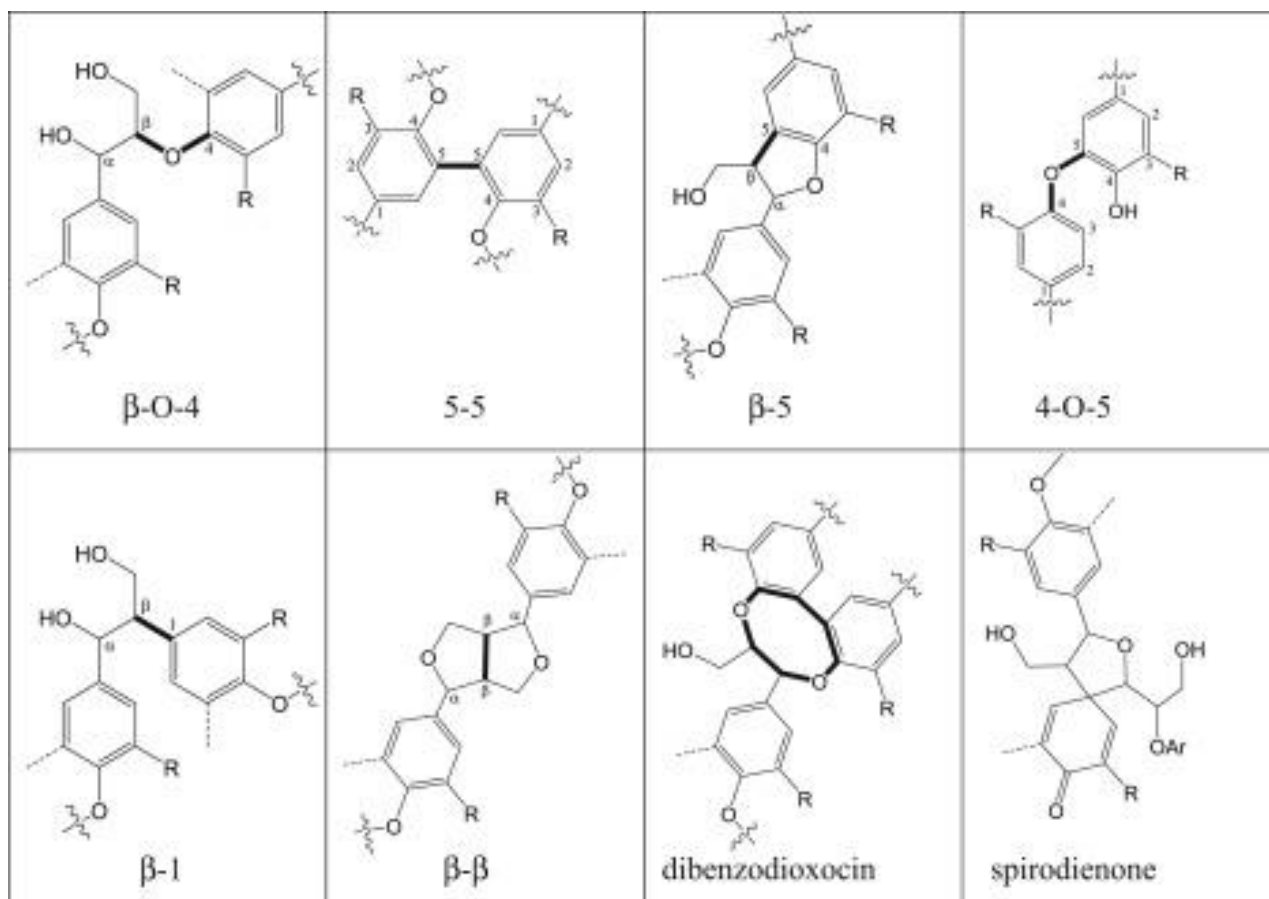


Figure 11 : Common inter-monomeric linkages in lignins (Patil et al., 2016). Numbers (1-6) and Greek letters (α , β , γ) indicate carbon atoms; bold lines represent the monolignol-monolignol bond.

Bond proportions, like those of monolignols, vary by species (Figure 12). The most abundant linkage is the β -O-4 linkage. With regards to the monolignols present, gymnosperm lignins are composed mainly of G units with small amounts of H. Dicotyledonous angiosperm lignins are composed of G and S units with small amounts of H units (Dixon & Barros, 2019). The proportion of monolignols also depends on the tissue and the stage of development. For example, the cell walls of vascular bundle cells in monocotyledons contain mostly G units, whereas interfascicular tissues contain mostly a mixture of G and S. Similarly, younger cells are less lignified than older cells.

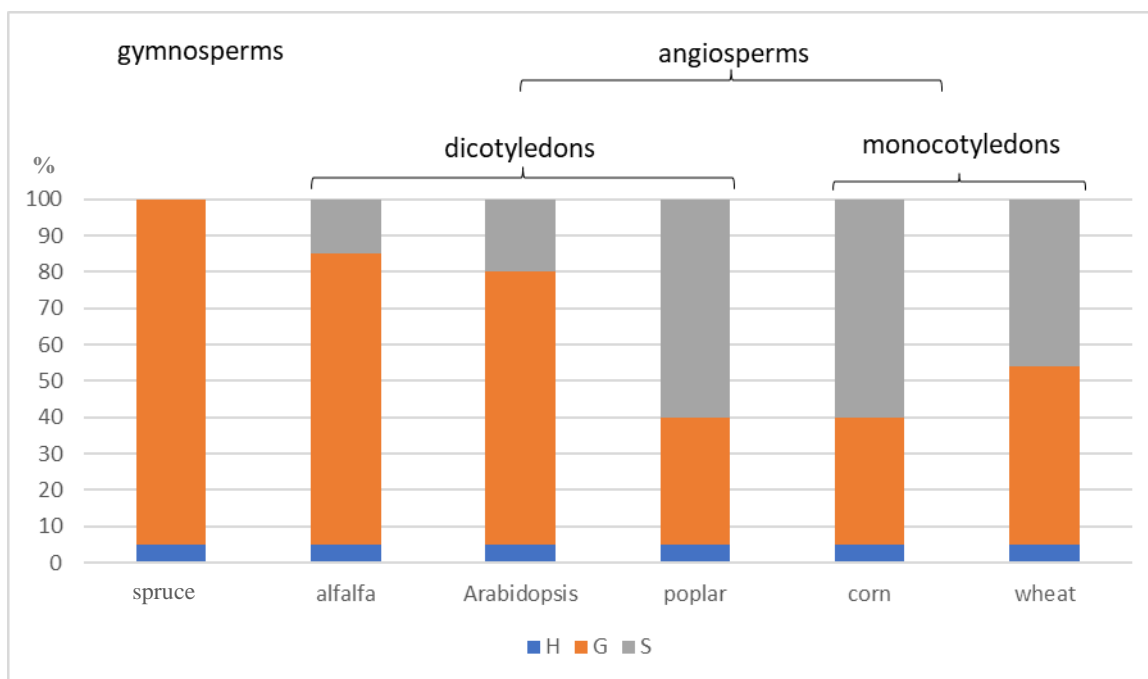


Figure 12 : Relative percentages of different lignins monomers in stems of different species according to (Dixon & Barros, 2019)

The laccases (EC 1.10.3.2) are part of the superfamily of multicopper oxidases. The laccases contain four copper atoms. The main oxidation site of the substrate is the copper center T1 (Agustin et al., 2021). They are involved in lignification, wound healing and polymerization of the integument (Gavnholt & Larsen, 2002).

Class III peroxidases (EC 1.11.1.7) are enzymes catalyzing the oxidation of several substrates in the presence of hydrogen peroxide (H₂O₂). They are involved in several physiological processes, including growth and resistance to biotic and abiotic constraints.

As said in the previous chapter, it is accepted that lignins polymerization is derived from the oxidative coupling by peroxidases and laccases of a monolignol on the growing lignins polymer. It appears that monolignol oxidizing enzymes have an important role in the spatial patterning of the lignins deposit. The presence of monolignol oxidizing enzymes in specific domains may play a role in guiding the spatial distribution of lignins at the tissue and subcellular levels. (Schuetz et al., 2014 ; Yi Chou et al., 2018 ; Hoffmann et al., 2020). In the Arabidopsis flower stem, some laccases and peroxidases are localized in the apoplast before lignins deposition (Tobimatsu & Schuetz, 2019)..

At the laccase level, their involvement in the lignification process could be demonstrated with several mutants. The double mutant *laccase4 (lac4) laccase 17 (lac17)* shows hypolignified fibers and collapsed xylem vessels in the floral stems (Berthet et al., 2011). When this mutant loses an additional laccase function *LAC11*, the *lac4 lac17 lac11* triple mutant suffers a growth defect and histochemical analysis does not detect lignins in the stem or roots (Q. Zhao et al., 2013). These studies on laccase mutants therefore suggest that the activity of certain laccases is essential for the lignification process in the xylem of Arabidopsis. Photobleaching analysis (FRAP) on LAC4 showed that LAC4 is very immobile after secretion into the secondary cell walls, (Yi Chou et al., 2018) suggesting that LAC4 is specifically secreted and tightly anchored to polysaccharide-rich secondary cell wall domains (Schuetz et al., 2014 ; Yi Chou et al., 2018). In *Chamaecyparis obtusa* wood (Japanese cypress), LACCASE (CoLac1) and LACCASE3 (CoLac3) are likely to be responsible for the deposition of H-type and G-type lignins in the walls of compression wood. (Hiraide et al., 2021).

Like laccases, class III peroxidases are involved in lignification. (Barros et al., 2015). In Arabidopsis, PEROXIDASE64 is involved in lignification in the Casparian strip and down-regulation of *ATPRX64* by microRNAs leads to a loss of function of the Casparian band (Lee et al., 2013). Knockout mutations of several peroxidase genes show a minor reduction in lignins content and/or alteration of lignins in inflorescence stems of Arabidopsis. The *PEROXIDASE 17* knockout shows a decrease in the amount of lignins (Cosio et al., 2017). Knockout of *ATPRX52* results in a reduction of syringyl units mainly in the interfascicular fibers of the stem and a decrease in the amount of lignins (Fernández-Pérez et al., 2015a). In the *atprx72* mutant, there is also a slight decrease in the amount of lignins (Fernández-Pérez et al., 2015b).

1.1.3.8. Polysaccharide and lignins interactions

The ultrastructure of the cell wall is complex. The primary cell wall is strong to resist tensile forces resulting from the pressure of extensible to allow relaxation of wall stresses that motivate cellular water uptake and physical enlargement of the cell (Hamant & Traas, 2010). The secondary wall has compressive and tensile strength, but is not extensible. Lignin-carbohydrate bonds hold the different wall polymers together and contribute to the properties of the wall. In 1866, the hypothesis of existence of links between lignins and carbohydrates

was put forward to explain the inability to separate lignins from carbohydrates (Erdmann, 1866). Among these links, there are different notable links between polymers.

- Cellulose/hemicelluloses interactions: in primary walls, the structure is currently described as consisting of cellulose microfibrils bound to xyloglucans with pectin filling spaces between microfibrils. Xyloglucan hemicelluloses generally have a main glucan chain similar to that of cellulose. This structure may allow hydrogen-bond-mediated binding to cellulose chains in the same way as in cellulose microfibrils (Grantham et al., 2017). These results were obtained either by microscopy or by chemical or enzymatic digestion, which limits the understanding of non-covalent binding. However, there are still doubts about this model because the binding between cellulose and xyloglucans is not dynamic. Moreover, the analysis of the cell wall by multidimensional NMR and characterization of mutants has provided new insights into cell wall structure. When observing xyloglucan-deficient mutants (*xylosyltransferase1/xylosyltransferase2 [xxt1/xxt2]*), they show a development close to that of the wild type (Park & Cosgrove, 2012) except for a reduced size. This result calls into question the role of xyloglucan.

- Cellulose-lignins interaction: bioinformatics modeling on lignins-cellulose interactions suggests that lignins binds preferentially to hydrophobic cellulose surfaces (Lindner et al., 2013)

- Hemicelluloses-lignins interaction: either by binding to the ferulate substituents of xylan, although this binding is poorly represented in dicots (Terrett & Dupree, 2019), or by methide re-aromatization of quinone (produced upon coupling of monolignols via their β -carbon) by nucleophilic addition at the α -position of nucleophilic groups of xylan and mannan (Mottiar et al., 2016) (Figure 13).

Despite the progress on the understanding of the wall structure, there are still many elements to be discovered to fully describe the relationship between the molecular structure and physical properties of the wall.

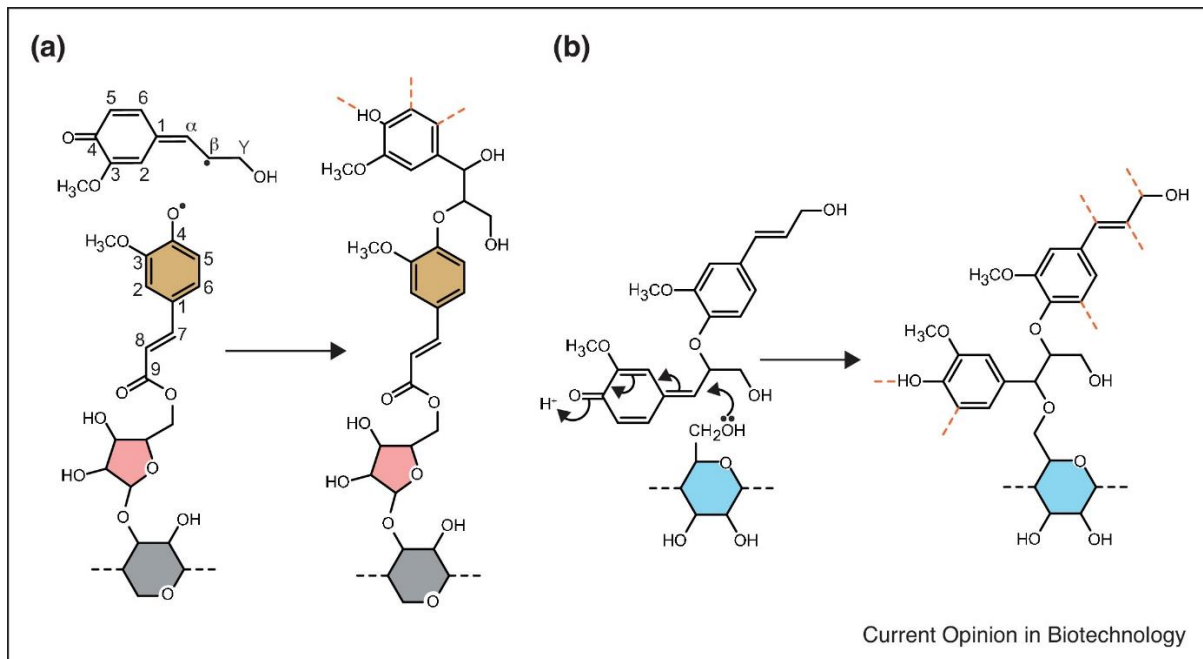


Figure 13 : hemicellulose:lignins cross-linking. (a) Radical coupling of a monolignol to ferulated xylan. The backbone xylosyl residue (grey) is substituted by 3-linked arabinosyl residue (pink), which is modified by a ferulate (brown). A β -O-4 linkage between the ferulate and a monolignol is shown, but other linkages can occur. (b) Re-aromatisation of the quinone methide intermediate by hemicellulose nucleophiles. The quinone methide intermediate of two monolignols forming a β -O-4 linkage is shown. The intermediate is re-aromatized by the carbon 6 hydroxyl of a mannosyl residue of galactoglucomannan. A mannosyl residue (blue) ether-linked to a dilignol is shown, but other glycosyl residues could form the bond. Curly arrows show the movement of electrons. Further lignins polymerisation can occur at carbons marked by orange dotted lines from (Terrett & Dupree, 2019)

1.2. Lignins analysis

A good understanding of lignins metabolism necessarily requires the use of techniques for their determination. In many articles, two approaches of "wet chemistry" have been preferred, according to the plant species and the tissues containing more or less amounts of lignins. These techniques require a preliminary step of chemical degradation. The plant material is first ground and lignins extracted with solvents. The degradation can be done by hydrolysis,

solvolysis, oxidative degradation or reductive cleavage and allows to isolate the lignins in poly- or monomeric form to analyse its structure. The analysis is sometimes coupled with chromatographic methods.

Thus, the method using the solubilisation of lignins by acetyl bromide (Morrison, 1972a ; Morrison, 1972b) is well adapted to herbaceous species, whereas the gravimetric Klason method (Johnson et al., 1961) is more suitable for woody species. More recently, a new method, named Cysteine-Assisted Sulfuric Acid (CASA,) was established for measuring the lignins content of lignocellulosic biomass by UV spectrophotometry, based on the full dissolution of whole biomass in 72% sulfuric acid (SA) containing cysteine (Lu et al., 2021).

There are also different methods for determining the H, G and S subunit composition, S/G ratio and more generally lignins structure. Historically, thioacidolysis (Lapierre et al., 1986) and nitrobenzene oxidation (Monties, 1989) methods were used, which are gradually being replaced by pyrolysis coupled with GC/MS (Wagner et al., 2007), NMR (Mansfield et al., 2012). and vibrational spectroscopy.

1.2.1. Quantification of lignins

Acetyl bromide, thioglycolic acid and Klason are the most commonly used methods to quantify lignins. The first two methods are based on the solubilization of lignins and the determination of absorbance values at 280 nm.

Acetyl bromide is used to solubilize lignins under acidic conditions (acetic acid). The free hydroxyl groups will be acetylated and the OH group of the α -carbon will be replaced by a bromide which allows a complete solubilization of the lignins in acidic conditions. Since this is not a direct method, an overestimation of the lignins content may occur due to the oxidative degradation of structural polysaccharides (e.g. xylans) during the incubation of the cell wall with the acid solution (Morrison, 1972a).

The thioglycolate method: Lignins in the presence of thioglycolic acid forms benzyl alcohol groups. Under alkaline conditions, the polymer will be solubilized. The lignins content can be underestimated due to the specificity of the reaction with ether bonded lignins types (Brinkmann et al., 2002).

The Klason method is a gravimetric test used for the direct quantification of lignins. In this method, an insoluble lignins fraction is extracted from plant tissues after digestion with 72% sulfuric acid. The cell wall polysaccharides are then partially solubilized. During the experiment, other non-extracted compounds can be measured, such as proteins and polysaccharides, which leads to an overestimation of the lignins content. On the other hand, a significant fraction of the soluble lignins cannot be measured, leading this time to an underestimation of the lignins content.

The CASA method Biomass is dissolved in 72% sulfuric acid containing 0.1 g/mL of l-cystein. The absorbance of the solution is measured at 283 nm (Lu et al., 2021).

1.2.2. Composition and structural characterization

Structural analysis by mass spectrometry: When lignins are pyrolyzed, before injection into the apparatus, the different bonds uniting the polymer are cleaved, releasing different fragments characteristic of the three main phenylpropanol units. The analysis of the fragments resulting from this pyrolysis by GC-MS thus makes it possible to trace the monolignol composition. This analysis technique has been widely described in the literature, proving its interest.(Del Río et al., 2012 ; Bule et al., 2013). The mass spectra obtained allow the identification of the derivatives of H, G and S units while the integration of the chromatogram peaks gives their relative proportions within the polymer. This technique is a good alternative to the older methods of chemical determination of lignins (Lupoi et al., 2015). Some lignins contaminants can also be detected during this analysis. This is for example the case of residual sugars. Indeed, during the pyrolysis, these last ones will be converted into furfural which will be detected in GC-MS. The presence of residual fatty acids can also be detected. Constant et al., 2016 observed these type of compounds in both soda and organosolv lignins, which proves that these molecules, naturally present in the plant, are resistant to the different methods of extraction of lignins.(Constant et al., 2016).

Structural analysis by NMR (Nuclear magnetic resonance) : NMR is probably the analytical technique that has provided the most information on the structures of lignins. It enables identification of the different bonds between the monomers and of the different chemical functions that the polymer carries. This last information is essential when a functionalization

of the polymer is envisaged in the context of its subsequent valorization. The 2-dimensional Heteronuclear Single Quantum Coherence Nuclear magnetic resonance (2-D HSQC NMR) has provided many details on the different types of bonds that link the aromatic units. A library of motifs present in lignins is now available (Lahive et al., 2020). This technology has proven to be particularly efficient to identify the different aromatic units composing the polymer (Del Río et al., 2012 ; Heikkinen et al., 2014). But it is technically limited for the quantification of these different units. Proton NMR is also used alone for the analysis of lignins and can allow the quantification of the amount of methoxy groups present in the polymer (Aberu & Freire, 1995). However, this method requires the prior acetylation of the material. Phosphorus NMR is a method of choice for determining the amount of alcohol, phenol and carboxylic acid functions present in lignins. This type of assay requires the prior functionalization of lignins with a reagent bearing a phosphorus atom, most often 2-chloro-4,4',5,5'-tetramethyl-1,3,2-dioxaphospholane (TMDP), and the introduction of an internal standard into the medium to quantify the different functions. This standard has a free hydroxyl group that will also react with TMDP. Cyclohexanol and cholesterol have been widely used for this purpose.(Crestini & Argyropoulos, 1997 ; Argyropoulos, 1994). However, it has recently been shown that the latter can lead to an underestimation of the quantity of functions actually present. The use of N-hydroxy-5-norbornene-2,3-dicarboximide is therefore recommended.(Balakshin & Capanema, 2015). In general, this method, although particularly sensitive, remains to be optimized and standardized (Santos et al., 2012 ; Bouxin et al., 2015).

Structural analysis by vibrational spectroscopy: The spectroscopic methods are simple to set up and easily applicable to lignins. The vibrational spectroscopy methods are based on the interaction between electromagnetic waves and the vibration mode of molecular chemical bonds. The spectra obtained show peaks specific to chemical bonds. This part will be detailed in part 0 Spectroscopy imaging technology.

1.2.3. Lignins imaging

The analysis of lignins does not only involve its quantitative characterization, but also its spatial characterization. With the methods described above, there is a loss of spatial information due to a destruction of the sample. Even if some spatial information can be preserved by microdissection for example, they are not precise enough to study lignification at the cellular level. Different techniques to access the spatial information of lignins will be described below.

Histochemistry

Histochemical staining techniques have been used for decades to visualize lignins. The evolution of these techniques has allowed a better precision in the localization of lignins.

The two most known stains are the Weisner reaction (phloroglucinol HCl) (Clifford, 1974) (Figure 14 A) and the Maüle reaction (Meshitsuka & Nakano, 1979) (Figure 14 B). The Weiser reaction is the reaction between phloroglucinol and cinnamaldehyde groups of lignins giving a red coloration visible in transmitted light in the presence of negative ions. This reaction is however not specific to lignins because it can also react with other phenolic compounds such as cimanyl alcohol. The reaction occurs with the three monomers of lignins and the composition of lignins does not influence this coloring. The Maüle reaction is specific to monomers derived from sinapyl alcohol and generates 3-methoxy-O-quinone structures and gives a red-violet coloration in transmitted light. The Maüle staining can be improved by replacing the ammonia buffer with Tris-HCl. This improvement allows to distinguish the S and G units in fluorescence microscopy under blue light (Yamashita et al., 2016).

Other histochemical stains can be used to visualize lignins. Basic fushin forms a fluorophore with the lignins polymer making it detectable by fluoroscopy (D. Dharmawardhana et al., 1992). Subsequently, it was shown that the amount of lignins influenced the signal, but that the composition did not (Kapp et al., 2015). Safranin can also be used to stain lignins (Figure 14 C). It forms π - π interactions with aromatic molecules and is not specific to lignins. It is therefore often used with Astra blue, cellulosic walls will appear blue and lignified walls red by transmission microscopy (Tolivia & Tolivia, 1987). Safranin can also be used alone, but in this case, it should be observed with a fluorescence microscope, the lignins-rich tissues will

see their emissivity spectra fade after 568 nm compared to a spectrum low in lignins when excited at 488 nm (Baldacci-Cresp et al., 2020).

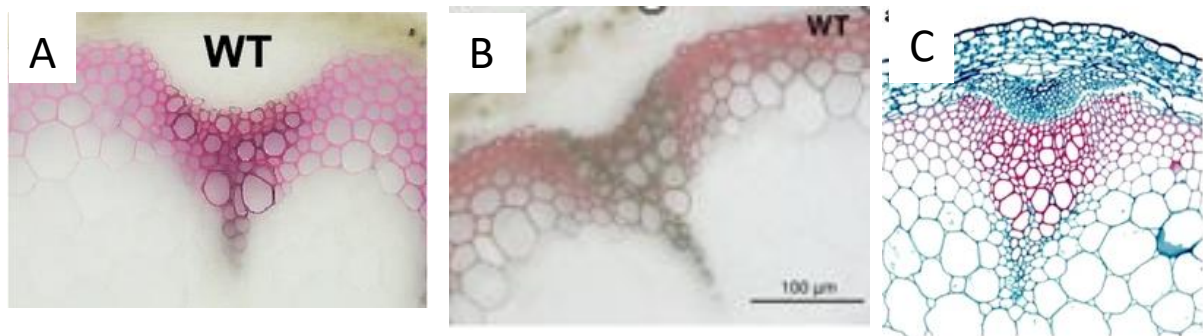


Figure 14 Different colorations with bright field observation on *Arabidopsis thaliana*. A) Phloroglucinol (Qin et al., 2020), B) Maüle (Ho-Yue-Kuang et al., 2016), C) Safranin and fast green (Li et al., 2019)

Immunolocalization

Anti-lignins antibodies were first obtained from synthetic H, G and mixed G-S lignins with predominantly β -O-4 liaison (Freudenberg, 1956). These antibodies were used on fixed corn sections and labeled with secondary antibodies bound to gold particles for observation by transmission electron microscopy. Subsequently, S-homopolymer antibodies were obtained (Joseleau et al., 2004). Similarly, antibodies directed against β -5' and β - β linkages (Kiyoto et al., 2015) were used on cypress wood. The problems with this method are that it requires time-consuming sample preparation and that commercial antibodies don't exist, which explains the limited development of this strategy despite its high resolution.

Autofluorescence

Lignins are naturally autofluorescent. The emission range of lignins is wide because it has different types of fluorophores. It can be excited by UV and visible wavelengths. Physical factors such as pH can influence the autofluorescence. The autofluorescence of lignins can be obtained by excitation between 240 nm and 320 nm to obtain a maximum emission at 360 nm (Albinsson et al., 1999) and used in spectroscopy. This fluorescence comes from the benzene ring of the lignins monomers and more particularly from the phenylcoumarans resulting from the bond between the monolignols. Depending on the substitution present on the ring, the emission of fluorescence will vary (Djikanović et al., 2007). It is therefore possible to identify different types of lignins from the shades observed. As far as imaging is concerned, lignins can be excited at 355 nm (UV), 488 nm (blue light) (Donaldson, 2013). The UV emission is due to

the phenolic molecules of the lignins, so it is possible to detect other phenolic compounds along with the lignins. However, this method has little contrast between highly lignified and poorly lignified walls, suggesting that the amount of lignins has a limited influence on the fluorescence intensity. On the other hand, autofluorescence produced by excitation at 488 nm shows a strong contrast between highly and low lignified areas (Donaldson, 2020). Several semi-quantitative methods can be used for the observation of lignins: total internal reflection fluorescence (TIRF), fluorescence lifetime imaging microscopy (FLIM), fluorescence recovery after photobleaching (FRAP), two-photon microscopy (TPM), Förster resonance energy transfer (FRET) and stimulated emission depletion (STED).

Bioorthogonal chemistry: biomolecule tagging with click chemistry

History

Biomolecules have roles and functions in an organism within a specific environment. It is therefore important to visualize these entities in the complexity of their environment to ensure that their functions are not impaired. To enable this visualization, different methods have been developed to graft labels onto the targeted biomolecules in order to distinguish them and study their behaviour.

The efforts developed to this end have led to major scientific discoveries such as the green fluorescent protein (GFP) and its different variants (Tsien, 1998 ; Zhang et al., 2002). The considerable impact of this discovery allowed Shimomura, Chalfie and Tsien to obtain the Nobel Prize in chemistry in 2008. This protein and its derivatives are still widely used today, notably by genetically engineering them into proteins of interest. The synthesized GFP-proteins are thus easily detectable by fluorescence microscopy. Despite its efficiency for the study of proteins, this technology also has several drawbacks. It is not compatible with the monitoring of other biomolecules such as nucleic acids, lipids, glycans as well as many proteins undergoing crucial post-translational modifications. Another limitation of GFP is its relatively large size (27 kDa) which can lead to structural changes and alter the localization and function of the protein on which it has been grafted.

More recently, new reactions have been developed using bio-orthogonal chemistry. They were initiated by the team of Pr. Carolyn Bertozzi (Hang et al., 2003) and are based on the optimization of some pre-existing highly specific reactions. These reactions have allowed to study the functions and localization of biomolecules, within various living systems. Such chemical reactions differ from classical "click" reactions and require that a number of different conditions (below) are met in order to be applied in a biological context:

- Biocompatibility: defines a reaction that can be carried out under physiological conditions (room temperature, atmospheric pressure, pH, aqueous medium and presence of oxygen) and compatible with a living system (non-toxic and not disrupting its metabolism);

- Selectivity: reaction in which the reagents react specifically with each other and irreversibly, without interacting with the functions of the biomolecules present in the medium (biological nucleophiles such as thiols and amines, enzymes...);
- Kinetics: the speed of such reactions must be fast in order to offer an efficient tool and minimize the possible disturbances or toxicity in the biological environment;
- Stability in aqueous medium: the reagents involved must be stable in biological medium (facing hydrolysis and oxidation), as well as the products resulting from their reaction (the bond formed must be covalent and stable)

To graft a label onto a biomolecule of interest via a bioorthogonal reaction, one must first incorporate a bioorthogonal reactive function. The probe can be added in a second step to label the biomolecule (Figure 15). Several methods have been developed to address the problem of incorporating the binding function. This integration can be done by a direct chemical modification, by incorporation of elementary building blocks (oses, amino acids, etc.) not naturally occurring, or by enzymatic modification.

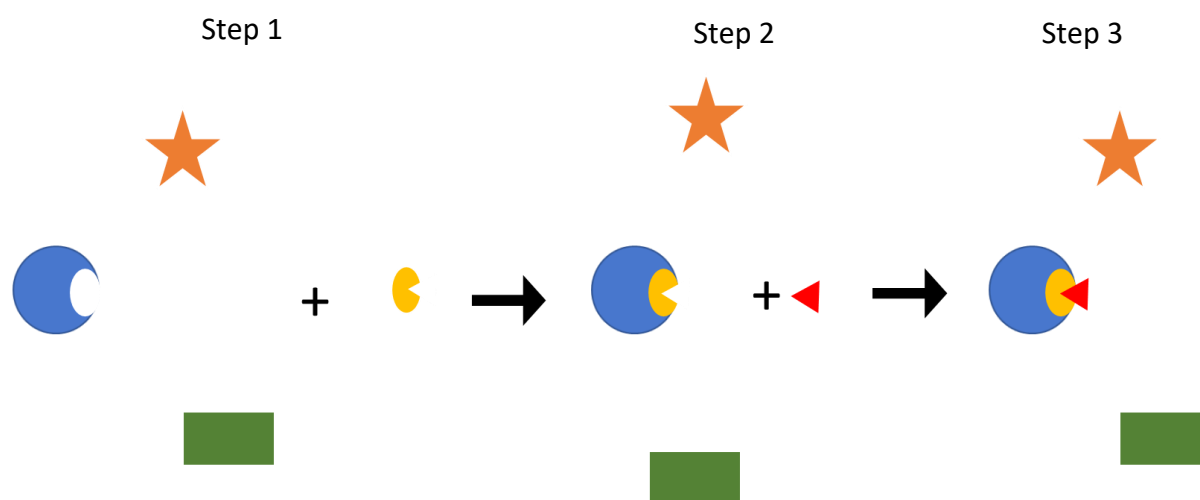


Figure 15 : Labelling of a biomolecule by bioorthogonal chemistry. Step 1 is the first step in which the chemical reporter (yellow oval) is added to the sample containing the target biopolymer (blue circle), as well as other molecules that not affected by the reaction (green rectangle and orange star). The reporter is the bioorthogonal compound with the reactive function to be incorporated. Step 2 is the addition of the probe (red triangle). Step 3 is the specific (bioorthogonal) reaction of the probe with the chemical reporter that leads to the specific labelling of the target biopolymer.

Principal bioorthogonal reactions

Staudinger reaction

Staudinger ligation involves completely artificial reaction partners, a phosphine and an azide (H. Staudinger & Meyer, 1919). It is the first bioorthogonal reaction with this attribute described in the literature. The azide used in this reaction is one of the most suitable functional groups for bioorthogonal chemistry. It is very stable under physiological conditions and does not react with chemical functions present in biomolecules.

It was in 2000 that Bertozzi's group discovered the usefulness of the azide function in bioorthogonal chemistry by developing the Staudinger ligation (Saxon & Bertozzi, 2000). This reaction is a variant of the reduction of azides to primary amines by triphenylphosphine described in 1919 by Staudinger and Meyer (von H. Staudinger & Meyer). In 1919, the classical reduction reaction, the addition of phosphine to the azide leads to an aza-ylide intermediate that is then hydrolyzed in aqueous media, giving the phosphine oxide and a primary amine. By installing an ester group in ortho of the phosphorus on one of the aromatic rings of the phosphine, it is possible to trap the aza-ylide intermediate leading to the formation of a very stable amide bond (Figure 16).

Subsequently, the ligation was adapted by reacting the azide with a thioester carried by the phosphine. The oxide of the phosphine will be removed to form a peptide bond, this reaction has been called "traceless Staudinger ligation" (Nilsson et al., 2000).

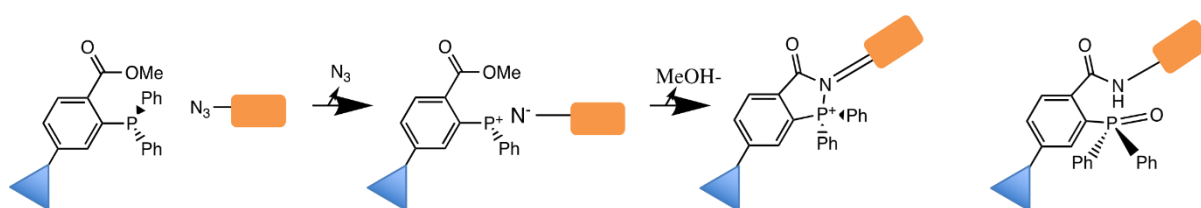


Figure 16 : Mechanisms of Staudinger- Bertozzi Ligation (Saxon et al., 2002). The first step is the attachment of the azide containing molecule (orange rectangle) to the triphenylphosphine containing molecule (blue triangle). An iminophosphorane intermediate is formed and reacts with the phosphine. The phosphorus of the phenyl traps the iminophosphorane and forms the amide bond.

CuAAC reaction

Among the bioorthogonal click chemistry reactions, there is the Copper(I)-Catalyzed Alkyne-Azide Cycloaddition (CuAAC). This is a 1,3 dipolar cycloaddition between an alkyne and an azide to form a 1,2,3-triazole by means of copper(I) catalysis (Figure 17) that can be carried out at room temperature and pressure (Rostovtsev et al., 2002). This reaction is an improvement of the Huisgen reaction (Huisgen et al., 1964) which takes place at high temperature and pressure, conditions incompatible with living systems. Moreover, the CuAAC reaction has higher kinetics. However, one problem with CuAAC is the toxicity of copper to living organisms. To overcome this problem, copper sulfate pentahydrate associated with sodium ascorbate which will reduce the copper *in situ* is added, thus allowing the use of CuAAC *in vivo*.

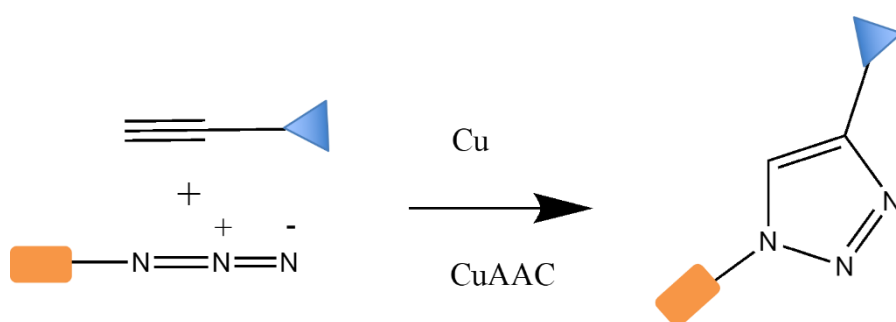


Figure 17 : Copper(I)-Catalyzed Alkyne-Azide Cycloaddition (CuAAC) mechanism. With copper, an alkyne containing molecule (blue triangle) reacts with an azide containing molecule (orange rectangle) to form a 1,2,3-triazole.

SPAAC reaction

The reaction between phenyl azide and cyclooctyne was described in 1960 (Wittig & Krebs, 1961). Cyclooctyne, the smallest stable cyclic alkyne, has angles of only 158° on either side of the alkyne function which induces an increased intrinsic reactivity allowing cycloaddition with azides without catalyst and at room temperature. There is also the Strain Promoted [3+2] Alkyne-Azide Cycloaddition (SPAAC) reaction (Figure 18). This reaction was born from the research of the Betozzi's team to overcome the non-compatibility of CuAAC with the biological system (Agard et al., 2004). It is a cycloaddition that does not use copper but the ring voltage

to achieve, which allows the reaction to be biocompatible. The terminal alkyne being replaced by a cyclooctyne, the ring tension will activate the carbon-carbon triple bond and allow the cycloaddition to take place (Figure 18).

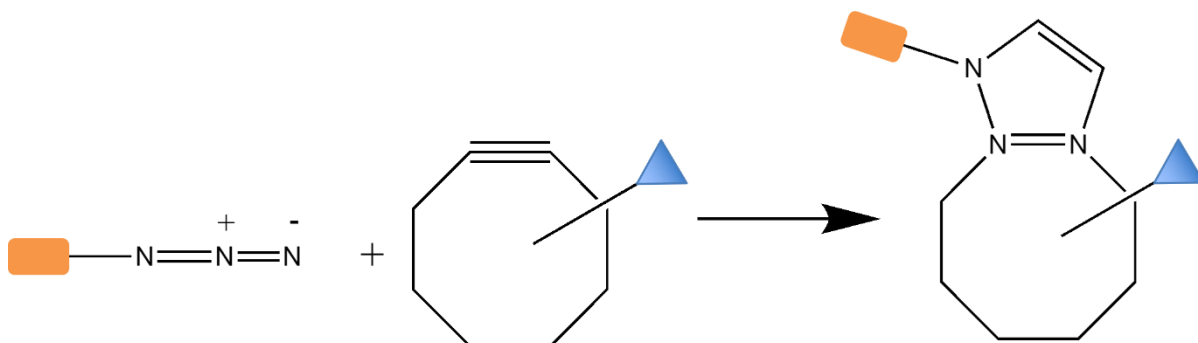


Figure 18 : Strain Promoted [3+2] Alkyne-Azide Cycloaddition (SPAAC) mechanism. Azide reacts with cyclic alkyne to form a triazol structure. The orange rectangle represents the rest of azide molecule and blue triangle the rest of cyclic alkyne.

DAinv reaction

The Diels-Alder reaction is an addition of an alkene or substituted alkyne to a conjugated diene (Hydrocarbon containing two carbon-carbon double bonds) to form a cyclohexene derivative. This reaction was elucidated in 1928 by O. Diels and K. Alder (Diels & Alder, 1928) who received the Nobel Prize in Chemistry in 1950 for their work on this reaction.

The inverse electron demand Diels-Alder (IEDDA) reaction is a reaction that has been developed recently thanks to the development of new dienophiles and the association with tetrazine (Figure 19). This reaction has faster kinetics than the two reactions presented previously. It has an excellent orthogonality and biocompatibility.

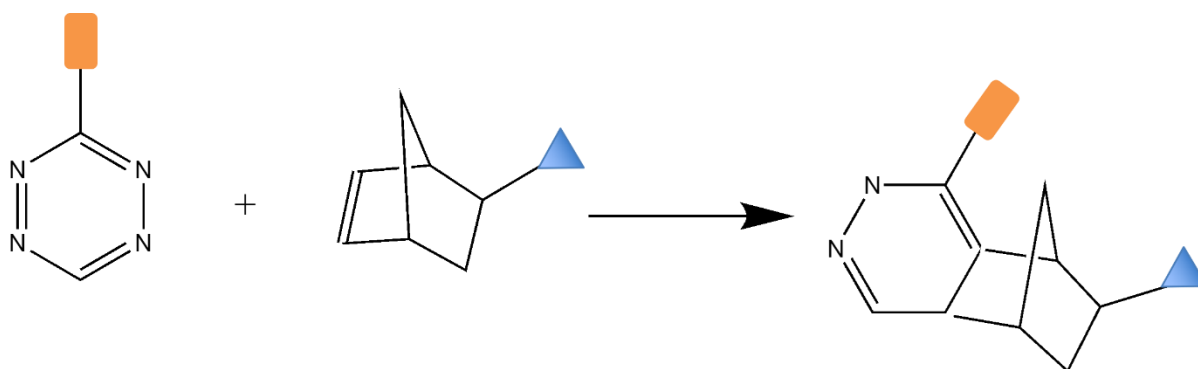


Figure 19 : Inverse electron demand Diels–Alder (IEDDA). Tetrazine reacts with the dienophile to form a cycloadduct. The orange rectangle represents the rest of the tetrazine molecule and blue triangle the rest of the dienophile.

Metabolic tagging in plants

Bioorthogonal chemistry is used to study the localization, distribution, trafficking, and activity of biomolecules. This non-invasive method can be performed at the level of cells, tissues and organisms. A range of different molecules have been studied in plants using this method.

Pectin labelling:

Pectin was the first plant cell wall molecule to be labelled using click chemistry. Anderson's team used CuAAC in 2012 to visualize the incorporation of a fucose analogue bearing an alkyne group (FucAl) (Anderson et al., 2012) (Figure 20 A) . This analog is incorporated into rhamnogalacturonan-I. After fixation of the fluorophore by click chemistry, observation by fluorescence microscopy shows incorporation into the root cell wall and plasmolyzed cells (Figure 20 B).

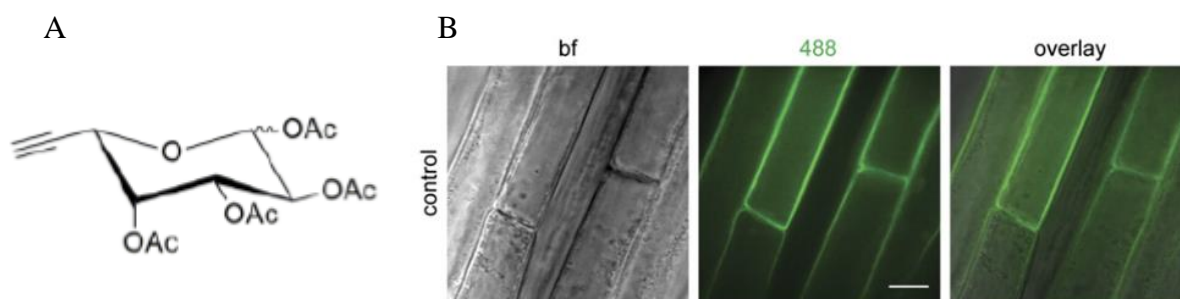


Figure 20 : A) FucAl molecule. B) localization of FuCAI incorporation in plasmolyzed *Arabidopsis thaliana* cells after click reaction with the Alexa 488-azide fluorophore. From left to right: bright field image, confocal 488 nm fluorescence image and superposition of bright field and 488 nm images. Scale bar 10 μ m. Adapted from (Anderson et al., 2012)

The same team used a chemical reporter analog of 3-deoxy-d-manno-oct-2-ulosonic acid (KDO) with an azide label (KDO-N₃) (Figure 21 a) to follow the incorporation into rhamnogalacturonan-II. Reporter incubation on *Arabidopsis* seedlings followed by fluorophore coupling by CuAAC click chemistry shows RGII labelling (Figure 21 b). Labelling of RGI and RGII via FucAl and KDO-N₃ on the same seedling using 2 consecutive CuAACs (Figure 21b) allowed the first double labelling of plant cells (Dumont et al., 2016).

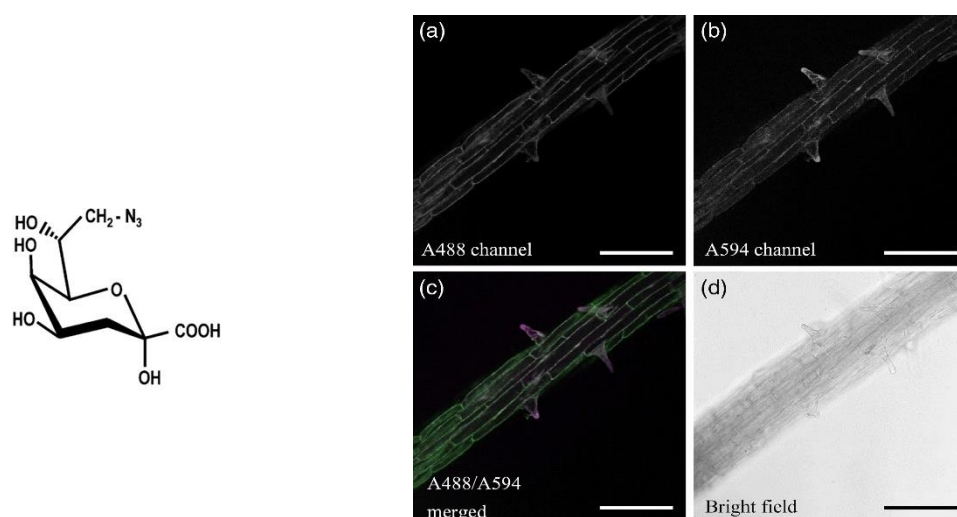


Figure 21 : a) Kdo-N3 molecule. Localization of the double labelling of pectins by FucAl and KDO-N3 of an *Arabidopsis* seedling root revealed by two consecutive CuAAC allowing Alexa Fluor ®488-alkyne (A488) and Alexa Fluor ®594-N 3 binding. (a) KDO-N3 labelling (b) FucAl labelling (c) superposition of 488 nm and 594 nm channels. (d) bright field. Adapted from (Dumont et al., 2016)

Other polysaccharide labelling:

Since these early successes in plant cell wall polymer labelling, other monosaccharides have been developed to study glycan synthesis. Azides of N-acetylglucosamine, N-acetylgalactosamine, L-fucose and L-arabinofuranose have been successfully integrated into glycans, but this time the click reaction was a Diels-Alder cycloaddition reaction to avoid copper toxicity (Hoogenboom et al., 2016).

Phospholipid labelling:

Phospholipids are important molecules of plant membranes. To visualize their dynamics, a structural analogue (propargylcholine) of choline has been used to label the main membrane lipids. This molecule has been successfully incorporated in *Arabidopsis thaliana* and revealed through a click reaction allowing to attach a fluorophore to the azide of propargylcholine in different cell types (Figure 22) (Paper et al., 2018).

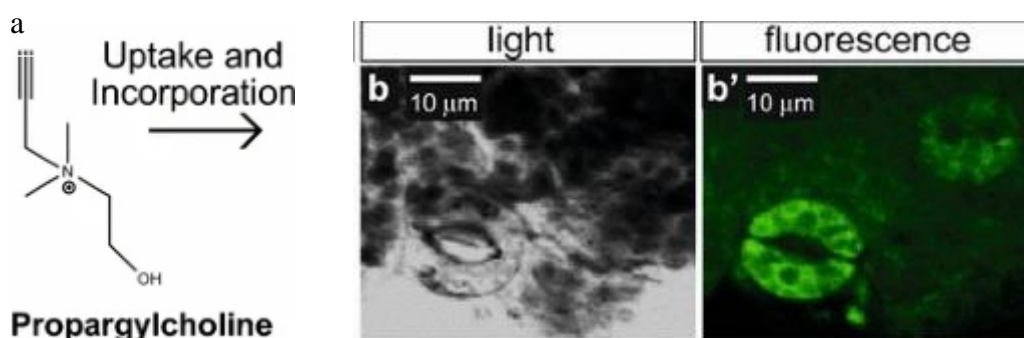


Figure 22 : Propargylcholine labelling of *Arabidopsis thaliana* guard cells in leaves after a click reaction with the Alexa 594-azide fluorophore. a) propargylcholine molecule. b) brightfield observation, b') propargylcholine labelling. Adapted from (Paper et al., 2018)

Hormone binding-site localization :

Click chemistry can also be used to localize hormone binding sites. This is the case for example for auxin. This molecule is important for the plant growth. Indole-3-propionic acid is an active structural analogue of auxin with a tag (Mravec, Kračun, Zemlyanskaya, et al., 2017). These studies revealed auxin binding sites different from the ABP1 site.

Lignins labelling:

The newly synthesized lignins can be visualized by metabolic incorporation techniques of lignins precursor analogs with a label allowing fluorophore binding. Fluorophores are fixed by a click reaction. The first studies using bioorthogonal chemistry to follow the lignification process were done with two different coniferyl alcohol (G unit) analogues (Tobimatsu et al., 2014 ; Bukowski et al., 2014). For the first G analogue, the alkyne was attached to the primary

alcohol via a peptide bond while the second substituted the methoxy group with a propargyl group. A third analogue was designed the following year by replacing the methoxy group by an alkyne group (Pandey et al., 2015). A CuAAC reaction was used to visualize the incorporation of the different molecules (Figure 23).

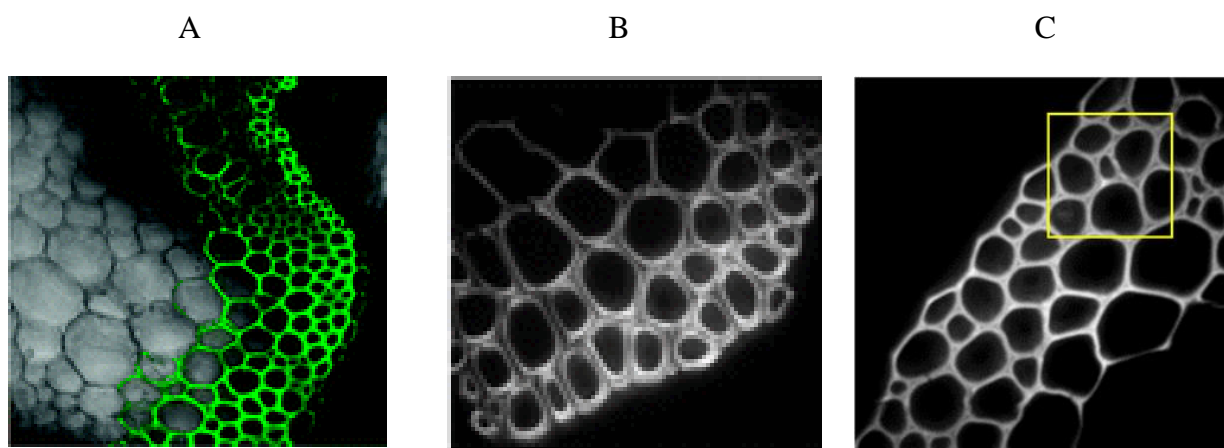


Figure 23 : Images of different G analogue incorporation profiles in Arabidopsis stems following a CuAAC bioorthogonal reaction. A) (Tobimatsu et al., 2014), B) (Bukowski et al., 2014), C) (Pandey et al., 2015).

Thanks to the creation of monolignol analogues, it was possible to follow the fluorescence and thus the incorporation into the newly synthesized lignins during the development of the stem (Pandey et al., 2016). This work used the analog of Pandey's 2015 paper. Labelling of different growth stages corresponded to the known lignification of *Arabidopsis*. Upon inhibition of several lignification factors, the labelling was weaker, indicating that incorporation of the reporter requires the machinery of lignification.

Subsequently, structural analogues of other monolignols were synthesized. The structural analogue of coumaryl alcohol (H unit) was synthesized by adding an azide function to the primary alcohol via an ethoxyethoxy linker to increase the accessibility of the azide. (Lion et al., 2017). Because the reporter label was different from that proposed for the G-unit analogue, it was possible to incorporate both analogs at the same time and subsequently perform the two click reactions sequentially, the SPAAC reaction (for the azide) first and the CuAAC reaction

second (for the alkyne). The use of the two analogues revealed a polarization in the lignification dynamics for two monolignol analogues at the cellular level.

To complete the study of the dynamics of lignification, the teams of Biot and Hawkins synthesized the structural analogue of the sinapyl alcohol (S unit)(Simon et al., 2018), thus providing click chemistry analogues for the three main units of lignins. The S analogue was synthesized by substituting the primary alcohol with a methylcyclopropene group. The addition of the fluorophore by click chemistry is done through a DAINV_{inv} reaction. The reaction being different from the reaction used for the labelling of the G and H analogues, it is possible to incorporate the three reporters in the same sample (Simon et al., 2018). With this triple bioorthogonal labelling, it's possible to see some differences in incorporation according to the cell wall layer (Figure 24). H_{az} is preferentially incorporated in the middle lamella, G_{alk} in the primary and secondary cell wall and S_{cp} in the secondary wall. There is also an orientation of incorporation. For G_{alk}, there is a stronger incorporation in the cells closer to the vascular cambium.

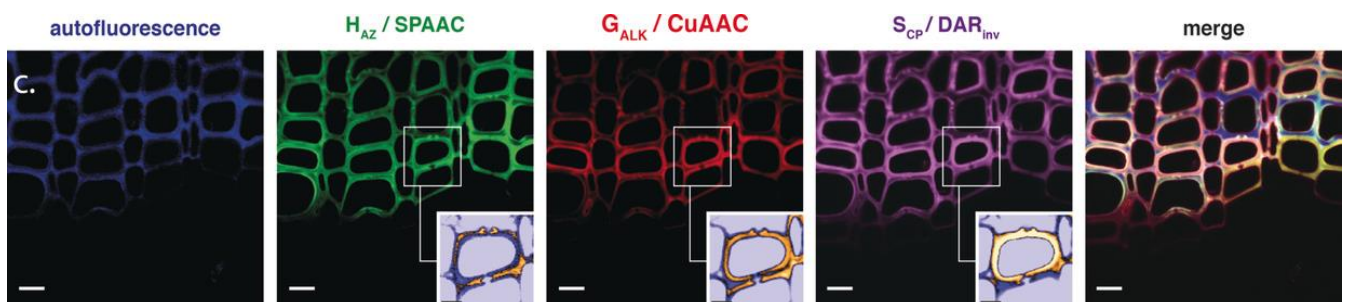


Figure 24 : Triple monolignol labelling of developing xylem in the stem of flax. Blue is lignins autofluorescence, green is H analogue incorporation (SPAAC/ DBCO-PEG4-Rhodamine Green), red is G analogue incorporation (CuAAC/ Azide-fluor 545), magenta is S analogue incorporation (magenta, DAR_{inv}/ tetrazine-Cy5). Scale bar = 5 μ m. Adapted from (Simon et al., 2018)

Spectroscopy imaging technology

Spectroscopy methods use the vibration of chemical bonds produced when an incident radiation brings an energy close to that of the vibration of a bond. There are different modes of vibration of molecules. A molecule is composed of atoms linked together by bonds that can be covalent, ionic or Van der Waals type. The molecule, in its fundamental state, has a maximum stability and its atoms are practically frozen in their equilibrium position. If an external factor, a photon, comes to disturb the molecule and if there is absorption, the atoms which constitute it have the possibility of vibrating around their position of balance. It is also possible to observe rotational movements of the atoms around the center of mass of the molecule. Molecular vibrations depend on the geometry of the molecule, the atoms that compose it and the nature of the bonds between the atoms. The study of vibrations allows us to extract information about the structure of the molecule. A molecular vibration occurs when the atoms of a molecule are in periodic motion while the molecule as a whole undergoes translational and rotational motion. The simple and most frequently encountered vibrations can be classified into two main groups: elongation vibrations and deformation vibrations, which can be classified according to their symmetry.

Stretching vibrations, also called valence vibration or "stretching" involve a symmetry variation (Figure 25 A) or asymmetric (Figure 25 B) of the interatomic distance without modification of the angles formed by these bonds. The deformation vibrations can be in the plane (Figure 25 C-D) or out of the plane (Figure 25 E-F) of the molecule and causes changes in the angles formed by the bonds while maintaining the interatomic distance.

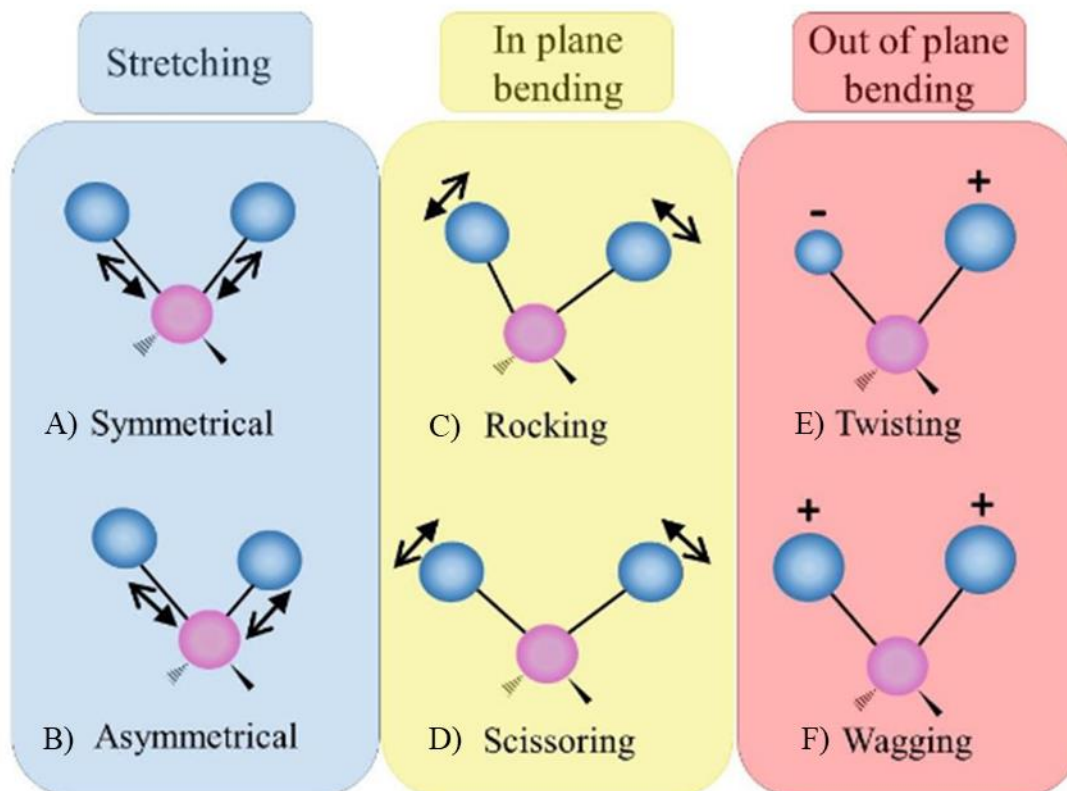


Figure 25 : Possible vibrational modes of molecules of CH_2 . Stretching elongation A) symmetrical and B) asymmetrical, In plane bending C) Rocking and D) Scissoring, Out of plane bending E) Twisting and F) Wagging. The arrows indicate the respective movements of the atoms

In each normal mode, each atom vibrates in phase with the same frequency but with its own amplitude. However, the frequency of vibration depends strongly on the forces acting on the individual atoms, taking into account the influence of the environment (with for example non-covalent bonds). This makes it possible to obtain a characteristic signature for each molecule and thus to obtain information on the molecular composition, the structure and/or the interactions within a sample.

Raman Imaging

Introduction

One objective of our work was to map lignins together with all the other polysaccharides. For this, Raman microspectroscopy was chosen, as this technique is non-destructive and delivers information on the molecules present in different parts of the wall. By Raman microscopy molecular vibrations are probed based on the energy change in inelastically scattered light due to interaction of monochromatic light with the sample (Stokes, Anti-Stokes, Figure 26). Inelastic scattering of light is very weak in intensity and therefore made a big step forward in its development as a microspectroscopic technique with the invention of powerful lasers (Zit). This section briefly presents the principles of Raman spectroscopies and its advantages.

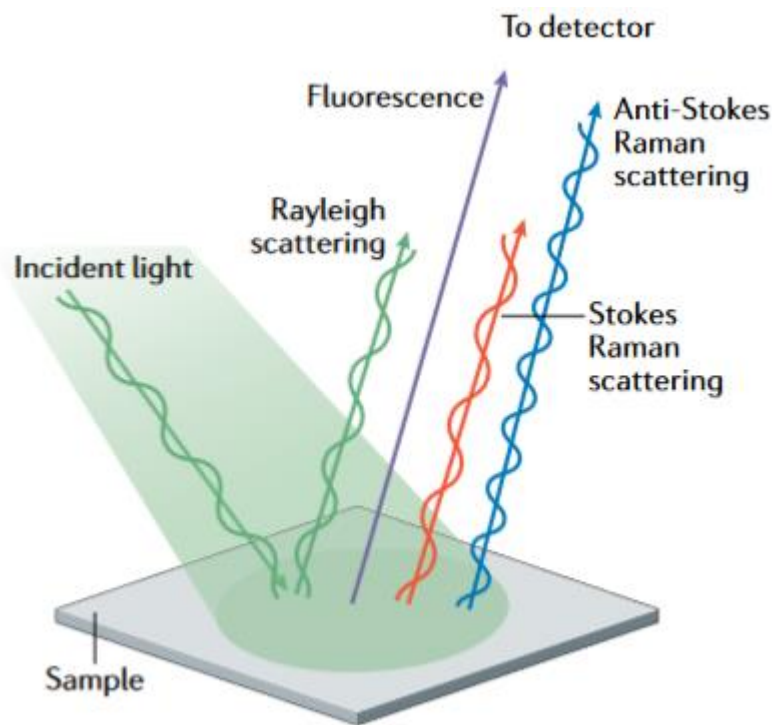


Figure 26 : The different phenomena that can happen when radiation interact with matter from (Mosca et al., 2021)

Generalities

The inelastic scattering is excited by the electromagnetic wave and corresponds to the creation of an induced dipole, which radiates. This induced dipole is linked to the polarizability of the molecule and corresponds to a deformation of its electronic cloud. For Raman scattering to occur, there must be a variation in the polarizability of the molecule (in a way, that the electronic cloud of the molecular structure is deformed) during the vibration. In Raman, the excitation is monochromatic, and thus has a fixed energy, higher in order of magnitude than that of the molecular vibrations. During the interaction, the molecule is carried in a high energy state with a short lifetime: it is called "virtual state" (Figure 25 : Possible vibrational modes of molecules of CH₂. Stretching elongation A) symmetrical and B) asymmetrical, In plane bending C) Rocking and D) Scissoring, Out of plane bending E) Twisting and F) Wagging. The arrows indicate the respective movements of the atoms. During the de-excitation of the molecule, three cases can be considered (Felidj, 2016) :

- The de-excitation occurs at the same frequency as the excitation: this is the elastic Rayleigh scattering.
- The de-excitation is done at a lower frequency than the excitation: this is the inelastic Stokes Raman scattering.
- The de-excitation is done at a frequency higher than the excitation frequency: it is the anti-Stokes inelastic Raman scattering.

For the last two cases, the energy difference corresponds to a difference in vibrational energy. On a Raman spectrum, the Rayleigh band is at the same frequency (energy) as the incident radiation, the Stokes bands are at lower frequency, and the anti-Stokes bands at higher frequency. The intensity of a Raman scattering line is proportional to the intensity of the exciting radiation, to the inverse of the fourth power of its excitation wavelength ($1/\lambda^4$), and to the square of the change in polarizability during vibration. Thus, it depends on the number of molecules present in the initial state. As shown in (Figure 27), the excitation in the case of anti-Stokes scattering occurs from a higher energy level than in Stokes scattering. Given the Boltzmann distribution of molecules, the probability of having molecules in an excited vibrational state is lower than that of having them in a ground state and therefore Stokes bands are more intense than anti-Stokes, and preferentially recorded (Long, 1977). In the context of

the analysis of biological materials (e.g. plants), fluorescence can arise and masks the Raman signal. This is the case, when molecules (e.g. phenolic components) reach an excited electronic level, followed by fluorescence emission (Figure 27 : Different energy transitions that can occur during a Raman analysis. ν_0 corresponds to the excitation frequency of the laser, ν_{vib} corresponds to the vibration frequency of the analyzed molecule.. It is possible to get rid of this phenomenon by using excitation wavelengths less energetic in the near infrared, such as 1064 nm. Compared to wavelength in the visible or UV range, the Raman signal will be less intense, compensated by a higher laser excitation power (Barbillat et al., 1999).

Raman spectroscopy can be considered completely non-destructive because it does not require any sampling, and even no contact with the sample. However, one experimental criterion is essential: the power of the laser. Indeed, a too high power could heat and degrade the sample. This degradation is not always visible and may correspond to structural modifications of the material: the resulting spectrum may then be that of the transformed products. Particular attention is therefore systematically paid to the spectra obtained in relation to the laser power used. The analysis requires to focus the laser beam with lenses or concave mirrors. The Raman spectrometer can be coupled with an optical microscope for the analysis of micro-samples, like the plant microsections used for this thesis. These focusing systems allow remote analysis, without contact with the sample or object. It is possible to analyse all types of materials, powders, liquids, gases by focusing the radiation through tubes containing the analytes, as well as complex heterogeneous samples thanks to the microscope, like biological sample.

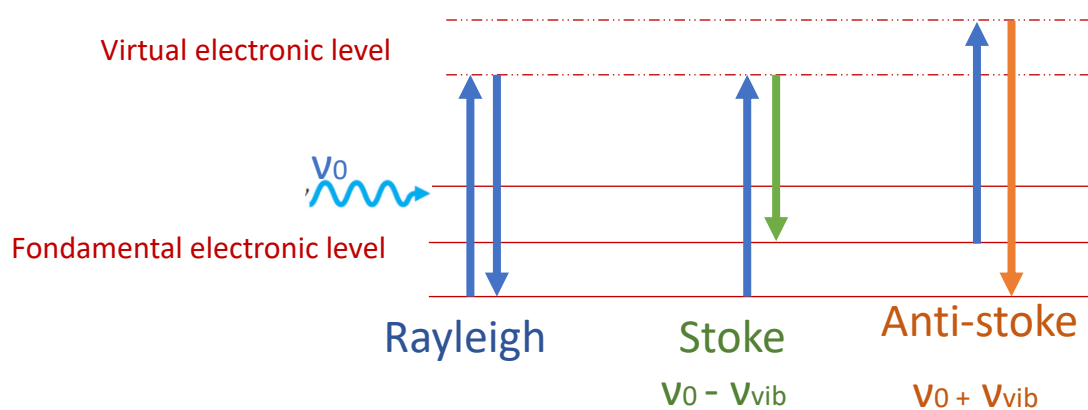


Figure 27 : Different energy transitions that can occur during a Raman analysis. ν_0 corresponds to the excitation frequency of the laser, ν_{vib} corresponds to the vibration frequency of the analyzed molecule.

Raman spectroscopy can be applied to biological samples and thus to plant samples (Mateu et al., 2020). The first Raman application on plants was the study of cellulose (Wiley & Atalla, 1987). Subsequently, different types of plant cellulosic fibers have been characterized in a general way, such as flax (Himmelsbach et al., 1999) or cotton (Edwards et al., 1997) and the distribution of the main components in different tissues (epidermis, liber fiber) has been demonstrated (Himmelsbach et al., 1999). Raman imaging, generating chemical images based on the spectra, was first used on wood cell walls (Agarwal, 2006 ; Gierlinger & Schwanninger, 2006). As wooden cell walls are more complex, it is necessary to consider the contribution of each element and assign bands to specific groupings allowing the identification of the components. A Raman image can be calculated by integrating a band of interest. This allows to visualize the spatial distribution of the compound under study. For example, integrating the band between 1545 and 1698 cm^{-1} allows to visualize a region rich in lignins. Inorganic substances can also be detected, like calcium oxalate (Macnish et al., 2003) , or silica (Dietrich et al., 2002)

Infrared spectroscopy

Like Raman spectroscopy, Fourier Transform InfraRed spectroscopy (FTIR) uses the vibration mode of molecular chemical bonds. Infrared spectroscopy (IR) is an analytical method based on the interaction of an electromagnetic wave with matter. As with all spectroscopic techniques, it can be used to identify compounds or to determine the composition of a sample. Infrared spectroscopy is a class of spectroscopy that deals with the infrared region of the electromagnetic spectrum. It covers a wide range of techniques, the most common being absorption spectroscopy. Infrared spectroscopy is based on the absorption of infrared radiation by the sample being analyzed. Infrared radiation, whose range extends from 14000 cm^{-1} to 10 cm^{-1} , is located between the visible region and the radio waves of the electromagnetic spectrum. This IR domain is divided into three regions: the near-IR, the middle-IR and the far-IR. The

near-IR, which is more energetic, is approximately between 14000-4000 cm^{-1} and allows the study of harmonic vibrations. The mid-IR between 4000-400 cm^{-1} has an energy that coincides with the energy of the internal motions of molecules. It is used to study fundamental and characteristic vibrations and the associated vibrational structure of chemical bonds. The far-IR, approximately from 400 cm^{-1} to 10 cm^{-1} , is less energetic and is used to study rotational spectroscopy

FTIR is widely used in the analysis of plant walls (Dokken et al., 2007). It allows the detection of different types of linkage allowing the identification of polymers and their functional group. In 1998, Boeriu et al were able to use near infrared spectroscopy (Boeriu et al., 1998) from green beans extract characterize the degree of esterification of cell wall pectin. Mid-IR spectroscopy can be used without extraction or solubilization to obtain information on parietal polysaccharides (Alonso-Simón et al., 2011). Different peaks can be related to the polymers. For lignins, the characteristic peaks are 1510, 1530-1540 and 1595 cm^{-1} (Smith-Moritz et al., 2011). This technique can be combined with optical microscopy (Gierlinger et al., 2008)

Objectives

The overall aim of this thesis is to increase our understanding of lignins formation in the plant cell wall. Lignins is a major cell wall polymer in vascular plants and a better understanding of its formation has both a scientific and an economic interest.

Lignins is a polyphenolic polymer insoluble in water that constitutes a hydrophobic matrix. It is polymerized in a radical way from three main monomeric units (monolignols): *p*-coumaryl alcohol, coumaryl alcohol and sinapyl alcohol that give rise to the lignin H, G and S units, respectively. Lignins show a great structural diversity due to the relative amount of different H, G and S units, as well as the existence of different inter-monomeric bonds. Lignification can be regulated at 3 different steps: during monomer biosynthesis, during monomer transport across the membrane and during monomer oxidation. This last step occurs within a complex matrix composed of polysaccharides such as cellulose, hemicelluloses and pectins, as well as cell wall proteins. In such a context, it is possible that the composition of the cell wall matrix might also affect the lignification process.

The objective of this PhD thesis was to test this hypothesis. For this purpose, it was decided to use a combination of different imaging techniques to investigate the lignification process in different cell wall mutants of *Arabidopsis thaliana*.

Three imaging approaches were chosen to analyze the walls: a technique for visualizing monolignol incorporation using a bioorthogonal approach, a technique for quantifying lignins using Safranin staining, and an analysis of wall Raman spectra. All these techniques had already been developed when my thesis began, but the analysis of the results had to be adapted to extract the maximum amount of information.

The Plant Cell Wall Dynamics team (UMR CNRS 8576 UGSF), in collaboration with the Chemical Glycobiology team (UMR CNRS 8576 UGSF) recently developed two novel *in situ* imaging methods for investigating lignification in plants. The first method is based upon the incorporation of monolignol chemical reporters in a bioorthogonal, “click-chemistry” approach (Simon et al., 2018). The second method is a semi-quantitative ratiometric technique based upon the fluorescence of safranin-O-stained sections (Baldacci-Cresp et al., 2020).

Examination of images acquired using the first method clearly showed that different reporters were incorporated into different cell wall layers (e.g., primary wall vs secondary wall vs cell corner) depending upon the cell type and/or the developmental stage analysed. However, at the start of this PhD there was no analytical pipeline in place for analysing such differences.

A first step was therefore to develop a suitable analytical technique for evaluating monolignol reporter incorporation into different cell wall layers. The development of this approach is described in the paper (Morel et al., 2022) presented in the chapter 0 of this thesis.

The algorithm developed for the analysis of chemical reporter incorporation into the different plant cell wall layers was then adapted to Safranin-O staining. This work (Morel et al., 2023) is described in the chapter 0 of this thesis.

Both the chemical reporter strategy and the safranin-O method provide detailed spatial information about lignification. Since the overall aim of this thesis was to explore the potential link between cell wall polysaccharides and lignification, it was necessary to implement another powerful imaging technique for characterizing these polymers. The BioNaMi team (BOKU University of Natural Resources and Life Sciences, Vienna) has considerable expertise in the use of Raman vibrational spectroscopy for characterizing the cell wall. Still with a view to extracting maximum data, Raman spectra analysis has been optimized for the walls studied. This advanced technique (Morel & Gierlinger, 2023) is described in the chapter 0 of this thesis.

Once the three analysis methods had been adjusted to the needs of this thesis, they were applied to characterize cell wall structure in the *Arabidopsis irx9* mutants. A publication project describing these results is presented in the chapter 0 of this thesis. The *irx9-2* (*irregular xylem 9*) mutation affects a gene encoding a β -1,4-xylosyltransferase involved in the elongation of the xylan chain of glucuronoxylans and is characterized by modifications to the cell wall hemicelluloses. The study of lignification in this mutant compared to WT plants should allow us to see whether modifications in cell wall polysaccharide matrix impact lignification.

Results and discussion

Paper I: Development of a novel analytical technique to quantify monolignol reporter incorporation into the cell wall

The triple lignins labelling technique allows us to obtain high quality images but the differences identified are subjective because each eye has its own vision of the colors. By the classical labelling technique, we can identify differences in monolignols incorporation. We have therefore developed a method to overcome the subjective vision through a measurement of fluorescence intensity. To allow us to obtain more information on the location of different reporters' incorporation, we developed an imageJ® macro to differentiate several sublayers of the cell wall. The segmented parts are: the cell corner (CC-), the compound middle lamella (CML = middle lamella and primary cell wall) and the secondary cell wall (SCW). These three sub-layers were chosen because it is known that their lignins and polysaccharide compositions change during development. We have developed the segmentation method by parametric segmentation and artificial intelligence. The possibility to use both methods is an advantage for users. They can use the second method if one of the two methods has difficulties to recognize the structures. To allow a better identification of the changes in the incorporation, two types of intensity ratio methods (RMs) were developed. The first ratio (RM1) represents the relative distribution of the total signal of a single reporter between the three sublayers. The second ratio (RM2) represents the relative signal proportion of each reporter within a given cell wall sublayer.

To show how this approach could be used to provide useful biological information, we used an *Arabidopsis thaliana* class III peroxidase mutant, *Populus tremula* x *Populus alba*, *Linium usitatissimum* and *Zea mays*. The *prx64* mutant is known to be involved in lignification.

This work has allowed us to obtain more information on the capacity of monolignols incorporation. It has allowed us to extract more precise information on the spatial distribution of incorporation as well as to compute more efficiently the incorporation differences through the ratiometric methods.

Personal contribution : For this article I realized the experiments, created the plug-in with the help of Dr. Corentin SPRIET and participated in the writing of the article with all the co-authors.

Morel, O., Lion, C., Neutelings, G., Stefanov, J., Baldacci-Cresp, F., Simon, C., Biot, C., Hawkins, S., & Spriet, C. (2022). REPRISAL: mapping lignification dynamics using chemistry, data segmentation, and ratiometric analysis. *Plant Physiology*, *188*(2), 816–830. <https://doi.org/10.1093/PLPHYS/KIAB490>

REPRISAL: mapping lignification dynamics using chemistry, data segmentation, and ratiometric analysis

Oriane Morel,^{1,2} Cedric Lion,¹ Godfrey Neutelings ,¹ Jonathan Stefanov,^{1,3} Fabien Baldacci-Cresp,¹ Clemence Simon ,^{1,3} Christophe Biot ,^{1,*†} Simon Hawkins^{1,†} and Corentin Spriet ,^{1,3,†}

- 1 Univ. Lille, CNRS, UMR 8576—UGSF—Unité de Glycobiologie Structurale et Fonctionnelle, Lille F 59000, France
 2 Institute of Biophysics, University of Natural Resources and Life Sciences, Vienna, Austria
 3 Univ. Lille, CNRS, Inserm, CHU Lille, Institut Pasteur de Lille, US 41—UMS 2014—PLBS, Lille F-59000, France

*Author for communication: christophe.biot@univ-lille.fr

†Senior authors.

C.B., S.H., and Co.S. conceived the project and supervised, respectively, the chemical, biological, and image data and segmentation experiments. C.L. and C.S. designed and synthesized the chemical reporters and elaborated the triple-click labeling method. O.M. performed the experiments and developed an analysis procedure with Co.S. J.S. developed the GUI integrating all algorithms. C.L., F.B.C., G.N., and Co.S. aided design and interpretation of experimental data. O.M., C.L., G.N., C.B., S.H., and Co.S. wrote the article with contributions of all of the authors.

The author responsible for distribution of materials integral to the findings presented in this article in accordance with the policy described in the Instructions for Authors (<https://academic.oup.com/plphys/pages/General-Instructions>) is: Christophe Biot (christophe.biot@univ-lille.fr).

Abstract

This article describes a methodology for detailed mapping of the lignification capacity of plant cell walls that we have called “REPRISAL” for REPorter Ratiometrics Integrating Segmentation for Analyzing Lignification. REPRISAL consists of the combination of three separate approaches. In the first approach, H*, G*, and S* monolignol chemical reporters, corresponding to *p*-coumaryl alcohol, coniferyl alcohol, and sinapyl alcohol, are used to label the growing lignin polymer in a fluorescent triple labeling strategy based on the sequential use of three main bioorthogonal chemical reactions. In the second step, an automatic parametric and/or artificial intelligence segmentation algorithm is developed that assigns fluorescent image pixels to three distinct cell wall zones corresponding to cell corners, compound middle lamella and secondary cell walls. The last step corresponds to the exploitation of a ratiometric approach enabling statistical analyses of differences in monolignol reporter distribution (ratiometric method [RM] 1) and proportions (RM 2) within the different cell wall zones. We first describe the use of this methodology to map developmentally related changes in the lignification capacity of wild-type *Arabidopsis* (*Arabidopsis thaliana*) interfascicular fiber cells. We then apply REPRISAL to analyze the *Arabidopsis* peroxidase (PRX) mutant *prx64* and provide further evidence for the implication of the AtPRX64 protein in floral stem lignification. In addition, we also demonstrate the general applicability of REPRISAL by using it to map lignification capacity in poplar (*Populus tremula* × *Populus alba*), flax (*Linum usitatissimum*), and maize (*Zea mays*). Finally, we show that the methodology can be used to map the incorporation of a fucose reporter into noncellulosic cell wall polymers.

Introduction

Lignin is a phenolic polymer found in the walls of certain plant cells where it makes up $\sim 25\%$ – 30% of the dry weight. Together with cellulose and xylan, it is one of the major constituents of wood and is the second most abundant plant polymer after cellulose on Earth. Both the quantity and the structure of lignin present in plant cell walls have a major effect on the mechanical and chemical properties of numerous plant-derived resources/products including wood, paper, and textiles (Huis et al., 2012). Lignin is also a major factor responsible for the recalcitrance of ligno-cellulose biomass in the industrial production of bio-ethanol for energy. For plants themselves, the presence of lignin in the cell wall contributes positively to mechanical support, facilitates water transport in xylem via its hydrophobicity, and helps to protect them against pathogens and physical injury (Boerjan et al., 2003). The appearance of lignin during evolution has played a major role in ensuring the survival of plants on dry land. The lignin polymer is also an important carbon sink and the formation of this polymer in the wood cells of long-lived tree species, therefore, contributes positively to the struggle against climate change.

Chemically, lignin is formed by the nonenzymatic polymerization of phenoxy radicals mainly derived from three main monomers: *p*-coumaryl alcohol, coniferyl alcohol, and sinapyl alcohol that are collectively referred to as “monolignols” (Ralph et al., 2004). Once incorporated into the polymer, these molecules form the hydroxyphenyl (H), guaiacyl (G), and syringyl (S) monomeric units. Lignin can also contain catechyl (C) units derived from caffeoyl alcohol in orchids and the cactaceae families (Chen et al., 2012) as well as triclin flavonoids and ferulates in grasses (Grabber et al., 2000; del Río et al., 2012) or hydroxystilbenes in palm fruit (del Río et al., 2017). The amount of lignin and the relative proportion of the different monomers in the cell wall varies according to the botanical group (e.g. gymnosperm lignin contains no/very few S units compared to angiosperm lignin which contains far higher quantities of S units); the organ (leaves are far less lignified than stems/roots), the tissue/cell type—in *Arabidopsis* (*Arabidopsis thaliana*), xylem vessels have a lower S/G ratio than fibers, and the cell wall layer (cells with only primary cell walls are generally non-lignified whereas cells with secondary cell walls [SCWs] become lignified) (Campbell and Sederoff, 1996). Monolignols are enzymatically synthesized via the phenylpropanoid pathway and are then exported into the developing cell wall across the plasma membrane. Several hypotheses including the involvement of monolignol-specific transporters, vesicle-related transport, and passive diffusion have all been advanced to explain monolignol transport, but the actual mechanism(s) involved have not as yet been categorically determined and further research is necessary on this point (Perkins et al., 2019). Once in the cell wall compartment, monolignols are oxidized by cell wall-located laccases and/or peroxidases (PRXs) before undergoing polymerization into the growing lignin polymer (Wang et al., 2013).

In order to understand the dynamics of lignification at the plant or organ scale, different analytical techniques have been developed over the last decades (Lupoi et al., 2015). They are generally adapted to the species studied (woody or not) and to the quantities of lignins present in their tissues. For example, the method using acetyl bromide solubilization of lignins (Johnson et al., 1961) is well suited for herbaceous species while the gravimetric Klason method (Effland, 1977) is more suited for woody species. There are also different methods for determining the H, G, and S subunit composition and the S/G ratio of lignins. Historically, thioacidolysis (Lapierre et al., 1986) and nitrobenzene oxidation (Billa and Monties, 1995) methods were used, and are now gradually replaced by pyrolysis coupled with GC/MS (Wagner et al., 2007) or NMR (Mansfield et al., 2012).

All these approaches provide relevant information on the different tissues/organs studied but involve cell homogenization, meaning that it is not possible to get information regarding quantities and compositions at the cellular level. Therefore, histochemical approaches are usually associated with these global analyses such as phloroglucinol staining (Wiesner reaction), which specifically reveals the cinnamaldehyde functions of S and G unit derivatives by producing a red chromogen whose intensity depends on the quantities (Clifford, 1974). The Maïle test uses potassium permanganate and hydrochloric acid to transform G and S residues into catechols, which are transformed into orange-brown quinones for G lignins and purple-red quinones for G-S lignins (Day et al., 2005). Other approaches exploit the autofluorescence of lignins (Donaldson, 2001) or the possibility to visualize them using fluorescent compounds such as auramine (Pesquet et al., 2005) and acriflavine (Donaldson, 2001). All these techniques, therefore, allow the acquisition of relatively fine spatial information about lignin that is already present in the cell wall of the sample analyzed. They do not, however, provide a clear view on the dynamics of lignification and the capacity of the cell wall machinery to incorporate monolignols into lignin since visualization of the active zones of monolignol polymerization in tissues is lacking.

Recent progress in the field of bioimaging has opened the door to novel chemical biology applications (Bukowski et al., 2014; Tobimatsu et al., 2014; Pandey et al., 2015; Simon et al., 2018). Bioorthogonal labeling strategy has emerged as a key technology to support the development of these applications in vitro, ex vivo, and in vivo in plants. Since 2014, several groups have demonstrated the feasibility and the robustness of the established protocols. In this context, we reported the design and characterization of a fully integrated pipeline, demonstrating the study of the dynamics of the plant cell wall formation in four different species: *Arabidopsis* (*A. thaliana*), flax (*Linum usitatissimum*), *Nicotiana benthamiana*, and poplar (*Populus tremula* \times *Populus alba*).

The bioorthogonal chemical reporter strategy thus enables the study of de novo lignin formation in living organisms

and is complementary to other histochemical/fluorescent approaches. In this two-step strategy, a synthetic derivative (the chemical reporter) of a monolignol is first introduced into the cell wall where it becomes oxidized by cell wall located PRXs and/or laccases and incorporated into the growing lignin polymer. The reporter carries a specific chemical group that enables subsequent interaction with a corresponding probe via a specific bioorthogonal chemical reaction. To enable integration, the group must be small and innocuous so as to minimize its impact on the physicochemical properties of the reporter and allow its recognition by the enzymatic machinery (Rigolot et al., 2021). Once metabolic incorporation has occurred, the reporter group must then react specifically and efficiently with an exogenous molecular probe (e.g. an adequately functionalized fluorophore) while being chemically inert to the surrounding biological environment. Different bioorthogonal reactions have been developed over the past 20 years and are mainly applied to glycan and protein labeling (Wallace and Chin, 2014; Palaniappan and Bertozzi, 2016). In 2014, Ralph and Zhu's teams simultaneously published the first use of coniferyl alcohol analogues as a lignin chemical reporter in a mono-labeling strategy (Bukowski et al., 2014; Tobimatsu et al., 2014). More recently our group elaborated a double-labeling, and then triple-labeling strategy to visualize active lignification areas in plants. For this, we designed three chemical reporters (G*, H*, and S*) mimicking the three main monolignols (G, H, and S), tagged with an alkyne group, an azide function, and a methylcyclopropene moiety, respectively) and exploited the three main bioorthogonal reactions, namely the copper-catalyzed alkyne-azide cycloaddition (CuAAC), the strain-promoted azide-alkyne cycloaddition (SPAAC) and the inverse electronic demand Diels–Alder (IEDDA) cycloaddition (Lion et al., 2017; Simon et al., 2018). The triple labeling strategy was then used to characterize the dynamics of lignification in flax (*L. usitatissimum* L.) and we also showed that the method could be transposed to other plant species (Arabidopsis, *N. benthamiana*, and poplar). This technology provided a powerful approach to investigate lignification at the cell wall/cell wall layer scale in different plant species. However, while a simple visual inspection of different samples is sufficient to detect “differences” in monolignol reporter incorporation profiles, often the sheer complexity of the data obtained makes it more or less impossible to qualify and/or quantify all but the most obvious differences (e.g. lignified versus non/poorly lignified walls) thereby limiting the biological potential of the chemical reporter approach.

We, therefore, decided to develop a segmentation approach that when combined with the chemical reporter strategy can be used for statistical determination of relative reporter incorporation into different cell wall zones based upon a ratiometric method (RM). In this paper, we present this combined methodology that we have called “REPRISAL” for REPorter Ratiometrics Integrating Segmentation for Analyzing Lignification. We describe the development of

REPRISAL and demonstrate how it can be used for detailed mapping of lignification in wild-type (WT) Arabidopsis, in the Arabidopsis PRX mutant *prx64*, as well as in poplar, flax, and maize.

Results and discussion

REPRISAL consists of three separate approaches: 1) bioorthogonal labeling of lignin with the three chemical reporters, 2) parametric or artificial intelligence (AI) segmentation of labeled cell walls, and 3) ratiometric analysis of fluorescence signal intensity (Figure 1). Each approach is described in more detail below.

Bioorthogonal labeling and imaging

Three synthetic monolignol surrogates H*, G*, and S* (the chemical reporters) equipped with click-reactive tags (Figure 2) were metabolically incorporated into *A. thaliana* stem cross-sections *ex vivo* using our previously reported triple bioorthogonal labeling methodology (Simon et al., 2018). Each incorporated reporter was then specifically linked to a fluorescent probe via a specific bioorthogonal ligation reaction thereby enabling subsequent fluorescence visualization and identification of the tagged substrates. H*-units were labeled with DBCO-Rhodamine Green (SPAAC bioorthogonal reaction), G*-units were labeled with Azide Fluor 545 (CuAAC bioorthogonal reaction), and S*-units were labeled with Tetrazine-Cy5 (IEDDA bioorthogonal reaction). Samples were then visualized by confocal microscopy to produce a set of images based on 3-channel detection (green for H*, red for G*, and magenta for S*) (Figure 2).

Parametric and AI-based segmentation

To map the localization of the incorporated monolignol reporters we decided to segment the cell wall into three main zones: the cell corner (CC), the compound middle lamella (CML) consisting of the middle lamella and the primary cell wall, and the SCW. Once successfully segmented, pixels can be assigned to the different cell wall sectors and the fluorescence intensity corresponding to each incorporated monolignol reporter determined. Two main strategies can be proposed for the crucial segmentation. Traditional parametric methods are mostly based on the intensity and spatial relationships of pixels, while trainable machine learning methods require the user to “teach” the software which pixel is part of what region. AI-based image analysis is highly complementary to classic parametric segmentation (PS) procedures and has strongly emerged as a valuable asset in the microscopy image analysis field over the last few years. For the REPRISAL methodology, we developed a global algorithm that enables the user to implement both parametric and AI segmentation (Figure 1).

For PS the initial image was acquired according to Nyquist sampling criteria and treated according to the algorithm presented in Figure 3. The transmission image is split into three fluorescence channels (green, red, and magenta) that are transformed into three binary masks using the Otsu

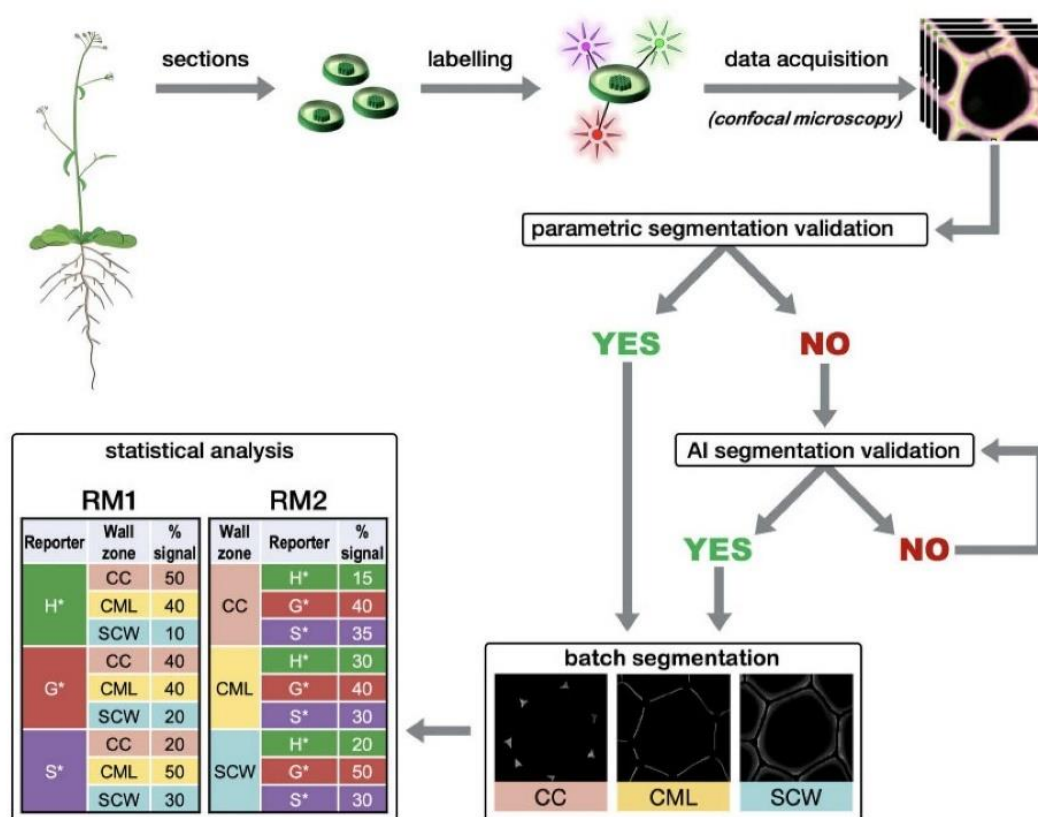


Figure 1 Global procedure workflow. Plant stem transversal cross-sections are incubated with H*, G*, and S* monolignol reporters that become metabolically incorporated into the growing lignin polymer. Incorporated reporters are identified via a bioorthogonal chemistry strategy specifically linking each type of reporter to a different fluorescent probe allowing imaging by confocal microscopy (see Figure 2). Following image acquisition, a first representative image of the series is selected and the most suitable segmentation method (parametric or AI) is chosen and applied automatically to all acquired images. The data are then extracted for three different cell wall zones (CC, CML, or SCW) and relative reporter distribution and proportion determined by RM1 and RM2. Please see text for more details.

threshold method (Otsu, 1979). These masks are then merged so that all the labeled lignin is taken into account in the automatic segmentation. A set of transforms are then applied to this new mask including the Distance map (Legland et al., 2016), Voronoi (Legland et al., 2016), Enhance Local Contrast (Pizer et al., 1987), and Find Maxima transforms (Grishagin, 2015). Binary subtraction operations then generate 3 masks corresponding to the CC, the CML, and the SCW.

For AI segmentation and in order to obtain an algorithm easily adaptable to different types of lignin fluorescence images, we chose to keep the first steps of binarization and fusion of binary masks used for PS step before implementing the AI segmentation. Images once binarized were manually labeled and then transformed by the Waikato Environment for Knowledge Analysis (WEKA) algorithm ("Gaussian Blur," "Sobel," "Hessian," "Differences of Gaussians," and "membrane projection" with a membrane patch size of 19 and a maximum sigma of 16). Transformed images were then used to train our network (200 initial trees and 4 initialization classes that is, background, CC, CML, and SCW). Once the training was validated on training images, it was applied to a new set of validation images. The classifier we

obtained was applied for batch analysis and provides probability maps of each pixel belonging to each category. Probability maps were then converted into binary masks using auto-threshold and despeckle.

To evaluate the efficiency of the developed algorithm, we applied it to confocal microscopy images of Arabidopsis floral stem cross-sections in which lignin was labeled by the bioorthogonal triple marking strategy (Figure 4). Visual inspection of the different areas confirms the efficiency of the segmentation. The form and location of the different objects obtained correspond to expectations: CCs are triangular in shape and located at the interstices where three or more cells are in contact, the CML corresponds to a line formed at the junction between two cells, and the SCW occupies the rest of the total cell wall zone. Overall, the parametric and AI segmentation methods give very similar results although some differences can be detected. The parametric method appears to be more accurate for fine structures whereas the AI method recognizes better the CCs and the middle lamella and follows more closely the curves of the cells. Nevertheless, the percentage distribution of fluorescence intensity values between the three cell wall zones is similar for both methods showing that they can be used

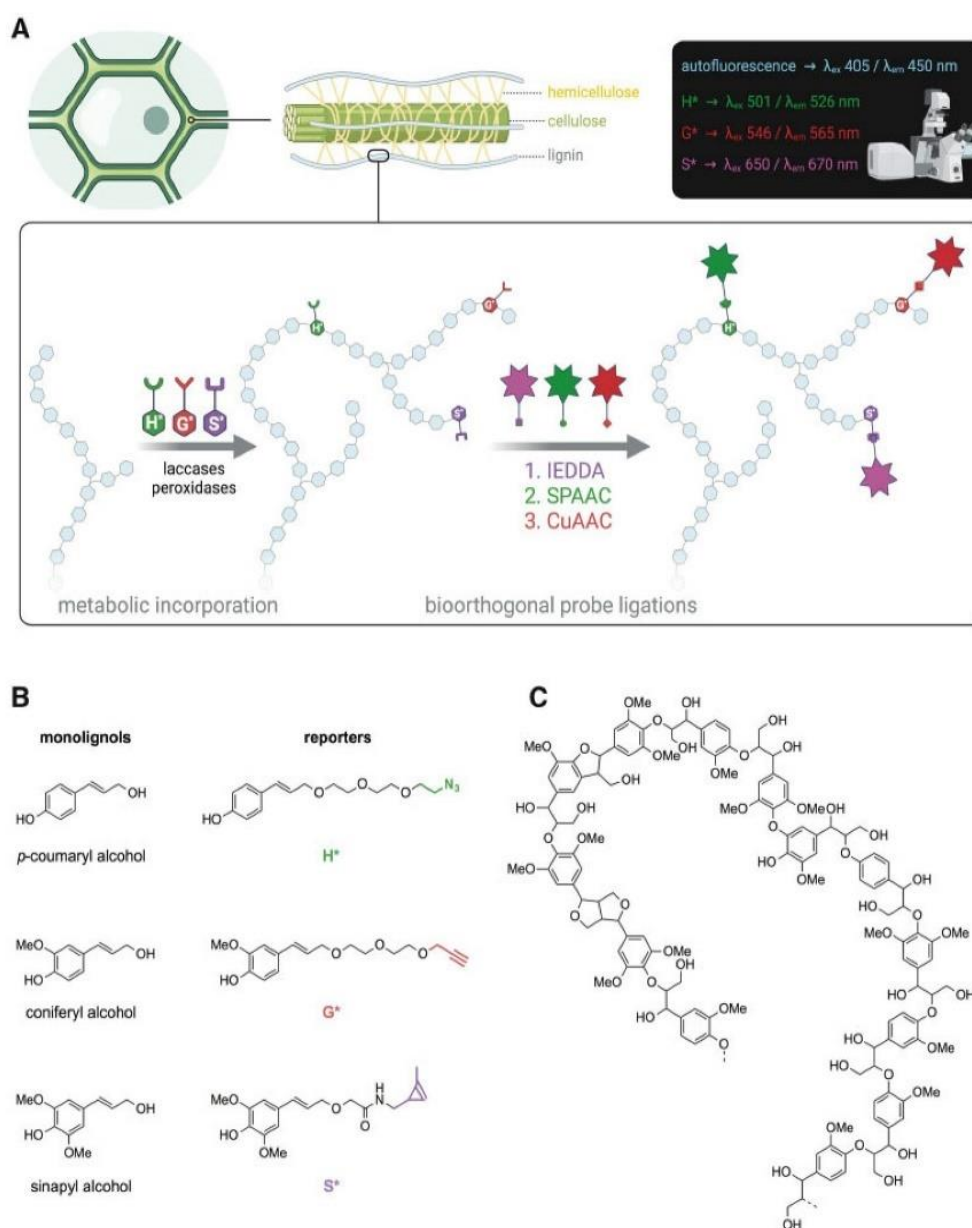


Figure 2 Lignin bioorthogonal triple labeling and chemical reporter structure. A, Schematic representation of the lignin bioorthogonal triple labeling strategy in plant cell walls. Monolignol chemical reporters H^* , G^* , and S^* are oxidized by cell wall located PRXs and/or laccases and become metabolically incorporated into the growing lignin polymer. Following reporter incorporation, green, red, and magenta fluorescent probes are added and become specifically linked to H^* , G^* , and S^* reporters, respectively, via three sequential bioorthogonal reactions: IEDDA (S^*), SPAAC (H^*), and CuAAC (G^*). Spatial localization of fluorophores is analyzed by confocal laser scanning microscopy (CLSM). B, Chemical structures of native lignin monolignols (left) and corresponding chemical reporters H^* , G^* , and S^* (right). Reporter tags involved in the bioorthogonal reaction with the corresponding fluorophores are shown in color: green—azide group, red—alkyne group, magenta—methyl cyclopropene group. C, Example of typical lignin oligomer structure.

interchangeably (Table 1). All subsequent results presented in this paper were obtained using PS.

Ratiometric analysis

During the bioorthogonal reactions, each incorporated monolignol becomes linked to a different fluorophore. Since different fluorophores do not give the same response in terms of the number of photons emitted for the same number of incorporated reporters it is not possible to directly compare the amounts of the different reporters incorpo-

To get around this problem and obtain quantitative data that can be statistically treated to provide information about differences in reporter incorporation we developed a ratiometric approach. The rationale for this is based on the fact that the ratios between the fluorescence signal of the different reporters do not change for the same biological sample/condition, thereby allowing the comparison of two or more cell wall zones. While this approach does not allow direct comparisons of the absolute quantity of an incorporated reporter, it does make it possible to determine

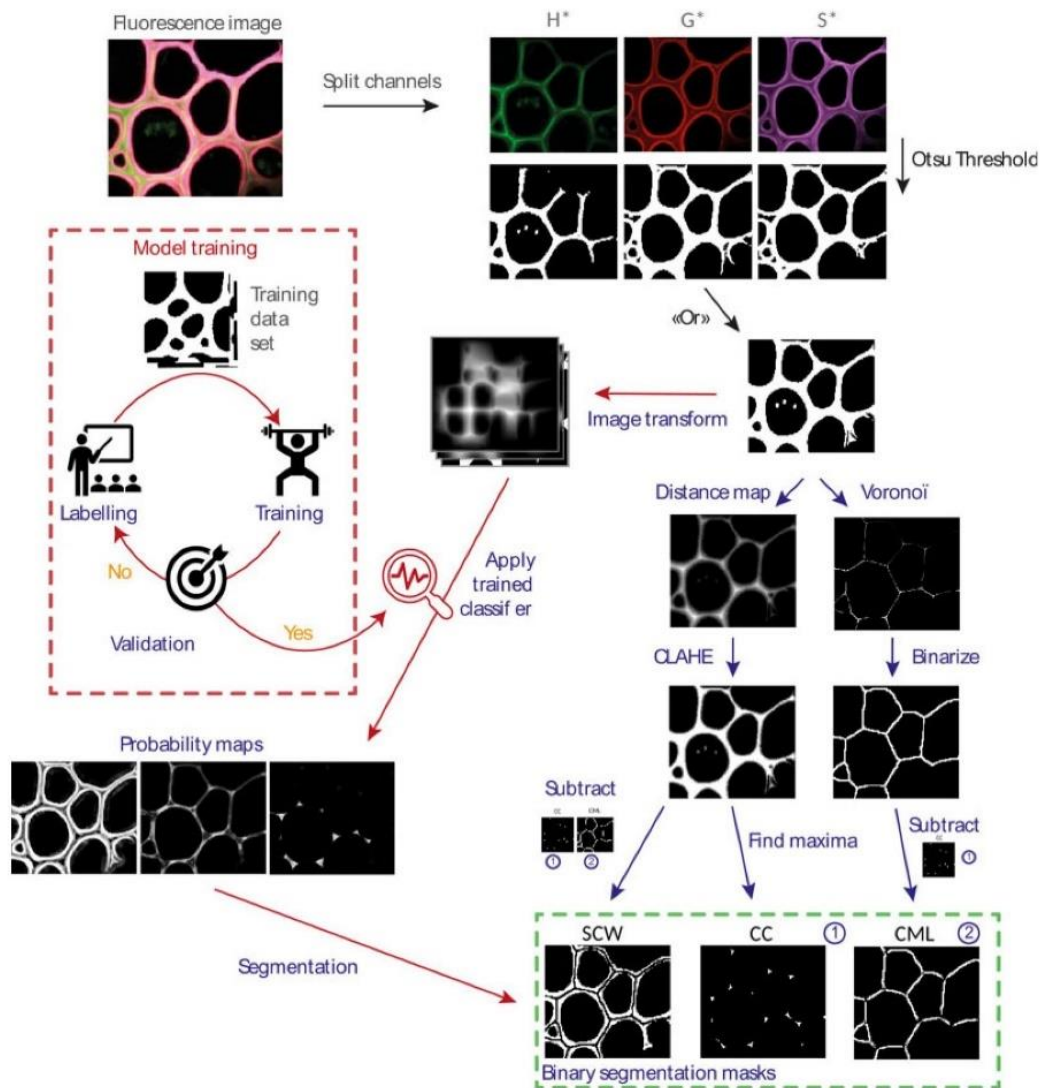


Figure 3 Scheme of the segmentation algorithm. After transforming the images of the individual channels into binary masks and then combining them, the algorithm allows the user to choose between segmentation based on 1) morphological parameters (blue path) or 2) learning (red path). Once segmented, a mask is created for the SCW, the CML, and the CC. It is then applied to each fluorescent channel corresponding to the three monolignol reporters (H^* , G^* , and S^*). For each fluorescence image, nine fluorescence intensity maps are thereby created and analyzed.

monolignols reporters incorporated into the cell wall zones of different samples.

In the ratiometric approach, relative monolignol reporter incorporation is calculated by two methods RM1 & RM2 that provide complementary information (Figure 5). RM1 evaluates the relative distribution of a given reporter in the different segmented cell wall regions (Figure 5, B). Here, the fluorescence intensity of a given reporter (H^* , G^* , and S^*) in a given cell wall region (CC, CML, or SCW) is divided by the total fluorescence intensity of that reporter in all three cell wall zones and expressed as a percentage (e.g. $[H^*CCintensity]/[\sum H^*]$). RM2 evaluates the relative proportion of each reporter in a given cell wall zone compared to the other reporters (Figure 5, C). Here, the fluorescence intensity of a given reporter (H^* , G^* , and S^*) in a given cell wall region (CC, CML, or SCW) is divided by the total fluorescence intensity of all three reporters in this particular

cell wall zone and expressed as a percentage (e.g. $[H^*CCintensity]/[\sum CCintensity]$). Our results (Figure 5) illustrate the interest of the combined chemical reporter strategy, segmentation, and ratiometric analysis approach for mapping developmentally related lignification in plants. In this experiment, we compared the capacity of different cell wall regions to incorporate monolignol reporters at different developmental stages by analyzing floral stem cross-sections sampled at three different heights from 7-week-old plants. Visual inspection of merged confocal microscopy images in the three cross-sections (Figure 5, A and Supplemental Figure S1) reveals that the three reporters have incorporated into fiber cell walls at all developmental stages from the “youngest” (23 cm) to the “oldest” (1 cm). Overall, the amount of signal increases during development reflecting reporter incorporation into the SCW. Further interpretation of these images by visual inspection is difficult

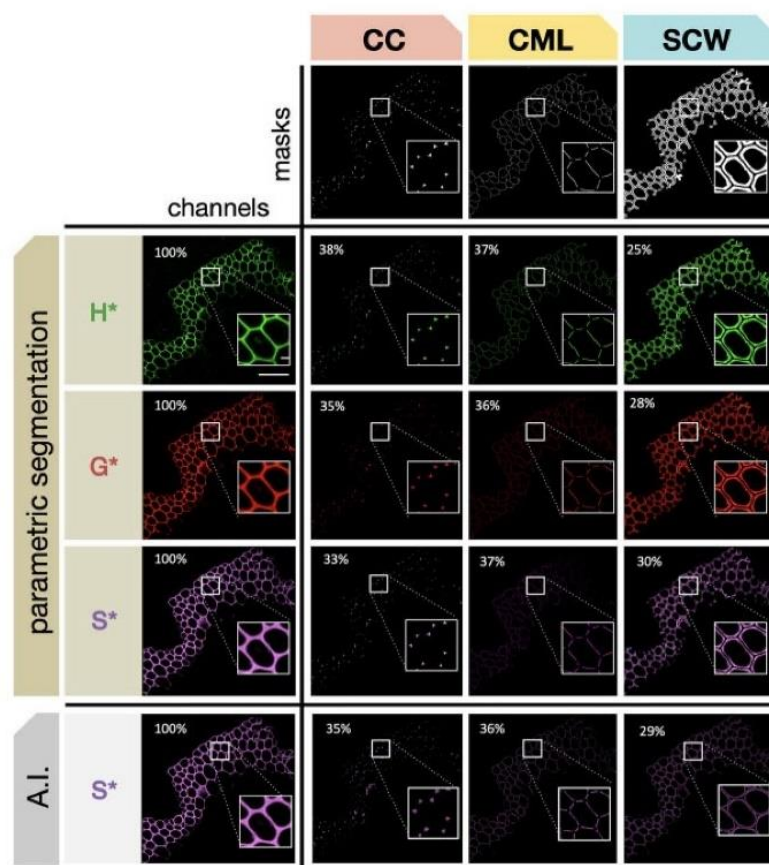


Figure 4 Automatic segmentation of different cell wall zones. The three masks (CC, CML, or SCW) are applied to cross-sections of Arabidopsis stems in which lignin has been labeled by the triple bioorthogonal strategy. Masks are applied to the three fluorescence channels corresponding to H⁺, G⁺, and S⁺ reporters. Percentage values indicate the relative proportion of total reporter signal intensity determined for each cell wall zone by PS (H⁺, G⁺, and S⁺) or AI segmentation where the value for S⁺ is shown for comparison (see Table 1 for corresponding H⁺ and G⁺ values). Scale bar main image = 50 μm, scale bar insert = 5 μm.

Table 1 Comparison of fluorescence signal distribution in different cell wall zones determined by PS and AI segmentation

Reporter	CW region	Intensity PS ^a	Intensity AI ^a	% Intensity PS	% Intensity AI
H ⁺	CC	1,807	1,805	38	40
	CML	1,767	1,631	37	36
	SCW	1,172	1,078	25	24
G ⁺	CC	515	543	35	38
	CML	530	503	36	35
	SCW	416	399	28	28
S ⁺	CC	1,147	1,214	33	35
	CML	1,277	1,252	37	36
	SCW	1,016	983	30	29

H⁺, G⁺, and S⁺ are monolignol reporters.

^aRaw fluorescence signal intensity.

due to the huge amount of data that they contain and it is, therefore, necessary to apply the segmentation approach.

In young stem sections, the use of RM1 (Figure 5, B) indicated that the relative distribution of the total signal in the different cell wall zones is very similar for all three reporters with the majority of signal being incorporated into the CC, followed by the CML and SCW (CC: 44%–46%; CML: 31%–34%; SCW: 22%–23%). While this distribution pattern did

not evolve over time for the H⁺ reporter clear changes could be observed for G⁺ and S⁺ reporters. The relative proportions of total G⁺ and S⁺ signal significantly decreased in the CC during development accompanied by an increase in the percentage of total signal observed in the SCW. No changes were observed in the relative distribution of signal in the CML. The differences in the relative distribution of the G⁺ and S⁺, but not H⁺ reporters suggest the existence of developmentally related changes in the capacity of the different cell wall zones to incorporate reporters. The increased capacity of the SCW to incorporate G⁺ and S⁺, but not H⁺ reporters, could indicate differences in the cell wall machinery that specifically favors the incorporation of these two reporters compared to H⁺ reporters. If the increased incorporation capacity was simply due to the fact that the SCW zone is bigger in older sections then one would also expect a similar increase in H⁺ incorporation. The fact that this is not so argues for the existence of a specific mechanism favoring G⁺ and S⁺ incorporation.

Analysis of the same images using RM2 (Figure 5, C) shows that the contribution of H⁺ to the total signal in the CC increases approximately four-fold (28%–79%) in older stem sections compared to younger stem sections. Since the

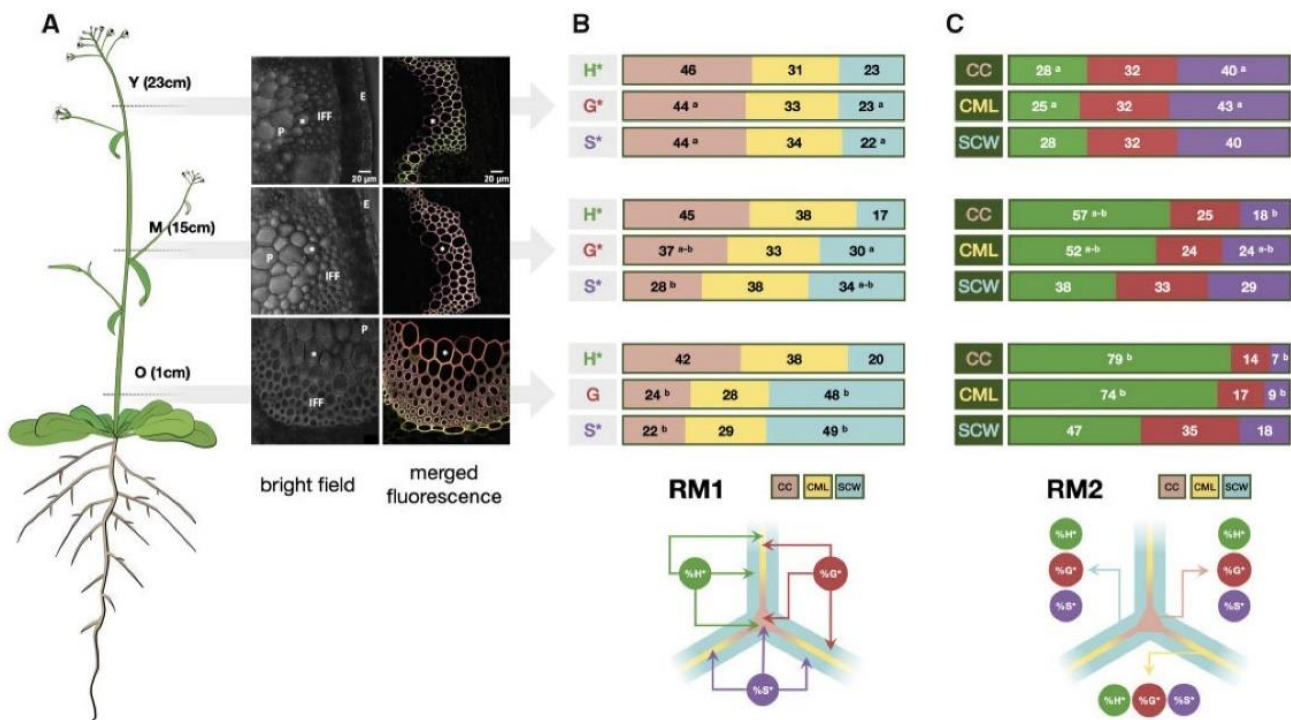


Figure 5 Monolignol reporter incorporation profiles in Arabidopsis stem fiber cell walls. A, CLSM images of IFF bundles in Arabidopsis stem cross-sections (Left) cartoon of plant indicating regions used to prepare cross-sections, Y = “young” stem region (23 cm from the base of the floral stem), M = “medium” stem region (15 cm from the base), O = “old” stem region (1 cm from the base), total stem height = 30 cm; (Right) bright-field image of stem region showing fibers analyzed and merged green (H*/DBCO-PEG₄-Rhodamine Green), red (G*/Azide-fluor 545), and magenta (S*/tetrazine-Cy5) channels revealing monolignol reporter incorporation in fiber cell wall lignin during metabolic feeding. P, pith, E, epidermis, * indicates the same cell shown in the merged image, scale bar = 20 μm. B, Relative distribution of each reporter incorporated into different fiber cell wall zones in Y, M, and O stem cross-sections analyzed by RM1, figures represent the percentage of total signal for a given reporter incorporated into the different wall zones, different letters indicate significantly different values (ANOVA, *P*-value < 0.05) between Y, M, and O sections, the absence of a letter indicates that differences are not significant. C, Relative contribution of all reporters to total signal in a given cell wall zone analyzed by RM2, figures represent the percentage contribution of each reporter’s signal to total signal intensity in each cell wall zone, different letters indicate significantly different values (ANOVA, *P*-value < 0.05) between Y, M, and O sections, the absence of a letter indicates that any differences are not significant.

relative distribution of total H* signal measured in the CC remains relatively stable (42%–46%) during development (Figure 5, B), this would suggest that the amounts of G* and/or S* incorporated into the CC decrease during development. This hypothesis is supported by the observations that i) the relative proportions of the total G* and S* signal observed in the CC decrease (Figure 5, B) and ii) that the relative contributions of S* to the total signal also decreases (Figure 5, C). The G* contribution also decreased, but not significantly. The fact that the relative contribution of the S* reporter is more heavily affected (six-fold reduction) than the G* reporter (two-fold reduction) suggests that older CCs are less able to incorporate S* reporters.

Analysis of the CML using RM2 gave rise to a similar result. Once again, the effect was more marked for S* compared with G*. In comparison to the CC and CML regions, the developmental pattern of reporter incorporation in the SCW showed a more complex pattern. RM2 (Figure 5, C) indicated that the contribution of H* to the total signal in this zone increased while the S* contribution decreased as previously observed for the CC and CML regions. In

contrast, the relative G* contribution remained unchanged. Although the S* contribution to total signal in the SCW decreased in older stem sections as for the CC and CML zones the extent of the reduction was far less (two-fold) compared to a six-fold reduction (CC) and four-fold reduction (CML). These results are coherent with those obtained by RM1 (Figure 5, B) showing that the relative proportion of the G* and S* total signals increased in the SCW.

Overall, these results indicate that while H* reporters are the most readily incorporated form into all three cell wall regions at all of the developmental stages examined, there is an increasing tendency to incorporate both G*, and especially S* reporters into the SCW of older stem sections. It is possible that these changes are functionally related to the developmentally related occurrence and distribution of lignin-related PRXs/laccases recently reported by the group of Lacey Samuels (Hoffmann et al., 2020). However, it is important to point out that lignification is a complex process, regulated at a number of different levels (e.g. regulation of monolignol biosynthesis genes and enzymes, transport/movement of monolignols across the plasma membrane

into the cell wall, oxidative polymerization, etc.). Nevertheless, the observation that differences exist between the incorporation capacity of different cell wall zones when reporters are supplied in equal concentrations hints at the existence of other mechanisms (e.g. redox enzyme-substrate specificity, local supply/transport of H_2O_2 or O_2 , differential diffusion of reporters within the polysaccharide matrix, etc.).

In conclusion, these results clearly demonstrate the potential of the REPRISAL methodology that combines chemical reporter + segmentation + ratiometric analysis approaches for mapping developmental lignification in Arabidopsis.

Lignification mapping in the Arabidopsis *prx64* mutant

Having demonstrated the interest of REPRISAL in WT plants we decided to use this approach to investigate whether it would be capable of revealing differences in the lignification profile of a lignin mutant compared to WT. For this, we chose the Arabidopsis PRX *prx64* mutant (AT5g42180). Several studies show that the AtPRX64 protein is associated with lignification; it is involved in Casparian strip lignification (Lee et al., 2013) and the AtPRX64-mCherry fusion protein becomes localized in the lignified CCs and middle lamella of Arabidopsis fiber cells in a developmentally related pattern (Yi Chou et al., 2018; Hoffmann et al., 2020). The AtPRX64 promoter is also active in both xylary and interfascicular fibers (IFFs; Smith et al., 2017). Despite this apparently clear link between PRX64 and lignification, the stem lignin content has not been investigated in this mutant and we, therefore, decided that it would be a good target to evaluate the efficiency of our methodology. A visual inspection of both UV autofluorescence and merged triple labeling images from WT and mutant plants suggested that lignification was affected in the mutant (Supplemental Figure S2).

Figure 6 shows the comparison of the application of RM1 for the G^* reporter (Figure 6, A) and RM2 for CC (Figure 6, B) in the *prx64* mutant compared to WT as an example of the information that can be obtained by our approach. Corresponding data for H^* and S^* , and CML and SCW are given in Supplemental Figure S3. Analysis by RM1 indicates significant differences in the relative distribution of total signal for all three reporters between mutant and WT samples for the Y (young) stage, but not medium (M) and old (O) stages. In Y samples, significantly higher amounts of all reporters are incorporated in the mutant CML compared with WT. At the same time, significantly lower amounts of H^* and G^* (but not S^*) are incorporated into the SCW. No significant differences are observed for the CC zones. These results would suggest that the capacity of the CML and SCW, but not CC, to incorporate monolignol reporters is modified in the *prx64* mutant compared with WT only in Y samples. This is intriguing on several levels; first, studies by the group of Lacey Samuels (Yi Chou et al., 2018; Hoffmann et al., 2020) have shown that the PRX64 protein is localized to the CC region and it could therefore be expected that the mutation would preferentially induce a modification in

this zone rather than the others. Secondly, the same group showed that the protein was not detected in Stage 1 (young) fiber CC, but only in the developmentally more advanced Stages 2 and 3 CC. However, our plants were grown in short-day conditions compared to those of Samuels and co-workers, similarly, our Y, M, and O samples were obtained from 30-cm high floral stems of 8-week-old plants (cf. 18 cm high, 5-week-old plants in the other study). As a result, our Y, M, and O samples are not directly comparable to the Stages 1–3 samples used by Samuels and it is possible that differences between the developmental stages analyzed could partly explain the observed discrepancy. Another interesting observation concerns the relative increase of all three reporters incorporated in the mutant CML zone of the mutant compared to WT since it would be expected that the KO of a lignin PRX gene would lead to a reduced reporter incorporation. However, it is also possible that the mutation provokes modifications in the expression profiles of other PRX and/or LAC genes thereby changing the overall incorporation capacity of the different cell wall regions. Future transcriptomics could help to clarify this point.

Analysis by RM2 (Figure 6 and Supplemental Figure S3) shows that the relative proportions of the three reporters in each cell wall region also change in the mutant compared with WT. A significantly lower and higher proportion of H^* and G^* reporters, respectively, are incorporated in all three cell wall regions of the mutant compared to WT in Y samples; the relative proportions of S^* reporters remain unchanged. In M samples, the trend is inverted with a significantly higher proportion of H^* reporter being incorporated in the CC and CML regions of the mutant compared to WT. In the mutant SCW layer, although the relative proportion of H^* increases, the difference is not significant. The analysis also shows that the relative proportions of S^* reporter incorporated into all three regions increase in the mutant compared with WT; G^* reporter proportions are not significantly affected. Finally, in O samples, the only significant change concerns the decrease in S^* reporter incorporation in the mutant SCW region compared with WT.

Taken together, our results show that both the RM1 and RM2 analyses, when combined with the bioorthogonal click chemistry and segmentation methodologies, reveal significant complex changes to the spatial lignification profile in the *prx64* mutant compared with WT. Such an observation first illustrates the complexity of lignification at the cell wall layer scale. A complete understanding of this process is complicated because of the number of different actors that are involved. In addition to the different redox enzymes such as laccases and PRXs it is necessary to take into account other factors such as the biosynthesis and transport of monolignols to the cell wall, as well as the supply of H_2O_2 for PRXs as recently demonstrated (Hoffmann et al., 2020). Second, our results also illustrate the enormous potential of the combined labeling + segmentation + ratiometrics to finely dissect changes in the lignification capacity

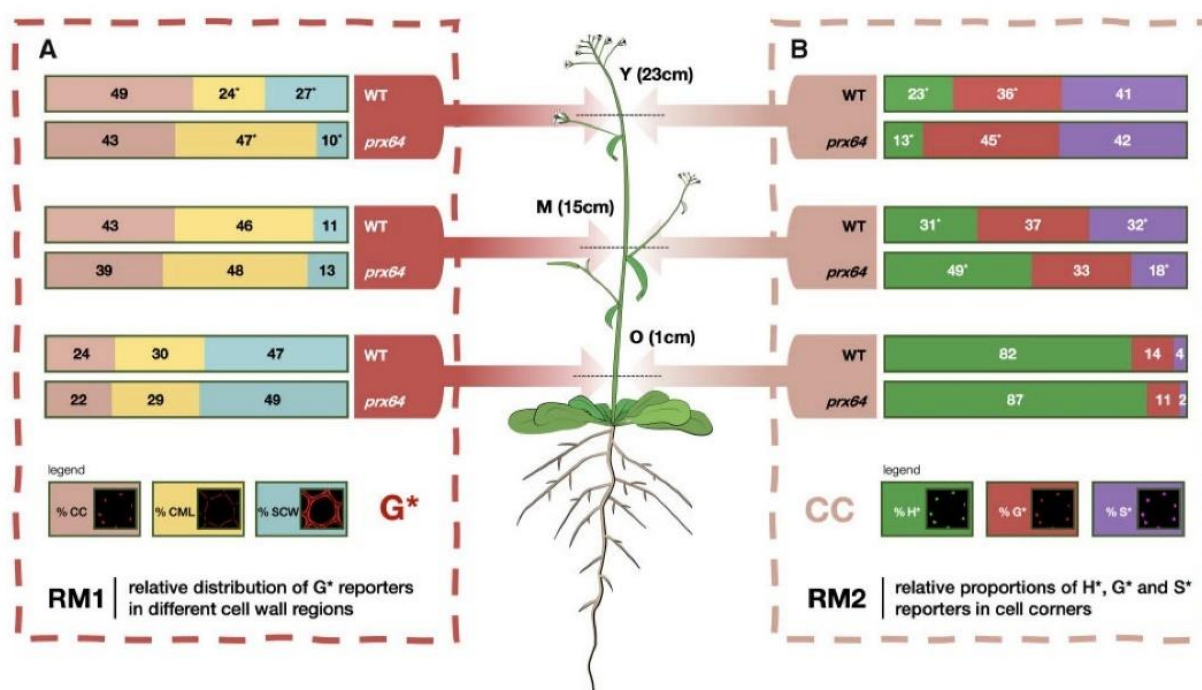


Figure 6 Example comparison of monoglignol reporter incorporation profiles in WT and *prx64* mutant Arabidopsis stem fiber cell walls. A, Relative distribution of G* reporter incorporated into different fiber cell wall zones in Y, M, and O stem cross-sections analyzed by RM1, figures represent the percentage of total G* signal incorporated into the different wall zones, Values marked with * indicate significantly different values (Student's t test, P -value < 0.05) between WT and mutant plants for a given stem height (Y, M, and O). B, Relative contribution of all reporters to total signal in the CC analyzed by RM2; figures represent the percentage contribution of each reporter's signal to the total CC signal intensity, Values marked with * indicate significantly different values (Student's t test, P -value < 0.05) between WT and mutant plants for a given stem height (Y, M, and O). Corresponding figures for H* and S* probes (RM1) and CML and SCW zones (RM2) are shown in Supplemental Figure S3.

of cell wall mutants, including those where classical approaches have previously failed to detect differences.

Lignification mapping in different plant species

To ensure the robustness of REPRISAL, and to evaluate its interest in mapping lignification we applied it to three other plant biomass species: poplar, flax, and maize (Figure 7 and Table 2). Our results first confirm that the bioorthogonal triple-labeling strategy is applicable to different plant species as previously observed (Simon et al., 2018). Second, they show that the developed macro is capable of successfully segmenting cell walls from different species into the three different zones (CC, CML, or SCW) previously analyzed in Arabidopsis. Closer examination of the percentage distribution of each reporter in the different cell wall zones revealed a number of potentially interesting differences in lignification in the different species.

In Arabidopsis, poplar and maize, data were obtained on cell walls in functionally similar "support tissues" consisting of IFFs (Arabidopsis), bark sclerenchyma fibers (poplar), and vascular bundle sclerenchyma (maize). Despite their biologically similar roles, the cell walls of poplar fibers incorporated the majority of the H* reporter into the SCW in comparison to Arabidopsis and maize where the reporter was preferentially incorporated into CC lignin. A similar difference was observed for S* reporter that was preferentially incorporated in the CC for poplar compared to the CML for the other

two species. In contrast, the distribution of incorporated G* reporter was similar in all three species. While such differences can most probably be related to the developmental stage of the cells/tissues analyzed the results clearly demonstrate the potential of our approach for large-scale and detailed mapping of cell wall lignification at the cell wall layer level in different species. Our results on flax also show that the approach can be successfully applied to lignifying cell walls in other tissues (xylem).

Lignification and noncellulosic polymer mapping

As previously demonstrated (Simon et al., 2018), the triple labeling strategy is also compatible with monosaccharide reporters and we, therefore, decided to test whether REPRISAL could also be successfully implemented to map the incorporation of other cell wall polymers such as pectin or hemicelluloses. For this, we performed a triple labeling experiment on flax stem cross-sections using H* and S* lignin reporters, together with a peracetylated alkyne-tagged fucose reporter that replaced the G* reporter. This monosaccharide is present in the side chains of xyloglucan hemicelluloses and in pectin rhamnogalacturonan I and II (RG-I, RG-II) motifs (Scheller and Ulvskov, 2010; Atmodjo et al., 2013) and has previously been used to label noncellulosic polysaccharides (NCPs) via a bioorthogonal labeling approach (Anderson et al., 2012). Our preliminary results (Supplemental Figure S4) show that it is indeed possible to

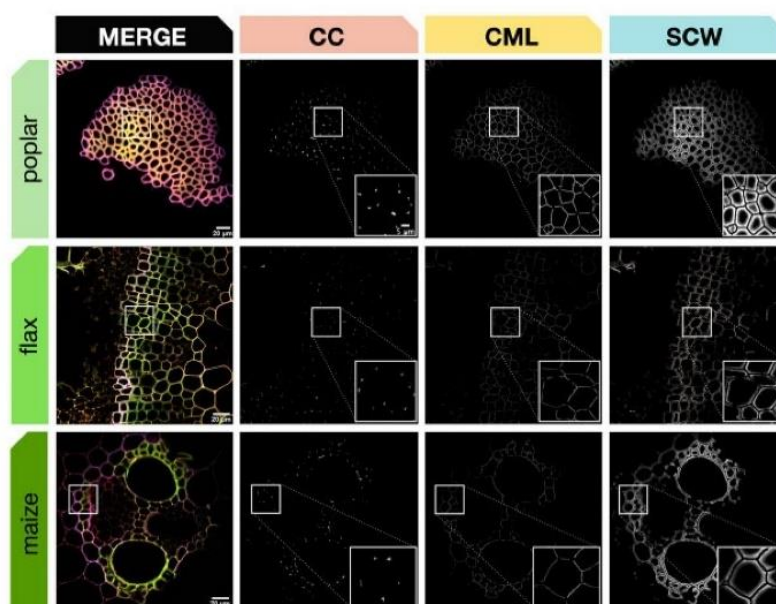


Figure 7 Automatic segmentation applied to different plant species. Top line: poplar stem bark fibers, middle line: flax stem xylem, bottom line: maize stem vascular bundle. First column: merged CLSM image of green, red, and magenta fluorescence channels, second to fourth columns: cell wall zone segmentation for CC, CML, and SCW. All samples were labeled by the triple lignin bioorthogonal chemical reporter strategy with H*, G*, and S* monolignol reporters. Square frames indicate the sample region magnified (bottom RHC, Columns 2–4). Scale bar main image = 20 μm , scale bar insert = 5 μm .

Table 2 Comparison of % total reporter distribution in different cell wall zones for different plant species determined by RM1

Reporter	CW region	% Int At	% Int Pop	% Int Flax	% Int Maize	Rank At	Rank Pop	Rank flax	Rank maize
H*	CC	38	31	31	35	H		L	H
	CML	37	28	37	35		L	H	H
	SCW	25	40	32	30	L	H		L
G*	CC	35	48	35	36		H	H	H
	CML	36	23	35	35	H	L	H	
	SCW	28	29	29	29	L		L	L
S*	CC	33	42	29	34		H	L	
	CML	37	25	39	37	H	L	H	H
	SCW	30	32	32	29	L			L

H*, G*, and S* are monolignol reporters. At, *A. thaliana*; pop, poplar Rank indicates the highest (H) and lowest (L) % values for a given reporter.

segment cell walls that have incorporated sugar reporters. As could be expected, monolignol reporters are very largely restricted to differentiating and more mature xylem cell walls but are present in much lower amounts in the phloem/vascular cambium region, whereas the fucose reporter shows the opposite profile. Interestingly, a slightly higher amount of fucose reporter found in the CML and SCW regions could be correlated with higher signal in what appeared to be the pit region between two adjacent cells suggesting that NCP deposition is still active within this specific cell wall structure at this developmental stage. Analyses of relative reporter incorporation using RM1 show that higher amounts of F* are incorporated into the CC and/or CML cell wall zones in tissue regions 1 and 2 in agreement with previous work by our group on NCP localization in flax (Chabi et al., 2017). In region 3 (more mature xylem), F* reporter was almost equally distributed between the CC, CML,

and SCW zones. This might be related to the continued NCP deposition in cell wall pits as hypothesized above, although further work would be necessary to confirm this. These results, while preliminary, would suggest that REPRISAL can also be used to map the dynamics of other (nonlignin) cell wall polymers.

Conclusions

In this paper, we have combined three different methods (chemical reporter + segmentation + ratiometric analysis) to generate a robust methodology for analyzing lignification in plants that we have termed REPRISAL. Central to this approach is the development of a segmentation method allowing automatic quantification of the fluorescence signal resulting from lignin bioorthogonal triple labeling in different cell wall zones. Pixel segmentation, that is, their distribution

between CCs, CML, and SCW is determined via two methods, one parametric and the other based on AI. As we have shown in Figure 4, these two methods produce very similar results, and while leading to the same biological conclusions, are not identical. On structures of such complexity, the labeling of pixels by two different human experts would also be expected to give slight variations and, in this case, it would be preferable that the analysis of the data set be done by a single expert for the sake of reproducibility. The two experts can also individually analyze all the data before subsequently comparing their interpretations. The same rigor must also be applied when using automated systems such as those proposed and it is therefore important not to mix segmentation methods during analysis even if any systematic bias is most likely minimal.

In the majority of this paper, we have focused on the use of PS to demonstrate its applicability to different conditions and plant models. We chose to validate this method because it is the one which is the least “flexible” in terms of use. While effective PS is usually simple and quick to use when applied to a given type of image, the determined parameters depend upon the size of the pixels, and on the size and shape of the structures. It is therefore often best suited for use at a given magnification, or even to a species or a plant tissue and requires a high expertise in order to be able to apply it to new types of samples. Nevertheless, as we have demonstrated our PS remains adaptable to a large number of situations and is, if possible, the method that should be privileged, because of a greater execution speed (seconds compared to minutes per image analyzed). On the other hand, the WEKA-based (AI) method is in essence adaptable to any sample by training it on new sets of samples representative of the condition to be analyzed. Furthermore, the number of transforms performed by the presented algorithm was deliberately limited to reduce computation time. Adding additional complementary filters such as, “kuwahara,” “Gabor,” or “neighbors” could further improve the ability of the algorithm to distinguish different cell wall areas. Nevertheless, the inclusion of a batch mode in our plugin makes it possible to launch the analysis on a large number of images overnight in order to optimize the analysis pipeline.

Our algorithm combines the advantages of these two methods by first proposing to test a parametric method on the samples. If this is validated, it can then be applied automatically on a large number of images. Otherwise, the user is offered to test a WEKA reference training set which can, in turn, be automated or used to initiate a new complementary training phase. Our overall segmentation methodology, therefore, benefits from the speed of execution of a PS when possible and from the flexibility of WEKA for samples that are too different from our training sets.

The second essential element that contributes to the potential of REPRISAL was the development of a ratiometric approach. Such an approach is necessary because different fluorophores emit different amounts of photons and the

measured fluorescence intensities obtained with different fluorophores do not therefore accurately reflect the amount of reporter incorporated. Our approach is based upon two robust and easily interpretable intensity ratios; RM1 evaluates the relative distribution of a given reporter in the different segmented cell wall regions while RM2 evaluates the relative proportion of each reporter in a given cell wall zone. These methods made it possible to extract quantitative information from the complex images generated by the triple monolignol reporter labeling strategy that can then be statistically analyzed to generate useful biological information as discussed above.

The final element necessary to REPRISAL was the implementation of the previously developed triple labeling strategy (Simon et al., 2018). When applied to the Arabidopsis *prx64* mutant, REPRISAL was able to detect statistically significant differences in the lignification pattern compared to WT even though a simple visual evaluation was unable to do this. In addition to confirming that the AtPRX64 protein does indeed play a role in cell wall lignification in stems, this observation also confirms previous results from our group showing that the chemical reporter approach is able to reveal mutant phenotypes undetectable by classical cell wall analyses (Baldacci-Cresp et al., 2020a).

In this paper, we focused on mapping lignification and we, therefore, used three monolignol chemical reporters. A number of monosaccharide reporters have been successfully used in mono-labeling approaches by other groups and could therefore be implemented for REPRISAL (Anderson et al., 2012; Dumont et al., 2016; Zhu et al., 2016).

Finally, it would also be interesting to adapt REPRISAL, or at least the segmentation component, to the analysis of cell wall images generated by other imaging techniques in order to multiply the information that can be obtained. Possible targets could include, for example, different histochemical reagents such as basic Fuchsin, Safranin, Toluidine blue O, or Auramine O that have been shown to be compatible with fluorescence microscopy (Ursache et al., 2018; Baldacci-Cresp et al., 2020b), as well as antibodies capable of recognizing a wide range of cell wall epitopes (Donaldson and Knox, 2012) and other fluorescence-based imaging techniques (DeVree et al., 2021). Another major direction could be to explore the possibilities of combining REPRISAL-type segmentation with the segmentation resulting from multivariate analyses of vibrational spectroscopic data such as Raman (Gierlinger et al., 2012) or Atomic Force Microscopy (Felhofer et al., 2020). Such approaches could be expected to contribute to our understanding, not only of lignification, but also of cell wall biology in general, thereby paving the way for exciting new discoveries in both fundamental and applied areas.

Materials and methods

Plant material

Arabidopsis (*A. thaliana*, Columbia-0) plants were used for experiments. Seeds were stratified at 4°C in 0.1% Phytigel

solution (w/v) for 3 d before being sowed. Plants were grown in growth chambers (GroBank, BB-XXL3+) under 12-h light cycles ($120 \mu\text{mol photon m}^{-2} \text{s}^{-1}$) at 23°C during the day and 20°C during the night. The *atprx64* insertion mutant (SALK_203548C) was purchased from the Nottingham Arabidopsis Stock Centre.

Flax (*L. usitatissimum*) and maize (*Zea mays*) plants were grown in growth chambers (Angelantoni Life Sciences, Massa Martana, Italy) at 22°C with a photoperiod of 16 h/8 h day/night. Poplar (*P. tremula* × *P. alba*) plants were grown in a phytotron with a 16-h light/8-h dark photoperiod, 24°C/21°C, with 35%–65% hygrometry under white light (HPI Master Plus Philips, metal halide) to maintain a light intensity of $120 \mu\text{mol m}^{-2} \text{s}^{-1}$.

Sample preparation and reporter labeling

Sample preparation was adapted from the protocol described in Simon et al. (2018). Sections of 80 μm thickness were made with a vibroslicer (VT-1000S, Leica, Wetzlar, Germany) at different heights (1 cm = O, 15 cm = M, and 23 cm = Y) from the base of the stem of embedded (3.5% w/v agarose) samples of flowering stems of *A. thaliana* plants (7 weeks). The sections were placed in sterile Murashige and Skoog half-strength (1/2 MS) solution and stored at 4°C prior to incubation with reporters. Maize, flax, and poplar sections were made from the stems of 8-week-old plants.

Bioorthogonal triple labeling of monolignol chemical reporters H*, G*, S* (Figure 2), and F* was performed as previously described (Simon et al., 2018) and outlined in Figure 2. Stem cross-sections were incubated in 300 μL 1/2 MS containing 5 μM of H*, S*, and G*/F* for 20 h in the light at 20°C (Grobank). Control samples were incubated in 300 μL 1/2 MS containing 5 μM corresponding untagged natural monolignols/fucose. After incubation, samples were extensively washed ($4 \times 1/2$ MS) prior to labeling with fluorophores via three sequential bioorthogonal reactions performed in the following order: (1) IEDDA (S*), (2) SPAAC (H*), and (3) CuAAC (G*, F*). Tetrazine Cy5 (Jena Bioscience, Jena, Germany) and Azide Fluor 545 (Sigma-Aldrich, Saint Louis, Missouri, USA) fluorophores were used at 5 μM ; DBCO-PEG4-Rhodamine Green fluorophore (Jena Bioscience, Jena, Germany) was used at 2.5 μM . All reactions were carried out in 300 μL 1/2 MS for 1 h in the dark and samples were washed ($4 \times 1/2$ MS) between reactions. Following the final reaction, samples were extensively washed ($2 \times 1/2$ MS, 5 min, $1 \times \text{MeOH } 70\%$, 60 min, $1 \times 1/2$ MS, 5 min, and $3 \times 1/2$ MS, 10 min) to fully remove any remaining free fluorophore.

Confocal microscopy

Image acquisitions were performed as previously described (Simon et al., 2018). Images from three independent biological replicates for each genotype and tissue were acquired. A Nikon A1R confocal equipped with a 60 \times /1.4 aperture oil immersion objective (Plan APO VC) and the NIS Element AR version 3.0 software was used (Nikon, Tokyo, Japan).

Acquisitions were performed on four channels corresponding to 1) lignin autofluorescence (laser line - λ ex: 405, Collection bandwidth - λ em: 450/50); 2) H units (λ ex: 488, λ em: 525/50); 3) G units (λ ex: 561, λ em: 595/50); 4) S units (λ ex: 561, λ em: 700/75); and 5) fucose (λ ex: 561, λ em: 595/50). Laser intensity and detectors gains are adjusted to ensure optimal signal-to-noise-ratio while avoiding photobleaching.

Segmentation

The graphical user interface has been created as a plugin for Fiji using Jython, a Java implementation of Python. Using this language made it possible to use Fiji methods in the Jython script, thereby enabling the creation of the GUI as well as a smooth interaction with Fiji. Fiji macros were used for both AI and PS, allowing the program to run with either type of segmentation. The overall analysis procedure was developed with ImageJ version 1.53 and JAVA version 1.8.

PS

PS was performed using a homemade ImageJ macro. Briefly, the macro first creates a binary mask for 1) SCWs, 2) CCs, and 3) CMLs. The binary mask of each region was applied to each fluorescence channel and fluorescence mean values were extracted for the nine newly created images. A recapitulative montage image was then created to quickly estimate segmentation quality. The ImageJ macro and sample images are available in the Zenodo repository (Supplemental Dataset S1: <http://doi.org/10.5281/zenodo.4809980>).

AI segmentation

The machine learning approach is based on the “Waikato Environment for Knowledge Analysis” (WEKA) implemented in ImageJ (Witten et al., 2016). We first defined a classification based on four categories: 1) SCW, 2) CCs, 3) CML, and 4) background. Our aim was to provide methods compatible with traditional computers and thus limited the training parameters to gaussian blur, Sobel filter, Hessian, Difference of Gaussians, and membrane projection with a maximum sigma of 16. These training features allowed unambiguous discrimination between the four classes after appropriate training of a random forest classifier with 200 initial trees. Manual labeling was performed on a pixel-by-pixel basis between the four classes. To avoid overlearning, training was performed on confocal images taken from various species, regions and using both WT and mutants. Each image is then segmented based on obtained probability maps (80% probability is used as a threshold) and compared with results achieved through manual segmentation. Once the training is achieved on reference images, the classifier is applied to new sets of images to validate the training step.

For more details, please see the “Results and discussion” section. The ImageJ plugin and sample images are available in the Zenodo repository (Supplemental Dataset S1: <http://doi.org/10.5281/zenodo.4809980>).

Ratiometric analysis

Two complementary (RMs) were used: RM1 evaluates the relative distribution of a given reporter in the different segmented cell wall regions. Fluorescence intensity of a given reporter (H*, G*, S*, and F*) in a given cell wall region (CC, CML, or SCW) is divided by the total fluorescence intensity of that reporter in all three cell wall zones and expressed as a percentage (e.g. $[H^*CC \text{ intensity}]/[\sum H^*]$). RM2 evaluates the relative proportion of each reporter in a given cell wall zone compared to the other reporters. Fluorescence intensity of a given reporter (H*, G*, S*, and F*) in a given cell wall region (CC, CML, or SCW) is divided by the total fluorescence intensity of all three reporters in this particular cell wall zone and expressed as a percentage (e.g. $[H^*CC \text{ intensity}]/[\sum CC \text{ intensity}]$). Statistical differences (P -value < 0.05) between samples were determined by the Student's t test and analysis of variance (ANOVA). Ten samples (cross-sections) per developmental stage (Y, M, and O) from three individual plants (WT, mutant) were analyzed for data.

Accession numbers

Arabidopsis PRX *prx64* gene: AT5g42180.

Supplemental data

The following materials are available in the online version of this article.

Supplemental Dataset S1. Supplemental dataset provided at <http://doi.org/10.5281/zenodo.4809980>.

Supplemental Figure S1. Bioorthogonal lignin triple (H*, G*, and S*) labeling in WT Arabidopsis floral stems.

Supplemental Figure S2. UV lignin autofluorescence and bioorthogonal lignin triple (H*, G*, and S*) labeling in Arabidopsis WT and *prx64* mutant floral stems.

Supplemental Figure S3. Comparison of monolignol reporter incorporation profiles in WT and *prx64* mutant Arabidopsis stem fiber cell walls.

Supplemental Figure S4. Automatic segmentation of cell wall zones in flax stem tissues showing relative distribution of lignin and NCP reporters.

Funding

O.M. gratefully acknowledges the joint financial support of the French Hauts-de-France Region and the Austrian Science Fund (Start project Y-728-B16) for a PhD fellowship; this study was partially funded by grants from the EU (CPER/FEDER project ALIBIOTECH).

Conflict of interest statement. None declared.

References

Anderson CT, Wallace IS, Somerville CR (2012) Metabolic click-labeling with a fucose analog reveals pectin delivery, architecture, and dynamics in Arabidopsis cell walls. *Proc Natl Acad Sci USA* **109**: 1329–1334

Atmodjo MA, Hao Z, Mohnen D (2013) Evolving views of pectin biosynthesis. *Annu Rev Plant Biol* **64**: 747–779

Baldacci-Cresp F, Le Roy J, Huss B, Lion C, Créach A, Spriet C, Duponchel L, Biot C, Baucher M, Hawkins S, et al. (2020a) UDP-GLYCOSYLTRANSFERASE 72E3 plays a role in lignification of secondary cell walls in Arabidopsis. *Int J Mol Sci* **21**: 1–22

Baldacci-Cresp F, Spriet C, Twyffels L, Blervacq A-S, Neutelings G, Baucher M, Hawkins S (2020b) A rapid and quantitative safranin-based fluorescent microscopy method to evaluate cell wall lignification. *Plant J* **102**: 1074–1089

Billa E, Monties B (1995) Molecular variability of lignin fractions isolated from wheat straw. *Res Chem Intermed* **21**: 303–311

Boerjan W, Ralph J, Baucher M (2003) Lignin biosynthesis. *Annu Rev Plant Biol* **54**: 519–546

Bukowski N, Pandey JL, Doyle L, Richard TL, Anderson CT, Zhu Y (2014) Development of a clickable designer monolignol for interrogation of lignification in plant cell walls. *Bioconjug Chem* **25**: 2189–2196

Campbell MM, Sederoff RR (1996) Variation in lignin content and composition: mechanisms of control and implications for the genetic improvement of plants. *Plant Physiol* **110**: 3–13

Chabi M, Goulas E, Leclercq CC, de Waele I, Rihouey C, Cenci U, Day A, Blervacq A-S, Neutelings G, Duponchel L, et al. (2017) A cell wall proteome and targeted cell wall analyses provide novel information on hemicellulose metabolism in flax. *Mol Cell Proteomics* **16**: 1634–1651

Chen F, Tobimatsu Y, Havkin-Frenkel D, Dixon RA, Ralph J (2012) A polymer of caffeyl alcohol in plant seeds. *Proc Natl Acad Sci USA* **109**: 1772–1777

Clifford MN (1974) Specificity of acidic phloroglucinol reagents. *J Chromatogr A* **94**: 321–324

Day A, Ruel K, Neutelings G, Crônier D, David H, Hawkins S, Chabbert B (2005) Lignification in the flax stem: evidence for an unusual lignin in bast fibers. *Planta* **222**: 234–245

DeVree BT, Steiner LM, Glazowska S, Ruhnnow F, Herburger K, Persson S, Mravec J (2021) Current and future advances in fluorescence-based visualization of plant cell wall components and cell wall biosynthetic machineries. *Biotechnol Biofuels* **14**: 78

Donaldson LA (2001) Lignification and lignin topochemistry - an ultrastructural view. *Phytochemistry* **57**: 859–873

Donaldson LA, Knox JP (2012) Localization of cell wall polysaccharides in normal and compression wood of radiata pine: relationships with lignification and microfibril orientation. *Plant Physiol* **158**: 642–653

Dumont M, Lehner A, Vauzeilles B, Malassis J, Marchant A, Smyth K, Linclau B, Baron A, Mas Pons J, Anderson CT, et al. (2016) Plant cell wall imaging by metabolic click-mediated labelling of rhamnogalacturonan II using azido 3-deoxy-d-manno-oct-2-ulosonic acid. *Plant J* **85**: 437–447

Effland MJ (1977) Modified procedure to determine acid-insoluble lignin in wood and pulp. *Tappi* **60**: 143–144

Felhofer M, Bock P, Singh A, Prats-Mateu B, Zirbs R, Gierlinger N (2020) Wood deformation leads to rearrangement of molecules at the nanoscale. *Nano Lett* **20**: 2647–2653

Gierlinger N, Keplinger T, Harrington M (2012) Imaging of plant cell walls by confocal Raman microscopy. *Nat Protocol* **7**: 1694–1708

Grabber JH, Ralph J, Hatfield RD (2000) Cross-linking of maize walls by ferulate dimerization and incorporation into lignin. *J Agric Food Chem* **48**: 6106–6113

Grishagin I V. (2015) Automatic cell counting with ImageJ. *Anal Biochem* **473**: 63–65

Hoffmann N, Benske A, Betz H, Schuetz M, Lacey Samuels A (2020) Laccases and peroxidases co-localize in lignified secondary cell walls throughout stem development. *Plant Physiol* **184**: 806–822

Huis R, Morreel K, Fliniaux O, Lucau-Danila A, Fénart S, Grec S, Neutelings G, Chabbert B, Mesnard F, Boerjan W, et al. (2012) Natural hypolignification is associated with extensive oligolignol accumulation in flax stems. *Plant Physiol* **158**: 1893–1915

- Johnson D, Moore WE, Zank LC** (1961) The spectrophotometric determination of lignin in small wood samples. *J Tech Assoc Pulp Pap Ind* **44**: 793–798
- Lapierre C, Monties B, Rolando C** (1986) Thioacidolyse von pappelholzligninen: nachweis von monomeren syringylverbindungen und charakterisierung von guajacyl-syringyl-ligninfractionen. *Holzforschung* **40**: 113–118
- Lee Y, Rubio MC, Alassimone J, Geldner N** (2013) A mechanism for localized lignin deposition in the endodermis. *Cell* **153**: 402–412
- Legland D, Arganda-Carreras I, Andrey P** (2016) MorphoLibJ: integrated library and plugins for mathematical morphology with ImageJ. *Bioinformatics* **32**: 3532–3534
- Lion C, Simon C, Huss B, Blervacq AS, Tirot L, Toybou D, Spriet C, Slomianny C, Guerardel Y, Hawkins S, et al.** (2017) BLISS: a bioorthogonal dual-labeling strategy to unravel lignification dynamics in plants. *Cell Chem Biol* **24**: 326–338
- Lupoi JS, Singh S, Parthasarathi R, Simmons BA, Henry RJ** (2015) Recent innovations in analytical methods for the qualitative and quantitative assessment of lignin. *Renew Sustain Energy Rev* **49**: 871–906
- Mansfield SD, Kim H, Lu F, Ralph J** (2012) Whole plant cell wall characterization using solution-state 2D NMR. *Nat Protocol* **7**: 1579–1589
- Otsu N** (1979) Threshold selection method from gray-level histograms. *IEEE Trans Syst Man Cybern* **SMC 9**: 62–66
- Palaniappan KK, Bertozzi CR** (2016) Chemical glycoproteomics. *Chem Rev* **116**: 14277–14306
- Pandey JL, Wang B, Diehl BG, Richard TL, Chen G, Anderson CT** (2015) A versatile click-compatible monolignol probe to study lignin deposition in plant cell walls. *PLoS ONE* **10**: 1–20
- Perkins M, Smith RA, Samuels L** (2019) The transport of monomers during lignification in plants: anything goes but how? *Curr Opin Biotechnol* **56**: 69–74
- Pesquet E, Ranocha P, Legay S, Digonnet C, Barbier O, Pichon M, Goffner D** (2005) Novel markers of xylogenesis in zinnia are differentially regulated by auxin and cytokinin. *Plant Physiol* **139**: 1821–1839
- Pizer SM, Amburn EP, Austin JD, Cromartie R, Geselowitz A, Greer T, ter Haar Romeny B, Zimmerman JB, Zuiderveld K** (1987) Adaptive histogram equalization and its variations. *Comput vision. Graph image Process* **39**: 355–368
- Ralph J, Lundquist K, Brunow G, Lu F, Kim H, Schatz PF, Marita JM, Hatfield RD, Ralph SA, Christensen JH, et al.** (2004) Lignins: natural polymers from oxidative coupling of 4-hydroxyphenylpropanoids. *Phytochem Rev* **3**: 29–60
- Rigolot V, Biot C, Lion C** (2021) To view your biomolecule, click inside the cell. *Angew Chem Int Ed* **60**: 23084–23105
- del Río J, Rencoret J, Gutiérrez A, Kim H, Ralph J** (2017) Hydroxystilbenes are monomers in palm fruit endocarp lignins. *Plant Physiol* **174**: 2072–2082
- del Río JC, Rencoret J, Prinsen P, Martínez ÁT, Ralph J, Gutiérrez A** (2012) Structural characterization of wheat straw lignin as revealed by analytical pyrolysis, 2D-NMR, and reductive cleavage methods. *J Agric Food Chem* **60**: 5922–5935
- Scheller HV, Ulvskov P** (2010) Hemicelluloses. *Annu Rev Plant Biol* **61**: 263–289
- Schwartz A, Wang L, Early E, Gaigalas A, Zhang Y-Z, Marti GE, Vogt RF** (2002) Quantitating fluorescence intensity from fluorophore: the definition of MESF assignment. *J Res Natl Inst Stand Technol* **107**: 83–91
- Simon C, Lion C, Spriet C, Baldacci-Cresp F, Hawkins S, Biot C** (2018) One, two, three: a bioorthogonal triple labelling strategy for studying the dynamics of plant cell wall formation in vivo. *Angew Chem Int Ed* **57**: 16665–16671
- Smith RA, Schuetz M, Karlen SD, Bird D, Tokunaga N, Sato Y, Mansfield SD, Ralph J, Samuels AL** (2017) Defining the diverse cell populations contributing to lignification in Arabidopsis stems. *Plant Physiol* **174**: 1028–1036
- Tobimatsu Y, Van De Wouwer D, Allen E, Kumpf R, Vanholme B, Boerjan W, Ralph J** (2014) A click chemistry strategy for visualization of plant cell wall lignification. *Chem Commun* **50**: 12262–12265
- Ursache R, Andersen TG, Marhavý P, Geldner N** (2018) A protocol for combining fluorescent proteins with histological stains for diverse cell wall components. *Plant J* **93**: 399–412
- Wagner A, Ralph J, Akiyama T, Flint H, Phillips L, Torr K, Nanayakkara B, Te Kiri L** (2007) Exploring lignification in conifers by silencing hydroxycinnamoyl-CoA: shikimate hydroxycinnamoyl-transferase in *Pinus radiata*. *Proc Natl Acad Sci USA* **104**: 11856–11861
- Wallace S, Chin JW** (2014) Strain-promoted sydnone bicyclo-[6.1.0]-nonyne cycloaddition. *Chem Sci* **5**: 1742–1744
- Wang Y, Chantreau M, Sibout R, Hawkins S** (2013) Plant cell wall lignification and monolignol metabolism. *Front Plant Sci* **4**: 1–14
- Witten I, Frank E, Hall M, Pal C** (2016) *Data Mining: Practical Machine Learning Tools and Techniques*, 4th edn. Todd Green, Cambridge
- Yi Chou E, Schuetz M, Hoffmann N, Watanabe Y, Sibout R, Samuels AL** (2018) Distribution, mobility, and anchoring of lignin-related oxidative enzymes in Arabidopsis secondary cell walls. *J Exp Bot* **69**: 1849–1859
- Zhu Y, Wu J, Chen X** (2016) Metabolic labeling and imaging of N-linked glycans in *Arabidopsis thaliana*. *Angew Chemie Int Ed* **55**: 9301–9305

Supplemental Dataset S1 : Dataset supporting the manuscript dedicated to lignin precursor incorporation analysis, bioorthogonal labelling, parametric and AI based segmentation.

The combination of chemical reporter-, segmentation- and ratiometric-methods enables high-quality mapping of lignification dynamics in plant cell walls

Are available:

-the algorithm with graphical user interface for imageJ and its installation procedure ("Cell_Wall_Segmentation " and "Tutorial Cell_Wall_Segmentation")

-a folder comprising a classifier and a data set compatible with the machine learning part of the algorithm "data and classifier for weka"

- representative images adapted for testing “representative images”

- the macro corresponding to the parametric segmentation procedure (see imageJ documentation for installation instructions) “parametric_segmentation”

Cell Wall Segmentation Tutorial

This program allows you to segment plant cell walls automatically using ImageJ. Original images must be acquired with

Channel1: Lignin autofluorescence

Channel 2,3,4: fluorescence from reporter 1,2,3

Channel 5: transmission

Three regions are then identified: cell corners, middle lamella and the rest of the cell wall.

Installation

[Downloading the zip file](#)

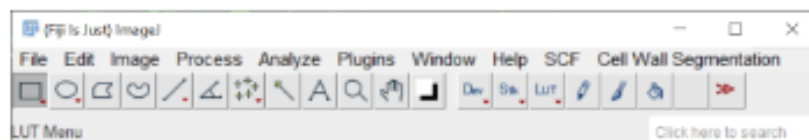
First, download " Cell_Wall_Segmentation " zip file

[Unzip the folder into Fiji](#)

Now that you have the right zip file, you have to unzip it into Fiji.app/scripts. Once done it should include 3 files: "_Run" , "ls_data.arff" and "ls_classifier.model" .

[Make sure the program is installed](#)

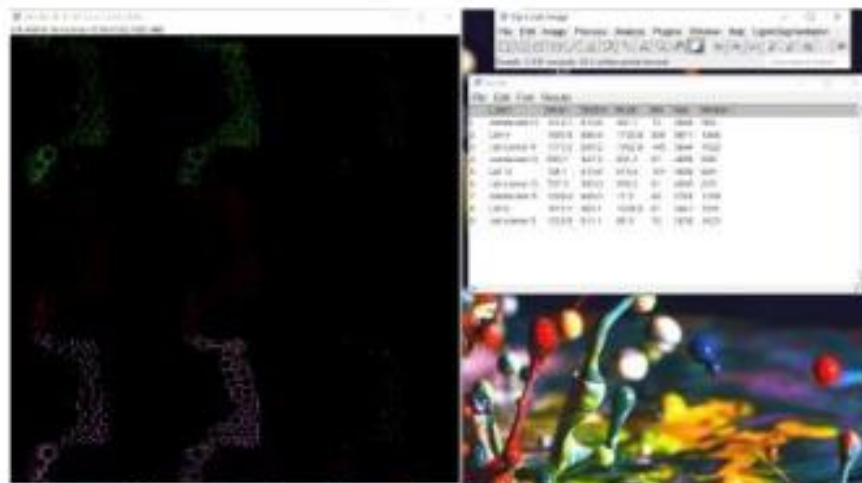
You should now see a new Cell_Wall_Segmentation tab on your Fiji app.



Processing

[Single Image](#)

If you want to segment a single image, you first have to open it in Fiji. Then click on Cell_Wall_Segmentation → Run and select "Single Image". You will then be asked if you want to perform a Parametric segmentation or an AI segmentation. After the segmentation is finished, you will be prompted with a result image and a result table.



Example of single image result.

Please note that the AI segmentation takes considerably more time than the parametric segmentation. Sometimes the software seems to be frozen but it's not. Please wait for the whole process to end before closing the windows.

Batch processing

The batch mode is somewhat different. There is no need to have any images opened in Fiji. Then click on Cell_Wall_Segmentation → Run and select Batch. You will then be asked if you want to perform a Parametric batch or an AI batch.

The next step is to choose the folder containing the images you want to segment. Once the batch process is finished, you will be prompted with a result table containing the average of all the data calculated during the batch process. You also will have access to a results folder located in the folder you had chosen right before. It contains all the results images and results tables of each picture.

New AI training

If you want to train a new WEKA model, use the Trainable Weka Segmentation plugin for imageJ:

<https://imagej.net/plugins/tws/>

Once trained, rename the data and classifier "ls_data.arff" and "ls_classifier.model" and replace the original version in the fiji.app/scripts/cell_wall_segmentation

Run.py

```
from ij.macro import Interpreter
from ij.io import DirectoryChooser, Opener
from ij.gui import GenericDialog, ProgressBar
import time
from ij.plugin import FolderOpener
from os import listdir
from os.path import isfile, join
from java.io import File
import os
from loci.plugins.in import ImporterOptions
from loci.plugins import BF
from ij import IJ
from ij.measure import ResultsTable
from ij.plugin.filter import Analyzer
from trainableSegmentation import WekaSegmentation
from trainableSegmentation.utils import Utils
from ij import WindowManager
import sys
import os.path
def parametric_macro():
    interpreter = Interpreter()
    interpreter.run("""// images must be high resolution images, respecting nyquist criterion
and with 12 to 16 bits
// with 5 channels: autofluorescence-H-G-S-transmission.
```

```

// Only channel 2 to 4 are used for calculation

// the macro provides a montage and stack of each segmentation channel (RGB) and quantified
data in

// the "result" window

//

// to operate, just open your image and click run on this macro

// you can select what you want to measure on the next line called set measurements:

setBatchMode(true);

run("Set Measurements...", "mean standard modal min median redirect=None decimal=1");

temp = getInfo("image.filename");

rename("image");

run("Split Channels");

////////// segmentation starts here//////////

// cell borders

selectWindow("C2-image");

run("Duplicate...", "title=[C2-contour cellule]");

setAutoThreshold("Huang");

run("Convert to Mask");

run("Fill Holes");

run("Dilate");

run("Dilate");

run("Fill Holes");

run("Voronoi");

selectWindow("C1-image");

run("Duplicate...", "title=[C1-cell corner]");

```

```
setAutoThreshold("Huang");
run("Convert to Mask");
run("Fill Holes");
run("Dilate");
run("Dilate");
run("Fill Holes");
//cell corner
run("Convert to Mask");
run("Distance Map");
run("Enhance Local Contrast (CLAHE)", "blocksize=127 histogram=256 maximum=3
mask=*None* fast_(less_accurate)");
run("Find Maxima...", "prominence=6 output=[Maxima Within Tolerance]");
run("Erode");
rename("cell corner");
//lamella
selectWindow("C2-contour cellule");
setThreshold(1, 65600);
run("Convert to Mask");
run("Dilate");
imageCalculator("Subtract create", "C2-contour cellule","cell corner");
selectWindow("Result of C2-contour cellule");
rename("lamelle moyenne");
//paroi
selectWindow("C1-image");
run("Duplicate...", "title=[C1-paroi]");
```

```

setAutoThreshold("Moments dark");
setOption("BlackBackground", true);
run("Convert to Mask");
run("Erode");
run("Dilate");
run("Dilate");
imageCalculator("Subtract create", "C1-paroi", "lamelle moyenne");
selectWindow("Result of C1-paroi");
rename("paroi");
imageCalculator("Subtract create", "paroi", "cell corner");
selectWindow("Result of paroi");
rename("parois");
close("paroi");
close("C1-cell corner");
close("C2-contour cellule");
close("C1-paroi");

////////// convert binay mask into 0-1 operators

selectWindow("lamelle moyenne");
run("Divide...", "value=255");
selectWindow("parois");
run("Divide...", "value=255");
selectWindow("cell corner");
run("Divide...", "value=255");

////////////////////////////////////calculations for H////////////////////////////////////

imageCalculator("Multiply create 32-bit", "parois", "C2-image");
75

```

```
selectWindow("Result of parois");
setAutoThreshold("Default dark");
setThreshold(10, 65600);
run("NaN Background");
rename("parois H");
run("Green");
imageCalculator("Multiply create 32-bit", "C2-image", "cell corner");
setAutoThreshold("Default dark");
setThreshold(10, 65600);
run("NaN Background");
rename("cell corner H");
imageCalculator("Multiply create 32-bit", "C2-image", "lamelle moyenne");
setAutoThreshold("Default dark");
setThreshold(10, 65600);
run("NaN Background");
rename("LM H");
////////////////////////////////calculations for G////////////////////////////////
imageCalculator("Multiply create 32-bit", "C3-image", "parois");
selectWindow("Result of C3-image");
setAutoThreshold("Default dark");
setThreshold(10, 65600);
run("NaN Background");
rename("paroi G");
imageCalculator("Multiply create 32-bit", "C3-image", "lamelle moyenne");
selectWindow("Result of C3-image");
```

```
setAutoThreshold("Default dark");
setThreshold(10, 65600);
run("NaN Background");
rename("LM G");
imageCalculator("Multiply create 32-bit", "C3-image", "cell corner");
setAutoThreshold("Default dark");
setThreshold(10, 65600);
run("NaN Background");
rename("cell corner G");
////////////////////////////////calculations for S////////////////////////////////
imageCalculator("Multiply create 32-bit", "C4-image", "parois");
selectWindow("Result of C4-image");
setAutoThreshold("Default dark");
setThreshold(10, 65600);
run("NaN Background");
rename("paroi S");
imageCalculator("Multiply create 32-bit", "C4-image", "lamelle moyenne");
selectWindow("Result of C4-image");
setAutoThreshold("Default dark");
setThreshold(10, 65600);
run("NaN Background");
rename("LM S");
imageCalculator("Multiply create 32-bit", "C4-image", "cell corner");
setAutoThreshold("Default dark");
setThreshold(10, 65600);
```

```
run("NaN Background");
rename("cell corner S");
//////////////////////////////////// measurements //////////////////////////////////////
run("Clear Results");
selectWindow("parois H");
run("Measure");
setResult("Label", 0, "membrane H")
run("RGB Color");
selectWindow("LM H");
run("Measure");
setResult("Label", 1, "LM H")
run("RGB Color");
selectWindow("cell corner H");
run("Measure");
setResult("Label", 2, "cell corner H")
run("RGB Color");
selectWindow("paroi G");
run("Measure");
setResult("Label", 3, "membrane G")
run("RGB Color");
selectWindow("LM G");
run("Measure");
setResult("Label", 4, "LM G")
run("RGB Color");
selectWindow("cell corner G");
```

```
run("Measure");
setResult("Label", 5, "cell corner G")
run("RGB Color");
selectWindow("paroi S");
run("Measure");
setResult("Label", 6, "membrane S")
run("RGB Color");
selectWindow("LM S");
run("Measure");
setResult("Label", 7, "LM S")
run("RGB Color");
selectWindow("cell corner S");
run("Measure");
setResult("Label", 8, "cell corner S")
run("RGB Color");
////////////////////////////////////final montage////////////////////////////////////
close("cell corner");
close("parois");
close("lamelle moyenne");
close("C1-image");
close("C2-image");
close("C3-image");
close("C4-image");
```

```

run("Concatenate...", "open image1=[parois H] image2=[LM H] image3=[cell corner H]
image4=[paroi G] image5=[LM G] image6=[cell corner G] image7=[paroi S] image8=[LM S]
image9=[cell corner S]");

run("Make Montage...", "columns=3 rows=3 scale=0.5 ");

selectWindow("Montage");

rename(temp);

run("Enhance Contrast", "saturated=0.35");

setBatchMode(false);

")

def parametric_segmentaion_single():

    gd1 = GenericDialog("Lignin Segmentation")

    gd1.addMessage("The parametric segmentation will begin. Please wait during the
process")

    gd1.hideCancelButton()

    gd1.showDialog()

    parametric_macro()

    time.sleep(1)

    gd2 = GenericDialog("Lignin Segmentation")

    gd2.addMessage("Parametric Segmentation Complete")

    gd2.hideCancelButton()

    gd2.showDialog()

    ""if gd2.wasOKed():

        # TODO: Batch over all images

        print 'Selected : yes'

    else:

```

```

        # TODO: Try Weka segmentation

        print 'Selected : no'"""

def ai_segmentation_batch():

    setBatchMode(True);

    interpreter = Interpreter()

    directory_chooser = DirectoryChooser("Select a folder - Lignin Segmentation")

    directory = directory_chooser.getDirectory()

    files = [f for f in listdir(directory) if isfile(join(directory, f))]

    results_path = directory + "results"

    results_path = results_path.replace(os.sep, '/')

    if os.path.exists(results_path):

        gd1 = GenericDialog("Lignin Segmentation")

        gd1.addMessage("A prior result file has been detected. Please move it or delete
it in order to make a new segmentation")

        gd1.hideCancelButton()

        gd1.showDialog()

        sys.exit()

    os.mkdir(results_path)

    gd2 = GenericDialog("Lignin Segmentation")

    gd2.addMessage("The AI batch will begin. Please wait during the process")

    gd2.hideCancelButton()

    gd2.showDialog()

    progress_bar = ProgressBar(200, 300)

    nbr = len(files)

    i = 0

```

```

mean_values = []

for f in files:
    try:

        # Batch
        progress_bar.show(i, nbr)

        file_path = directory + f

        file_path = file_path.replace(os.sep, '/')

        interpreter.run('run("Bio-Formats Windowless Importer", "open=[' +
file_path + ']");')

        ai_macro()

        #IJ.selectWindow(f)

        IJ.saveAs("jpg", results_path + "/segmentation-" + f)

        interpreter.run('close("'" + f + "'");')

        IJ.selectWindow("Results")

        results_table = Analyzer.getResultsTable()

        temp_mean = results_table.getColumn(1)

        strlist = ".join([str(elem) for elem in temp_mean])

        strlist = strlist.replace('.', ")

        print strlist

        if "nan" in strlist:

            print 'BAD FILE'

        else:

            mean_values.append(temp_mean)

        IJ.saveAs("Results", results_path + "/results-" + f + ".csv")

```

```

        #interpreter.run('saveAs("Results", ' + results_path + "/results-" + f +
');)

        interpreter.run('close("Results");')

        interpreter.run('close("*");')

        i += 1

    except Exception as e:

        pass

# Creating final Results table
x = tuple(mean_values)

mean_values = [sum(y) / len(y) for y in zip(*x)]

final_results = ResultsTable()

final_results.setDefaultHeadings()

final_results.setValue(0, 0, "membrane H")

final_results.setValue(0, 1, "LM H")

final_results.setValue(0, 2, "cell corner H")

final_results.setValue(0, 3, "membrane G")

final_results.setValue(0, 4, "LM G")

final_results.setValue(0, 5, "cell corner G")

final_results.setValue(0, 6, "membrane S")

final_results.setValue(0, 7, "LM S")

final_results.setValue(0, 8, "cell corner S")

i = 0

while i < 9:

    final_results.setValue(1, i, str(mean_values[i]))

    i += 1

```

```

final_results.show("Final-Results")

def parametric_segmentaion_batch():

    interpreter = Interpreter()

    directory_chooser = DirectoryChooser("Select a folder - Lignin Segmentation")

    directory = directory_chooser.getDirectory()

    files = [f for f in listdir(directory) if isfile(join(directory, f))]

    results_path = directory + "results"

    results_path = results_path.replace(os.sep, '/')

    if os.path.exists(results_path):

        gd1 = GenericDialog("Lignin Segmentation")

        gd1.addMessage("A prior result file has been detected. Please move it or delete
it in order to make a new segmentation")

        gd1.hideCancelButton()

        gd1.showDialog()

        sys.exit()

    os.mkdir(results_path)

    gd2 = GenericDialog("Lignin Segmentation")

    gd2.addMessage("The paramateric batch will begin. Please wait during the process")

    gd2.hideCancelButton()

    gd2.showDialog()

    progress_bar = ProgressBar(200, 300)

    nbr = len(files)

    i = 0

    mean_values = []

```

```

for f in files:
    try:
        # Batch
        progress_bar.show(i, nbr)
        file_path = directory + f
        file_path = file_path.replace(os.sep, '/')
        interpreter.run('run("Bio-Formats Windowless Importer", "open=[' +
file_path + ']");')

        parametric_macro()
        IJ.selectWindow(f)
        IJ.saveAs("jpg", results_path + "/segmentation-" + f)
        interpreter.run('close("'" + f + "'");')
        IJ.selectWindow("Results")
        results_table = Analyzer.getResultsTable()
        temp_mean = results_table.getColumn(1)
        strlist = ".join([str(elem) for elem in temp_mean])
        strlist = strlist.replace('.', ")
        print strlist
        if "nan" in strlist:
            print 'BAD FILE'
        else:
            mean_values.append(temp_mean)
        IJ.saveAs("Results", results_path + "/results-" + f + ".csv")
        #interpreter.run('saveAs("Results", ' + results_path + "/results-" + f +
');')

```

```

        interpreter.run('close("Results");')

        i += 1

    except Exception as e:

        pass

# Creating final Results table
x = tuple(mean_values)
mean_values = [sum(y) / len(y) for y in zip(*x)]

final_results = ResultsTable()
final_results.setDefaultHeadings()
final_results.setValue(0, 0, "membrane H")
final_results.setValue(0, 1, "LM H")
final_results.setValue(0, 2, "cell corner H")
final_results.setValue(0, 3, "membrane G")
final_results.setValue(0, 4, "LM G")
final_results.setValue(0, 5, "cell corner G")
final_results.setValue(0, 6, "membrane S")
final_results.setValue(0, 7, "LM S")
final_results.setValue(0, 8, "cell corner S")

i = 0

while i < 9:

    final_results.setValue(1, i, str(mean_values[i]))

    i += 1

final_results.show("Final-Results")

def ai_segmentation_single():

```

```

gd1 = GenericDialog("Lignin Segmentation")
gd1.addMessage("The AI segmentation will begin. Please wait during the process")
gd1.hideCancelButton()
gd1.showDialog()
ai_macro()
def ai_macro():
    original_imp = WindowManager.getCurrentImage()
    original_title = original_imp.getTitle()
    original_imp_clone = original_imp.clone()
    interpreter = Interpreter()
    interpreter.run("")
    setBatchMode(true);
    rename("image");
    setAutoThreshold("Default");
    //run("Threshold...");
    setAutoThreshold("Otsu dark");
    setOption("BlackBackground", false);
    run("Convert to Mask", "method=Otsu background=Dark calculate");
    run("Despeckle", "stack");
    run("Split Channels");
    imageCalculator("Add create", "C1-image","C2-image");
    selectWindow("Result of C1-image");
    imageCalculator("Add create", "C3-image","C4-image");
    selectWindow("Result of C3-image");
    imageCalculator("Add create", "Result of C1-image","Result of C3-image");

```

```

selectWindow("Result of Result of C1-image");
selectWindow("Result of C3-image");
close();
selectWindow("Result of C1-image");
close();
selectWindow("C4-image");
close();
selectWindow("C3-image");
close();
selectWindow("C2-image");
close();
selectWindow("C1-image");
close();
selectWindow("Result of Result of C1-image");
run("Fill Holes");
setBatchMode(false);")
imp = WindowManager.getCurrentImage()
imp_clone = imp.clone()
segmentator = WekaSegmentation(imp)
segmentator.loadClassifier('scripts/Cell_Wall_Segmentation/ls_classifier.model')
segmentator.loadTrainingData('scripts/Cell_Wall_Segmentation/ls_data.arff')
segmentator.applyClassifier(True)
result = segmentator.getClassifiedImage()
result.show()
interpreter.run("")

```

```

run("Stack to Images");
selectWindow("int cell");
close();

////////////////////////////////////

selectWindow("wall");
setAutoThreshold("Minimum dark");
setOption("BlackBackground", false);
run("Convert to Mask");
selectWindow("medium lamella");

//run("Enhance Local Contrast (CLAHE)", "blocksize=127 histogram=256
maximum=3 mask=*None* fast_(less_accurate)");
setAutoThreshold("Moments dark");
run("Convert to Mask");
selectWindow("cell corner");

//run("Enhance Local Contrast (CLAHE)", "blocksize=127 histogram=256
maximum=3 mask=*None* fast_(less_accurate)");
setAutoThreshold("Moments dark");
run("Convert to Mask");

////////////////////////////////////

imageCalculator("Subtract create", "wall", "medium lamella");
imageCalculator("Subtract create", "Result of wall", "cell corner");
selectWindow("Result of Result of wall");
run("Erode");
run("Dilate");
rename("parois");

```

```

////////////////////////////////////
imageCalculator("Subtract create", "medium lamella","cell corner");
selectWindow("Result of medium lamella");
run("Erode");
run("Dilate");
rename("lamelle moyenne");
////////////////////////////////////
selectWindow("cell corner");
run("Erode");
run("Dilate");
rename("cell corner");
////////////////////////////////////
close("medium lamella");
close("Result of wall");
close("wall");
")
# Re opening the original image
    original_imp_clone.show()
print 'cloned'
    interpreter.run("
////////////////////////////////////
// 12 - 14 macro para
temp = getInfo("image.filename");
rename("image");
run("Split Channels");")

```

```

print 'here'

interpreter.run("""

    //////////////////// convert binay mask into 0-1 operators

selectWindow("lamelle moyenne");

run("Divide...", "value=255");

selectWindow("parois");

run("Divide...", "value=255");

selectWindow("cell corner");

run("Divide...", "value=255");

////////////////////////////////////calculations for H////////////////////////////////////

imageCalculator("Multiply create 32-bit", "parois","C2-image");

selectWindow("Result of parois");

setAutoThreshold("Default dark");

setThreshold(10, 65600);

run("NaN Background");

rename("parois H");

run("Green");

imageCalculator("Multiply create 32-bit", "C2-image","cell corner");

setAutoThreshold("Default dark");

setThreshold(10, 65600);

run("NaN Background");

rename("cell corner H");

```

```

imageCalculator("Multiply create 32-bit", "C2-image", "lamelle moyenne");

setAutoThreshold("Default dark");

setThreshold(10, 65600);

run("NaN Background");

rename("LM H");

////////////////////////////////calculations for G////////////////////////////////

imageCalculator("Multiply create 32-bit", "C3-image", "parois");

selectWindow("Result of C3-image");

setAutoThreshold("Default dark");

setThreshold(10, 65600);

run("NaN Background");

rename("paroi G");

imageCalculator("Multiply create 32-bit", "C3-image", "lamelle moyenne");

selectWindow("Result of C3-image");

setAutoThreshold("Default dark");

setThreshold(10, 65600);

run("NaN Background");

rename("LM G");

imageCalculator("Multiply create 32-bit", "C3-image", "cell corner");

setAutoThreshold("Default dark");

setThreshold(10, 65600);

run("NaN Background");

rename("cell corner G");

////////////////////////////////calculations for S////////////////////////////////

```

```

imageCalculator("Multiply create 32-bit", "C4-image", "parois");
selectWindow("Result of C4-image");
setAutoThreshold("Default dark");
setThreshold(10, 65600);
run("NaN Background");
rename("paroi S");
imageCalculator("Multiply create 32-bit", "C4-image", "lamelle moyenne");
selectWindow("Result of C4-image");
setAutoThreshold("Default dark");
setThreshold(10, 65600);
run("NaN Background");
rename("LM S");
imageCalculator("Multiply create 32-bit", "C4-image", "cell corner");
setAutoThreshold("Default dark");
setThreshold(10, 65600);
run("NaN Background");
rename("cell corner S");

```

////////////////////////////////// measurements //////////////////////////////////

```

run("Clear Results");
selectWindow("parois H");
run("Measure");
setResult("Label", 0, "membrane H")
run("RGB Color");

```

```
selectWindow("LM H");  
run("Measure");  
setResult("Label", 1, "LM H")  
run("RGB Color");  
selectWindow("cell corner H");  
run("Measure");  
setResult("Label", 2, "cell corner H")  
run("RGB Color");  
selectWindow("paroi G");  
run("Measure");  
setResult("Label", 3, "membrane G")  
run("RGB Color");  
selectWindow("LM G");  
run("Measure");  
setResult("Label", 4, "LM G")  
run("RGB Color");  
selectWindow("cell corner G");  
run("Measure");  
setResult("Label", 5, "cell corner G")  
run("RGB Color");  
selectWindow("paroi S");  
run("Measure");  
setResult("Label", 6, "membrane S")  
run("RGB Color");  
selectWindow("LM S");
```

```

run("Measure");
setResult("Label", 7, "LM S")
run("RGB Color");
selectWindow("cell corner S");
run("Measure");
setResult("Label", 8, "cell corner S")
run("RGB Color");

////////////////////////////////////final montage////////////////////////////////////

close("cell corner");
close("parois");
close("lamelle moyenne");
close("C1-image");
close("C2-image");
close("C3-image");
close("C4-image");

run("Concatenate...", "open image1=[parois H] image2=[LM H] image3=[cell corner
H] image4=[paroi G] image5=[LM G] image6=[cell corner G] image7=[paroi S] image8=[LM
S] image9=[cell corner S]");

run("Make Montage...", "columns=3 rows=3 scale=0.5 ");
selectWindow("Montage");

//rename(temp);

run("Enhance Contrast", "saturated=0.35");")
result_imp = WindowManager.getCurrentImage()

```

```

interpreter.run("""
selectWindow('Montage');
close("\\Others");
""")

#new_title = "Result-" + original_title
result_imp.setTitle(original_title)

def main():

    # Dialog asking if we want to process a Single Image or Batch
    gd1 = GenericDialog("Lignin Segmentation")
    gd1.addChoice("What action do you want to perform?", ["Single Image", "Batch"],
"Single Image")

    gd1.hideCancelButton()

    gd1.showDialog()

    gd2 = GenericDialog("Lignin Segmentation")
    gd2.addChoice("_What type if segmentation do you want to perform?", ["Parametric
Segmentation", "AI Segmentation", ], "Parametric Segmentation")

    gd2.hideCancelButton()

    if gd1.getNextChoice() == "Single Image":

        # Single Image selected
        gd2.showDialog()

        choice_2 = gd2.getNextChoice()

        if choice_2 == "Parametric Segmentation":

            parametric_segmentaion_single()

        elif choice_2 == "AI Segmentation":

            ai_segmentation_single()

```

```

else:
    # User does not know. Will process by parametric then by AI
segmentation if the parametric doesn't work
    pass
else:
    gd2.showDialog()
    choice_2 = gd2.getNextChoice()
    if choice_2 == "Parametric Segmentation":
        parametric_segmentaion_batch()
    elif choice_2 == "AI Segmentation":
        ai_segmentation_batch()
    else:
        # User does not know. Will process by parametric then by AI
segmentation if the parametric doesn't work
        pass
if __name__ == "__main__":
    main()
"""from ij.macro import Interpreter
from ij import WindowManager
import time
interpreter = Interpreter()
imp = WindowManager.getCurrentImage()
imp_clone = imp.clone()
imp.close()
time.sleep(2)

```

```
imp_clone.show()""
```

parametric_segmentation.ijm :

```
// images must be high resolution images, respecting nyquist criterion and with 12 to 16 bits
```

```
// with 5 channels: autofluorescence-H-G-S-transmission.
```

```
// Only channel 2 to 4 are used for calculation
```

```
// the macro provides a montage and stack of each segmentation channel (RGB) and quantified data in
```

```
// the "result" window
```

```
//
```

```
// to operate, just open your image and click run on this macro
```

```
// you can select what you want to measure on the next line called set measurements:
```

```
run("Set Measurements...", "mean redirect=None decimal=0");
```

```
temp = getInfo("image.filename");
```

```
rename("image");
```

```
run("Split Channels");
```

```
////////// segmentation starts here//////////
```

```
selectWindow("C4-image");
```

```
run("Duplicate...", "title=C4-masque ");
```

```
//run("Threshold...");
```

```
setAutoThreshold("Otsu dark");
```

```
setOption("BlackBackground", true);  
run("Convert to Mask");  
run("Despeckle");  
  
selectWindow("C3-image");  
run("Duplicate...", "title=C3-masque ");  
setAutoThreshold("Otsu dark");  
//run("Threshold...");  
setAutoThreshold("Otsu dark");  
run("Convert to Mask");  
run("Despeckle");  
  
selectWindow("C2-image");  
run("Duplicate...", "title=C2-masque ");  
setAutoThreshold("Otsu dark");  
//run("Threshold...");  
setAutoThreshold("Otsu dark");  
run("Convert to Mask");  
run("Despeckle");  
  
selectWindow("C1-image");  
run("Duplicate...", "title=C1-masque ");  
setAutoThreshold("Otsu dark");  
//run("Threshold...");  
setAutoThreshold("Otsu dark");
```

```
run("Convert to Mask");
run("Despeckle");

////merge of masque
imageCalculator("OR create 32-bit", "C1-masque","C2-masque");
imageCalculator("OR create 32-bit", "C3-masque","C4-masque");
imageCalculator("OR create 32-bit", "Result of C1-masque","Result of C3-masque");
close("C4-masque");
close("C3-masque");
close("C2-masque");
close("C1-masque");
close("Result of C1-masque");
close("Result of C3-masque");

run("Duplicate...", "title=[C1-contour cellule]");
run("Invert");
setOption("ScaleConversions", true);
run("8-bit");
run("Fill Holes");
run("Despeckle");
run("Voronoi");

//cell corner
selectWindow("Result of Result of C1-masque");
100
```

```
run("Convert to Mask");
run("Distance Map");
run("Enhance Local Contrast (CLAHE)", "blocksize=127 histogram=256 maximum=3
mask=*None* fast_(less_accurate)");
run("Find Maxima...", "prominence=6 output=[Maxima Within Tolerance]");
run("Erode");
rename("cell corner");
```

```
//lamella
```

```
selectWindow("C1-contour cellule");
setThreshold(1, 65600);
run("Convert to Mask");
imageCalculator("Subtract create", "C1-contour cellule", "cell corner");
selectWindow("Result of C1-contour cellule");
rename("lamelle moyenne");
```

```
//cell wall
```

```
imageCalculator("Subtract create", "Result of Result of C1-masque", "lamelle moyenne");
imageCalculator("Subtract create", "Result of Result of Result of C1-masque", "cell corner");
selectWindow("Result of Result of Result of Result of C1-masque");
setThreshold(1, 65600);
run("Convert to Mask");
rename("parois");
```

```
101
```

```
close("C1-contour cellule");  
close("C1-paroi");  
close("Result of Result of Result of C1-masque");  
close("Result of Result of C1-masque");
```

```
////////// convert binay mask into 0-1 operators
```

```
selectWindow("lamelle moyenne");  
run("Divide...", "value=255");  
selectWindow("parois");  
run("Divide...", "value=255");  
selectWindow("cell corner");  
run("Divide...", "value=255");
```

```
////////////////////////////////////calculations for H////////////////////////////////////
```

```
imageCalculator("Multiply create 32-bit", "parois","C2-image");  
selectWindow("Result of parois");  
setAutoThreshold("Default dark");
```

```
setThreshold(10, 65600);  
run("NaN Background");  
102
```

```
rename("parois H");  
run("Green");  
imageCalculator("Multiply create 32-bit", "C2-image", "cell corner");  
setAutoThreshold("Default dark");  
  
setThreshold(10, 65600);  
run("NaN Background");  
rename("cell corner H");  
imageCalculator("Multiply create 32-bit", "C2-image", "lamelle moyenne");  
setAutoThreshold("Default dark");  
setThreshold(10, 65600);  
run("NaN Background");  
rename("LM H");
```

```
////////////////////////////////calculations for G////////////////////////////////
```

```
imageCalculator("Multiply create 32-bit", "C3-image", "parois");  
selectWindow("Result of C3-image");  
setAutoThreshold("Default dark");  
setThreshold(10, 65600);  
run("NaN Background");  
rename("paroi G");  
  
imageCalculator("Multiply create 32-bit", "C3-image", "lamelle moyenne");  
103
```

```
selectWindow("Result of C3-image");
setAutoThreshold("Default dark");
setThreshold(10, 65600);
run("NaN Background");
rename("LM G");
```

```
imageCalculator("Multiply create 32-bit", "C3-image", "cell corner");
setAutoThreshold("Default dark");
setThreshold(10, 65600);
run("NaN Background");
rename("cell corner G");
```

```
////////////////////////////////calculations for S////////////////////////////////
```

```
imageCalculator("Multiply create 32-bit", "C4-image", "parois");
selectWindow("Result of C4-image");
setAutoThreshold("Default dark");
setThreshold(10, 65600);
run("NaN Background");
rename("paroi S");
```

```
imageCalculator("Multiply create 32-bit", "C4-image", "lamelle moyenne");
selectWindow("Result of C4-image");
setAutoThreshold("Default dark");
```

```
setThreshold(10, 65600);
```

```
run("NaN Background");
```

```
rename("LM S");
```

```
imageCalculator("Multiply create 32-bit", "C4-image", "cell corner");
```

```
setAutoThreshold("Default dark");
```

```
setThreshold(10, 65600);
```

```
run("NaN Background");
```

```
rename("cell corner S");
```

```
////////////////////////////////// measurements //////////////////////////////////
```

```
run("Clear Results");
```

```
selectWindow("parois H");
```

```
run("Measure");
```

```
run("RGB Color");
```

```
selectWindow("LM H");
```

```
run("Measure");
```

```
run("RGB Color");
```

```
selectWindow("cell corner H");
```

```
run("Measure");
```

```
run("RGB Color");
```

```
selectWindow("paroi G");
```

```
run("Measure");
```

```
run("RGB Color");
```

```
selectWindow("LM G");
run("Measure");
run("RGB Color");
selectWindow("cell corner G");
run("Measure");
run("RGB Color");
selectWindow("paroi S");
run("Measure");
run("RGB Color");
selectWindow("LM S");
run("Measure");
run("RGB Color");
selectWindow("cell corner S");
run("Measure");
run("RGB Color");
```

//////////////////////////////////final montage//////////////////////////////////

```
close("cell corner");
close("parois");
close("lamelle moyenne");
close("C1-image");
close("C2-image");
close("C3-image");
```

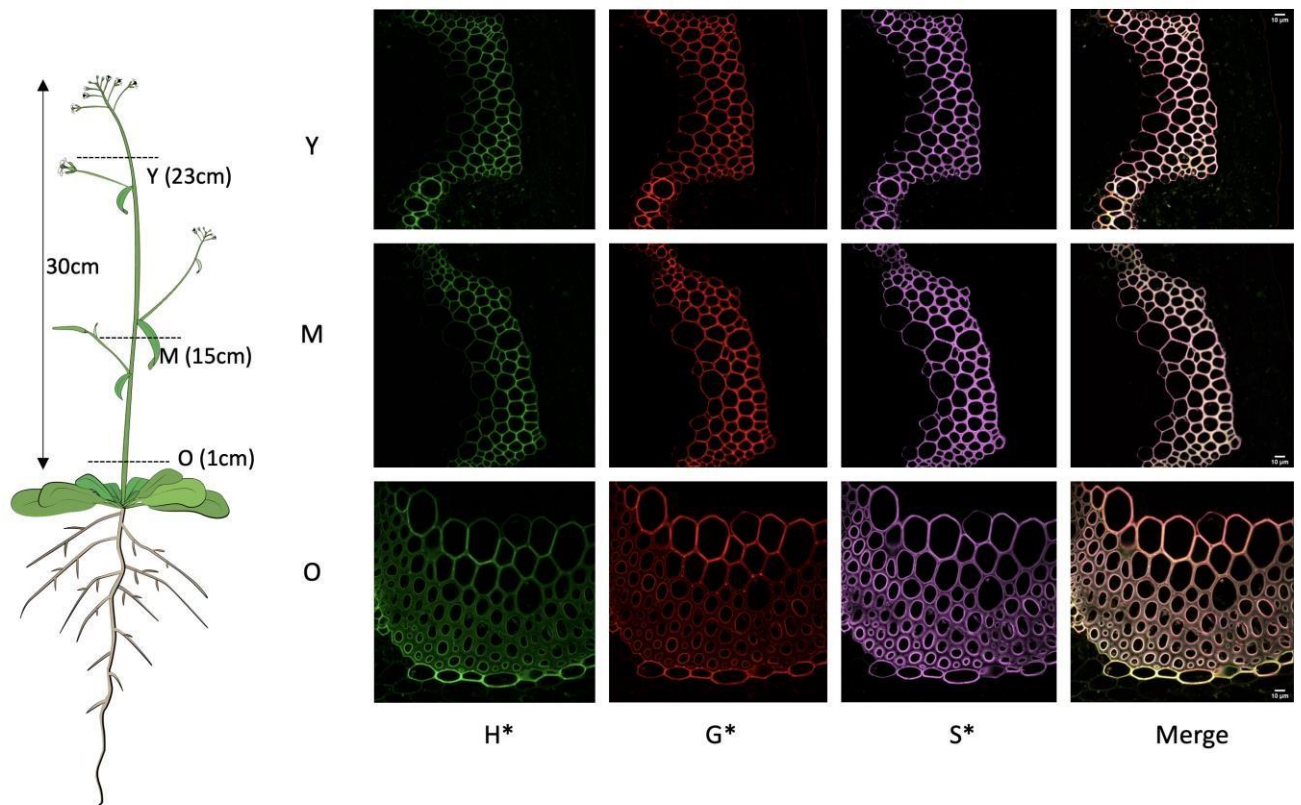
```
close("C4-image");  
  
run("Concatenate...", "open image1=[parois H] image2=[LM H] image3=[cell corner H]  
image4=[paroi G] image5=[LM G] image6=[cell corner G] image7=[paroi S] image8=[LM S]  
image9=[cell corner S]");  
  
run("Make Montage...", "columns=3 rows=3 scale=0.5 ");  
  
selectWindow("Montage");  
  
rename(temp);  
  
run("Enhance Contrast", "saturated=0.35");
```

Supplemental Figure S1. Bioorthogonal lignin triple (H*, G*, and S*) labelling in WT Arabidopsis floral stems.

Supplemental dataset provided at <http://doi.org/10.5281/zenodo.4809980> This dataset

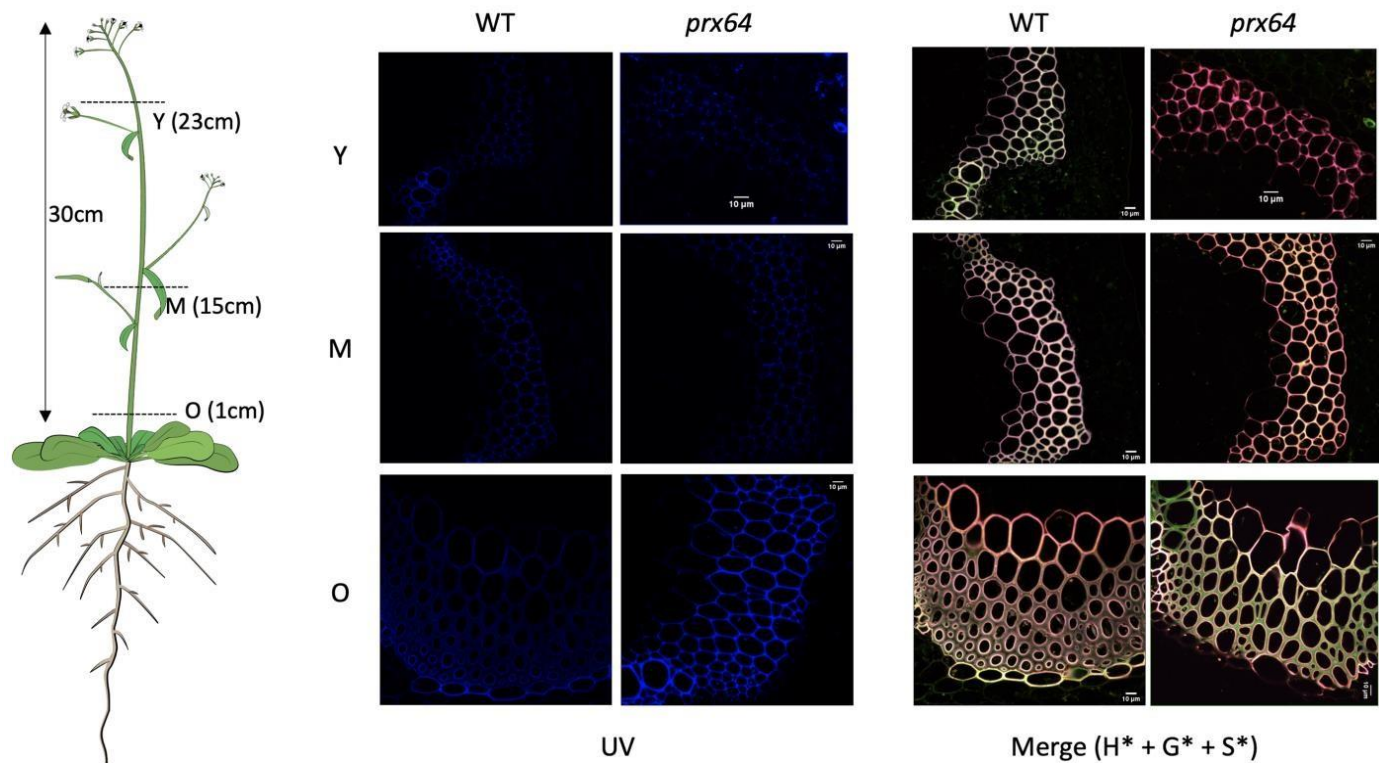
contains:

- the algorithm with graphical user interface for imageJ and its installation procedure ("Cell_Wall_Segmentation" and "Cell_Wall_SegmentationTutorial")
- a folder comprising a classifier and a dataset compatible with the machine learning part of the algorithm: "data and classifier for weka"
- representative images adapted for testing: "representative images"
- the macro corresponding to the parametric segmentation procedure (see imageJ documentation for installation instructions): "parametric_segmentation"



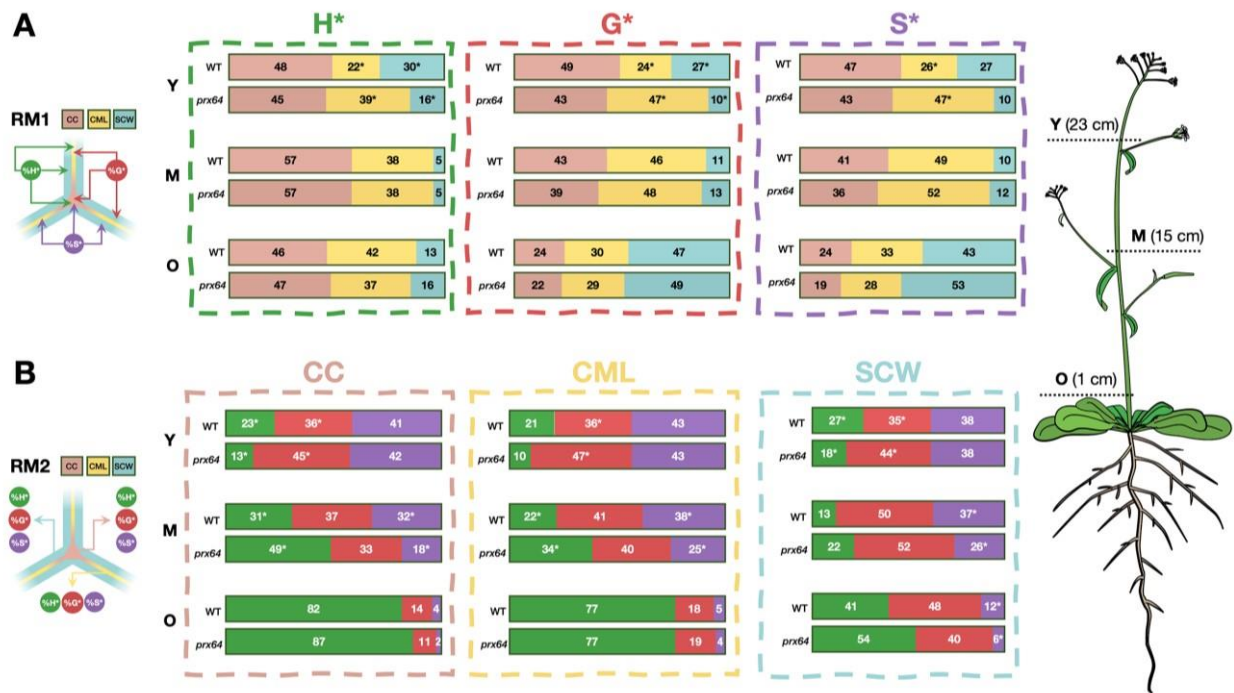
Supplemental Figure S1: Bioorthogonal lignin triple labelling of interfascicular fiber cell walls in cross-sections made at different heights (Y - young, M - medium, O - old) of wild-type (WT) Arabidopsis floral stems. H*, G* and S* = green/red/magenta CLSM channel images revealing incorporation of the corresponding H*, G* and S* reporters. Merge = merged channels. Scale bar = 10 µm.

Supplemental Figure S2. UV lignin autofluorescence and bioorthogonal lignin triple (H*, G*, and S*) labelling in Arabidopsis WT and *prx64* mutant floral stems



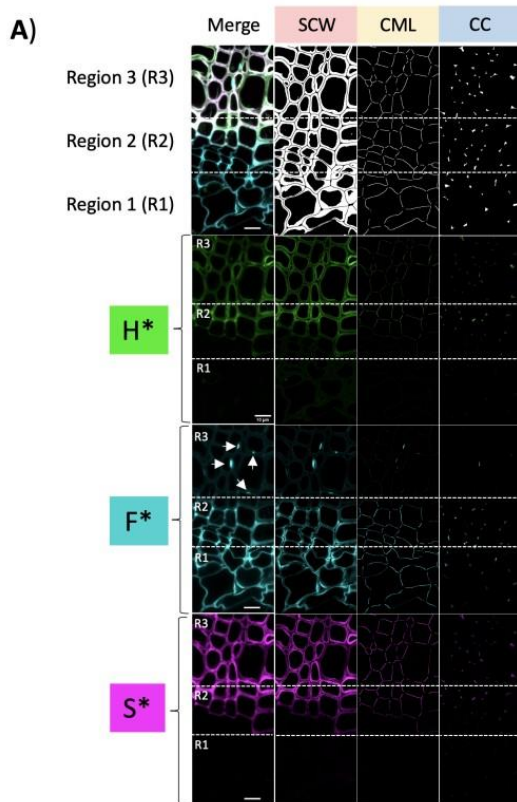
Supplemental Figure S2: Bioorthogonal lignin triple (H*, G*, S*) labelling in interfascicular fibers of cross-sections made from different heights in Arabidopsis WT and *prx64* mutant floral stems. Lignin autofluorescence (blue) and merged channels. Y = young, M = medium, O = Old. Scale bar = 10 μm.

Supplemental Figure S3. Comparison of monolignol reporter incorporation profiles in WT and *prx64* mutant Arabidopsis stem fiber cell walls.



Supplemental Figure S3. Comparison of monolignol reporter incorporation profiles in WT and *prx64* mutant Arabidopsis stem fiber cell walls. **A**) Relative distribution of H*, G* and S* reporters incorporated into different fiber cell wall zones in Y (young), M (medium) and O (old) stem cross sections analyzed by ratiometric method 1 (RM1), CC = cell corner, CML = compound middle lamella, SCW = secondary cell wall; figures represent the percentage of total H*, G* and S* signal incorporated into the different wall zones, Values marked with * indicate significantly different values (Students Ttest, p-value = 0.05) between WT and mutant plants for a given stem height (Y, M, O). **B**) Relative contribution of all reporters to total signal in the cell corner (CC) analyzed by ratiometric method 2 (RM2); figures represent the percentage contribution of each reporter's signal to the total signal intensity in different cell wall zones. Values marked with * indicate significantly different values (Students T-test, p-value = 0.05) between WT and mutant plants for a given stem height (Y, M, O).

Supplemental Figure S4. Automatic segmentation of cell wall zones in flax stem tissues showing relative distribution of lignin and NCP reporters.



B)

Reporter	CW zone	% Total Intensity		
		Region 1	Region 2	Region 3
H*	CC	11 %	44 %	45 %
	CML	13 %	38 %	49 %
	SCW	13 %	38 %	49 %
F*	CC	43 %	44 %	13 %
	CML	43 %	40 %	17 %
	SCW	43 %	38 %	20 %
S*	CC	11 %	40 %	49 %
	CML	12 %	35 %	53 %
	SCW	12 %	36 %	52 %

C)

Reporter	CW zone	% Intensity (RM1)		
		Region 1	Region 2	Region 3
H*	CC	34 %	41 %	36 %
	CML	33 %	30 %	33 %
	SCW	32 %	29 %	32 %
F*	CC	40 %	43 %	33 %
	CML	32 %	31 %	34 %
	SCW	27 %	25 %	33 %
S*	CC	16 %	38 %	44 %
	CML	16 %	32 %	46 %
	SCW	67 %	30 %	10 %

Supplemental figure S4. Automatic segmentation of cell wall zones in flax stem tissues showing relative distribution of lignin and non-cellulosic polysaccharide reporters. **A)** The 3 masks (CC, CML, SCW) are applied to three fluorescence channels of CLSM images of flax stem cross-sections incubated with H* and S* monolignol reporters and F* peracetylated alkyne-tagged fucose (Ac₄FucAlk) reporter according to the triple bioorthogonal strategy. **B)** Table indicating the relative percentage of total signal for reporters in a given cell wall zone found in each of the three different tissue regions (1, 2, 3) analyzed. **C)** Ratiometric analysis 1 (RM1) of the relative amounts of total reporter signal found in the different cell wall zones. H*, S* = monolignol reporters; F* = fucose reporter; CC = cell corner, CML = compound middle lamella, SCW = secondary cell wall, scale bar = 10 μm; red values in tables = highest %, green values in tables = lowest %. Region 1 corresponds to the phloem/vascular cambium, Region 2 corresponds to the vascular cambium/young differentiating xylem, Region 3 corresponds to more mature xylem tissue, arrows indicate xylem pits.

Paper II : Application of plant cell wall segmentation to safranin-O staining

The implementation of the REPRISAL segmentation technique on the images obtained after triple labelling gives access to subcellular information and allowed us to identify different patterns of monolignol reporter incorporation depending on developmental stage and/or mutation-related events. However, while this strategy provides detailed information on the *potential* of cell walls to undergo lignification, it does not inform us about the total amount of lignins present in the different cell wall layers (reporters are only poorly/not incorporated into already lignified walls).

It is therefore important to be able to quantify the lignins in the wall. Our choice was to use a technique based on safranin-O fluorescence recently developed at the UGSF (Baldacci-Cresp et al., 2020). This approach allows us to obtain semi-quantitative spatial information on the amount of lignins in the walls. In the following chapter we demonstrate how the segmentation and ratiometric approach previously developed can also be successfully applied to the determination of lignins content by safranin-O staining in the stems of wild type and mutant *thaliana* plants. Two different mutants were used, *prx72*, a class III peroxidase involved in lignification (Herrero et al., 2013) and (GAUT1) *gaut9* (Galacturonosyltransferase 9), an α 1,4-D-galacturonosyltransferase (Caffall et al., 2009) with a decrease of GalA.

The advantage of using the same image processing approach is that it allows the association of results obtained by the two methods, thereby providing complementary spatial information about lignification.

Personal contribution : For this article I realized the experiments, adapted the plug-in with the help of Dr. Corentin Spriet and participated to the writing with all the co-authors.

Morel, O., Spriet, C., Lion, C., Baldacci-Cresp, F., Pontier, G., Baucher, M., Biot, C., Hawkins, S., & Neutelings, G. (2023). Ratiometric Fluorescent safranin-O Staining Allows the Quantification of Contents In Muro. *Methods in Molecular Biology (Clifton, N.J.)*, 2566, 261–268. https://doi.org/10.1007/978-1-0716-2675-7_21/COVER



Chapter 21

Ratiometric Fluorescent Safranin-O Staining Allows the Quantification of Lignin Contents In Muro

Oriane Morel, Corentin Spriet, Cédric Lion, Fabien Baldacci-Cresp, Garance Pontier, Marie Baucher, Christophe Biot, Simon Hawkins, and Godfrey Neutelings

Abstract

In some specific vascular plant tissues, lignin can impregnate the entire cell wall to make it more rigid and hydrophobic. Different techniques have been developed in the past years to make possible the quantification of this polyphenolic polymer at the organ or tissue level, but difficulties of access to the cellular level remain. Here we describe an approach based on ratiometric emission measurements using safranin-O and the development of a macro adapted for the FIJI software, which makes it possible to quantify lignin in three different layers of the cell wall on images captured on a fluorescent confocal microscope.

Key words Lignin quantification, Safranin-O, Cell wall, Segmentation, Confocal microscopy

1 Introduction

Lignin is a major component of plant cell walls present in some specialized tissues of vascular plants. This polyphenolic polymer is mainly derived from the polymerization of *p*-coumaryl, coniferyl, and sinapyl alcohols differing in their degree of methoxylation. After their incorporation, these three *p*-hydroxycinnamyl alcohol precursors (monolignols) give rise to *p*-hydroxyphenyl (H), guaiacyl (G), and syringyl (S) units, respectively. Lignin is responsible for water transport in the xylem vessel elements and confers strength to cell walls contributing to the general mechanical support necessary for plant upright growth [1]. Studies on lignin biosynthesis are motivated by the need to understand its role in plant physiology but also by the increasing use of biomass in agro-industry [2].

A good understanding of lignin metabolism necessarily requires the use of techniques allowing its quantification. Two main “wet chemistry” approaches are commonly used for

quantifying lignin, depending upon the plant species and, more importantly, whether the tissues contain more or less quantities of lignins. Thus, the method using the solubilization of lignins by acetyl bromide [3, 4] is well adapted to herbaceous species whereas the gravimetric Klason method [5] is more suitable for woody species. There are also different methods to determine the H, G, and S subunit composition and the S/G ratio of lignins. Historically, thioacidolysis [6] and nitrobenzene oxidation [7] methods were used, but they are now gradually replaced by pyrolysis coupled with gas chromatography/mass spectrometry (GC/MS) [8] or nuclear magnetic resonance (NMR) [9]. These approaches provide relevant information on the different tissues/organs studied, but their use leads to irreversible tissue destruction. It is therefore not possible to obtain information concerning lignin quantities and compositions at the cellular level.

Therefore, histochemical approaches were also developed such as phloroglucinol staining (Wiesner reaction), which specifically reveals the cinnamaldehyde functions of S and G unit derivatives. In this case, the intensity of the coloration will depend on the quantity of the red chromogen produced by the reaction [10]. The Mañile test, on the other hand, uses potassium permanganate and hydrochloric acid to transform G and S residues into catechols, which then give rise to orange-brown quinones in the case of G lignins and purple-red quinones for G-S lignins [11]. Other approaches exploit the autofluorescence of lignins [12] or the possibility to visualize them by using fluorescent compounds such as auramine [13] and acriflavine [14]. All these techniques can therefore provide relatively detailed spatial information, but without offering the possibility to produce quantitative data.

Safranin-O has an interesting potential as a fluorescent probe [15]. Indeed, the emission spectrum of safranin-O depends on the amount of lignin present in the cell wall (Fig. 1). When present in high amounts, the emission will be more intense in the red part. The emission spectrum (at an excitation of 488 nm) always shows a maximum at 568 nm. Before this value, the aspect of the graph is invariable whatever the amount of lignin. On the other hand, in the orange/red area between 568 and 600 nm, it is dependent on the cell wall environment. Indeed, emission values are higher in the lignified tissues (xylem) compared to the non-lignified tissues. Based on these observations, our group developed an approach including a ratiometric method allowing the relative quantification of lignins by comparing the emissions between 540–560 nm (stable portion) and 570–600 nm (variable portion) [16].

In this chapter, we first describe the methodology allowing the quantification of lignin at the cellular level following confocal microscopy acquisition. In a second step, we demonstrate the possibility to apply a segmentation approach [17] to subdivide the cell wall on these images in an automatic way in order to obtain

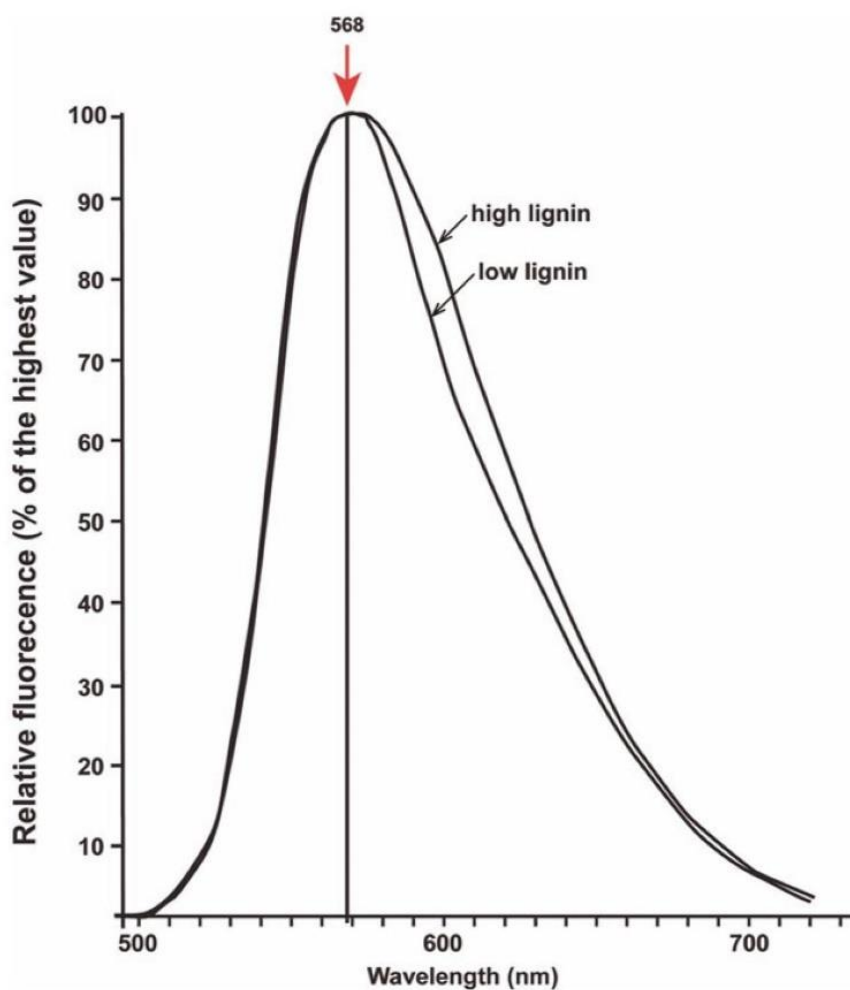


Fig. 1 Average safranin-O spectra (with excitation at 488 nm) of cell walls from different flax (*Linum usitatissimum*) tissues containing low amounts (bast fiber and cambial cell walls) or high amounts (xylem cell walls) of lignins

information on lignification in the cell corners, the compound middle lamella, and the secondary cell walls.

2 Materials

2.1 Plant Growth

1. Plant seeds. In this study we used *Arabidopsis thaliana* as an example.
2. Pots filled with potting soil.

2.2 Sample Preparation

1. 50% and 70% (v/v) ethanol solutions.
2. 4% (w/v) agarose solution in ultrapure water.
3. Cyanoacrylate glue.

4. 0.2% safranin-O in a 50% (v/v) aqueous ethanol solution kept in the dark.

2.3 Equipment and Software

1. Plant growth chamber in which temperature and artificial light variations are possible.
2. Vibratome (e.g., VT-1000S, Leica, Wetzlar, Germany) for cutting sections to a thickness of 80 μm (*see Note 1*).
3. Microplate shaker.
4. Confocal laser scanning microscope [we use a Nikon AIR confocal (Nikon, Tokyo, Japan) equipped with a 60 \times /1.4 aperture oil immersion objective (Plan APO VC) and the NIS Element AR3.0 software].
5. FIJI v2.0 [18]. This software can be downloaded at <https://fiji.sc>.
6. The associated FIJI macro developed for the quantification of fluorescence and segmentation has the following assigned doi, 10.5281/zenodo.5775647, and can be downloaded from the Zenodo website (<https://zenodo.org/record/5775647#.YbiaNi17RhE>).

3 Methods

3.1 Plant Growth

In our experiment, we used *Arabidopsis thaliana* seeds that were stratified during 72 h at 4 °C in the dark. Plants were cultivated in a growth chamber under 12 h light (100 PAR light intensity) at 22 °C and 12 h dark at 20 °C for 6 weeks. The photoperiod was then changed to 16 h light and 8 h dark, and the floral stems were cut when they reached a size of 30 cm.

3.2 Sample Preparation

1. Collect floral stem samples of 0.5-cm length.
2. Melt the 4% agarose solution and maintain it at 55 °C (*see Note 2*).
3. Pour 1.5 mL of this solution in enough wells of a 48-well cell culture plate, and let the agarose cool down until it becomes thicker but still stays liquid.
4. Place the floral stem samples in the center of each well with tweezers, and maintain in a vertical position until the agarose hardens.
5. Leave the plate on the bench for another 10 min, and then unmold with a thin spatula.
6. Cut the basis of the agarose perfectly perpendicular to the fragment with a razor blade.
7. Glue the agarose-embedded fragment on the specimen holder with cyanoacrylate glue (*see Note 3*).

8. Cut 80- μm -thick fragments with the vibratome (*see Note 4*).
9. Place the sections in a 48-well cell culture plate containing 1-mL 50% (v/v) ethanol solution.

3.3 Sample Staining

1. Replace the ethanol in the section-containing well by a fresh or daily thawed 0.2% safranin-O solution (*see Note 5*), and incubate for 10 min on a microplate shaker in the dark, at room temperature. The shaking intensity should be high enough to allow good mobility of the section in the liquid.
2. Remove all safranin-O solution, and replace with 50% ethanol. Incubate with shaking for 10 min in the dark.
3. Remove the solution and rinse twice with ultrapure water for 15 min under the same shaking parameters.
4. Mount the sections in water on a glass slide and place a cover-slip (*see Note 6*).

3.4 Image Capture

1. Perform the acquisition on the tissues by using three independent channels. The first is on autofluorescence excitation at 405 nm and emission at 450/500 nm; the second is on the green channel with excitation at 488 nm and emission at 530–560 nm. The third is on the red channel with excitation at 561 nm and emission at 570–600 nm. All tracks must be acquired sequentially, and parameters must be kept constant for all acquisitions.
2. Select a flat region and adjust your focus to perform images between 6 and 9 μm deep from the surface (*see Note 7*).

3.5 Image Analysis

1. Crop the sharp area of the images acquired in Subheading 3.4.
2. Treat images using FIJI v2.0 and the associated homemade macro developed for this method (*see Note 8*). First open the Fiji app; open the macro and finally the image cropped in 1. Run the macro and follow the instructions. The macro includes two steps:
 - (a) First, a ratio image is generated as previously described [16] (Fig. 2). The result appears as a ratiometric image with a color range between 0 (purple) and 2 (red). The intensity ratio values also appear in the results window and can be used for quantification.
 - (b) Combining safranin fluorescence and lignin autofluorescence information, the ratio image obtained in Subheading 3.5.1 is then segmented, as previously described [17], into three cell walls regions: the cell corner (CC), the compound middle lamella (CML) consisting of the middle lamella and the primary cell wall, and the secondary cell wall (SCW) (Fig. 3) (*see Note 9*).

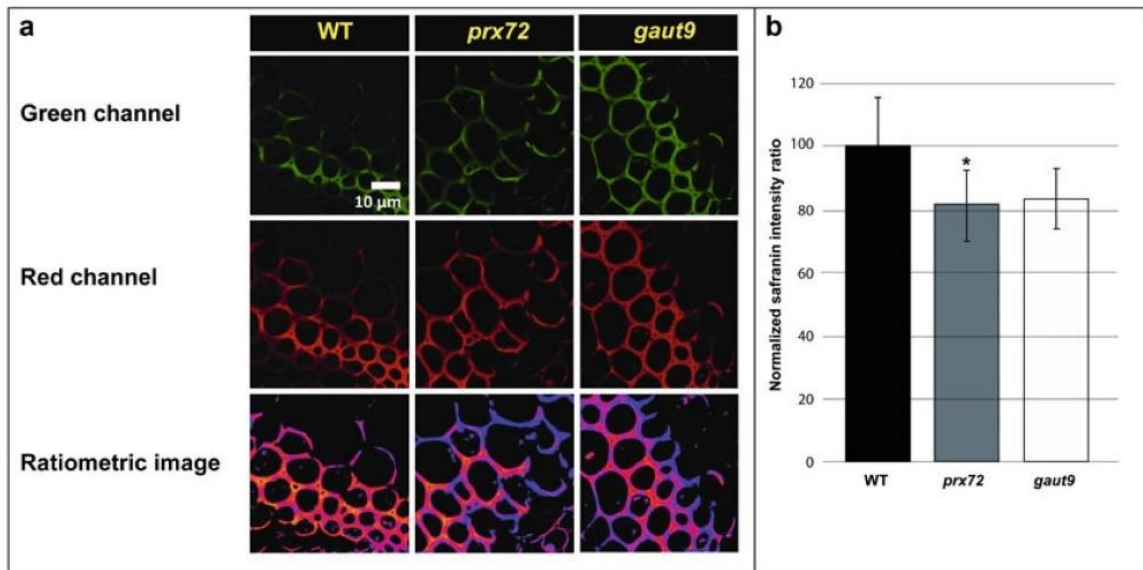


Fig. 2 Local lignin content determination on *Arabidopsis* floral stems (wild type and mutants) using safranin-O fluorescence-based method. (a) Green and red channels correspond to safranin fluorescence. The ratiometric image was obtained by applying the specific FIJI macro on both images. (b) The normalized safranin intensity ratios (\pm SD) are represented (WT = 100%). The quantification was performed on interfascicular fibers. Means (\pm SD) with an asterisk are significantly different according to Student *t*-test (p -value < 0.05 , $n = 3$). WT, wild type; *prx72*, Salk_136893 mutant; *gaut9*, SALK_040287 mutant

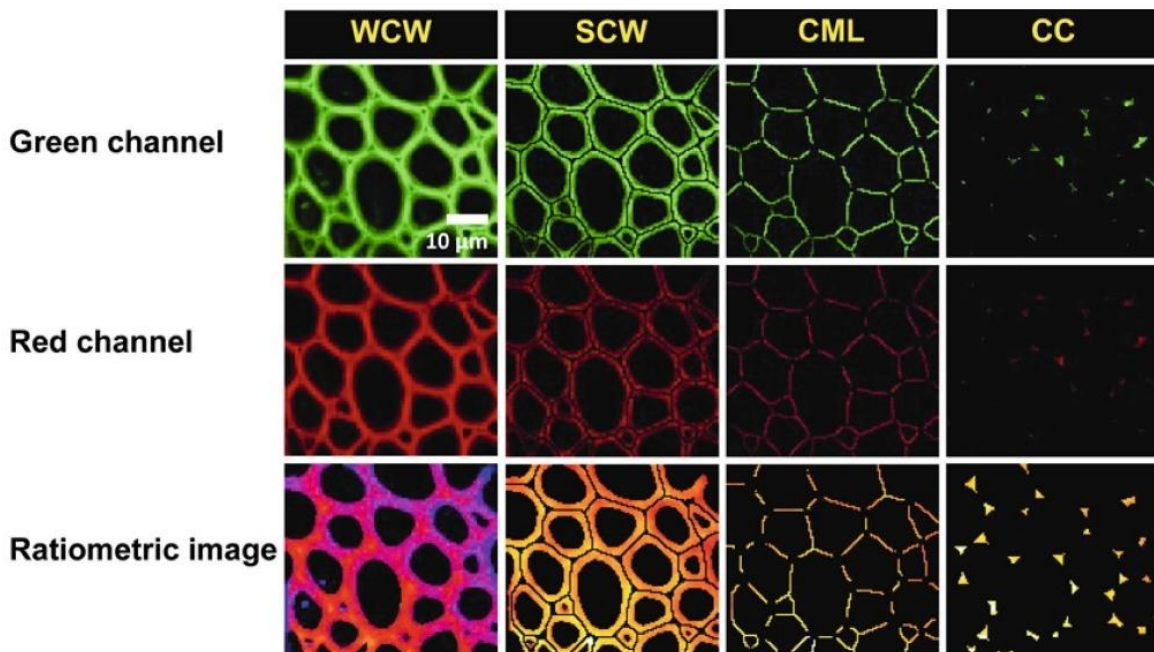


Fig. 3 Automatic segmentation of different cell wall zones. Three masks were applied to images of *Arabidopsis* flowering stem cross sections stained with safranin-O and observed by confocal laser scanning microscopy. Green and red channels correspond to safranin-O fluorescence. WCW, whole cell walls; SCW, secondary cell walls; CML, compound middle lamella; CC, cell corner

4 Notes

1. The use of a vibratome ensures regular homogenous sectioning of the plant tissues. However, hand sectioning with a sharp razor blade can also be performed. The sections should then be checked under the microscope, and only the most fine and regular ones should be selected for the safranin-O staining.
2. If using a vibratome, the agarose solution must be used within the week. In our protocol, we suggest to use multi-well cell culture plates, but it is also possible to use 1.5-mL microtubes. Their bottom conical part should first be cut off and placed inside the rest of the tube. Both parts are then sealed with a piece of parafilm. The melted agarose can then be poured in the tube and the sample placed in the center. When the gel has cooled down, it can be unmolded by pressing on the bottom conical portion of the tube.
3. On the Leica VT-1000S vibroslicer, it is possible to place up to three samples on one holder.
4. The speed and the frequency depend on the tissue. For a fragment taken at the base of the floral stem, use a speed of 0.4 mm/s (position 6 on the Leica model) and a frequency of 70 Hz (position 7).
5. The 0.2% safranin-O in a 50% (v/v) ethanol solution can be stored for several months at $-20\text{ }^{\circ}\text{C}$. When the solution is thawed, it should be stored in the dark and used within 24 h.
6. The samples must be stained and processed in the same day in order to be compared. Each characterization of mutants, for example, must be done with the corresponding wild type.
7. When using the confocal microscope, the focus is more accurate when using the red channel.
8. Accurate analysis should be performed on at least three different plants on which five sections were performed and at least two images captured per section (total = 30 images).
9. The segmentation macro also allows access to the intensity ratio values in the three layers of the cell wall. It is therefore possible to perform accurate quantification and statistics on lignin amounts.

References

1. Boerjan W, Ralph J, Baucher M (2003) Lignin biosynthesis. *Annu Rev Plant Biol* 54: 519–546. <https://doi.org/10.1146/annurev.arplant.54.031902.134938>
2. Li X, Weng JK, Chapple C (2008) Improvement of biomass through lignin modification. *Plant J* 54:569–581. <https://doi.org/10.1111/j.1365-313X.2008.03457.x>
3. Morrison I (1972) Improvements in the acetyl bromide technique to determine lignin and digestibility and its application to legumes. *J Sci Food Agric* 23:1463–1469

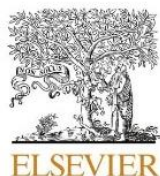
4. Morrison I (1972) A semi-micro method for the determination of lignin and its use in predicting the digestibility of forage crops. *J Sci Food Agric* 23:455–463
5. Johnson D, Moore WE, Zank LC (1961) The spectrophotometric determination of lignin in small wood samples. *J Tech Assoc Pulp Pap Ind* 44:793–798
6. Lapierre C, Monties B, Rolando C (1986) Thioacidolyse von Pappelholzligninen: Nachweis von monomeren Syringylverbindungen und Charakterisierung von Guajacyl-Syringyl-Ligninfraktionen. *Holzforschung* 40: 113–118. <https://doi.org/10.1515/hfsg.1986.40.2.113>
7. Monties B (1989) Lignins. In: Dey PM, Harborne JB (eds) *Methods in plant biochemistry*. Academic Press, pp 113–147
8. Wagner A, Ralph J, Akiyama T, Flint H, Phillips L, Torr K et al (2007) Exploring lignification in conifers by silencing hydroxycinnamoyl-CoA: shikimate hydroxycinnamoyltransferase in *Pinus radiata*. *Proc Natl Acad Sci U S A* 104:11856–11861. <https://doi.org/10.1073/pnas.0701428104>
9. Mansfield SD, Kim H, Lu F, Ralph J (2012) Whole plant cell wall characterization using solution-state 2D NMR. *Nat Protoc* 7: 1579–1589. <https://doi.org/10.1038/nprot.2012.064>
10. Clifford MN (1974) Specificity of acidic phloroglucinol reagents. *J Chromatogr A* 94: 321–324. [https://doi.org/10.1016/S0021-9673\(01\)92389-1](https://doi.org/10.1016/S0021-9673(01)92389-1)
11. Day A, Ruel K, Neutelings G, Crônier D, David H, Hawkins S et al (2005) Lignification in the flax stem: evidence for an unusual lignin in bast fibers. *Planta* 222:234–245. <https://doi.org/10.1007/s00425-005-1537-1>
12. Donaldson LA, Radotic K (2013) Fluorescence lifetime imaging of lignin autofluorescence in normal and compression wood. *J Microsc* 251: 178–187. <https://doi.org/10.1111/jmi.12059>
13. Pesquet E, Ranocha P, Legay S, Dignonnet C, Barbier O, Pichon M et al (2005) Novel markers of xylogenesis in zinnia are differentially regulated by auxin and cytokinin. *Plant Physiol* 139:1821–1839. <https://doi.org/10.1104/pp.105.064337>
14. Donaldson LA (2001) Lignification and lignin topochemistry – an ultrastructural view. *Phytochemistry* 57:859–873. [https://doi.org/10.1016/S0031-9422\(01\)00049-8](https://doi.org/10.1016/S0031-9422(01)00049-8)
15. Bond J, Donaldson L, Hill S, Hitchcock K (2008) Safranin fluorescent staining of wood cell walls. *Biotech Histochem* 83:161–171. <https://doi.org/10.1080/10520290802373354>
16. Baldacci-Cresp F, Spriet C, Twyffels L, Blervacq A-S, Neutelings G, Baucher M et al (2020) A rapid and quantitative safranin-based fluorescent microscopy method to evaluate cell wall lignification. *Plant J* 102: 1074–1089. <https://doi.org/10.1111/tpj.14675>
17. Morel O, Lion C, Neutelings G, Stefanov J, Baldacci-Cresp F, Simon C et al (2022) REPRISAL: mapping lignification dynamics using chemistry, data segmentation, and ratio-metric analysis. *Plant Physiol* 188(2):816–830. <https://doi.org/10.1093/plphys/kiab490>
18. Schindelin J, Arganda-Carreras I, Frise E, Kaynig V, Longair M, Pietzsch T et al (2012) Fiji: an open-source platform for biological-image analysis. *Nat Methods* 9: 676–682. <https://doi.org/10.1038/nmeth.2019>

Paper III : Adaptation of Raman spectra analysis

Raman spectrometry is a powerful tool for the molecular analysis of plant walls. In the analyzed spectra, it is easy to have information on the dominant molecules thanks to the region of the spectrum corresponding to a major characteristic vibration. This is the case for ligninlignins, whose vibration at 1600 cm^{-1} is characteristic of the phenylpropanoid cycle, and carbohydrates with a vibration at 1080 cm^{-1} . We wanted to be able to identify in more detail the molecules present in the samples and to distinguish the different polysaccharides, and more specifically, different hemicellulose. For this, we used and compared several methods of spectrum analysis. The results obtained are presented in the following article presently in press.

Personal contribution : For this article I participated in the experiments and the analysis, and participated in the writing of the article.

Morel, O., & Gierlinger, N. (2023). Chemical tissue heterogeneity of young *Arabidopsis* stems revealed by Raman imaging combined with multivariate data analysis. *Microchemical Journal*.(pre proof)



Chemical tissue heterogeneity of young Arabidopsis stems revealed by Raman imaging combined with multivariate data analysis

Oriane Morel^{a, b}, Notburga Gierlinger^{a, *}

^a Institute of Biophysics, Department of Bionanosciences, University of Natural Resources and Life Sciences Vienna (BOKU), Vienna, Austria

^b CNRS, UMR 8576—UGSP—Unité de Glycobiologie Structurale et Fonctionnelle, University of Lille, Lille, France

ARTICLE INFO

Keywords:

Chemical imaging
Unmixing algorithm
Orthogonal matching pursuit
Cellulose
Lignin
Hemicellulose

ABSTRACT

Structural and chemical tissue heterogeneity in plant stems is essential to fulfil the many different functions for growth and survival. Cutting microsection of young developing stems of the model plant *Arabidopsis* opened the view on vascular bundles (transport of water, nutrients, food, and other chemicals), interfascicular fibers (mechanical support), parenchyma (production, storage) and the epidermis with cuticle (protection, barrier, exchange,...). Mapping such a cross-section with a Confocal Raman microscope resulted in hyperspectral datasets, which are the basis to image chemical heterogeneity with a spatial resolution of 300 nm in context with the microstructure. We generated the images based on three different multivariate approaches: unmixing to find the most pure components, cluster analysis to segment the dataset into clusters with spectral similarity, and orthogonal matching pursuit to fit the original spectra at every pixel by a linear combination of plant component reference spectra. All three visualized chemical heterogeneity and confirmed in a complementary way the distribution of carbohydrates and aromatic components. The true component analysis was superior to cluster analysis in specificity and added information on lipids and starch distribution. Due to the multicomponent nature of plant tissues no “pure” components were retrieved, wherefore a subsequent mixture analysis of extracted component spectra with a reference database followed. This led to details on the molecular composition of the spectra and tissues and was essential input for a final reference component fit at every pixel. By the last analysis, different aromatic components and hemicelluloses were discriminated and a similarity of their distribution patterns elucidated. Insights into starch and lipid distribution as well as the aromatic and protein co-location (mixtures) of cell contents were gained. The fit of the latter lumen content was inferior to the other fits due to noisier spectra (higher fluorescence background) and relevant protein and enzyme spectra were missing in our database. The gained comprehensive view on plant stem tissue heterogeneity showed the potential for future studies to unravel plant species characteristics and adaptations, but also to follow plant developmental processes and/or stress responses and/or genetic modifications.

1. Introduction

Arabidopsis thaliana is a widely used model plant. Its rapid growth and the many available mutants [1–2] make it more interesting for developmental studies than other plants. Another advantage is the thin stem, which allows to image several different tissue types at once and in a short period of time. Among the various imaging methods to visualize the components of plant cells and their walls, histochemical staining is used since many years to visualize different components in transmitted light: e.g. Wiesner stain for lignin [3], Congo red for cellulose or ruthenium red for pectin [4]. These stains are not quantitative and often lack specificity and/or accessibility due to the multicomponent na-

ture of plant tissues and cell walls. With fluorescence microscopy lignin can be visualized by its auto fluorescence properties [5], or by using safranin staining [6]. The different cell wall polysaccharides can be detected by specific antibodies and then revealed by secondary antibodies coupled to a fluorophore [7–9]. Only a limited number of fluorophores can be used at the same time and all approaches are not cumulative to allow visualization of different constituents at the same time, but are limited to one or by using counterstains to two component classes.

Microspectroscopic approaches overcome the limit to detect only one component class as the recorded spectra represent molecular fingerprints including all components of plant tissues, from carbohydrates

* Corresponding author.

E-mail address: burgi.gierlinger@boku.ac.at (N. Gierlinger).

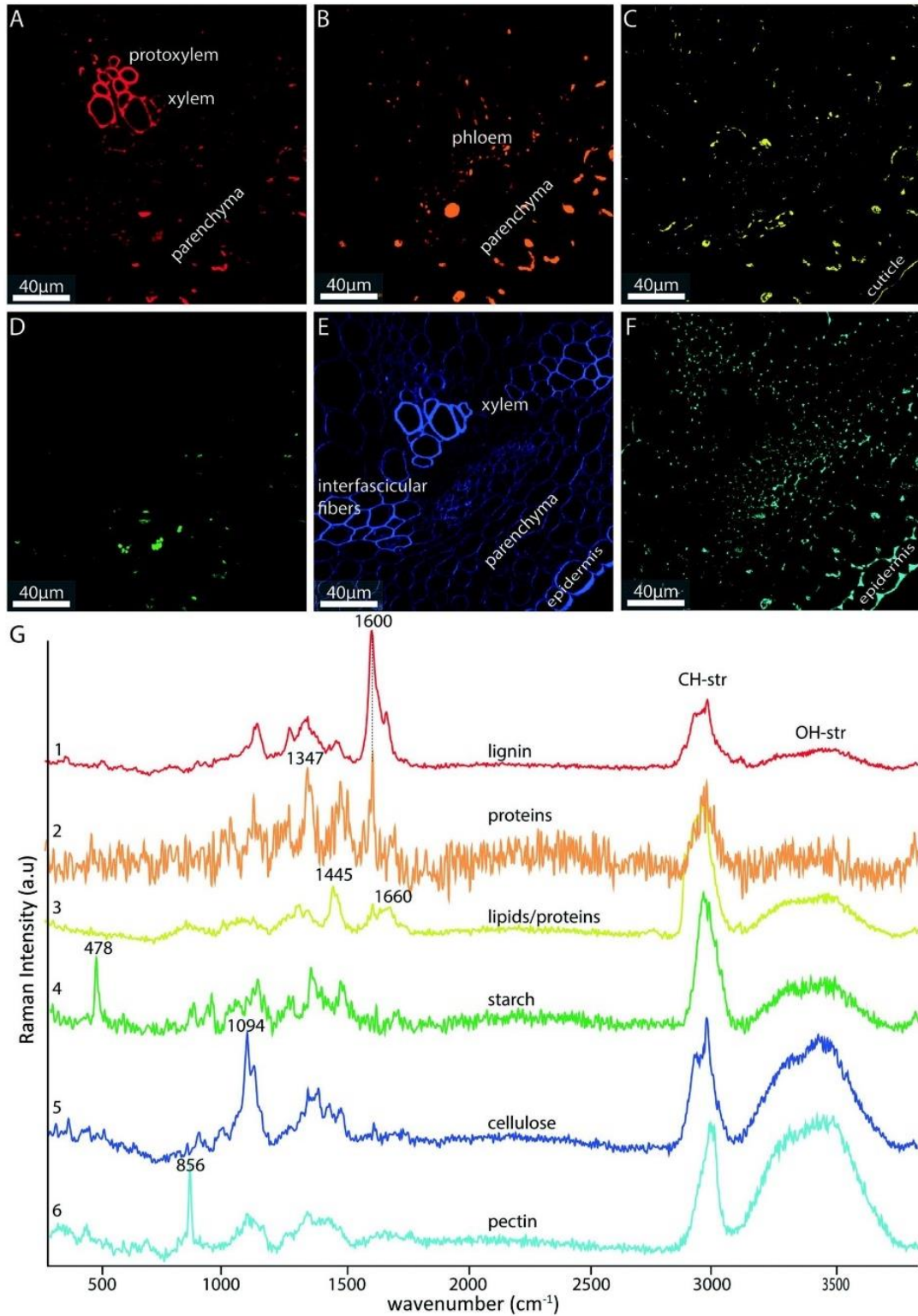


Fig. 1. Raman imaging based on “true component analysis” distinguished six chemically different regions in the developing Arabidopsis stem. A: Protoxylem and cell corners (red) with the highest lignin content B) lumen content in the parenchyma tissues C) lipidic components lining cell walls and on top of the epidermis (cuticle) D)starch storage granules in the parenchyma E) cell wall of all tissues F) epidermal layer and cell corners G) The corresponding spectra confirmed the high lignin content of protoxylem and cell corners 1st spectrum, red). The cell contents showed bands attributed to aromatic components (1600 cm^{-1} band) and proteins (1004 cm^{-1} band) (2nd spectrum, orange), lipids (1445 cm^{-1} band)(3rd spectrum, yellow) and starch (478 cm^{-1} band) (4th spectrum green). Spectra corresponding to cell walls showed marker bands of cellulose (1094 cm^{-1}) (5th spectrum, blue) and the epidermal layer and cell corners in unligified tissues a stronger pectin

to aromatic components to lipids to proteins to minerals [10]. Pure component spectra collections and assignments (e.g. [11], cellulose [12, 13], pectin [14], lignin [15], carbohydrates [16], lipids [17], flavonoid [18], proteins [19]) are the basis to interpret the plant Raman spectra, define marker bands for different components and/or component classes as well as to use the spectra for a comprehensive semi-quantification based on fitting algorithms. The latter one was shown on plant cuticles [20,21], but not yet on Arabidopsis. Raman spectroscopy has already been used in *Arabidopsis thaliana* to identify differences between wt and carbohydrate [22] and lignin [23] mutants. Recently, loss-of-function mutants with altered lignin amount and/or composition have been used together with synthetic monomers and synthetic lignin polymers to benchmark Raman microspectroscopy for in situ semi-quantification of lignin [24]. Beside the multicomponent assessment and molecular specificity, one major asset of Raman microscopy is to image the distribution of the different components with a spatial resolution of about 250 nm by univariate and multivariate imaging [10]. On senescent *A.thaliana* stems, carbohydrate and lignin distribution was visualized by selecting C-H stretching bands (2820–2935 cm⁻¹) and aromatic ring stretching (1550–1700 cm⁻¹), respectively [25]. In another Arabidopsis study the combination of Raman imaging with multivariate analysis (vertex component analysis) revealed more details, including pectin, lignin and cutin distribution as well as changes in cellulose microfibril angle [26]. With a similar multivariate approach four constituents, the cell wall, pigments, protein, and lipids, were decomposed and imaged in Arabidopsis leaves and primary roots by stimulated Raman microscopy (SRS) [27]. SRS had the advantage that plant autofluorescence (by e.g. lignin or plant pigments) do not hinder the analysis, but the wavenumber range is restricted to the CH stretching region (2800 to 3100 cm⁻¹) and thus only four main constituents were distinguished.

In this study, we succeeded to go a step further by imaging component classes and unravelling details on chemical heterogeneity in the different tissue types of *A.thaliana*. For this we scanned microsections of young developing Arabidopsis stems, which were small enough to include different tissue types in one map and less lignified to widen the view on carbohydrates. By multivariate data analysis the most pure (true component analysis) and most similar (cluster analysis) spectra were retrieved, and spectral assignments and verifications done with a plant component Raman database. Retrieving the most relevant underlying reference spectra was the basis for a final linear combination at every pixel to visualize selectively a variety of different aromatic components, carbohydrates, lipids and proteins.

2. Material and methods

2.1. Plant growth

The plants were grown from *Arabidopsis thaliana* seeds, which before were stratified 72 h at 4 °C in the dark. Their culture was done in mixed soil (NEUHAUS) in a growth chamber under 12 h of light (light intensity of 100 PAR) at 22 °C and 12 h of darkness at 20 °C for 6 weeks. After 6 weeks, the photoperiod was changed to 16 h of light, 8 h of darkness. Flower stems were harvested, when they had reached a height of 30 cm.

2.2. Sample preparation

A 5 mm long stem section was taken between 6.5 cm and 7 cm from the top of the plant and was placed in an embedding solution (50% PEG 1500/50% water) for 2 days at 50 °C. The samples were then placed in melted PEG 1500 (50 °C), polymerized at room temperature and the

PEG blocks were cut with a microtome (Leica Rm2065). The microsections (10 µm thick) were placed on a glass slide and rinsed with water to remove the PEG. Afterwards a coverlip was placed on top and sealed onto the glass slide with nail polish to avoid water evaporation during the Raman mapping. A detailed protocol for plant embedding and sample preparation for Raman imaging was published in Gierlinger et al 2012 [28].

2.3. Raman imaging

2.3.1. Raman spectra acquisition

Raman images were acquired using a confocal Raman microscope (alpha300RA, WITec GmbH, Germany) equipped with a 100 × oil immersion objective (NA 1.4 with 0.17 mm coverslip correction) (Carl Zeiss, Germany). On a microscopic stitching image of the *A.thaliana* stem microsection an area of interest was selected to include the following different tissues: interfascicular fibers, vessels, parenchyma and epidermis with cuticle. During mapping every pixel (0.3 × 0.3 µm) was excited 0.04 s with a 532 nm linearly polarized laser set at 40 mW. The backscattered Raman signal was collected through an optical multifiber (50 µm diameter) associated with a UHTS300 spectrometer (WITec, Germany) (600gmm – Iarray) and a CCD camera (Andor DU401 BV, Belfast, Northern Ireland). The acquisition software Control FIVE (WITec, Germany) was used for the experimental setup. Spectrum pre-processing and data analysis was done using the FIVE Plus project software (WITec, Germany). The spectra were cut at 100 cm⁻¹, the cosmic rays were removed and the baseline corrected (polynomial method with sections cut between 730 and 1794 cm⁻¹ and between 2686 cm⁻¹ and 3609 cm⁻¹). The cut-offs for the baseline correction correspond to the part of the spectrum with pronounced peaks depending on the wall layer. By removing this part, we have removed the inconsistency of correction by promoting the linear part of the spectrum. The multivariate data analysis was done with and without baseline correction, with the whole wavenumber range and restricting the spectra to the lower more specific wavenumber region from 300 cm⁻¹ and 1800 cm⁻¹.

2.3.2. Multivariate spectra analysis:

The hyperspectral datasets were fitted as linear combinations of the basis or component spectra using the following equation:

$$D = \left(\left[\text{Recorded Spectrum} \right] - a \times \vec{BS}_A - b \times \vec{BS}_B - c \times \vec{BS}_C \right)^2$$

by varying the weighting factors a, b, c, \dots of the basis spectra BS (“true component analysis” and “basis analysis” in Project FIVE Plus WITec) [29]. Following the fit of each recorded spectrum of the hyperspectral dataset, the algorithm constructed one image for each component spectrum showing the factors a, b, c, \dots and one image for the fitting error D . The number of components were tested from 3 to 10 on more than three samples and datasets and the result with the most distinguished (and interpretable) components is exemplarily shown. Carbohydrate, lipid and aromatic components were distinguished and their distribution visualized within the scanned area. For comparison, Cluster analysis was used to segment the hyperspectral dataset into clusters according spectral similarity based on Euclidean distance. The algorithm was also run with 3 to 10 clusters, but for comparison only the result based on 7 clusters was shown (6 clusters attributed to different plant components and 1 water/background cluster not shown).

To get detailed insights into the compositions of the different cell walls and lumen components and to verify their “purity”, we also modelled the true component spectra as a linear combination of measured reference plant component spectra (Supplementary Table S1) using the

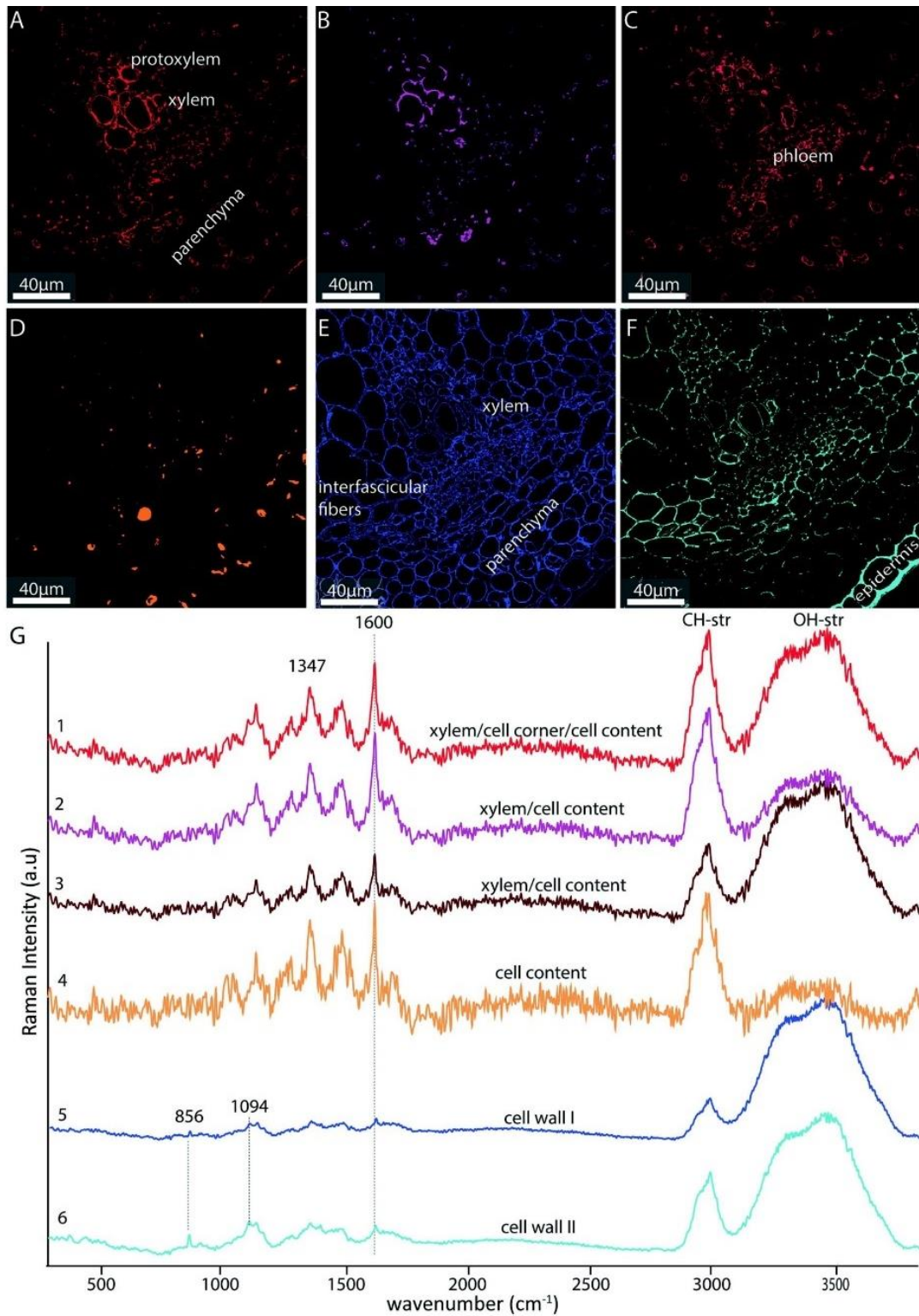


Fig. 2. Raman imaging based on “cluster analysis” of the developing Arabidopsis stem. A-C: three different clusters were derived from xylem and cell contents in the lumen, D: one was restricted to the cell contents and E-F: two clusters separated different cell walls. G: the extracted average cluster spectra confirmed the aromatic nature of the lignified xylem and aromatic nature of cell contents (spectrum 1–4.); carbohydrate bands and a weak lignin band represented the cell wall cluster spectra (spectrum 5–6).

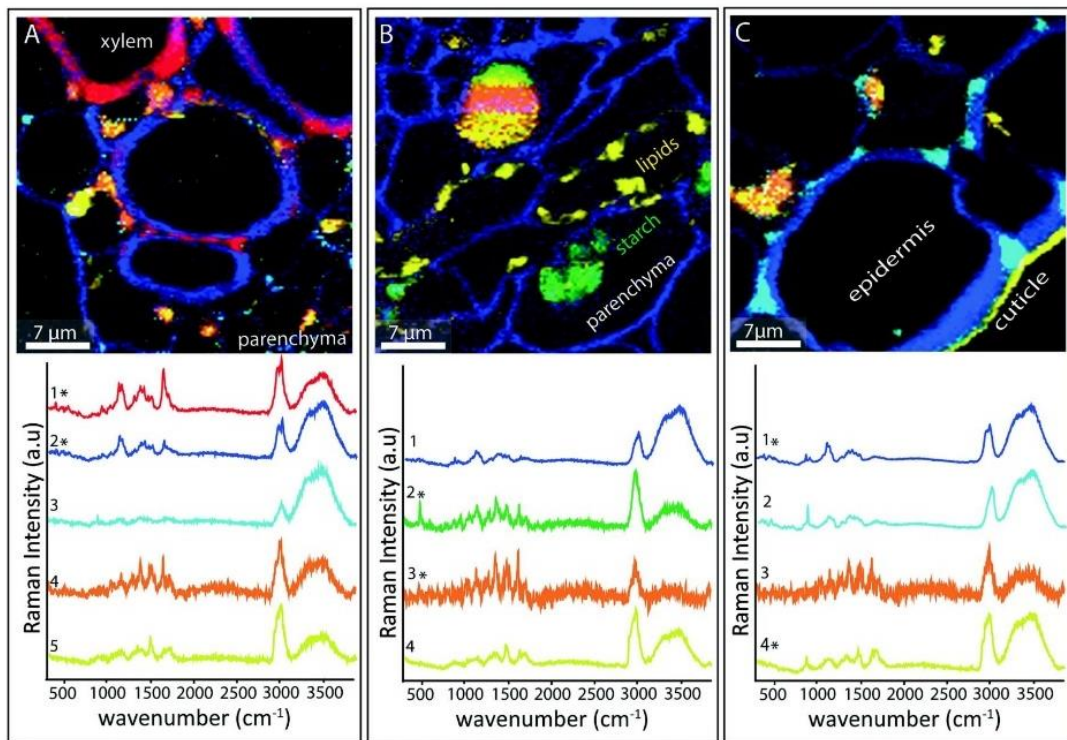


Fig. 3. True component analysis of three different tissue types of a young developing *Arabidopsis* stem revealed the distribution of the cell wall and cell contents and their Raman signatures: A) secondary cell walls of the xylem with increased lignification in cell corners (red) accompanied by primary cell wall of parenchyma cells with proteins and lipids B) parenchyma cells lined with lipids (yellow) and/or filled with starch (green) and aromatic proteins (orange) C) epidermal layer with lipidic cuticle and underlying parenchyma with lipids and proteins. Spectra with asterisk were analysed in detail in Fig. 4. (For interpretation of the references to colour in this Fig. legend, the reader is referred to the web version of this article.). (For interpretation of the references to colour in this figure legend, the reader is referred to the web version of this article.)

Orthogonal Matching Pursuit (OMP) algorithm [30]. A sparse approximation found the “best matching” projections of the plant spectra onto the span of a library of reference spectra. At each iteration, the best correlated reference spectrum was sought for, added to the predictor set as long as the desired threshold for the residual error was reached. The threshold was set as low as results were reasonable and interpretable (0.11–0.16). The predictor set of the final model held the selected constituents of the mixture, and the coefficients indicated the abundance of the respective compounds. Depending on the uniqueness of the mix, different combinations of reference spectra led to a similar error, wherefore the selection of reference spectra, parameters, final models and interpretation of the results needed an experienced operator as well as testing on several Raman mappings. Finally, when knowing the most relevant reference components representing our *Arabidopsis* spectra, we used these to fit the whole hyperspectral dataset as a combination of the selected reference spectra. With this final basis analysis [29] (see formula above) we got the most comprehensive view on the *Arabidopsis* stem with insights into the distribution of different carbohydrates, aromatic and lipidic components as well as the orientation of cellulose microfibrils.

3. Results and discussion

3.1. Comparison of unmixing and segmentation algorithm: True component vs cluster analysis

The scanned region of interest included interfascicular fibers, vessels, parenchyma, and epidermis with cuticle to probe the tissue heterogeneity in *Arabidopsis* stems. In a first approach, we analysed the whole wavenumber spectra without baseline correction of the hyperspectral map acquired from the *A.thaliana* microsections. We compared on the

same sample set two algorithms 1) an unmixing algorithm finding the most different (pure component) spectra in the dataset, fitting every pixel spectrum with the component spectra and visualising their distribution based on the weighting factors (Fig. 1A-G) and 2) a hierarchical cluster segmentation algorithm to sort and visualise the most similar spectral regions as clusters and extract average cluster spectra and (Fig. 2A-G). For both methods, we had to decide on how many components/clusters the calculation was based on. We screened from 3 up to 10 components and finally decided to show the result based on 7 components/clusters, as the 7 true component spectra reflected the most different Raman signatures (Fig. 1G, 1st to 6th spectrum, 7th component was water and was not shown).

The first distinguished component was visualized mainly in the smaller vessels of the protoxylem, the cell corners of the xylem and partly also as cell content in the lumen of the parenchyma cells (Fig. 1A). The corresponding component spectrum showed a strong band at 1600 cm^{-1} (Fig. 1G, 1st red spectrum), which is attributed to the aromatic stretching vibration of lignin units, mainly coniferyl alcohol and coniferyl aldehyde [16]. So, the protoxylem was at this stage the most lignified tissue followed by the cell corners of the xylem and interfascicular fibers. This is in agreement with earlier studies based on UV microscopy [31], in which these positions have also been reported as the first lignified ones. The partly included lumen contents in the parenchyma cells were due to the similarity to the next component (Fig. 1B, 2nd orange spectrum), which was mainly located in the lumen of parenchyma and phloem cells. Also this component spectrum showed a band around 1600 cm^{-1} (Fig. 1G, orange spectrum), pointing to an aromatic nature. Compared to the lignin spectrum a stronger 1247 cm^{-1} band was observed, a higher fluorescence background and thus noisier spectra (Fig. 1G, orange spectrum). The high variability and high fluorescence background in the lumen contents was also reflected in a

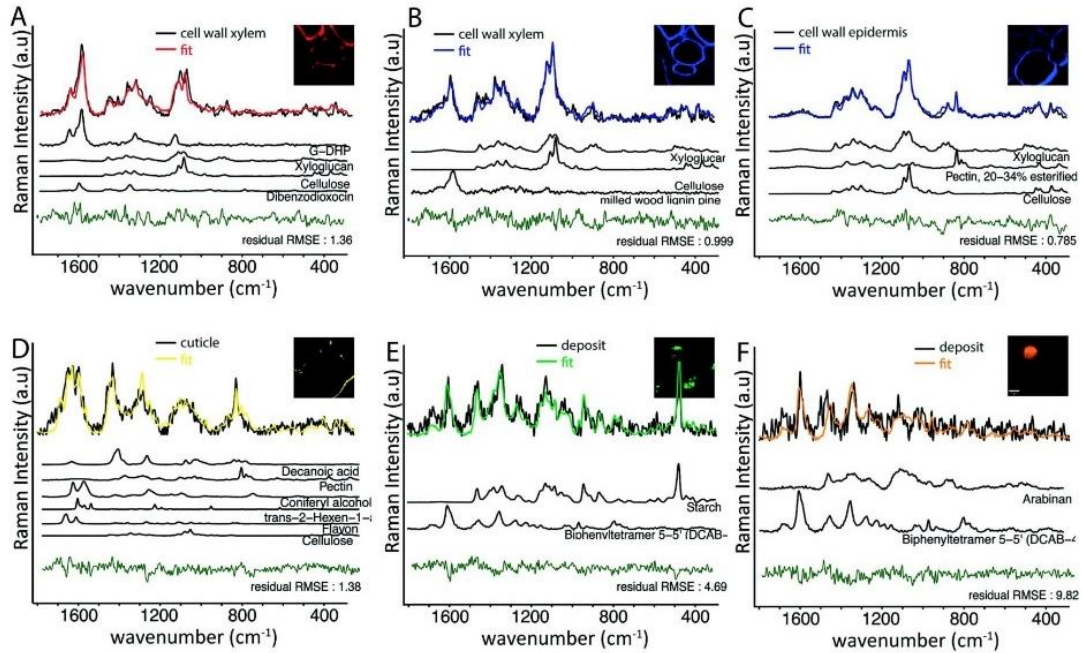


Fig. 4. True component Raman spectra of different *Arabidopsis* cell walls, cuticle and cell contents were modelled as a linear combination of reference spectra using the Orthogonal Matching Pursuit method. The original spectra are plotted together with the fit, below the chosen reference spectra are listed according to the coefficients and on the bottom the residual error of each model: A) The lignified secondary cell wall spectrum towards the protoxylem is represented mainly by lignin structures, beside Xyloglucan and Cellulose B) In the less lignified secondary cell wall towards the cambium Xyloglucan and Cellulose dominate and milled wood lignin accounts for minor amounts. C) Epidermal cell wall was fitted by three different carbohydrates. D) Cuticle was modelled by lipids, aromatics and carbohydrates E-F) cell contents were best explained by a mixture of carbohydrates and aromatic biphenyls.

higher residual error of the fit than in the rest of the tissues (Fig. S1A). Also, the third (Fig. 1C, yellow) and fourth component (Fig. 1D, green) were located mainly in the lumen of the parenchyma cells. The broad band at 1660 cm^{-1} might represent the amide I band of proteins [19] and the 1446 cm^{-1} band pointed towards lipids [17] (Fig. 1G, 3rd yellow spectrum). The latter lipidic component was also attributed to the outer cuticle layer (Fig. 1C), which is known to be composed of fatty acid esters and waxes [21]. The other cell contents (Fig. 1D) were assigned to starch with a marker band at 478 cm^{-1} [16] (Fig. 1G, 4th green spectrum). Our sample preparation with PEG embedding preserved many of the storage components (proteins, lipids, starch) and Raman imaging differentiated them within the cells. The shown approach has thus potential to study their distribution and re-localization and/or transformation during seasonal development.

The 5th component was found in the cell wall of all tissue types (Fig. 1E: xylem, interfascicular fibers, parenchyma, and epidermis) and the 6th component emphasized the epidermal layer and the cell corners between all cells (Fig. 1F). The component spectra revealed cellulose with a strong band at 1094 cm^{-1} (Fig. 1G, 5th spectrum) [12] and pectin with the 856 cm^{-1} marker band (Fig. 1G, 6th spectrum) [15]. With this early young stage and the true component analysis it was thus possible to visualize carbohydrate signals in all cell walls (Fig. 1E).

In contrast to the unmixing method, the cluster analysis resulted in three components reflecting lignified xylem and cell lumen contents (Fig. 2A-C) and one component restricted only to the lumen content (Fig. 2D). The region below 1800 cm^{-1} was quite similar in all these average cluster spectra, while especially the OH-stretching changed (Fig. 2G, 1st, 2nd, 3rd and 4th spectrum). The remaining two components described the cell wall (Fig. 2E-F) as both spectra had signals from cellulose (1095 cm^{-1}), lignin (1600 cm^{-1}) and the latter one additionally the pectin band at 856 cm^{-1} (Fig. 2F, 5th and 6th spectrum).

The fact that one cluster is represented as an area of the same composition, the cluster images (Fig. 2) give less information than true component images (Fig. 1), which represent the distribution of the weight-

ing factors and by this deliver a semi-quantitative information on the component distribution. Furthermore, component spectra can be derived as the most pure component spectra and by this be more component specific and ease spectra interpretation compared to average cluster spectra. Our comparison of the two algorithms emphasized the potential of the true component analysis, if a visualization based on different components is aimed for (Fig. 1, Fig. S1B). In case of the cluster analysis, OH-stretching as well as CH-stretching strongly influenced the segmentation and made it therefore less component specific; e.g. no lipids and starch were segmented (Fig. 2). Instead, it was more density specific: clusters towards the lumen (Fig. 2C, Fig. 2E) with higher OH-stretching (e.g. Fig. 2G, 3rd) and more dense parts with high CH-stretching (e.g. Fig. 2G, 6th spectrum vs 5th spectrum) were separated. To get more components specific information based on cluster analysis, the next step would be to restrict the wavenumber regions to the lower wavenumber region (e.g. 1800 cm^{-1} to 300 cm^{-1}) and apply a baseline correction.

3.2. Zoom in and specify: Restricting the region of interest and verifying composition

To zoom in and get more detailed insights into the composition of the different tissue types, the xylem region (Fig. 3A), the parenchyma with cell contents (Fig. 3B) and the epidermal layer including the outer cuticle (Fig. 3C) was cut out and analysed separately by true component analysis.

In the xylem five different component spectra were retrieved: secondary cell wall with high (Fig. 3A, red, 1st spectrum) and moderate lignification (blue, 2nd spectrum) and pectin rich cell wall and cell corner of parenchyma cells (turquoise, 3rd spectrum). The onset of lignification is seen in more detail with higher lignin content towards the protoxylem (pith) and ongoing lignification of cell corners and cell walls towards the cambium. The parenchyma cells around the vessels reveal also in this zoom aromatics and proteins (Fig. 3A, orange, 4th spec-

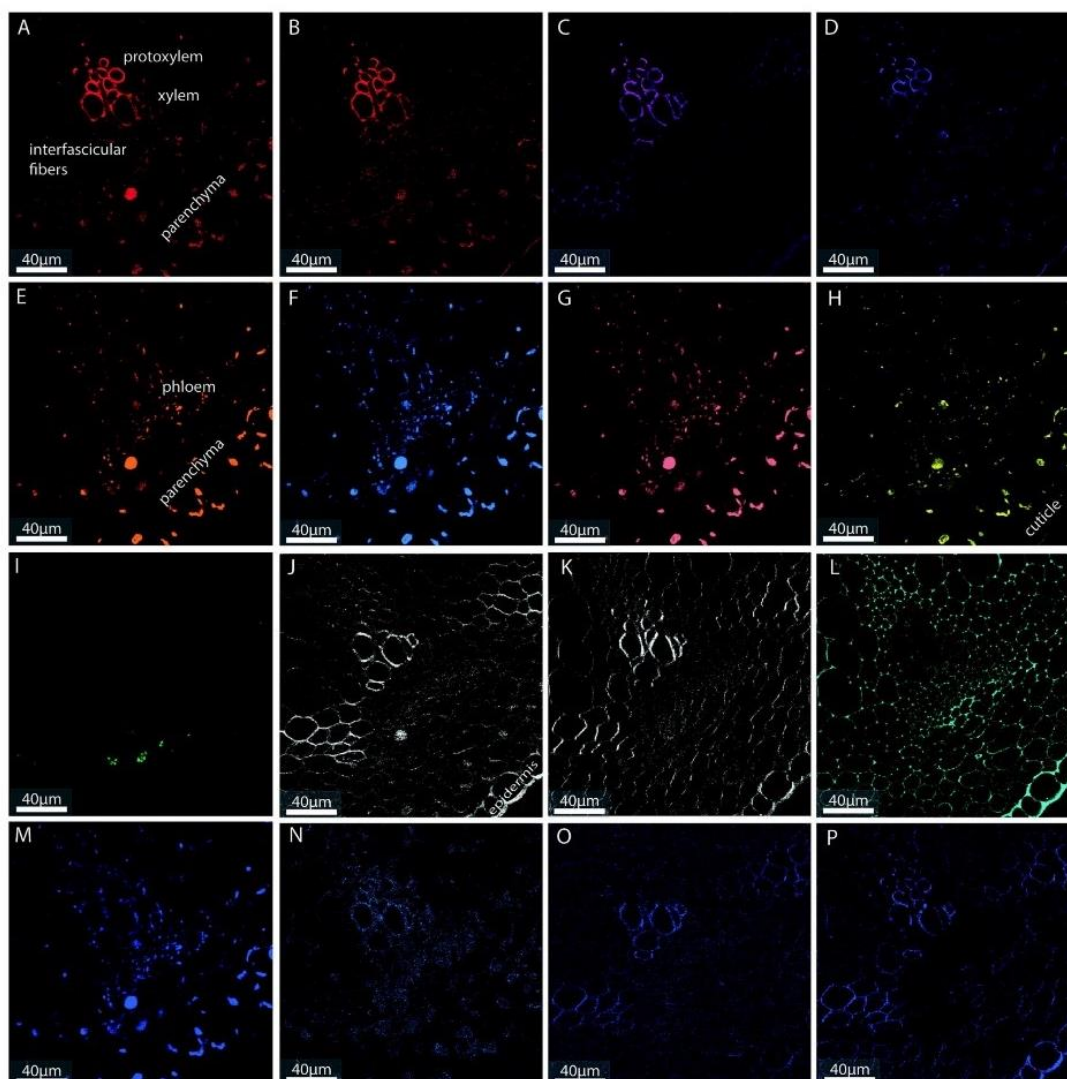


Fig. 5. Basis analysis unravels details on aromatics, lipids, proteins and carbohydrates, and cutin in the young *Arabidopsis* cross section. The hyperspectral dataset is visualized as a linear combination of the following reference spectra: A) G-DHP, B) milled wood lignin from pine, C) Dibenzenodioxin, D) coniferyl alcohol, E) Biphenyl with two coniferyl alcohols, F) arabinan, G) phenylalanine, H) decanoic acid, I) starch (potato), J) cellulose (Ramie fiber parallel to laser polarisation), K) cellulose (Ramie fiber perpendicular to laser polarisation), L) pectin, M) Xyloglucan (tamarind), N) 4-O-Methyl-D-glucurono-D-xylan, O) Arabinoxylan, P) Glucomannan. Residual image of the fit is shown in Supplementary Fig. S2.

trum) and lipids (yellow, 5th spectrum). The good neighbour hypothesis proposes that lignin precursors are synthesized in nonlignified cells and exported to the walls of adjacent lignifying cells [32,33,34] and was recently verified for xylem cells in *Arabidopsis*[35]. The cell contents of the parenchyma cells surrounding the xylem (Fig. 3A, orange) and the spectral similarity to lignin pointed to aromatic precursors and proteins/enzymes supporting lignification.

In the parenchyma cells (Fig. 3B) additionally to the aromatics/proteins (orange) and lipids (yellow), starch (green) was found as storage compound. The lipids lined the cell wall and might partly represent the plasma membrane, whereas the aromatic/proteins and starch filled more the lumen of the cells. On the outer surface the lipidic cuticle was highlighted (Fig. 3C, yellow) and pectin (turquoise) accumulated especially in the cell corners of the epidermis (Fig. 3C, cyan).

To verify our interpretation of the Raman signatures and unravel any multicomponent nature of the retrieved “pure” component spectra, we applied a mixture analysis (orthogonal matching pursuit) using a spectral data base of plant components ($n = 372$ plant component spectra) on selected spectra (marked with an asterisk in Fig. 3). The lig-

nified secondary cell wall of the xylem (Fig. 3A red spectrum) was fit by a combination of guaiacyl-dehydrogenation polymer (G-DHP), xyloglucan, cellulose and dibenzodioxin (Fig. 4A). G-DHP is a lignin model polymer replicating the lignin structure by stepwise combinatorial radical coupling of monolignols and dibenzodioxin represents the 5–5 linking motifs in lignin [36]. Dibenzodioxin substructure were found in differentiating Norway spruce and silver birch cell walls [37]. The less lignified cell wall (Fig. 3A, 2nd spectrum) was fitted by xyloglucan, cellulose and a spectrum acquired from milled wood lignin of pine (Fig. 4B). Different lignin model component spectra were chosen by the algorithm, but all were based on guaiacyl (G-) units. The region of interest included mainly vessels and it was shown in *Arabidopsis* stems that the lignin of the vascular with the vessel cells primarily contains G units [38]. For the epidermis cell wall, we identified a mixture of 3 carbohydrates, xyloglucan, pectin, but no lignin (Fig. 4C). So the epidermal cell wall revealed to be rich in pectin, while in the secondary cell walls (4A-B) lignin based on G-units was verified at this early developmental stage.

For the cuticle part, decanoic acid was chosen as lipidic component, from carbohydrates pectin and cellulose and some aromatic components (coniferyl alcohol, flavon). Although at this developmental stage the cuticle was smaller than 0.5 μm (Fig. 1C, Fig. 3C), the multicomponent nature was detected. That Raman imaging and multivariate data analysis is a promising and powerful tool in cuticle research was shown in several studies, recently [20,21,39,40].

For the cell contents, the mixture analyses confirmed the aromatic nature by choosing a biphenyltetramer together with carbohydrates (Fig. 4 E-F). While in the first cell content spectrum (Fig. 4E) starch was included with the strong band at 478 cm^{-1} , the arabinan was taken in the second cell content spectrum (Fig. 4F). The arabinan spectrum was less specific and seemed to be taken to account for the noisy background and might therefore also be replaced by other components. Compared to the cell wall fits the residual errors were higher (Fig. 4), as the spectra were noisier and the database might lack the right components. Our database had no enzymes and only three types of proteins included, but the suggested biphenyl- carbohydrate mixture might point to the right direction. Extensins, for example, might represent such structures as they are highly repetitive plant O-glycoproteins forming a tridimensional network through inter and intra-Tyr linkages [41]. Besides, enzymes might contribute to these spectral signatures as e.g. peroxidases and laccases were found during stem development in both, lignified and unlignified cell wall regions [31]. For a detailed study on the cell contents the Raman spectra reference library needs to be expanded with phospholipids (plasma-membrane), enzymes (e.g. laccases, peroxidases,...) and cell wall proteins (e.g. extensins,...). Furthermore, including different developmental stages and other imaging methods (e.g. immunolabeling), will bring data interpretation a big step forward.

3.3. Fitting every spectrum of the hyperspectral data set as a combination of selected plant reference spectra

The ultimate aim was to retrieve detailed component information at every pixel of the hyperspectral dataset and get information on tissue heterogeneity behind component classes. Based on the results from the mixture analysis of the extracted component spectra (Fig. 4), we choose the relevant reference spectra to fit the whole hyperspectral dataset. At every pixel a linear combination of all the reference spectra was calculated to display the distribution of the chosen references (Fig. 5). The aromatic components found in the mixture analysis (Fig. 4), G-DHP, milled wood lignin pine and Dibenzodioxin were fit into the secondary cell walls of the xylem and cell corner and middle lamella of interfascicular fibers (Fig. 5A-C) and in the protoxylem also coniferyl alcohol added to the spectral signature (Fig. 5D). The references pointed to a lignin rich in G- units in this early developmental stage. Similar like with the other algorithms (true component analysis, Fig. 1, cluster analysis Fig. 2) the spectral similarity and aromatic nature of the cell contents was evident as the model lignins were also taken into account to fit the cell contents (Fig. 5A-B). Nevertheless, the major contribution in the cell contents was again a biphenyl based on two coniferyl units (Fig. 5E) together with arabinan (Fig. 5F). We added phenylalanine to account eventually for proteins and, indeed, it was fit into the cell content spectra (Fig. 5G). Hexadeconic acid was taken as a substitute for lipids and was lining the cell wall (plasma membrane), highlighting the cuticle and as storage components within the lumen of the cells (Fig. 5H). The co-location of glycosylated aromatics, proteins and lipids became clear in the lumen of many cells (Fig. 5 E-H), while starch granules as storage components were restricted to a few cells (Fig. 5I). To draw conclusions on a preferred orientation of the cellulose microfibrils in the cell wall [12], we added two cellulose spectra: one acquired with the laser polarisation parallel to the Ramie fiber and the other perpendicular. By this regions with high microfibril angle were highlighted in x and y direction, respectively (Fig. 5 J-L). From the difference between the two pictures we conclude on microfibrils with high microfibril

angle in the xylem vessels, whereas in the epidermal layer similar intensities of both spectra were observed and thus no preferred cellulose orientation. In the epidermal layer and in the cell corners of the parenchyma cells again the high content of pectin was confirmed (Fig. 5M). In the mixture analysis before Xyloglucan was fit into the cell wall spectrum (Fig. 4A-C), but from experience we know that xyloglucan has spectral similarities with cellulose if orientated perpendicular to the surface (Supplementary Fig. S3). Depending on the cellulose orientation of the spectra selected in the model fit, xyloglucan might be over or underestimated. By adding two cellulose with different orientation, the xyloglucan was considered as less important and visualized only in the xylem vessels (Fig. 5M) and similar like arabinan in the lumen contents (Fig. 5F). We added other hemicelluloses to the fit and finally revealed different distribution of 4-O-Methyl-D-glucurono-D-xylan (Fig. 5N), Arabinoxylan (Fig. 5O) and Glucomannan (Fig. 5P). While the 4-O-Methyl-D-glucurono-D-xylan was restricted to the xylem vessels, the Arabinoxylan highlighted also the interfascicular fibers and the glucomannan also the epidermal layer (Fig. 5N-P). It was interesting to note that the different lignins and hemicellulose showed similar pattern: e.g. G-DHP (Fig. 5A) and Xyloglucan (Fig. 5M) or dibenzodioxin (Fig. 5C) and arabinoxylan (Fig. 5O).

4. Conclusions

All different algorithms enabled to visualize chemical heterogeneity in young Arabidopsis stem tissues and confirmed in a complementary way the distribution of aromatic components and carbohydrates. The true component analysis visualized six different component classes, whereas cluster analysis segmented mixed classes based on density differences (OH- and CH-stretching) and aromatic content (fluorescence background). Due to the multicomponent nature of plant tissues even unmixing methods were not able to retrieve "pure" components, wherefore a subsequent mixture analysis of extracted component and cluster average spectra is suggested. This leads to more detailed information on the molecular composition of the spectra and can serve as essential input for fitting a hyperspectral dataset based on defined plant reference spectra at every pixel. By this, we unravelled the distributions patterns of different aromatic components and distinguished different hemicelluloses. Tissue heterogeneity was revealed in terms of plant cell walls, but also cell contents with proteins, enzymes and storage components can be probed. With this comprehensive view on plant tissues, a better understanding of developmental processes, genetic mutations, biotic and abiotic stresses as well as plant treatments can be gained. The potential for future studies is evident, but stands and falls with careful sample preparation, data acquisition of hyperspectral data sets as well as being able to include all relevant reference spectra in the analysis.

Grant support.

Y 728/FWF/Austrian Science Fund FWF/Austria.

Declaration of Competing Interest

The authors declare that they have no known competing financial interests or personal relationships that could have appeared to influence the work reported in this paper.

Data availability

Data will be made available on request.

Appendix A. Supplementary data

Supplementary data to this article can be found online at <https://doi.org/10.1016/j.microc.2023.108900>.

References

- [1] U. Kadam, C.A. Moeller, J. Irudayaraj, B. Schulz, Effect of T-DNA insertions on mRNA transcript copy numbers upstream and downstream of the insertion site in *Arabidopsis thaliana* explored by surface enhanced Raman spectroscopy, *Plant Biotechnol. J.* 12 (5) (Jun. 2014) 568–577, <https://doi.org/10.1111/PBI.12161>.
- [2] S. Kushwah, A. Banasiak, N. Nishikubo, M. Derba-Maceluch, M. Majda, S. Endo, V. Kumar, L. Gomez, A. Gorzdas, S. McQueen-Mason, J. Braam, B. Sundberg, E.J. Mellerowicz, *Arabidopsis XTH4 and XTH9 Contribute to Wood Cell Expansion and Secondary Wall Formation*, *Plant Physiol.* 182 (4) (2020) 1946–1965.
- [3] C. Vallet, B. Chabbert † §, Y. Czaniński, and B. Monties, “Histochemistry of Lignin Deposition during Sclerenchyma Differentiation in Alfalfa Stems,” *Ann. Bot.*, vol. 78, pp. 625–632, 1996, Accessed: Sep. 06, 2022. [Online]. Available: <https://academic.oup.com/aob/article/78/5/625/2587536>.
- [4] D.E. Hanke, D.H. Northcote, Molecular visualization of pectin and DNA by ruthenium red, *Biopolymers* 14 (1) (Jan. 1975) 1–17, <https://doi.org/10.1002/BIP.1975.360140102>.
- [5] L. Donaldson, “Autofluorescence in Plants,” *Mol. 2020, Vol. 25, Page 2393*, vol. 25, no. 10, p. 2393, May 2020, doi: 10.3390/MOLECULES25102393.
- [6] F. Baldacci-Cresp, C. Spriet, L. Twyffels, A.-S. Blervacq, G. Neutelings, M. Baucher, S. Hawkins, A rapid and quantitative safranin-based fluorescent microscopy method to evaluate cell wall lignification, *Plant J.* 102 (5) (2020) 1074–1089.
- [7] L. McCartney, S.E. Marcus, J.P. Knox, Monoclonal antibodies to plant cell wall xylans and arabinoxylans, *J. Histochem. Cytochem.* 53 (4) (Apr. 2005) 543–546, <https://doi.org/10.1369/jhc.4B6578.2005>.
- [8] S. Pattathil, U. Avci, D. Baldwin, A.G. Swennes, J.A. McGill, Z. Popper, T. Bootten, A. Albert, R.H. Davis, C. Chennareddy, R. Dong, B. O’Shea, R. Rossi, C. Leoff, G. Freshour, R. Narra, M. O’Neil, W.S. York, M.G. Hahn, A Comprehensive Toolkit of Plant Cell Wall Glycan-Directed Monoclonal Antibodies, *Plant Physiol.* 153 (2) (2010) 514–525.
- [9] C. Hervé, S.E. Marcus, J.P. Knox, Monoclonal antibodies, carbohydrate-binding modules, and the detection of polysaccharides in plant cell walls, *Methods Mol. Biol.* 715 (2011) 103–113, https://doi.org/10.1007/978-1-61779-008-9_7/COVER.
- [10] N. Gierlinger, New insights into plant cell walls by vibrational microspectroscopy, *Applied Spectroscopy Reviews* 53 (7) (2018) 517–551.
- [11] J. De Gelder, K. De Gussem, P. Vandenebeele, L. Moens, Reference database of Raman spectra of biological molecules, *J. Raman Spectrosc.* 38 (9) (Sep. 2007) 1133–1147, <https://doi.org/10.1002/JRS.1734>.
- [12] J.H. Wiley, R.H. Atalla, Band assignments in the raman spectra of celluloses, *Carbohydrate Research* 160 (1987) 113–129.
- [13] N. Gierlinger, S. Luss, C. König, J. Konnerth, M. Eder, P. Fratzl, Cellulose microfibril orientation of *Picea abies* and its variability at the micron-level determined by Raman imaging, *J. Exp. Bot.* 61 (2) (Jan. 2010) 587–595, <https://doi.org/10.1093/JXB/ERP325>.
- [14] A. Synytsya, J. Čopíková, P. Matějka, V. Machovič, Fourier transform Raman and infrared spectroscopy of pectins, *Carbohydr. Polym.* 54 (1) (Oct. 2003) 97–106, [https://doi.org/10.1016/S0144-8617\(03\)00158-9](https://doi.org/10.1016/S0144-8617(03)00158-9).
- [15] P. Bock, N. Gierlinger, Infrared and Raman spectra of lignin substructures: Coniferyl alcohol, abietin, and coniferyl aldehyde, *J. Raman Spectrosc.* 50 (6) (Jun. 2019) 778–792, <https://doi.org/10.1002/JRS.5588>.
- [16] E. Wiercigroch, E. Szafraniec, K. Czamara, M.Z. Pacia, K. Majzner, K. Kochan, A. Kaczor, M. Baranska, K. Malek, “Raman and infrared spectroscopy of carbohydrates: A review”, *Spectrochim. Acta Part A Mol. Biomol. Spectrosc.* 185 (2017) 317–335.
- [17] K. Czamara, K. Majzner, M.Z. Pacia, K. Kochan, A. Kaczor, M. Baranska, Raman spectroscopy of lipids: a review, *J. Raman Spectrosc.* 46 (1) (Jan. 2015) 4–20, <https://doi.org/10.1002/JRS.4607>.
- [18] M. Krysa, M. Szymańska-Chargot, A. Zdunek, FT-IR and FT-Raman fingerprints of flavonoids – A review, *Food Chem.* 393 (Nov. 2022) 133430, <https://doi.org/10.1016/J.FOODCHEM.2022.133430>.
- [19] A. Rygula, K. Majzner, K.M. Marzec, A. Kaczor, M. Pilarczyk, M. Baranska, Raman spectroscopy of proteins: a review, *J. Raman Spectrosc.* 44 (8) (Aug. 2013) 1061–1076, <https://doi.org/10.1002/JRS.4335>.
- [20] A. G. Moreno *et al.*, “3D (x-y-t) Raman imaging of tomato fruit cuticle: Microchemistry during development,” *Plant Physiol.*, vol. 191, no. 1, pp. 219–232, Jan. 2023, doi: 10.1093/PLPHYS/KIAC369.
- [21] P. Bock, M. Felhofer, K. Mayer, N. Gierlinger, A Guide to Elucidate the Hidden Multicomponent Layered Structure of Plant Cuticles by Raman Imaging, *Front. Plant Sci.* 12 (Dec. 2021) 2886, <https://doi.org/10.3389/FPLS.2021.793330/BIBTEX>.
- [22] S. Dinant, N. Wolff, F. De Marco, F. Vilaine, L. Gissot, E. Aubry, C. Sandt, C. Bellini, R. Le Hir, Synchrotron FTIR and Raman spectroscopy provide unique spectral fingerprints for *Arabidopsis* floral stem vascular tissues, *J. Exp. Bot.* 70 (3) (2019) 871–884.
- [23] B. De Meester, L. de Vries, M. Özparpucu, N. Gierlinger, S. Corneille, A. Pallidis, G. Goeminne, K. Morreel, M. De Bruyne, R. De Rycke, R. Vanholme, W. Boerjan, Vessel-Specific Reintroduction of CINNAMOYL-COA REDUCTASE1 (CCR1) in Dwarfed *crr1* Mutants Restores Vessel and Xylary Fiber Integrity and Increases Biomass, *Plant Physiol.* 176 (1) (2018) 611–633.
- [24] L. Blaschek, || Nuoendagula, || Zoltán, Z. Bacsik, S. Kajita, and E. Pesquet, “Determining the Genetic Regulation and Coordination of Lignification in Stem Tissues of *Arabidopsis* Using Semiquantitative Raman Microspectroscopy,” *ACS Sustain. Chem. Eng.*, vol. 8, no. 12, pp. 4900–4909, Mar. 2020, doi: 10.1021/ACSSUSCHEMENG.0C00194.
- [25] M. Schmidt, A.M. Schwartzberg, A. Carroll, A. Chaibang, P.D. Adams, P.J. Schuck, Raman imaging of cell wall polymers in *Arabidopsis thaliana*, *Biochem. Biophys. Res. Commun.* 395 (4) (May 2010) 521–523, <https://doi.org/10.1016/J.BBRC.2010.04.055>.
- [26] B.P. Mateu, M.T. Hauser, A. Heredia, N. Gierlinger, Waterproofing in *Arabidopsis*: following phenolics and lipids in situ by Confocal Raman microscopy, *Front Chem* 4 (2020) 10.
- [27] T. Iino, K. Hashimoto, T. Asai, K. Kuchitsu, Y. Ozeki, Multicolour chemical imaging of plant tissues with hyperspectral stimulated Raman scattering microscopy, *Analyst* 146 (4) (Feb. 2021) 1234–1238, <https://doi.org/10.1039/D0AN02181D>.
- [28] N. Gierlinger, T. Keplinger, M. Harrington, Imaging of plant cell walls by confocal Raman microscopy, *Nat Protoc* 7 (9) (2012) 1694–1708.
- [29] T. Dieing, W. Ibach, “Software requirements and data analysis in confocal Raman microscopy”. In: Dieing T, Hollricher O, Toporski J (eds) *Confocal Raman microscopy*. Springer Berlin Heidelberg, Berlin, Heidelberg, pp 61–89. 2011 doi: https://doi.org/10.1007/978-3-642-12522-5_4.
- [30] Y.C. Pati, R. Rezaifar, P.S. Krishnaprasad, Orthogonal matching pursuit: recursive function approximation with applications to wavelet decomposition, *Conf Rec Asilomar Conf Signals Syst Comput* 1 (1993) 40–44, <https://doi.org/10.1109/ACSSC.1993.342465>.
- [31] N. Hoffmann, A. Benske, H. Betz, M. Schuetz, A.L. Samuels, Laccases and peroxidases co-localize in lignified secondary cell walls throughout stem development, *Plant Physiol.* 184 (2) (2020) 806–822.
- [32] M. Hosokawa, S. Suzuki, T. Umezawa, Y. Sato, Progress of Lignification Mediated by Intercellular Transportation of Monolignols During Tracheary Element Differentiation of Isolated *Zinnia Mesophyll* Cells, *Plant Cell Physiol.* 42 (9) (Sep. 2001) 959–968, <https://doi.org/10.1093/PCP/PCE124>.
- [33] N. Tokunaga, N. Sakakibara, T. Umezawa, Y. Ito, H. Fukuda, Y. Sato, Involvement of Extracellular Dilignols in Lignification During Tracheary Element Differentiation of Isolated *Zinnia Mesophyll* Cells, *Plant Cell Physiol.* 46 (1) (Jan. 2005) 224–232, <https://doi.org/10.1093/PCP/PCI017>.
- [34] E. Pesquet, B.o. Zhang, A. Gorzdas, T. Puhakainen, H. Serk, S. Escamez, O. Barbier, L. Gerber, C. Courtois-Moreau, E. Alatalo, L. Paulin, J. Kangasjärvi, B. Sundberg, D. Goffner, H. Tuominen, Non-Cell-Autonomous Postmortem Lignification of Tracheary Elements in *Zinnia elegans*, *Plant Cell* 25 (4) (2013) 1314–1328.
- [35] R.A. Smith, M. Schuetz, M. Roach, S.D. Mansfield, B. Ellis, L. Samuels, Neighboring Parenchyma Cells Contribute to *Arabidopsis* Xylem Lignification, while Lignification of Interfascicular Fibers Is Cell Autonomous, *Plant Cell* 25 (10) (Nov. 2013) 3988–3999, <https://doi.org/10.1105/TPC.113.117176>.
- [36] C.W. Lahive, P.C.J. Kamer, C.S. Lancefield, P.J. Deuss, An Introduction to Model Compounds of Lignin Linking Motifs; Synthesis and Selection Considerations for Reactivity Studies, *ChemSusChem* 13 (17) (Sep. 2020) 4238–4265, <https://doi.org/10.1002/CSSC.202000989>.
- [37] E. M. Kukkola *et al.*, “The dibenzodioxocin lignin substructure is abundant in the inner part of the secondary wall in Norway spruce and silver birch xylem,” *Planta*, vol. 218, no. 3, pp. 497–500, Jan. 2004, doi: 10.1007/S00425-003-1107-3.
- [38] C. Chapple, T. Vogt, B.E. Ellis, C. Somerville, *Arabidopsis* mutant defective in phenylpropanoid pathway, *Plant Cell* 4 (1994) 1413–1424, <https://doi.org/10.1105/tpc.4.11.1413>.
- [39] N. Sasani, P. Bock, M. Felhofer, N. Gierlinger, Raman imaging reveals in-situ microchemistry of cuticle and epidermis of spruce needles, *Plant Methods* 17 (1) (Dec. 2021) 1–15, <https://doi.org/10.1186/S13007-021-00717-6/FIG.S/5>.
- [40] N. Reynoud *et al.*, “The cutin polymer matrix undergoes a fine architectural tuning from early tomato fruit development to ripening,” *Plant Physiol.*, vol. 190, no. 3, pp. 1821–1840, Oct. 2022, doi: 10.1093/PLPHYS/KIAC392.
- [41] E. Marzol, C. Borassi, M. Bringas, A. Sede, D.R. Rodríguez García, L. Capece, J.M. Estevez, Filling the Gaps to Solve the Extensin Puzzle, *Mol. Plant* 11 (5) (2018) 645–658.

SUPPLEMENTARY INFORMATION

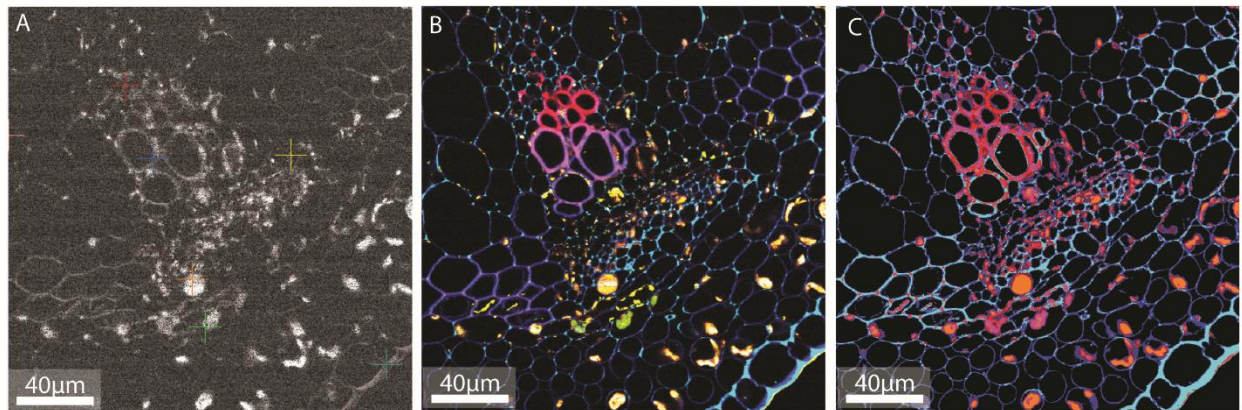


Figure. S1: A Residuals of “true component analysis” shown in Figure 1 and B) Combined Raman image of true component analysis in comparison to C) the combined Raman image based on cluster analysis

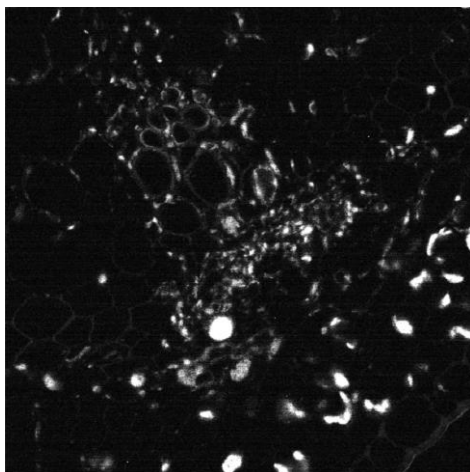


Figure. S2: A Residuals of basis analysis shown in Figure 5

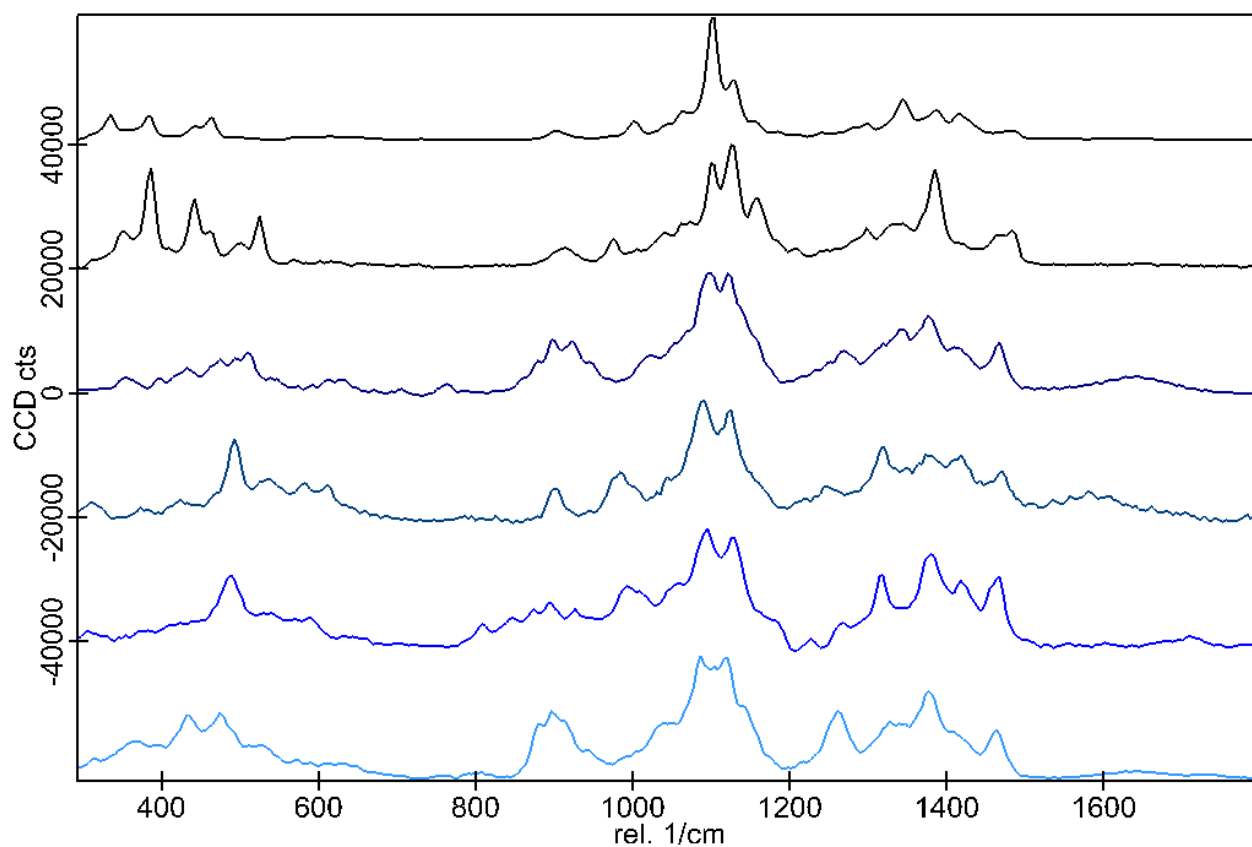


Figure. S3: Carbohydrate reference spectra used in mixture analysis: 1) cellulose parallel to laser polarisation, 2) cellulose perpendicular to laser polarisation, 3) Xyloglucan (tamarind), 4) 4-O-Methyl-D-glucurono-D-xylan, 5) Arabinoxylan, 6) Glucomannan

Multimodal analysis of the impact of hemicellulose matrix modification on lignins polymers in the *Arabidopsis thaliana* *irx9-2* mutant.

With the three previous articles, we have adapted and/or developed powerful imaging methods enabling us to visualize the dynamics of lignification in plants. In this section we use these techniques to see whether lignification is affected by a modification of the polysaccharide matrix. For this, we have used the *Arabidopsis thaliana irx9-2* mutant, involved in hemicellulose xylan synthesis. The results presented will be submitted to a journal once the final version of the paper is written.

Introduction

With an estimated 450 Gt of carbon, plants represent 82% of the planet's biomass. Most of this biomass consists of plant cell wall polymers: cellulose, lignins, hemicelluloses, pectins and proteins. The lignins polymer is essential to plant life and plays a central role in many different physiological processes, including growth, reproduction, and defence. The amount and composition of lignins affects the "quality" of many plant resources, including wood, paper, and textiles. This polymer impacts the recalcitrance of lignocellulosic biomass during biofuel production, and, in biorefineries, it is the feedstock to produce many different chemical synthons (Wenger et al., 2020). Because plant cell walls are an important sink for atmospheric carbon, the lignins polymer also contributes to climate change, particularly in long-lived forest tree species. Given the importance of lignins, it is not surprising that the biosynthesis and deposition of this polymer in the plant cell wall has been the focus of intense research efforts by scientists and industry. We currently have a relatively clear idea of its chemical/physical structure and the genes/enzymes involved in the biosynthesis and polymerization of lignins monomers (monolignols). Nevertheless, other factors also affect lignification, for example, we know that lignification is developmentally coordinated with the formation of other cell wall polymers and that it cannot occur without the prior deposition of polysaccharides. However, there is no systematic understanding of how the amount, composition, and organization of cell wall polysaccharides (CWPs) affect lignification. This lack of understanding can be attributed to two main reasons: 1. Analyses of cell wall composition in CWP mutants are very often

limited to the effect on CWPs, lignins is not analyzed since the goal is to confirm the role of the targeted gene. 2. Analyses are very often limited to "destructive" chemical and/or physical techniques leading to the loss of detailed spatial information and to a simplified view of the effect of the mutation on the biology of the cell wall.

The cell wall structure (polymer composition and organization) can be characterized by a wide variety of chemical and physical techniques that can be grouped into two main types: "destructive" and "non-destructive". In destructive techniques, plant material is crushed and a cell wall residue is extracted for analysis. Although this approach provides quantitative data, it often masks more subtle, cell-specific differences and results in an incomplete understanding of the biological process. In contrast, non-destructive techniques preserve the structural integrity of cells/tissues, providing spatial information about the structure and organization of the wall at the cellular level. The biological value of using such a non-destructive technique was recently demonstrated in the *Arabidopsis lac4/lac17* double laccase mutant (Baldacci-Cresp et al. 2020). Previous destructive characterization of the mutant indicated a 30-40% reduction in lignins content in stem compared to WT plants with Klason method. However, analyses using a non-destructive imaging approach revealed that while the cell walls of the interfascicular fibers of the mutants were less lignified, the cell walls of the xylem vessels had higher levels of lignins, demonstrating the existence of cell-specific phenotypes.

Several studies show that CWP amounts/structures affect lignification, for example, lignins deposition is not observed without prior polysaccharide deposition (Taylor et al., 1992) , and ectopic lignification has been observed in *Arabidopsis* cellulose synthase mutants containing reduced cellulose levels in the cell walls (Caño-Delgado et al., 2003)

We therefore decided to explore the *irx9-2* mutant to identify possible impacts on lignification of the polysaccharide matrix modification. This *Arabidopsis irx9-2* hemicellulose mutant targets the gene encoding a GT43 β -1,4 xylosyltransferase. This mutant is characterized by a dwarf phenotype, an irregular xylem (IRX) phenotype, reduced cell wall thickness and a 70% decrease in glucuronoxylan content (Peña et al., 2007) However, no information on the lignins content is available. We used several methods to investigate this mutant. For all the methods, the analysis was performed on three sections of the plant stem. The three sections allow to have different stages of development, a young part, a medium part and an old part and thus to have information on the dynamics of the wall development during the plant maturation. First a

transcriptional analysis was performed to confirm the mutation and to look for transcriptional changes of some genes known to be involved in lignification. The wall components were analyzed using Raman vibrational spectroscopy. To get more information on the amount of lignins the safranin-O staining was used. The incorporation of monolignols in the wall was studied using the triple labelling technique.

Material and methods

plant material

The plants studied were derived from *Arabidopsis thaliana* seeds (wt and *irx9-2* mutant, SALK_057033C, AT2G37090, N656523). Before their culture, they were stratified 72 h at 4 °C in the dark. Their culture was done in a growth chamber under 12 h of light (light intensity of 100 Photosynthetic Active Radiation) at 22 °C and 12 h of darkness at 20 °C for 6 weeks. After 6 weeks, the photoperiod was changed to 16 h of light, 8 h of darkness. Plants were collected at 30 cm for WT and 15 cm for *irx9* mutant (1 weeks)

Different samples were taken from the stems at a pre-mature stage: in the upper part, which corresponds to a young developmental stage of the plant, in the middle of the stem, which corresponds to an intermediate stage, and in the lower part, which corresponds to an old stage. Since the *irx9-2* mutant has a dwarf phenotype (stem of about 18 cm), the distance between the samples from the apex was adapted for the WT (stem of about 30 cm). Thus, in the mutant, the three samples were taken at 12.5, 7.5 and 1 cm from bottom respectively and for the WT at 23, 15 and 1 cm from bottom. These sections were chosen so as to be comparable.

The same strategy for sample collection was applied for Raman microscopy, click chemistry and RT-qPCR for easier comparison.

Raman acquisition:

To perform the Raman acquisition, we followed the previously described protocol (Morel & Gierlinger, 2023) and it was applied to the different sections. Each sample was cut with cryocutting to obtain 3 sections of 10 μm thickness.

Raman images were acquired using a confocal Raman (alpha300RA, WITec GmbH, Germany) with a $100\times$ oil immersion objective (NA 1.4 with 0.17 mm coverslip correction) (Carl Zeiss, Germany). The selected areas contained interfascicular fibers. The Raman signal was obtained after excitation at 532 nm by a linearly polarized laser set at 40 mW. The detection of the signal was done with an optical multifiber (50 μm diameter) associated with a UHTS300 spectrometer (WITec) (600 gmm -1 array) and a CCD camera (Andor DU401 BV, Belfast, Northern Ireland). The acquisition software Control FIVE (WITec) was used for the experimental setup. Spectral data were obtained by scanning the slice in 0.3 μm steps with an integration time of 0.05 s. Spectrum processing and data analysis was done using the FIVE Plus project software (WITec). The spectra were cut at 100 cm^{-1} , then the cosmic rays were removed, and the baseline corrected (polynomial method with sections cut between 730 and 1794 cm^{-1} and between 2686 cm^{-1} and 3609 cm^{-1}). The cut-offs for the baseline correction corresponded to the part of the spectrum with pronounced peaks depending on the wall layer. By removing this part, we removed the inconsistency of correction by promoting the linear part of the spectrum. The analysis of the spectrum is done between 300 cm^{-1} and 1800 cm^{-1} . The part of the spectrum after 1800 cm^{-1} was removed from the analysis to limit the impact of focus difference. Then, spectra have been extracted from reference spectra to allow a localization of the compounds searched as described in (Morel et al., 2023)

Bioorthogonal lignins labelling:

To perform the triple bioorthogonal labelling of monolignols, we followed the previously described protocol (Simon et al, 2018). The protocol was applied to the different sections. Each sample was cut with a vibratome to obtain 10 sections of 80 μm thickness that were incubated in 300 μL of $\frac{1}{2}$ MS containing 5 mM of H*, S* and G or natural (i.e. not modified by the addition of a tag) monolignols for control. The whole was placed 20 h at 21°C. After incubation, 4 successive rinses were performed with $\frac{1}{2}$ MS before labelling with fluorophores via three successive bioorthogonal reactions, IEDDA for S*, SPAAC for H* and CuAAC for

G*. Each reaction allows the association of a different fluorophore, Tetrazine Cy5 (Jena Bioscience, Jena, Germany), Azide Fluor 545 (Sigma- Aldrich, Saint Louis, Missouri, USA) and alexa fluor 488 (Jena Bioscience, Jena, Germany). Each reaction was run in 300 μ L of $\frac{1}{2}$ MS for 1 h in the dark. Samples were rinsed 4 times with $\frac{1}{2}$ MS for 10 min between each reaction. After the final reaction, the samples were rinsed, first 2 times with $\frac{1}{2}$ MS 10 minutes and then 1 h with 70% MeOH to completely remove any remaining free fluorophore. A new wash was performed with distilled water 2 times 10 minutes to remove MeOH.

safranin-O coloration:

For safranin-O coloration, we used samples of the same stem and same cutting process as for bio-orthogonal labelling. After cutting, sections are placed in ethanol 50% and at 4°C until use. To perform the staining, the sections were placed in 0.2% safranin-O diluted in a 50% ethanol solution and incubated for 10 minutes in the dark under agitation. The safranin-O solution was washed for 10 minutes with 50% ethanol in the dark and then 15 minutes with ultrapure water. The sections were mounted between slide and coverslip in water.

Confocal microscopy

For bio-orthogonal sample, image acquisitions were performed as previously described (Morel et al, 2021). Images from three independent biological replicates for each genotype and tissue were acquired. A Nikon A1R confocal equipped with a 60_/1.4 aperture oil immersion objective (Plan APO VC) and the NIS Element AR version 3.0 software was used (Nikon, Tokyo, Japan). Acquisitions were performed on 3 channels corresponding to 1) H* units (λ_{ex} : 488, λ_{em} : 525/550); 2) G* units (λ_{ex} : 561, λ_{em} : 595/650); and 3) S* units (λ_{ex} : 561, λ_{em} : 700/775). Laser intensity and detectors gains are adjusted to ensure optimal signal-to-noise-ratio while avoiding photobleaching.

For safranin sample : Image acquisitions were performed as previously described (Morel et al., 2023). Microscope was the same than for bio-orthogonal sample. Acquisitions were performed on 3 channels, lignins autofluorescence (λ_{ex} : 405, λ_{em} : 450/500), green channel (λ_{ex} : 488, λ_{em} : 530/560) and red channel (λ_{ex} : 561, λ_{em} : 570/600).

Segmentation:

Segmentation was performed as previously described (Morel et al, 2021) with the REPRISAL method for biorthogonal labelling and with method described in (Morel et al., 2023) for safranin-O.

RT-qPCR:

Three biological repetitions were collected for each genotype. Each biological repetition included three plants. Plant material was stored at -80 °C.

RNA extraction and purification

We used the TRI REAGENT for the RNA extraction (Molecular research Center, INC, Ohio, USA). We purified RNA samples on spin columns (RNasy Plant min kit, Qiagen, Valencia, CA). Concentration and quality of RNA were evaluated by the spectrophotometric method.

Samples were treated by DNaseI (DNA-free Kit, Ambion), and used as template in the reverse transcription reaction (iScript Reverse Transcription Supermix for RT-qPCR, Bio-Rad, Inc., Hercules, CA, USA). Each reaction of the cDNA synthesis was accompanied by no reverse transcriptase control (NRT).

qPCR

We evaluated the expression level of genes that are involved in cell wall metabolism (Table 1).

Table 1 – Arabidopsis gene list for the expression study. Genome obtained from *A.thaliana* TAIR 10

No	Gene ID	GENE DESCRIPTION	Gene name
1	AT2G38080	ARABIDOPSIS LACCASE-LIKE MULTICOPPER OXIDASE 4	LAC4
2	AT5G60020	LACCASE 17	LAC17
3	AT5G42180	PEROXIDASE 64	PRX64
4	AT5G64120	PEROXIDASE 71	PRX71
5	AT5G66390	PEROXIDASE 72	PRX72
6	AT1G64060	RESPIRATORY BURST OXIDASE PROTEIN F	RBOHF
7	AT1G15950	CINNAMOYL COA REDUCTASE 1	CCR1
8	AT1G80820	CINNAMOYL COA REDUCTASE ISOFORM	CCR2
9	AT3G19450	CINNAMYL ALCOHOL DEHYDROGENASE 1	CAD1
10	AT4G34230	CINNAMYL ALCOHOL DEHYDROGENASE 5	CAD5
11	AT2G37090	IRREGULAR XYLEM 9, A PUTATIVE FAMILY 43 GLYCOSYL TRANSFERASE;	IRX9-2
12	AT3G23820	UDP-D-GLUCURONATE 4-EPIMERASE INVOLVED IN PECTIN BIOSYNTHESIS	GAE6-2
13	AT5G05170	CELLULOSE SYNTHASE A3	CESA3
14	AT5G44030	CELLULOSE SYNTHASE A4	CESA4
15	AT1G13320	THE 65 KDA REGULATORY SUBUNIT OF PROTEIN PHOSPHATASE 2A	PP2AA3
16	AT5G25760	UBIQUITIN-CONJUGATING ENZYME 21	PEROXIN4

We used the iQ SYBR Green Supermix (Bio-Rad) for qPCR. The final volume of PCR mix was 20 μ L, concentration of forward and reverse primers was 0.4 μ M.

Results

RT-qPCR

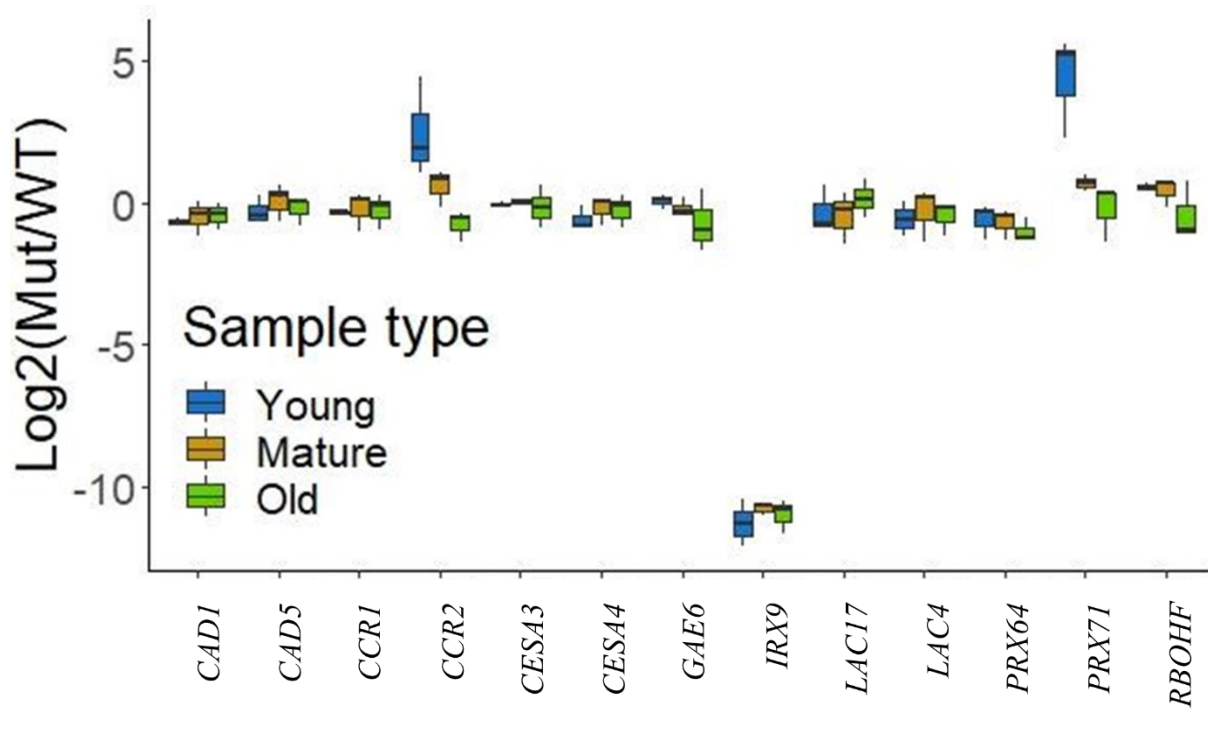


Figure 28 : Relative (to the reference genes and to the wild type plant samples) expression level of the studied genes. Colors indicate the three different parts of the stem analyzed. See Table 1 for gene description.

First, we verified that the *irx9-2* mutant studied under-expressed the corresponding gene (*IRX9*). For the expression of the *IRX9* gene, it is under expressed in the three different parts of the stem. Among the test genes, we notice that the expression of *PRX71* is different from that of WT in the *irx9-2* mutant, which has an altered cell wall, we note that the expression of the gene is strongest in the upper parts of the plant and progressively decreases to WT-levels

in the lower part of the stem. Another gene whose expression is modified is *CCR2*. We notice that it has the same expression profile as *PRX71*. In the upper part of the plant, the expression level is higher in the mutant than in the WT. The expression then decreases progressively to reach an expression like that of the WT. The expression of *CCR1* in the mutant is not different from that in the WT. Expression of the other genes are similar in WT and mutant. (Figure 28).

Modification of the polysaccharide matrix

For the analysis we have chosen to use BIOMANI's own spectrum database. When looking at the spectral images after processing, for the upper part (Figure 29Y), all molecules are detectable (cellulose, glucomannan, arabinoxylan and xyloglucan).

For the middle part, this time arabinoxylan is detectable (Figure 29 M), in smaller amounts than WT, but xyloglucan (Figure 29) is not detectable.

For the basal part of the plant, we notice an absence of detection of arabinoxylan and xyloglucan (Figure 29 O).

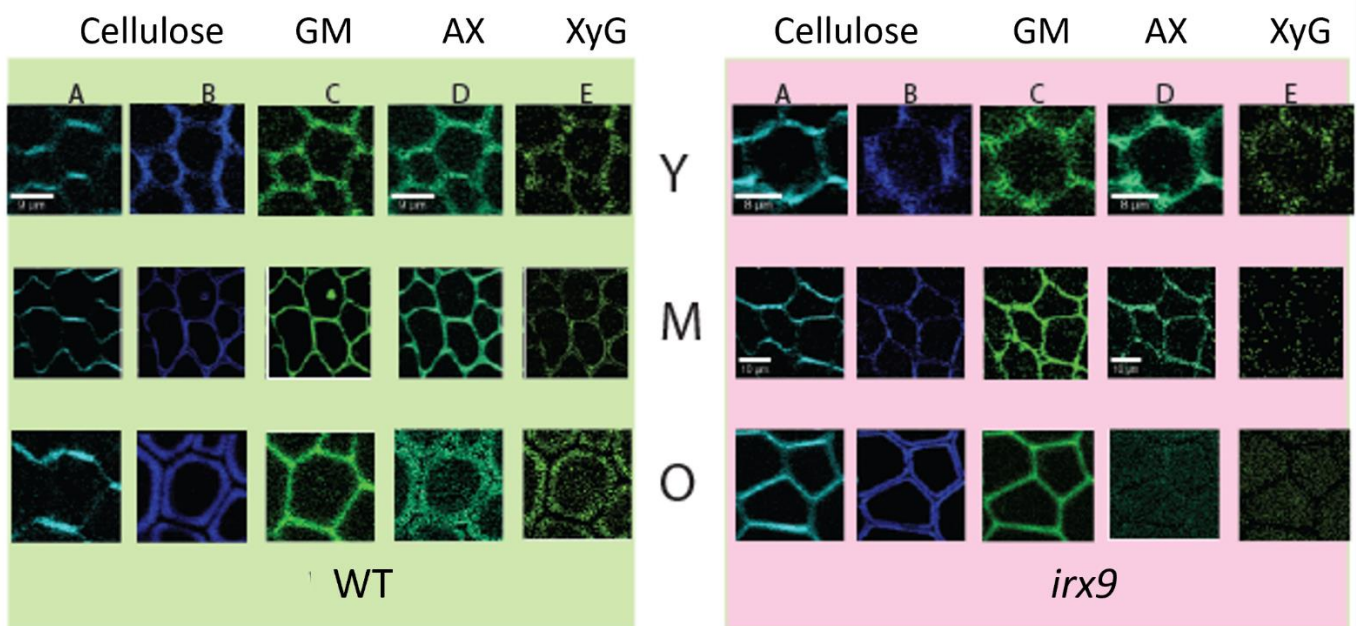


Figure 29 : Spectral image of the upper (Y), middle (M), and lower (O) part of *Arabidopsis.thaliana* interfascicular fibers cells cellulose: 2 different microfibril orientations, GM : glucomannan ; AX : arabinoxylan ; XyG : xyloglucan. WT (left) and mutant (right).

Impact on lignification

We could see in the previous part that the mutation causes a change in the hemicellulose composition and could have an impact on the lignification, that is why the quantity of lignins was studied with the safranin-O technique and the quality of lignins by Raman spectroscopy.

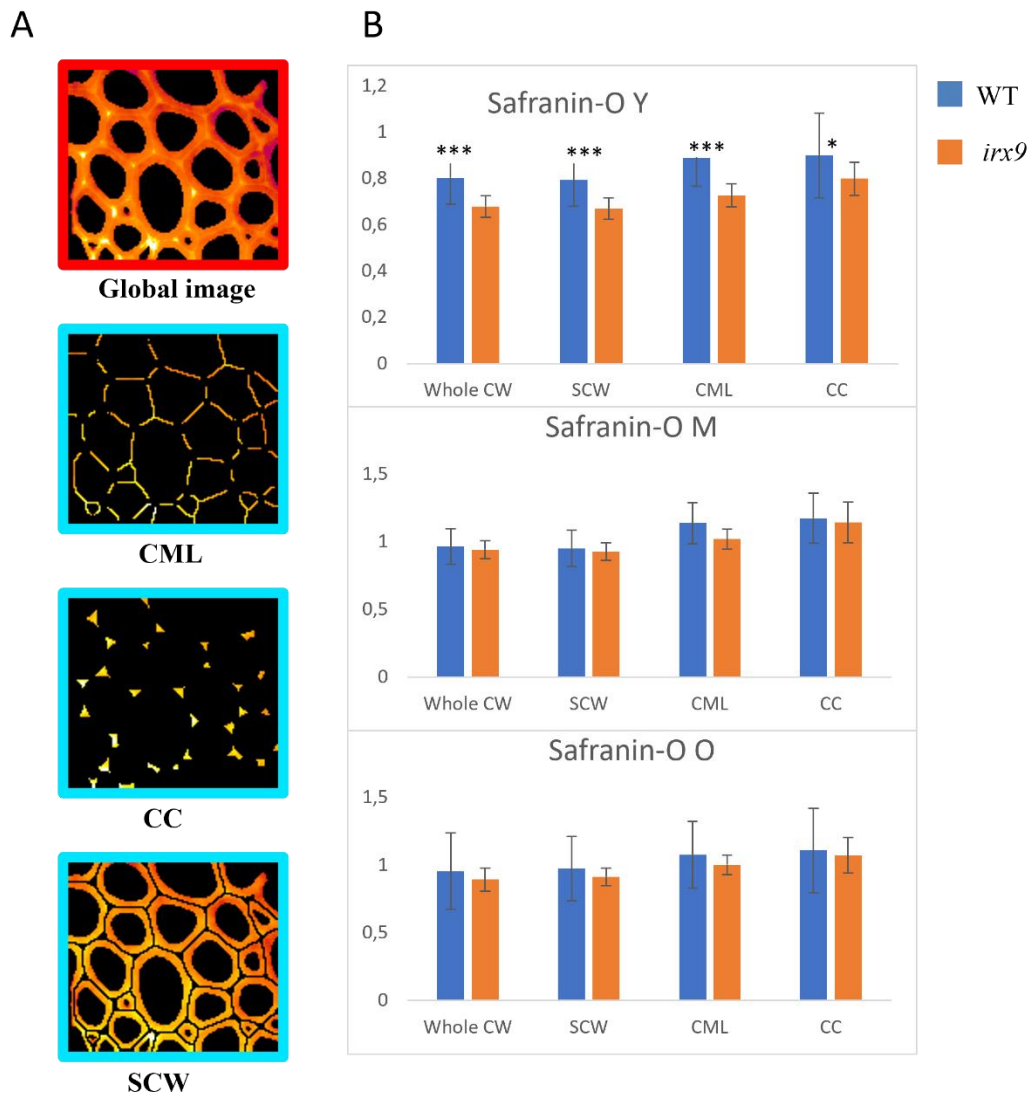


Figure 30 : Study of lignins with safranin coloration on *irx9-2* mutant and WT. A) segmentation example of medium stem region, B) safranin ratio in all of cell wall, secondary cell wall (SCW), compound middle lamella (CML) and cell corner (CC) for young (Y), medium (M) and old (O) parts. Statistics: t-test $* < 0.5$; $** < 0.1$; $*** < 0.001$

First, we analysed cell wall with safranin coloration. This staining allows us to have a global view of the quantity of lignins present in the cell wall. Application of the safranin-O method to

the interfascicular fibers of the *irx9-2* mutant showed that, for the upper part of the plant, there is less lignins in the mutant compared to the WT regardless of the sublayer considered (Figure 30 B-Y). When the cells are older, in the middle of the stem (Figure 30 B-M), the decrease is restricted to the middle lamella and for the oldest lower part (Figure 30 B-O)., there is no significant difference anymore. The impact of the mutation is thus more pronounced in the younger parts of the plant and attenuated in the older parts.

In a second time, we used Raman spectroscopy to have more information about distribution of G and S lignins. For Raman analysis, when we look at the distribution pattern of predominantly G lignins (**Erreur ! Source du renvoi introuvable.**-2) and predominantly S lignins (**Erreur ! Source du renvoi introuvable.**-3), we notice that for the top part, the mutant shows predominantly S lignins mainly in the cell corners whereas for the WT, the detection is also done in the rest of the wall.

For the medium part (**Erreur ! Source du renvoi introuvable.** Medium), the spectral images do not differ between the WT and the mutant. For the aged part (**Erreur ! Source du renvoi introuvable.** old), if we look at the composite image for bottom part, (**Erreur ! Source du renvoi introuvable.** bottom 1), we notice that the CML and CC part has a more pronounced G lignins in the WT than in the mutant. from the SCW.

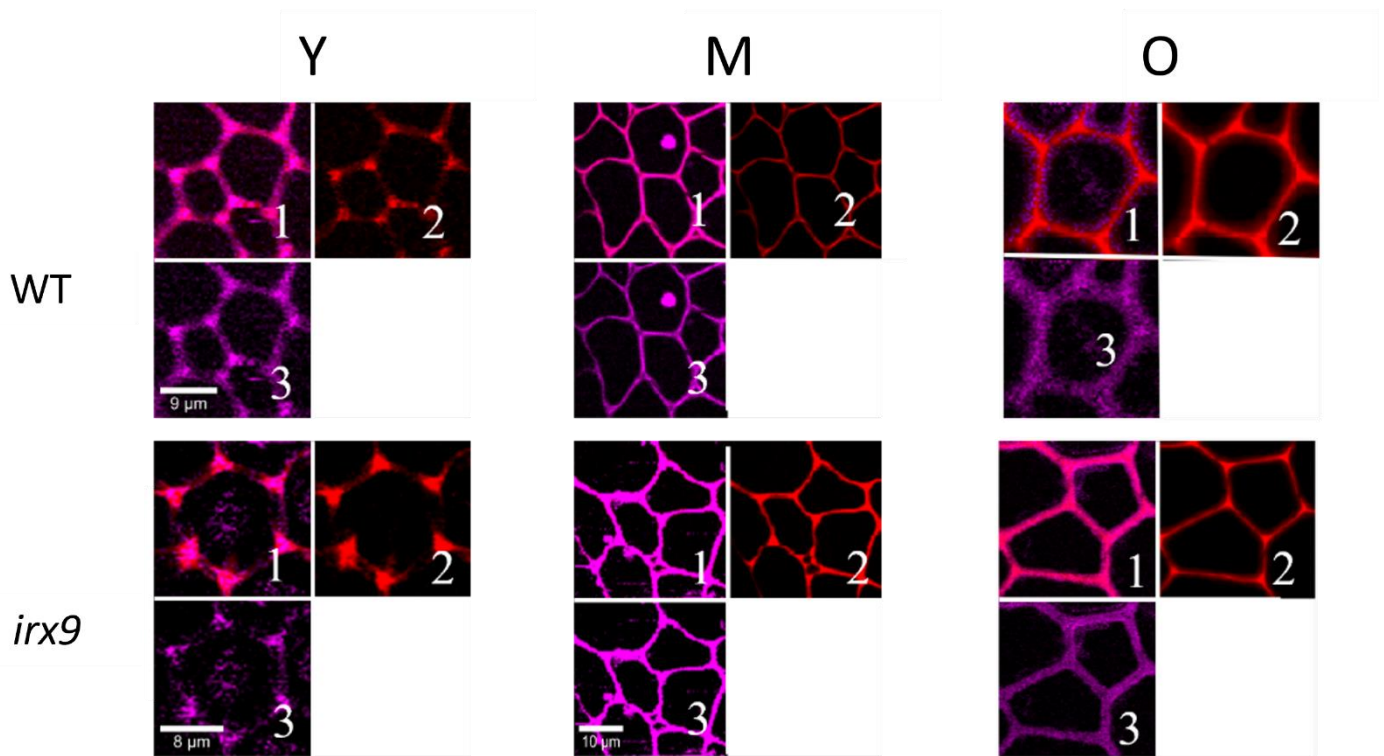


Figure 31 : Spectral images of sections of young (Y), medium (M) and old (O) parts on WT and *irx9-2* for lignins. (1) the composite image, (2) lignins rich in G units and (3) in S units

Monolignol incorporation

For the analysis of the incorporation capacity of the H*, G* and S* reporters corresponding to the 3 monolignols, the REPRISAL (REPorter Ratiometrics Integrating Segmentation for Analyzing Lignification) method was used (Morel et al., 2022) on the three developmental stages (young, medium and old) on the mutant and the WT (Figure 32). When looking at the fluorescence intensities in the young parts of the stem, the mutant has a higher incorporation capacity than the WT for H* and G* regardless of the sublayer analysed (Figure 32 Y), less incorporation for H*, more incorporation of G* in CC in medium part (Figure 32 M) and less incorporation of H* and G* in SGW but more incorporation of S* in SCW and CLM ((Figure 32 O).

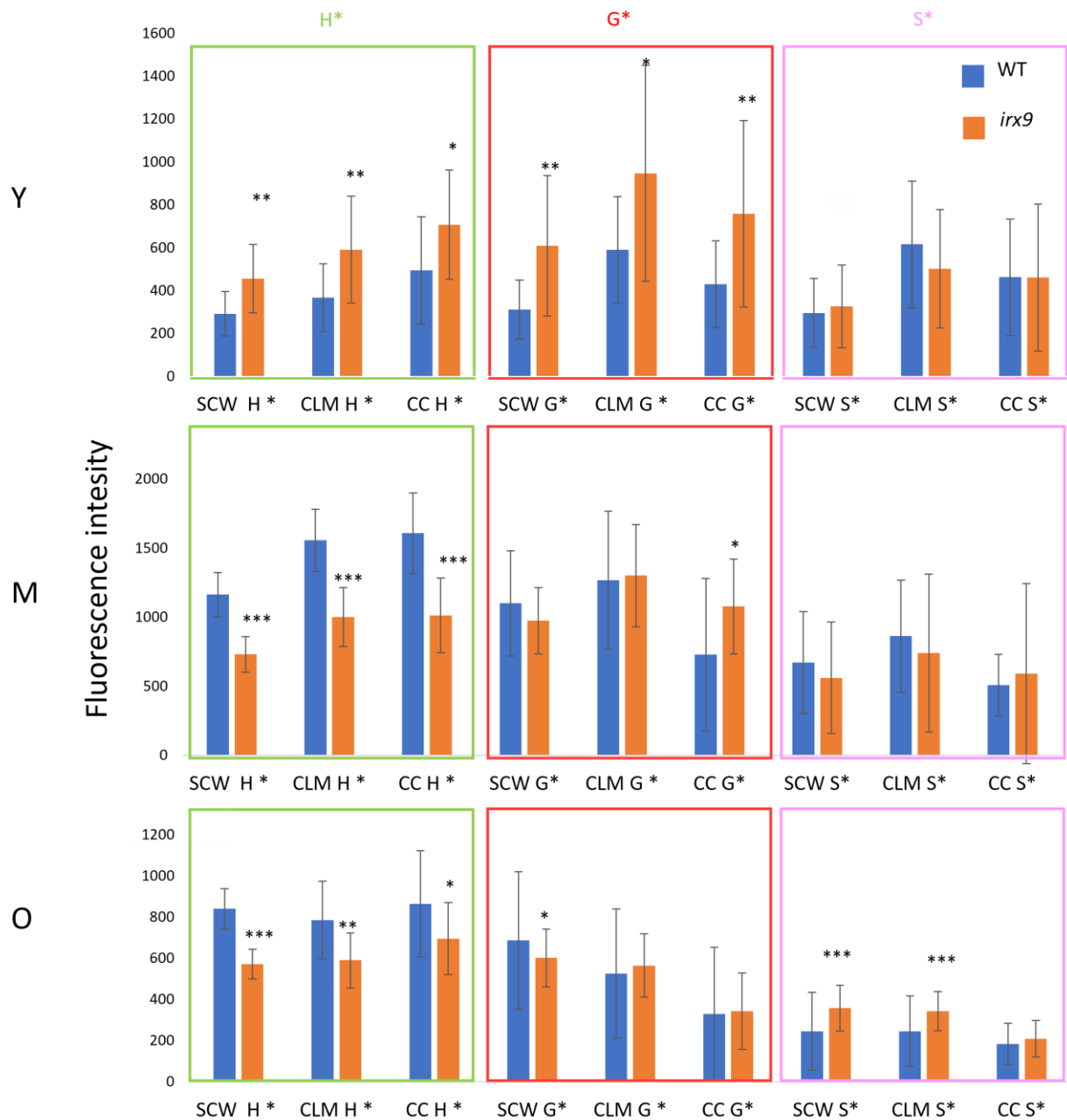


Figure 32 : Measurement of fluorescence intensity for triple monolignol labelling on *Arabidopsis thaliana* WT and *irx9-2*. The three different stages were analysed for the incorporation of H*, G* and S*. H* is labeled by Alexa fluor 488, G* by Azide Fluor 545, S* by Tetrazine Cy5. Statistics: t-test * <0.5 ; ** <0.1 ; *** <0.001

Like in Morel et al (2022), we calculated two different ratios. The ratio comparing the distribution of a reporter in different sublayers is R1 and the ratio values of monolignols in a sublayer is R2. R1 is identical between the mutant and the WT for the young part, showing that the increase in incorporation is homogeneous in the different sublayers (Figure 33 R1 Y). For

medium part (Figure 33 R1 M), it has difference in SCW and CC for G* and in CML and CC for S*. For old part (Figure 33 R1 O), it has difference in SCW and CML for G* and SCW, CML and CC for S* in old part. However, the ratio values of monolignols in a sublayer (R2) are different in young part for G and S* in SCW; for H*, G*, S* in CML and H* in CC. (Figure 33 R2 y). In medium part, it has differences for H* and G* for the 3 sublayers (Figure 33 R2 M). In the old part, it has difference in H* in the 3 sublayer and G* in CC (Figure 33 R2 O).

For the combined analyses of intensity measurements and ratios, we can see that, for the secondary wall, there is an increase for G*, while for H* it decreases, meaning that the increase of incorporation in G* in the secondary wall is more important than the increase of incorporation of H*. In the middle part, the incorporation profile changes in comparison to that of the young part. This time, there is a decrease in the incorporation capacity of H* in all sublayers. For G*, there remains only an increase in the cell corners. For the R1 ratio, there are differences for S* in the different sublayers, although there is no significant difference in intensity alone. Thus, there appears to be the beginning of a change, but it is not detectable at this stage of development. For the basal part, there is a decrease in the ability to incorporate H* in all sublayers and a decrease in G* in the secondary wall. There is also an increase for S* in the secondary wall and the middle lamella.

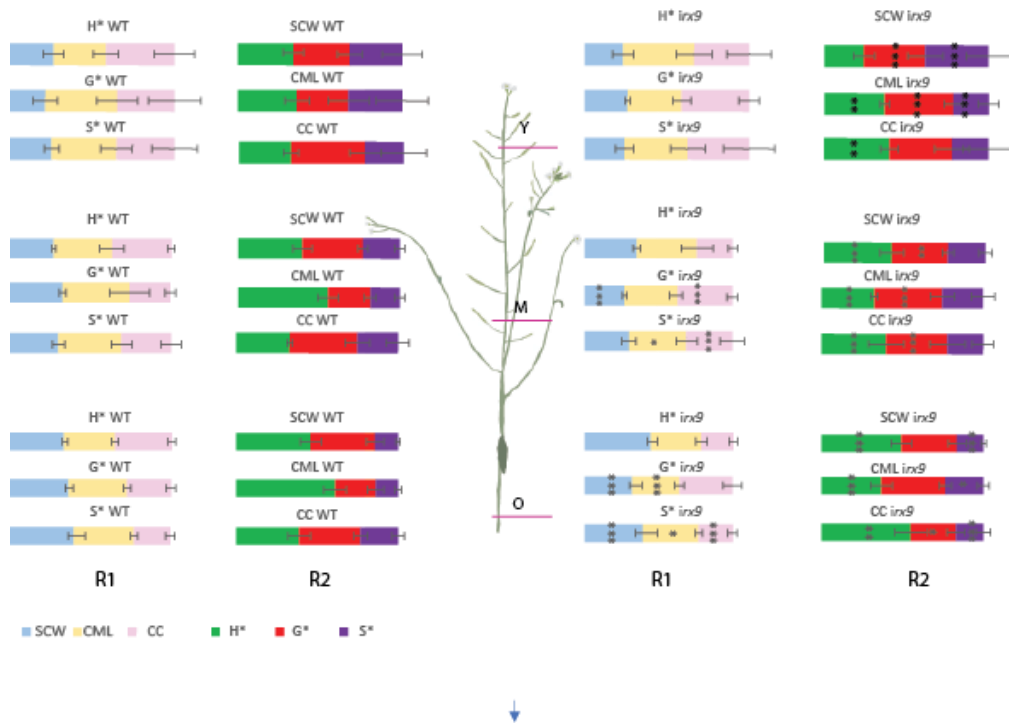


Figure 33 : Ratiometric method of analysis of the triple bioorthogonal labelling on the 3 stages of development, young (Y), medium (M) and old (O). R1 comparing the distribution of a reporter (H*, G* and S*) in different sublayers (SCW, CML and CC) and R2 the ratio values of monolignols in one sublayer.

Discussion

The results obtained show that the capacities of the cell wall to incorporate the different monolignol reporters change during the growth of the mutant in comparison with the WT, and this according to the monolignol studied. At the beginning of growth, safranin-O coloration shows less lignins in the mutant compared to the WT and Raman spectroscopy shows a modification in the deposition pattern for S-lignin. . These two complementary results suggest a delay in the activation of lignins deposition in the wall, possibly related to modifications in the structure of other wall polymers that do not allow an optimal binding with lignins. According to the literature, lignins binds covalently to hemicelluloses either by binding to the ferulate substituents of xylan, although this binding is poorly represented in dicots (Terrett & Dupree, 2019), or by methide re-aromatization of quinone (produced upon coupling of monolignols via their β -carbon) by nucleophilic addition at the α -position of nucleophilic groups of xylan and mannan (Mottiar et al., 2016). Thus, the binding between lignins and hemicelluloses can occur with either xyans or mannans. The Raman spectra show that the amount of arabinoxylan decreases in the mutant compared to WT, but not glucomanan. It is therefore possible that there is not enough xylan to make the bonds at the beginning of lignins deposition, which would explain the decrease in the amount of lignins at the beginning of growth for the mutant. The plant could try to compensate for this loss of lignification by increasing the capacity of H and G incorporation, as shown by triple labelling. To better understand the possible underlying biological mechanisms, the expressions (at the three developmental stages) of different genes were determined by (RT-qPCR) in the laboratory by a postdoctoral researcher (Dmitry Galinousky). These results showed that in the *irx9-2* mutant, which has an altered wall, the expression of *PRX71* is stronger in the upper part of the plant and progressively decreases to reach an expression comparable to that of the WT at the bottom of the stem. *PRX71* has been shown to play a role in lignification (Shigeto et al., 2013). It is thought to be involved in plant growth and in the response to wall damage and is thought to contribute to cell wall reinforcement, thereby limiting cell expansion, during normal growth and in response to cell wall damage (Raggi et al., 2015). With regards to the other genes tested, the expressions of *CESA3* (primary cell wall) and *CESA4* (secondary cell wall) don't change. This suggests that there is no change in cellulose synthesis. This hypothesis is confirmed with

Raman analysis. For pectin synthesis, *GAE6* expression doesn't change suggesting no effect on pectin synthesis, but it needs to be confirmed by other pectin gene analyses. For monolignol biosynthesis genes, there is no change in the expression of *CAD1*, *CAD5* and *CCR1*, but the expression of *CCR2* increases. *CCR2* is involved in the phenylpropanoid biosynthesis pathway especially during infection by pathogens whereas *CCR1* is involved in normal growth conditions (Fraser & Chapple, 2011). The plant thus seems to put in place mechanisms like those put in place during protection against pathogens. So it may be that the modification of hemicellulose structure induced this defense-related CCR, possibly contributing to an increase in monolignol supply related to the increased lignification in the young part of the stem.

In this context, it is possible that the mutant sets up defence mechanisms to strengthen the walls. It would increase the capacity to incorporate H and G units to reinforce lignins,. When the cells are sufficiently reinforced, the expression of *PRX71* decreases, leading to a decrease in the incorporation of monolignols. The hypothesis of the activation of a defence system agrees with the increase in the expression of the *CCR2* gene. This gene is involved in the response to pathogens (Lauvergeat et al., 2001) and has already been shown to be overexpressed in the *irx8* mutant (Hao & Mohnen, 2014).

Conclusion

All these results allow a better understanding of the dynamics of the lignification process in the *irx9* hemicellulose mutant and thus validate the relevance of this strategy using multiple approaches. The staining with safranin-O allows a semi-quantification of lignins with a localization of this one, information impossible to obtain by chemical methods. The addition of triple labelling allows the visualization of the dynamics of lignification and finally Raman spectroscopy allows to put this lignification process in the context of the plant wall and its different domains. The use of these three methods on the same developmental stages has shown that the dynamics of lignification is disturbed during the modification of the hemicelluloses of the wall. The lignins does not seem to be able to start making correctly covalent links with hemicellulose, potentially because there are not enough ferulate substituents because there are fewer xylans. The plant would therefore trigger a wall reinforcement mechanism by increasing the expression of *PRX71* which increases the capacity of incorporation of H and G. When the cells are sufficiently reinforced, the plant decreases this defence mechanism as suggested by the progressive decrease of *PRX71* expression and a decrease in the capacity of incorporation.

Discussion and perspectives

Lignins and polysaccharides in the plant wall are linked by different interactions. Cellulose and lignins are bound by hydrophobic interactions, and hemicellulose is bound to lignins by bonds to ferulate substituents or by methide re-aromatization of the quinone. In this thesis, we have therefore explored the influence of the modification of different cell wall compound on the lignification process from a spatial point of view. To carry out this work, it was necessary to develop the approach to be used to extract as much information as possible on the spatial distribution of the elements studied. For this purpose, existing approaches were refined, such as triple bioorthogonal labelling to visualise the incorporation capacity of monolignols, safranin-O staining for the quantification of lignins and Raman spectroscopy for the detection of other components.

Lignins investigation

- Followed by the incorporation of monolignols by triple bio-orthogonal labelling.

In the paper "REPRISAL: mapping lignification dynamics using chemistry, data segmentation, and ratiometric analysis", we developed an approach to extract data more efficiently from triple bio-orthogonal labelling. We have developed a segmentation approach allowing the automatic quantification of the fluorescence signal obtained by triple bioorthogonal labelling of lignins in different areas of the cell wall. The distribution of the pixels in the different classes, CC, CML and SCW, is determined by two methods, one parametric and the other based on AI. These two methods lead to the same biological conclusion despite their difference. We were able to successfully apply this method to a first arabidopsis mutant already characterised as involved in lignification, the *prx64* mutant. This allowed us to confirm that this approach allows the visualisation of small variations in the lignification process and specially to have a spatio-temporal approach to the visualisation of monolignol incorporation.

Here we explored bio-orthogonal chemistry to visualise the modification of monolignol incorporation in *Arabidopsis thaliana* mutants. Bioorthogonal chemistry can also be used to explore other processes in the plant, for example used the BONCAT (Bioorthogonal Noncanonical Amino Acid Tagging) (Glenn et al., 2017) technique to visualise protein production under mild stress. This technique consists in tagging the plant with an alanine

analogue comprising an azide tag. This tag is then clicked with a fluorophore to visualise protein production or clicked to beads to allow their extraction. We could adapt this technique to identify for example modifications in laccase or peroxydases.

It is also possible to use triple lignins labelling to monitor lignification during stress in plants that have been injured, This work is underway in my host laboratory (UGSF) (unpublished results). The work shows that during an injury, the incorporation capacity of monolignols changes in the vicinity of the injury, but also on the opposite side of stem of the injury.

- Lignins quantification

As with the triple labelling, the safranin-O stain was adapted to allow us to obtain information on different parts of the wall. safranin coloration has several advantages, it is semi-quantitative and therefore allows comparison between normal growth conditions and unusual conditions (mutation, stress) without destroying the structure of the cells

- Global analysis of cell wall polymers by RAMAN spectroscopy

We also optimised the analysis of the RAMAN spectra in order to extract the best possible information on the composition of cell walls. The different algorithms used showed complementary results, however, we were not able to get sufficiently pure composites. This is why we proceeded first to extract the average spectra and then to analyse these spectra with reference spectra. This allowed us to refine our results by differentiating between different hemicellulose (glucomannan, arabinoxylan, xyloglucan) and aromatic compounds. We were able to differentiate different hemicellulose. Thanks to this method, we can visualise the heterogeneity of the tissues.

In this work, we were interested in the detection of compounds without prior treatment of the sample. It is however possible to perform different treatments to help target a molecule or to increase the signal obtained. When Raman spectroscopy was in its infancy, Resonance Raman labels were sometimes used to visualise biological functions (Carey, 1998). Since then, the sensitivity of the spectroscopes has improved significantly, but the reporters are still used. For example, there are new reporters that allow both fluorescence microscopy and Raman spectroscopy for lipid droplets (Lin et al., 2021). RAMAN labels have also been created to allow specific detection of molecules. This technique uses bioorthogonal chemistry to add nitril or alkyne labels associated with an surface enhanced Raman scattering (SERS) to the molecule

being synthesised (Z. Zhao et al., 2017). We have started to investigate the possibility of monitoring bioorthogonal labelling by RAMAN spectroscopy. We tried several monolignol analogue molecules. The first one used was the alkyne-tagged G-monolignol, previously used for some bioorthogonal labelling experiments. The triple bond has a characteristic peak in RAMAN between 2200 and 2000 cm^{-1} , which is a blank area in the plant wall analysis. Despite the use of SERS to amplify the signal, we were unable to detect the labelled alkyne probably because the lignins signal is too strong and masks the triple bond peak. Another approach was therefore considered. The new approach is to take inspiration from the triple labelling used in confocal fluorescence microscopy. A molecule of monolignol coniferyl alcohol with azide tag (G_{az}) is incorporated into the lignins and then a second molecule with a peak of interest (detectable in Raman) is clicked onto the incorporated G_{az} . The first molecule tested is cinnamyl alcohol with a triple bond to allow the CuAAC reaction. Cinnamic alcohol is interesting because it has a peak with a strong signal at around 1000cm^{-1} , which is also a blank area in the wall spectrum. Unfortunately, no peak at this value was found, probably for the same reason as for the first test. To continue, a non-aromatic molecule with a long carbon chain was chosen. The long carbon chain with an alternation of double bonds allows to have a reasoning of the bonds amplifying the signal. The molecule chosen was lutein. A molecule was then synthesised from lutein to add a triple bond to allow the CuAAC reaction to take place. With this molecule, we expected a peak at 1012 cm^{-1} . Traces of this peak could be detected, suggesting that the labelling was not specific. These results are encouraging as we were able to detect the lutein molecule in a spectrum containing a large proportion of lignins.

This thesis has therefore made a technological contribution to the study of the plant cell wall. We will now look at the scientific contribution it has made by combining the three techniques. Different *Arabidopsis thaliana* mutants already known to have modifications in their walls, either in the lignins or in the polysaccharide matrix, were investigated.

The thesis presents the results obtained for the *irx9* mutant, a mutant known to have a modification in the length of its glucuronoxylans. The use of these three methods on the same developmental stages showed that the dynamics of lignification is disrupted by the modification of the wall hemicelluloses. Our hypothesis is that the lignins does not seem to be able to start its polymerisation properly, possibly because there are not enough ferulate

substituents because there are fewer xylans. And maybe, the plant therefore triggers a wall strengthening mechanism by increasing the expression of *PRX71*, which increases the capacity for H and G incorporation. When the cells are sufficiently reinforced, the plant decreases this defence mechanism as suggested by the progressive decrease in *PRX71* expression and the decrease in incorporation capacity.

The *gae6* mutant (mutation on UDP-D-glucuronate-4-epimerase) was also studied, although the results are not presented here. Analysis of this mutant, characterised by a decrease in the amount of pectin (20%) (Bethke et al., 2016) also shows differences in the lignification process, mainly in the young part of the stem with a decrease in the capacity to incorporate monolignols this time, with an amount of lignins comparable to WT.

These two mutants show that the polysaccharide matrix has an influence on lignification and on the incorporation capacity of monolignols. Depending on the modified polysaccharide, the effect on the dynamics of lignification is not the same.

There are still many questions to be answered to understand all the mechanisms involved in the modification of lignification following a modification of the polysaccharide matrix. Different hypotheses can be proposed to explain this phenomenon.

The modification would lead to:

- a change in the production of monolignols. This hypothesis seems possible, since in the analysis of gene expression in the *irx9* mutant, the expression of the gene coding for *CCR2*, which is involved in the synthesis of monolignols under stress (Fraser & Chapple, 2011) is modified. Other monolignol biosynthesis pathway enzymes could also be explored.
- A change in the mobility of monolignols. If monolignols access more or less easily to the wall, the enzymes responsible for lignification would be able to synthesize lignin more or less easily.
- A change in the mobility of enzymes. The location of the enzymes responsible for lignification will determine the location of lignification. It was shown that LAC4 was mobile in the primary wall but, immobile in the secondary wall (Yi Chou et al., 2018). It could be that the mobility of the enzymes is altered and thus influences lignification.

- A change in the physico-chemical properties of the wall. This hypothesis could be explored by measuring, for example, the resistance of the stem or the pH of the wall using fluorophores that change their emission wavelength according to the pH.

In this work, we were interested in the effect of hemicellulose modification on lignification. We can also consider applying Raman, safranin-O coloration, and REPRISAL to cellulose mutants to see how this modification influences lignification. It is already known that the lack of cellulose influences lignification. Work has shown that in cell culture of *Zinnia elegans*, in the presence of a cellulose synthesis inhibitor, lignification has a different distribution than the control (Taylor et al., 1992), but this work has been done on cell cultures. It would be interesting to visualize the dynamics of lignification on whole plant. Mutants could also be used. These could be knock out mutants of the 10 cellulose synthases known for *Arabidopsis thaliana*. CESA1, CESA2, CESA3, CESA5, CESA6, and CESA9 (McFarlane & Persson, 2014) are required for primary wall synthesis and CESA4, CESA7 and CESA8 for the secondary wall. It would therefore be interesting to study lignification for CESA mutant in the primary and secondary wall. In the study of the CESA6 mutant of *Arabidopsis*, it was shown that the lignins content did not change, despite the decrease in crystalline cellulose (Peng et al., 2001), we could with this mutant see if the non-functional CESA6 modifies the monolignol reporter incorporation capacity and if other molecules of the wall are affected. For the CESAs involved in secondary cell wall synthesis, it has been shown that knocking out these CESAs induces an irregular xylem phenotype, respectively called *irx5*, *irx3* (Taylor et al., 2003) and *irx1* (Taylor et al., 1999) It would be interesting here to see if the *irx* phenotype caused by a mutation on cellulose synthesis and not on hemicellulose synthesis has the same effect on lignification.

We have seen that, depending on the growth stage of the *Arabidopsis* stem, the dynamics of lignification changes. We worked on a fast-growing model. We could continue the study over a longer period by using multi-annual plants, like pine. It is already known that the season influences lignification. In pine, it has been shown that lignins changes at each stage of

lignification depending on the wood type (Antonova et al., 2019). It would be interesting to look at whether this change is related to a change in other wall constituents.

List of abbreviations

2 D HSQC NMR = 2 Dimensions Heteronuclear Single Quantum Coherence Nuclear Magnetic Resonance

4CL = 4-Coumarate-CoA Ligase

5HG = 5-HydroxyGuaiacyl

AceA = L-Acerate

AGP = ArabinoGalactan Protein

Api = D-apiose

AtCESA6 = *Arabidopsis thaliana* CELLULOSE SYNTHASE 6

BOKU = BOden Kultur Universität

BioNaMi : Biological materials on the Nano and Micro scale

C = catechyl unit

C4H = Cinnamate 4-Hydroxylase

CAD = Cinnamyl Alcohol Dehydrogenase

CASA : Cysteine-Assisted Sulfuric Acid

CAZy = Carbohydrate-Active enZymes

CCD Camera = Charge Coupled Device

CCoAOMT = Caffeoyl CoA 3-O-MethylTransferase

CCR = Cinnamoyl CoA Reductase

CCR2 = Cinnamoyl CoA Reductase 2

CE = Carbohydrate Esterase

CESA = CELLulose SynthAse

CML = middle lamella and primary cell wall

CMU = Companion of cellulose synthase-Microtubule Uncoupling

CNRS = Centre National de la Recherche Scientifique

COMT = Caffeic acid/5-hydroxyconiferaldehyde 3/5-O-MethylTransferase

CSC = Cellulose Synthesis Complex

CSI = Cellulose Synthase Interacting

CuAAC = Copper(I)-Catalyzed Alkyne-Azide Cycloaddition

CWPr = Cell Wall Protein

CWP = Cell Wall Polysaccharides

DAMP = Damage-Associated Molecular Pattern

Dha = 2-keto-3-Deoxy-D-lyxo-2-heptulosaric acid

DUF = Domain of Unknown Function

ER = Endoplasmic Reticulum

EXT = Extensin

F5H = Ferulic acid/coniferaldehyde 5-Hydroxylase

FLA = Fasciclin-Like AGP

FRAP = Fluorescence Recovery After Photobleaching

FTIR = Fourier Transform InfraRed spectroscopy

FucAl = Fucose Alkyne

G = guaiacyl unit

G* = G chemical reporter

GAE6 = UDP-D-GLUCURONATE 4-EPIMERASE 6

GAX = GlucuronoArabinoXylan

GFP = Green Fluorescent Protein

GH = Glycoside Hydrolase

G-layer = Gelatinous layer

GRP = Glycine-Rich Protein

H = hydroxyphenyl unit

H* = H chemical reporter

H₂O₂ = hydrogen peroxide

HG = HomoGalacturonan

HRGP = Hydroxyproline-Rich GlycoProtein

Hyp = Hydroxyproline

IEDDA = Inverse Electron Demand Diels-Alder

IRX = IRREGULAR XYLEM

Kdo = 2-keto-3-deoxy-D-manno octulosonate

Kdo-N3 = 3-deoxy-d - manno -oct-2-ulosonic acid-azide

KNAT = KNOTTED1-LIKE HOMEBOX GENE

KNOT3 = KNOTTED ARABIDOPSIS THALIANA 3

LAC11 = LACCASE 11

LAC17 = LACCASE 17

LAC4 = LACCASE 4

LRR = Leucine-Rich Repeat

LTP = Lipid Transfer Protein

MATE = Multidrug And Toxic Compound Extrusion

MFS = Major Facilitator Superfamily

MYB = MY eloB lastosis

NCP = Non-Cellulosic Polysaccharide

NST1 = NAC Secondary wall THICKENING PROMOTING factor

PAL = Phenylalanine Ammonia Lyase

PAMP = Pathogen-Associated Molecular Pattern

PL = Polysaccharide Lyase

PME = Pectin MethylEsterase

PRP = Pro-Rich Protein

PRX71 = PeRoXidase 71

R1 = ratio comparing the distribution of a reporter

R2 = ratio values of monolignols

REPRISAL = REPorter Ratiometrics Integrating Segmentation for Analyzing Lignification

RGI = RhamnoGalacturonan I

RGII = RhamnoGalacturonan II

Rha = Rhamnose

RM1 = the first ratio

RM2 = the second ratio

RM = Ratio Method

RT-qPCR = Reverse Transcriptase quantitative Polymerase Chain Reaction

S = syringyl unit

S* = S chemical reporter

SA = Sulfuric Acid

SCW = Secondary Cell Wall

SERS = Surface Enhanced Raman Scattering

SPAAC = Strain Promoted [3+2] Alkyne-Azide Cycloaddition

TAL = Tyrosine Ammonia Lyase

TMDP = 2-chloro-4,4',5,5'-TetraMethyl-1,3,2- Dioxaphospholane

UGSF = Unité de Glycobiologie Structurale et Fonctionnelle

UGT = Uridine-di-Phosphate Dependent Glycosyltransferase

UMR = Unité Mixte de Recherche

VND = Vascular-related Nac-Domain protein

XGA = XyloGALacturonan

XTH = Xyloglucan endoTransglucosylase/Hydrolase

XXT1 = XylosylTransferase1

XXT2 = XylosylTransferase2

xylan = arabinoxylan

List of figures

Figure 1 : Schematic representation of the different cell wall layers in tracheid cells (left) and gelatinous fibers from tension wood (right).	3
Figure 2 : Cellulose structure from (Baghaei & Skrifvars, 2020).	4
Figure 3 : Model for cellulose biosynthesis	5
Figure 4 : Schematic representation of hemicelluloses.	7
Figure 5 : Schematic representation of pectin.	9
Figure 6 : Schematic representation of poplar lignins polymer predicted by NMR (Nuclear magnetic resonance) analysis.	12
Figure 7 : Various transformation processes of lignocellulosic biomass.....	13
Figure 8 : biosynthesis pathway of monolignols.	16
Figure 9 : A scheme of transcriptional regulation of lignin biosynthetic genes in plants	18
Figure 10 : Laccase- and peroxidase-mediated oxidation of coniferyl alcohol.	20
Figure 11 : Common inter-monomeric linkages in lignins	21
Figure 12 : Relative percentages of different lignins monomers in stems of different species.....	22
Figure 13 : hemicellulose:lignins cross-linking.	25
Figure 14 Different colorations with bright field observation on <i>Arabidopsis thaliana</i> . A)	30
Figure 15 : Labelling of a biomolecule by bioorthogonal chemistry.	33
Figure 16 : Mechanisms of Staudinger- Bertozzi Ligation.....	34
Figure 17 : Copper(I)-Catalyzed Alkyne-Azide Cycloaddition (CuAAC) mechanism. 35	
Figure 18 : Strain Promoted [3+2] Alkyne-Azide Cycloaddition (SPAAC) mechanism..	36
Figure 19 : Inverse electron demand Diels–Alder (IEDDA)..	37
Figure 20 : A) FucAI molecule. B) localization of FuCAI incorporation in plasmolyzed <i>Arabidopsis thaliana</i> cells after click reaction with the Alexa 488-azide fluorophore. 38	
Figure 21 : Localization of the double labelling of pectins by FucAI and KDO-N3 of an <i>Arabidopsis</i> seedling root revealed by two consecutive CuAAC allowing Alexa Fluor ®488-alkyne (A488) and Alexa Fluor ®594-N 3 binding.	38

Figure 22 : Propargylcholine labelling of <i>Arabidopsis thaliana</i> guard cells in leaves after a click reaction with the Alexa 594-azide fluorophore.....	39
Figure 23 : Images of different G analogue incorporation profiles in <i>Arabidopsis</i> stems following a CuAAC bioorthogonal reaction..	40
Figure 24 : Triple monolignol labelling of developing xylem in the stem of flax.	41
Figure 25 : Possible vibrational modes of molecules of CH ₂ . Stretching elongation ..	43
Figure 26 : The different phenomena that can happen when radiation interact with matter from	44
Figure 27 : Different energy transitions that can occur during a Raman analysis. ν_0 corresponds to the excitation frequency of the laser, ν_{vib} corresponds to the vibration frequency of the analyzed molecule.	47
Figure 28 : Relative (to the reference genes and to the wild type plant samples) expression level of the studied genes.....	143
Figure 29 : Spectral image of the upper (Y), middle (M), and lower (O) part of <i>Arabidopsis.thaliana</i> interfascicular fibers cells cellulose.	145
Figure 30 : Study of lignins with safranin coloration on <i>irx9-2</i> mutant and WT.	146
Figure 31 : Spectral images of sections of young (Y), medium (M) and old (O) parts on WT and <i>irx9-2</i> for lignins.	148
Figure 32 : Measurement of fluorescence intensity for triple monolignol labelling on <i>Arabidopsis thaliana</i> WT and <i>irx9-2</i>	150
Figure 33 : Ratiometric method of analysis of the triple bioorthogonal labelling on the 3 stages of development, young (Y), medium (M) and old (O).....	152

Bibliography

- Aberu, H. D. S., & Freire, M. (1995). Methoxyl content determination of lignins by ^1H NMR. *An. Bras. Ci.*, 67(January 1995), 379382. <https://www.researchgate.net/publication/236246928>
- Agard, N. J., Prescher, J. A., & Bertozzi, C. R. (2004). A strain-promoted [3 + 2] azide-alkyne cycloaddition for covalent modification of biomolecules in living systems. *Journal of the American Chemical Society*, 126, 46, 15046–15047. <https://doi.org/10.1021/ja044996f>
- Agarwal, U. P. (2006). Raman imaging to investigate ultrastructure and composition of plant cell walls: Distribution of lignin and cellulose in black spruce wood (*Picea mariana*). *Planta*, 224(5), 1141–1153. <https://doi.org/10.1007/S00425-006-0295-Z/FIGURES/13>
- Agustin, M. B., de Carvalho, D. M., Lahtinen, M. H., Hilden, K., Lundell, T., & Mikkonen, K. S. (2021). Laccase as a tool in building advanced lignin-based materials. *ChemSusChem*, 14(21), 4615–4635. <https://doi.org/10.1002/CSSC.202101169>
- Albenne, C., Canut, H., & Jamet, E. (2013). Plant cell wall proteomics: The leadership of *Arabidopsis thaliana*. *Frontiers in Plant Science*, 4(MAY), 111. <https://doi.org/10.3389/FPLS.2013.00111/BIBTEX>
- Albinsson, B., Li, S., Lundquist, K., & Stomberg, R. (1999). The origin of lignin fluorescence. *Journal of Molecular Structure*, 508(1–3), 19–27. [https://doi.org/10.1016/S0022-2860\(98\)00913-2](https://doi.org/10.1016/S0022-2860(98)00913-2)
- Alejandro, S., Lee, Y., Tohge, T., Sudre, D., Osorio, S., Park, J., Bovet, L., Lee, Y., Geldner, N., Fernie, A. R., & Martinoia, E. (2012). AtABCG29 is a monolignol transporter involved in lignin biosynthesis. *Current Biology*, 22(13), 1207–1212. <https://doi.org/10.1016/j.cub.2012.04.064>
- Alonso-Simón, A., García-Angulo, P., Mélida, H., Encina, A., Álvarez, J. M., & Acebes, J. L. (2011). The use of FTIR spectroscopy to monitor modifications in plant cell wall architecture caused by cellulose biosynthesis inhibitors. *Plant Signaling & Behavior*, 6(8), 1104–1110. <https://doi.org/10.4161/PSB.6.8.15793>
- Anderson, C. T., Wallace, I. S., & Somerville, C. R. (2012). Metabolic click-labeling with a fucose analog reveals pectin delivery, architecture, and dynamics in *Arabidopsis* cell

walls. *Proceedings of the National Academy of Sciences of the United States of America*, 109 (4) 1329-1334. <https://doi.org/10.1073/pnas.1120429109>

Antonova, G. F., Varaksina, T. N., Zheleznichenko, T. V., & Bazhenov, A. V. (2019). Changes in lignin structure during earlywood and latewood formation in Scots pine stems. *Wood Science and Technology* 2019 53:4, 53(4), 927–952. <https://doi.org/10.1007/S00226-019-01108-W>

Anwar, Z., Gulfraz, M., & Irshad, M. (2014). Agro-industrial lignocellulosic biomass a key to unlock the future bio-energy: A brief review. *Journal of Radiation Research and Applied Sciences*, 7(2), 163–173. <https://doi.org/10.1016/J.JRRAS.2014.02.003>

Argyropoulos, D. S. (1994). Quantitative phosphorus-31 nmr analysis of six soluble lignins. *Journal of Wood Chemistry and Technology*, 14(1), 65–82. <https://doi.org/10.1080/02773819408003086>

Bacete, L., Schulz, J., Engelsdorf, T., Bartosova, Z., Vaahtera, L., Yan, G., Gerhold, J. M., Ticha, T., Øvstebø, C., Gigli-Bisceglia, N., Johannessen-Starheim, S., Margueritat, J., Kollist, H., Dehoux, T., McAdam, S. A. M., & Hamann, T. (2022). THESEUS1 modulates cell wall stiffness and abscisic acid production in *Arabidopsis thaliana*. *Proceedings of the National Academy of Sciences of the United States of America*, 119(1). <https://doi.org/10.1073/pnas.2119258119>

Baghaei, B., & Skrifvars, M. (2020). All-Cellulose Composites: A Review of Recent Studies on Structure, Properties and Applications. *Molecules* 2020, 25(12): 2836. <https://doi.org/10.3390/MOLECULES25122836>

Bai, Y., Wu, D., Liu, F., Li, Y., Chen, P., Lu, M., & Zheng, B. (2017). Characterization and functional analysis of the poplar pectate Lyase-like gene PtPL1-18 reveal its role in the development of vascular tissues. *Frontiers in Plant Science*, 8, 1123. <https://doi.org/10.3389/FPLS.2017.01123/BIBTEX>

Balakshin, M., & Capanema, E. (2015). On the Quantification of Lignin Hydroxyl Groups With 31P and 13C NMR Spectroscopy. *Journal of Wood Chemistry and Technology*, 35(3), 220–237. <https://doi.org/10.1080/02773813.2014.928328>

Baldacci-Cresp, F., Spriet, C., Twyffels, L., Blervacq, A. S., Neutelings, G., Baucher, M., & Hawkins, S. (2020). A rapid and quantitative safranin-based fluorescent microscopy method to evaluate cell wall lignification. *The Plant Journal*, 102(5), 1074–1089.

<https://doi.org/10.1111/TPJ.14675>

- Barbillat, J., Roussel, B., & Da Silva, E. (1999). Use of Multi-notch Filter for Simultaneous Recording of Stokes and Anti-Stokes Raman Signals Close to the Exciting Line. *Journal of Raman spectroscopy*, 30, 745–755. [https://doi.org/10.1002/\(SICI\)1097-4555\(199909\)30:9<745::AID-JRS422>3.0.CO;2-7](https://doi.org/10.1002/(SICI)1097-4555(199909)30:9<745::AID-JRS422>3.0.CO;2-7)
- Barceló, A. R., & Pomar, F. (2001). Oxidation of cinnamyl alcohols and aldehydes by a basic peroxidase from lignifying *Zinnia elegans* hypocotyls. *Phytochemistry*, 57(7), 1105–1113 [https://doi.org/10.1016/S0031-9422\(01\)00050-4](https://doi.org/10.1016/S0031-9422(01)00050-4)
- Barros, J., Serk, H., Granlund, I., & Pesquet, E. (2015). The cell biology of lignification in higher plants. *Annals of Botany*. <https://doi.org/10.1093/aob/mcv046>
- Berthet, S., Demont-Caulet, N., Pollet, B., Bidzinski, P., Cézard, L., le Bris, P., Herve, J., Blondet, E., Balzergue, S., Lapierre, C., & Jouanin, L. (2011). Disruption of *LACCASE4* and *17* Results in Tissue-Specific Alterations to Lignification of *Arabidopsis thaliana* Stems. *The Plant Cell*, 23(3), 1124–1137. <https://doi.org/10.1105/TPC.110.082792>
- Bethke, G., Thao, A., Xiong, G., Li, B., Soltis, N. E., Hatsugai, N., Hillmer, R. A., Katagiri, F., Kliebenstein, D. J., Pauly, M., & Glazebrook, J. (2016). Pectin biosynthesis is critical for cell wall integrity and immunity in *Arabidopsis thaliana*. *The Plant Cell*, 28(2), 537–556. <https://doi.org/10.1105/TPC.15.00404>
- Boeriu, C. G., Stolle-Smits, T., & Dijk, C. van. (1998). Characterisation of Cell Wall Pectins by near Infrared Spectroscopy. 6(A), A299–A301. <https://doi.org/10.1255/JNIRS.211>
- Boija, E., & Johansson, G. (2006). Interactions between model membranes and lignin-related compounds studied by immobilized liposome chromatography. *Biochimica et Biophysica Acta (BBA) - Biomembranes*, 1758(5), 620–626. <https://doi.org/10.1016/J.BBAMEM.2006.04.007>
- Boller, T., & Felix, G. (2009). A Renaissance of Elicitors: Perception of Microbe-Associated Molecular Patterns and Danger Signals by Pattern-Recognition Receptors. *Annual Review of Plant Biology*. 60:379-406. <https://doi.org/10.1146/annurev.arplant.57.032905.105346>
- Bouxin, F. P., McVeigh, A., Tran, F., Westwood, N. J., Jarvis, M. C., & Jackson, S. D. (2015). Catalytic depolymerisation of isolated lignins to fine chemicals using a Pt/alumina catalyst: part 1—impact of the lignin structure. *Green Chemistry*, 17(2), 1235–1242.

<https://doi.org/10.1039/C4GC01678E>

- Brinkmann, K., Blaschke, L., & Polle, A. (2002). Comparison of Different Methods for Lignin Determination as a Basis for Calibration of Near-Infrared Reflectance Spectroscopy and Implications of Lignoproteins. *Journal of Chemical Ecology* 28(12), 2483–2501. <https://doi.org/10.1023/A:1021484002582>
- Bukowski, N., Pandey, J. L., Doyle, L., Richard, T. L., Anderson, C. T., & Zhu, Y. (2014). Development of a clickable designer monolignol for interrogation of lignification in plant cell walls. *Bioconjugate Chemistry*, 25(12), 2189–2196. <https://doi.org/10.1021/bc500411u>
- Bule, M. V., Gao, A. H., Hiscox, B., & Chen, S. (2013). Structural modification of lignin and characterization of pretreated wheat straw by ozonation. *Journal of Agricultural and Food Chemistry*, 61(16), 3916–3925. https://doi.org/10.1021/JF4001988/SUPPL_FILE/JF4001988_SI_001.PDF
- Buschmann, H., & Borchers, A. (2020). Handedness in plant cell expansion: a mutant perspective on helical growth. *New Phytologist*, 225(1), 53–69. <https://doi.org/10.1111/NPH.16034>
- Caffall, K. H., Pattathil, S., Phillips, S. E., Hahn, M. G., & Mohnen, D. (2009). Arabidopsis thaliana T-DNA Mutants Implicate GAUT Genes in the Biosynthesis of Pectin and Xylan in Cell Walls and Seed Testa. *Molecular Plant*, 2(5), 1000–1014. <https://doi.org/10.1093/MP/SSP062>
- Cannon, M. C., Terneus, K., Hall, Q., Tan, L., Wang, Y., Wegenhart, B. L., Chen, L., Lamport, D. T. A., Chen, Y., & Kieliszewski, M. J. (2008). Self-assembly of the plant cell wall requires an extensin scaffold. *Proceedings of the National Academy of Sciences of the United States of America*, 105(6), 2226–2231. https://doi.org/10.1073/PNAS.0711980105/SUPPL_FILE/11980TABLE4.PDF
- Caño-Delgado, A., Penfield, S., Smith, C., Catley, M., & Bevan, M. (2003). Reduced cellulose synthesis invokes lignification and defense responses in *Arabidopsis thaliana*. *The Plant Journal*, 34(3), 351–362. <https://doi.org/10.1046/J.1365-313X.2003.01729.X>
- Carey, P. R. (1998). Resonance Labels and Labels Raman Raman. *journal of raman spectroscopy*, 29, 861–868. [https://doi.org/10.1002/\(SICI\)1097-4555\(199810/11\)29:10/11](https://doi.org/10.1002/(SICI)1097-4555(199810/11)29:10/11)

- Cassab, G. I. (1998). plant cell wall proteins. *Annual Review of Plant Physiology and Plant Molecular Biology*. <https://doi.org/10.1146/annurev.arplant.49.1.281>
- Chepyshko, H., Lai, C. P., Huang, L. M., Liu, J. H., & Shaw, J. F. (2012). Multifunctionality and diversity of GDSL esterase/lipase gene family in rice (*Oryza sativa* L. japonica) genome: New insights from bioinformatics analysis. *BMC Genomics*, *13*(1), 1–19. <https://doi.org/10.1186/1471-2164-13-309/FIGURES/6>
- Clifford, M. N. (1974). Specificity of acidic phloroglucinol reagents. *Journal of Chromatography A*, *94*(C), 321–324. [https://doi.org/10.1016/S0021-9673\(01\)92389-1](https://doi.org/10.1016/S0021-9673(01)92389-1)
- Constant, S., Wienk, H. L. J., Frissen, A. E., Peinder, P. De, Boelens, R., Van Es, D. S., Grisel, R. J. H., Weckhuysen, B. M., Huijgen, W. J. J., Gosselink, R. J. A., & Bruijninx, P. C. A. (2016). New insights into the structure and composition of technical lignins: a comparative characterisation study. *Green Chemistry*, *18*(9), 2651–2665. <https://doi.org/10.1039/C5GC03043A>
- Cosio, C., Ranocha, P., Francoz, E., Burlat, V., Zheng, Y., Perry, S. E., Ripoll, J.-J., Yanofsky, M., & Dunand, C. (2017). The class III peroxidase *PRX17* is a direct target of the MADS-box transcription factor *AGAMOUS-LIKE15* (*AGL15*) and participates in lignified tissue formation. *New Phytologist*, *213*(1), 250–263. <https://doi.org/10.1111/NPH.14127>
- Crestini, C., & Argyropoulos, D. S. (1997). Structural Analysis of Wheat Straw Lignin by Quantitative ³¹P and 2D NMR Spectroscopy. The Occurrence of Ester Bonds and α -O-4 Substructures. *Journal of Agricultural and Food Chemistry*, *45*(4), 1212–1219. <https://doi.org/10.1021/jf960568k/asset/images/large/jf960568kf00005.jpeg>
- Curry, T. M., Peña, M. J., & Urbanowicz, B. R. (2023). An update on xylan structure, biosynthesis, and potential commercial applications. *The Cell Surface*, *9*, 100101. <https://doi.org/10.1016/J.TCSW.2023.100101>
- D. A. Long. (1977). *raman spectroscopy*. https://books.google.fr/books?hl=fr&lr=&id=DzUXBQAAQBAJ&oi=fnd&pg=PA149&dq=Long,+1977+raman&ots=oZlyDd5U6T&sig=hFYzdDIVIPahcN-GIHZWLi5rz_E#v=onepage&q&f=false
- Deepak, S., Shailasree, S., Kini, R. K., Muck, A., Mithöfer, A., & Shetty, S. H. (2010). Hydroxyproline-rich Glycoproteins and Plant Defence. *Journal of Phytopathology*, *158*(9), 585–593. <https://doi.org/10.1111/J.1439-0434.2010.01669.X>

- Del Río, J. C., Rencoret, J., Prinsen, P., Martínez, Á. T., Ralph, J., & Gutiérrez, A. (2012). Structural characterization of wheat straw lignin as revealed by analytical pyrolysis, 2D-NMR, and reductive cleavage methods. *Journal of Agricultural and Food Chemistry*, *60*(23), 5922–5935. <https://doi.org/10.1021/jf301002n>
- Dharmawardhana, D. P., Ellis, B. E., & Carlson, J. E. (1992). Characterization of vascular lignification in *Arabidopsis thaliana*. *Canadian Journal of Botany*, *70*(11), 2238–2244. <https://doi.org/10.1139/b92-277>
- Dharmawardhana, D. P., Ellis, B. E., & Carlson, J. E. (1995). A β -glucosidase from lodgepole pine xylem specific for the lignin precursor coniferin. *Plant Physiology*, *107*(2), 331–339. <https://doi.org/10.1104/pp.107.2.331>
- Diels, O., & Alder, K. (1928). Synthesen in der hydroaromatischen Reihe. *Justus Liebigs Annalen Der Chemie*, *460*(1), 98–122. <https://doi.org/10.1002/JLAC.19284600106>
- Dietrich, D., Hemeltjen, S., Meyer, N., Bäucker, E., Rühle, G., Wienhaus, O., & Marx, G. (2002). A new attempt to study biomineralised silica bodies in *Dactylis glomerata* L. *Analytical and Bioanalytical Chemistry*, *374*(4), 749–752. <https://doi.org/10.1007/S00216-002-1486-5/METRICS>
- Dixon, R. A., & Barros, J. (2019). Lignin biosynthesis: old roads revisited and new roads explored. *Open Biology*, *9*(12), 190215. <https://doi.org/10.1098/rsob>
- Djikanović, D., Kalauzi, A., Radotić, K., Lapierre, C., & Jeremić, M. (2007). Deconvolution of lignin fluorescence spectra: A contribution to the comparative structural studies of lignins. *Russian Journal of Physical Chemistry A* *81*(9), 1425–1428. <https://doi.org/10.1134/S0036024407090142>
- Dokken, K. M., Davis, L. C., & Marinkovic, N. S. (2007). Use of Infrared Microspectroscopy in Plant Growth and Development., *Applied Spectroscopy Reviews*, *40*(4), 301–326. <https://doi.org/10.1080/05704920500230898>
- Donaldson, L. (2013). Softwood and Hardwood Lignin Fluorescence Spectra of Wood Cell Walls in Different Mounting Media. *IAWA Journal*, *34*(1), 3–19. <https://doi.org/10.1163/22941932-00000002>
- Donaldson, L. (2020). Autofluorescence in Plants. *Molecules*, *25*(10), 2393. <https://doi.org/10.3390/MOLECULES25102393>

- Dumont, M., Lehner, A., Vauzeilles, B., Malassis, J., Marchant, A., Smyth, K., Linclau, B., Baron, A., Mas Pons, J., Anderson, C. T., Schapman, D., Galas, L., Mollet, J. C., & Lerouge, P. (2016). Plant cell wall imaging by metabolic click-mediated labelling of rhamnogalacturonan II using azido 3-deoxy-d-manno-oct-2-ulosonic acid. *The Plant Journal*, *85*(3), 437–447. <https://doi.org/10.1111/TPJ.13104>
- Ebringerová, A., Hromádková, Z., & Heinze, T. (2005). Hemicellulose. In *Advances in Polymer Science*. <https://doi.org/10.1007/b136816>
- Edwards, H. G. M., Farwell, D. W., & Webster, D. (1997). FT Raman microscopy of untreated natural plant fibres. *Spectrochimica Acta Part A: Molecular and Biomolecular Spectroscopy*, *53*(13), 2383–2392. [https://doi.org/10.1016/S1386-1425\(97\)00178-9](https://doi.org/10.1016/S1386-1425(97)00178-9)
- Eklöf, J. M., & Brumer, H. (2010). The *XTH* gene family: an update on enzyme structure, function, and phylogeny in xyloglucan remodeling. *Plant Physiology*, *153*(2), 456–466. <https://doi.org/10.1104/PP.110.156844>
- Erdmann, J. (1866). Ueber die Concretionen in den Birnen. *Justus Liebigs Annalen Der Chemie*, *138*(1), 1–19. <https://doi.org/10.1002/JLAC.18661380102>
- Farquharson, K. L. (2009). Cortical Microtubules Regulate the Insertion of Cellulose Synthase Complexes in the Plasma Membrane. *The Plant Cell*, *21*(4), 1028. <https://doi.org/10.1105/TPC.109.210411>
- Felidj, N. (2016). Introduction à... La spectroscopie Raman et la diffusion exaltée de surface. *Photoniques*, *81*, 46–49. <https://doi.org/10.1051/PHOTON/20168146>
- Fernández-Pérez, F., Pomar, F., Pedreño, M. A., & Novo-Uzal, E. (2015a). The suppression of AtPrx52 affects fibers but not xylem lignification in Arabidopsis by altering the proportion of syringyl units. *Physiologia Plantarum*, *154*(3), 395–406. <https://doi.org/10.1111/PPL.12310>
- Fernández-Pérez, F., Pomar, F., Pedreño, M. A., & Novo-Uzal, E. (2015b). Suppression of Arabidopsis peroxidase 72 alters cell wall and phenylpropanoid metabolism. *Plant Science*, *239*, 192–199. <https://doi.org/10.1016/J.PLANTSCI.2015.08.001>
- Fornalé, S., Sonbol, F. M., Maes, T., Capellades, M., Puigdomènech, P., Rigau, J., & Caparrós-Ruiz, D. (2006). Down-regulation of the maize and *Arabidopsis thaliana* caffeic acid O-methyl-transferase genes by two new maize R2R3-MYB transcription factors. *Plant*

Molecular Biology, 62(6), 809–823. <https://doi.org/10.1007/S11103-006-9058-2/METRICS>

Fraser, C. M., & Chapple, C. (2011). The phenylpropanoid pathway in *arabidopsis*. *the arabidopsis book / american society of plant biologists*, 9, e0152. <https://doi.org/10.1199/TAB.0152>

Fujita, M., & Harada, H. (1979). Autoradiographic investigations of cell wall development, (2). *Mokuzai Gakkai-Shi*, 25(2), 89–94. http://inis.iaea.org/Search/search.aspx?orig_q=RN:11508311

Gavnholt, B., & Larsen, K. (2002). Molecular biology of plant laccases in relation to lignin formation. *Physiologia Plantarum*, 116(3), 273–280. <https://doi.org/10.1034/J.1399-3054.2002.1160301.X>

Gawkowska, D., Cybulska, J., & Zdunek, A. (2018). structure-related gelling of pectins and linking with other natural compounds: A Review. *Polymers*, 10(7), 762. <https://doi.org/10.3390/POLYM10070762>

Gierlinger, N., Goswami, L., Schmidt, M., Burgert, I., Coutand, C., Rogge, T., & Schwanninger, M. (2008). In situ FT-IR microscopic study on enzymatic treatment of poplar wood cross-sections. *Biomacromolecules*, 9(8), 2194–2201. https://doi.org/10.1021/BM800300B/ASSET/IMAGES/MEDIUM/BM-2008-00300B_0008.GIF

Gierlinger, N., & Schwanninger, M. (2006). Chemical imaging of poplar wood cell walls by confocal raman microscopy. *Plant Physiology*, 140(4), 1246–1254. <https://doi.org/10.1104/PP.105.066993>

Giovane, A., Servillo, L., Balestrieri, C., Raiola, A., D'Avino, R., Tamburrini, M., Ciardiello, M. A., & Camardella, L. (2004). Pectin methylesterase inhibitor. *Biochimica et Biophysica Acta (BBA) - Proteins and Proteomics*, 1696(2), 245–252. <https://doi.org/10.1016/J.BBAPAP.2003.08.011>

Glenn, W. S., Stone, S. E., Ho, S. H., Sweredoski, M. J., Moradian, A., Hess, S., Bailey-Serres, J., & Tirrell, D. A. (2017). Bioorthogonal noncanonical amino acid tagging (BONCAT) enables time-resolved analysis of protein synthesis in native plant tissue. *Plant Physiology*, 173(3), 1543–1553. <https://doi.org/10.1104/PP.16.01762>

- Grantham, N. J., Wurman-Rodrich, J., Terrett, O. M., Lyczakowski, J. J., Stott, K., Iuga, D., Simmons, T. J., Durand-Tardif, M., Brown, S. P., Dupree, R., Busse-Wicher, M., & Dupree, P. (2017). An even pattern of xylan substitution is critical for interaction with cellulose in plant cell walls. *Nature Plants*, 3(11), 859–865. <https://doi.org/10.1038/s41477-017-0030-8>
- Hamant, O., & Traas, J. (2010). The mechanics behind plant development. *New Phytologist*, 185(2), 369–385. <https://doi.org/10.1111/J.1469-8137.2009.03100.X>
- Hang, H. C., Yu, C., Kato, D. L., & Bertozzi, C. R. (2003). A metabolic labeling approach toward proteomic analysis of mucin-type O-linked glycosylation. *Proceedings of the National Academy of Sciences of the United States of America*, 100(25), 14846. <https://doi.org/10.1073/PNAS.2335201100>
- Hao, Z., & Mohnen, D. (2014). A review of xylan and lignin biosynthesis: Foundation for studying Arabidopsis irregular xylem mutants with pleiotropic phenotypes. *Cox Crit Rev Biochem Mol Biol*, 49(3), 212–241. <https://doi.org/10.3109/10409238.2014.889651>
- Harholt, J., Suttangkakul, A., & Scheller, H. V. (2010). Biosynthesis of pectin. *Plant Physiology*, 153(2), 384–395. <https://doi.org/10.1104/pp.110.156588>
- Heikkinen, H., Elder, T., Maaheimo, H., Rovio, S., Rahikainen, J., Kruus, K., & Tamminen, T. (2014). Impact of steam explosion on the wheat straw lignin structure studied by solution-state nuclear magnetic resonance and density functional methods. *Journal of Agricultural and Food Chemistry*, 62(43), 10437–10444. https://doi.org/10.1021/JF504622J/ASSET/IMAGES/LARGE/JF-2014-04622J_0007.JPEG
- Herrero, J., Fernández-Pérez, F., Yebra, T., Novo-Uzal, E., Pomar, F., Pedreño, M. Á., Cuello, J., Guéra, A., Esteban-Carrasco, A., & Zapata, J. M. (2013). Bioinformatic and functional characterization of the basic peroxidase 72 from Arabidopsis thaliana involved in lignin biosynthesis. *Planta*, 237(6), 1599–1612. <https://doi.org/10.1007/S00425-013-1865-5/FIGURES/9>
- Himmelsbach, D. S., Khahili, S., & Akin, D. E. (1999). Near-infrared–Fourier-transform–Raman microspectroscopic imaging of flax stems. *Vibrational Spectroscopy*, 19(2), 361–367. [https://doi.org/10.1016/S0924-2031\(98\)00065-4](https://doi.org/10.1016/S0924-2031(98)00065-4)
- Hiraide, H., Tobimatsu, Y., Yoshinaga, A., Lam, P. Y., Kobayashi, M., Matsushita, Y., 177

- Fukushima, K., & Takabe, K. (2021). Localised laccase activity modulates distribution of lignin polymers in gymnosperm compression wood. *New Phytologist*, *230*(6), 2186–2199. <https://doi.org/10.1111/NPH.17264>
- Ho-Yue-Kuang, S., Alvarado, C., Antelme, S., Bouchet, B., Cézard, L., Le Bris, P., Legée, F., Maia-Grondard, A., Yoshinaga, A., Saulnier, L., Guillon, F., Sibout, R., Lapierre, C., & Chateigner-Boutin, A. L. (2016). Mutation in *Brachypodium* caffeic acid O-methyltransferase 6 alters stem and grain lignins and improves straw saccharification without deteriorating grain quality. *Journal of Experimental Botany*, *67*(1), 227–237. <https://doi.org/10.1093/JXB/ERV446>
- Hoffmann, N., Benske, A., Betz, H., Schuetz, M., & Lacey Samuels, A. (2020). Laccases and peroxidases co-localize in lignified secondary cell walls throughout stem development. *Plant Physiology*, *184*(2), 806–822 <https://doi.org/10.1104/pp.20.00473>
- Hoogenboom, J., Berghuis, N., Cramer, D., Geurts, R., Zuilhof, H., & Wennekes, T. (2016). Direct imaging of glycans in *Arabidopsis* roots via click labeling of metabolically incorporated azido-monosaccharides. *BMC Plant Biology*, *16*(1), 1–11. <https://doi.org/10.1186/S12870-016-0907-0/FIGURES/7>
- Huisgen, R., Gotthardt, H., Bayer, H. O., & Schaefer, F. C. (1964). A new type of mesoionic aromatic compound and its 1,3-dipolar cycloaddition reactions with acetylene derivatives. *angewandte chemie internationale edition in english*, *3*(2), 136-137 <https://doi.org/10.1002/anie.196401361>
- Jamet, E., Albenne, C., Boudart, G., Irshad, M., Canut, H., & Pont-Lezica, R. (2008). Recent advances in plant cell wall proteomics. *Proteomics*, *8*(4), 893-908 <https://doi.org/10.1002/pmic.200700938>
- Jamet, E., & Dunand, C. (2020). Plant Cell Wall Proteins and Development. *International Journal of Molecular Sciences* *2020*, *21*(8), 2731. <https://doi.org/10.3390/IJMS21082731>
- Johnson, D., Moore, W. E., & Zank, L. C. (1961). The spectrophotometric determination of lignin in small wood samples. *Tappi* *44*(11): 793-8. <https://eurekamag.com/research/014/272/014272813.php>
- Jones, J. D. G., & Dangl, J. L. (2006). The plant immune system. *Nature*, *444*, pages 323–329. <https://doi.org/10.1038/nature05286>

- Jourez, B. (1997). Le bois de tension. 1. Définition et distribution dans l'arbre. *BASE*, 1. <https://popups.uliege.be/1780-4507/index.php?id=16124>
- Jung, H. Y., Lee, J. S., Han, H. T., Jung, J., Eom, K., & Lee, J. T. (2022). Lignin-Based Materials for Sustainable Rechargeable Batteries. *Polymers*, 14(4). <https://doi.org/10.3390/POLYM14040673>
- Kaneda, M., Rensing, K. H., Wong, J. C. T., Banno, B., Mansfield, S. D., & Samuels, A. L. (2008). Tracking monolignols during wood development in lodgepole pine. *Plant Physiology*, 147(4), 1750–1760. <https://doi.org/10.1104/pp.108.121533>
- Kumar, A. K., & Sharma, S. (2017). Recent updates on different methods of pretreatment of lignocellulosic feedstocks: a review. *Bioresources and Bioprocessing*, 4(1), 1–19. <https://doi.org/10.1186/S40643-017-0137-9>
- Lahive, C. W., Kamer, P. C. J., Lancefield, C. S., & Deuss, P. J. (2020). An Introduction to Model Compounds of Lignin Linking Motifs; Synthesis and Selection Considerations for Reactivity Studies. *ChemSusChem*, 13(17), 4238–4265. <https://doi.org/10.1002/CSSC.202000989>
- Lauvergeat, V., Lacomme, C., Lacombe, E., Lasserre, E., Roby, D., & Grima-Pettenati, J. (2001). Two cinnamoyl-CoA reductase (CCR) genes from *Arabidopsis thaliana* are differentially expressed during development and in response to infection with pathogenic bacteria. *Phytochemistry*, 57(7), 1187–1195. [https://doi.org/10.1016/S0031-9422\(01\)00053-X](https://doi.org/10.1016/S0031-9422(01)00053-X)
- Le Gall, H., Philippe, F., Domon, J. M., Gillet, F., Pelloux, J., & Rayon, C. (2015). Cell wall metabolism in response to abiotic stress. *Plants*, 4(1), 112–166. <https://doi.org/10.3390/plants4010112>
- Le Roy, J., Huss, B., Creach, A., Hawkins, S., & Neutelings, G. (2016). Glycosylation is a major regulator of phenylpropanoid availability and biological activity in plants. *Frontiers in Plant Science*, 7, 735. <https://doi.org/10.3389/fpls.2016.00735>
- Lee, Y., Rubio, M. C., Alassimone, J., & Geldner, N. (2013). A mechanism for localized lignin deposition in the endodermis. *Cell*, 153(2), 402–412. <https://doi.org/10.1016/j.cell.2013.02.045>
- Li, J., Huang, X., Huang, H., Huo, H., Nguyen, C. D., Pian, R., Li, H., Ouyang, K., & Chen,

- X. (2019). Cloning and characterization of the lignin biosynthesis genes NcCSE and NcHCT from *Neolamarckia cadamba*. *AMB Express*, 9(1), 1–11. <https://doi.org/10.1186/S13568-019-0860-Z/TABLES/2>
- Lin, J., Graziotto, M. E., Lay, P. A., & New, E. J. (2021). A bimodal fluorescence-raman probe for cellular imaging. *Cells*, 10(7), 1699. <https://doi.org/10.3390/CELLS10071699/S1>
- Lindner, B., Petridis, L., Schulz, R., & Smith, J. C. (2013). Solvent-driven preferential association of lignin with regions of crystalline cellulose in molecular dynamics simulation. *Biomacromolecules*, 14(10), 3390–3398. https://doi.org/10.1021/BM400442N/SUPPL_FILE/BM400442N_SI_001.PDF
- Lion, C., Simon, C., Huss, B., Blervacq, A. S., Tiroit, L., Toybou, D., Spriet, C., Slomianny, C., Guerardel, Y., Hawkins, S., & Biot, C. (2017). BLISS: a bioorthogonal dual-labeling strategy to unravel lignification dynamics in plants. *Cell Chemical Biology*, 24(3), 26–338. <https://doi.org/10.1016/j.chembiol.2017.02.009>
- Liu, C. J. (2012). Deciphering the Enigma of Lignification: Precursor Transport, Oxidation, and the Topochemistry of Lignin Assembly. *Molecular Plant*, 5(2), 304–317. <https://doi.org/10.1093/MP/SSR121>
- Liu, C. J., Miao, Y. C., & Zhang, K. W. (2011). Sequestration and transport of lignin monomeric precursors. *Molecules*, 16(1), 710. <https://doi.org/10.3390/MOLECULES16010710>
- Lu, F., Wang, C., Chen, M., Yue, F., & Ralph, J. (2021). A facile spectroscopic method for measuring lignin content in lignocellulosic biomass. *Green Chemistry*, 23(14), 5106–5112. <https://doi.org/10.1039/D1GC01507A>
- Lupoi, J. S., Singh, S., Parthasarathi, R., Simmons, B. A., & Henry, R. J. (2015). Recent innovations in analytical methods for the qualitative and quantitative assessment of lignin. In *Renewable and Sustainable Energy Reviews* 49, 871–906. <https://doi.org/10.1016/j.rser.2015.04.091>
- Macnish, A. J., Irving, D. E., Joyce, D. C., Vithanage, V., Wearing, A. H., Webb, R. I., & Frost, R. L. (2003). Identification of intracellular calcium oxalate crystals in *Chamelaucium uncinatum* (Myrtaceae). *Australian Journal of Botany*, 51(5), 565–572. <https://doi.org/10.1071/BT03035>

- Mateu, B. P., Bock, P., & Gierlinger, N. (2020). Raman Imaging of Plant Cell Walls. *Methods in Molecular Biology*, 2149, 251–295. https://doi.org/10.1007/978-1-0716-0621-6_15
- McFarlane, H. E., & Persson, S. (2014). The Cell Biology of Cellulose Synthesis. *Annual Review of Plant Biology* 65, 69–94. <https://doi.org/10.1146/ANNUREV-ARPLANT-050213-04024>
- Meshitsuka, G., & Nakano, J. (1979). Studies on the mechanism of lignin color reaction. XIII. Maeule color reaction. 9. *Mokuzai Gakkaishi*, 25(9), 588–594.
- Miao, Y. C., & Liu, C. J. (2010). ATP-binding cassette-like transporters are involved in the transport of lignin precursors across plasma and vacuolar membranes. *Proceedings of the National Academy of Sciences of the United States of America*, 107(52), 22728–22733. https://doi.org/10.1073/PNAS.1007747108/SUPPL_FILE/PNAS.201007747SI.PDF
- Minic, Z., & Jouanin, L. (2006). Plant glycoside hydrolases involved in cell wall polysaccharide degradation. *Plant Physiology and Biochemistry*, 44(7–9), 435–449. <https://doi.org/10.1016/J.PLAPHY.2006.08.001>
- Mohnen, D. (2008). Pectin structure and biosynthesis. *Current Opinion in Plant Biology*, 11(3), 266–277. <https://doi.org/10.1016/j.pbi.2008.03.006>
- Morel, O., & Gierlinger, N. (2023). Chemical tissue heterogeneity of young Arabidopsis stems revealed by Raman imaging combined with multivariate data analysis. *Microchemical Journal*.
- Morel, O., Lion, C., Neutelings, G., Stefanov, J., Baldacci-Cresp, F., Simon, C., Biot, C., Hawkins, S., & Spriet, C. (2022). REPRISAL: mapping lignification dynamics using chemistry, data segmentation, and ratiometric analysis. *Plant Physiology*, 188(2), 816–830. <https://doi.org/10.1093/PLPHYS/KIAB490>
- Morel, O., Spriet, C., Lion, C., Baldacci-Cresp, F., Pontier, G., Baucher, M., Biot, C., Hawkins, S., & Neutelings, G. (2023). Ratiometric fluorescent safranin-o staining allows the quantification of lignin contents in muro. *Methods in Molecular Biology* , 2566, 261–268. https://doi.org/10.1007/978-1-0716-2675-7_21/COVER
- Morrison, I. M. (1961). Improvements in the acetyl bromide technique to determine lignin and digestibility and its application to legumes. *Journal of the Science of Food and Agriculture*, 23(12), 1463–1469. <https://doi.org/10.1002/JSFA.2740231211>

- Morrison, I. M. (1972). A semi-micro method for the determination of lignin and its use in predicting the digestibility of forage crops. *Journal of the Science of Food and Agriculture*, 23(4), 455–463. <https://doi.org/10.1002/JSFA.2740230405>
- Mosca, S., Conti, C., Stone, N., & Matousek, P. (2021). Spatially offset Raman spectroscopy. *Nature Reviews Methods Primers 2021 1:1*, 1(1), 1–16. <https://doi.org/10.1038/s43586-021-00019-0>
- Mottiar, Y., Vanholme, R., Boerjan, W., Ralph, J., & Mansfield, S. D. (2016). Designer lignins: Harnessing the plasticity of lignification. *Current Opinion in Biotechnology*, 37, 190–200. <https://doi.org/10.1016/J.COPBIO.2015.10.009>
- Mravec, J., Kračun, S. K., Rydahl, M. G., Westereng, B., Pontiggia, D., De Lorenzo, G., Domozych, D. S., & Willats, W. G. T. (2017). An oligogalacturonide-derived molecular probe demonstrates the dynamics of calcium-mediated pectin complexation in cell walls of tip-growing structures. *The Plant Journal*, 91(3), 534–546. <https://doi.org/10.1111/TPJ.13574>
- Mravec, J., Kračun, S. K., Zemlyanskaya, E., Rydahl, M. G., Guo, X., Pičmanová, M., Sørensen, K. K., Růžička, K., & Willats, W. G. T. (2017). Click chemistry-based tracking reveals putative cell wall-located auxin binding sites in expanding cells. *Scientific Reports*, 7(1). <https://doi.org/10.1038/S41598-017-16281-W>
- Nieuwland, J., Feron, R., Huisman, B. A. H., Fasolino, A., Hilbers, C. W., Derksen, J., & Mariani, C. (2005). Lipid transfer proteins enhance cell wall extension in tobacco. *Plant Cell*, 17(7), 2009–2019. <https://doi.org/10.1105/tpc.105.032094>
- Nilsson, B. L., Kiessling, L. L., & Raines, R. T. (2000). Staudinger ligation: A peptide from a thioester and azide. *Organic Letters*, 2(13), 1939–1941. https://doi.org/10.1021/OL0060174/SUPPL_FILE/OL0060174_S1.PDF
- Nixon, B. T., Mansouri, K., Singh, A., Du, J., Davis, J. K., Lee, J. G., Slabaugh, E., Vandavasi, V. G., O'Neill, H., Roberts, E. M., Roberts, A. W., Yingling, Y. G., & Haigler, C. H. (2016). Comparative Structural and Computational Analysis Supports Eighteen Cellulose Synthases in the Plant Cellulose Synthesis Complex. *Scientific Reports 2016 6:1*, 6(1), 1–14. <https://doi.org/10.1038/srep28696>
- Pandey, J. L., Kiemle, S. N., Richard, T. L., Zhu, Y., Cosgrove, D. J., & Anderson, C. T. (2016). Investigating biochemical and developmental dependencies of lignification with a click-

- compatible monolignol analog in arabidopsis thaliana stems. *Frontiers in Plant Science*, 7. <https://doi.org/10.3389/fpls.2016.01309>
- Pandey, J. L., Wang, B., Diehl, B. G., Richard, T. L., Chen, G., & Anderson, C. T. (2015). A versatile click-compatible monolignol probe to study lignin deposition in plant cell walls. *PLOS ONE*, 10(4), 121334. <https://doi.org/10.1371/JOURNAL.PONE.0121334>
- Pang, S. (2019). Advances in thermochemical conversion of woody biomass to energy, fuels and chemicals. *Biotechnology Advances*, 37(4), 589–597. <https://doi.org/10.1016/J.BIOTECHADV.2018.11.004>
- Paper, J. M., Mukherjee, T., & Schrick, K. (2018). Bioorthogonal click chemistry for fluorescence imaging of choline phospholipids in plants. *Plant Methods*, 14(1), 1–14. <https://doi.org/10.1186/S13007-018-0299-2/FIGURES/8>
- Park, Y. B., & Cosgrove, D. J. (2012). Changes in cell wall biomechanical properties in the xyloglucan-deficient *xxt1/xxt2* mutant of *Arabidopsis*. *Plant Physiology*, 158(1), 465. <https://doi.org/10.1104/PP.111.189779>
- Patil, N. D., Tanguy, N. R., & Yan, N. (2016). Lignin Interunit Linkages and Model Compounds. In *Lignin in Polymer Composites* (pp. 27–47). Elsevier. <https://doi.org/10.1016/B978-0-323-35565-0.00003-5>
- Pauly, M., Gille, S., Liu, L., Mansoori, N., de Souza, A., Schultink, A., & Xiong, G. (2013). Hemicellulose biosynthesis. *Planta*. <https://doi.org/10.1007/s00425-013-1921-1>
- Peña, M. J., Zhong, R., Zhou, G. K., Richardson, E. A., O'Neill, M. A., Davill, A. G., York, W. S., & Yeb, Z. H. (2007). *Arabidopsis irregular xylem8 and irregular xylem9*: implications for the complexity of glucuronoxylan biosynthesis. *The Plant Cell*, 19(2), 549–563. <https://doi.org/10.1105/TPC.106.049320>
- Peng, L., Xiang, F., Roberts, E., Kawagoe, Y., Greve, L. C., Kreuz, K., & Delmer, D. P. (2001). The experimental herbicide CGA 325'615 inhibits synthesis of crystalline cellulose and causes accumulation of non-crystalline beta-1,4-glucan associated with CesA protein. *Plant Physiology*, 126(3), 981–992. <https://doi.org/10.1104/PP.126.3.981>
- Perkins, M., Smith, R. A., & Samuels, L. (2019). The transport of monomers during lignification in plants: anything goes but how? *Current Opinion in Biotechnology*, 56, 69–74. <https://doi.org/10.1016/j.copbio.2018.09.011>

- Pickett-Heaps, J. D. (1968). Xylem wall deposition - Radioautographic investigations using lignin precursors. *Protoplasma*, 65(1–2), 181–205. <https://doi.org/10.1007/BF01666378/METRICS>
- Qin, S., Fan, C., Li, X., Li, Y., Hu, J., Li, C., & Luo, K. (2020). LACCASE14 is required for the deposition of guaiacyl lignin and affects cell wall digestibility in poplar. *Biotechnology for Biofuels*, 13(1), 1–14. <https://doi.org/10.1186/S13068-020-01843-4/FIGURES/6>
- Qin, W., Yin, Q., Chen, J., Zhao, X., Yue, F., He, J., Yang, L., Liu, L., Zeng, Q., Lu, F., Mitsuda, N., Ohme-Takagi, M., & Wu, A. M. (2020). The class II KNOX transcription factors KNAT3 and KNAT7 synergistically regulate monolignol biosynthesis in *Arabidopsis*. *Journal of Experimental Botany*, 71(18), 5469–5483. <https://doi.org/10.1093/JXB/ERAA266>
- Raggi, S., Ferrarini, A., Delledonne, M., Dunand, C., Ranocha, P., de Lorenzo, G., Cervone, F., & Ferrari, S. (2015). The *Arabidopsis* class III peroxidase *atprx71* negatively regulates growth under physiological conditions and in response to cell wall damage. *Plant Physiology*, 169(4), 2513–2525. <https://doi.org/10.1104/PP.15.01464>
- Rinaldi, R., Jastrzebski, R., Clough, M. T., Ralph, J., Kennema, M., Bruijninx, P. C. A., & Weckhuysen, B. M. (2016). Paving the way for lignin valorisation: recent advances in bioengineering, biorefining and catalysis. *Angewandte Chemie International Edition*, 55(29), 8164–8215. <https://doi.org/10.1002/ANIE.201510351>
- Rostovtsev, V. V., Green, L. G., Fokin, V. V., & Sharpless, K. B. (2002). A stepwise Huisgen cycloaddition process: Copper(I)-catalyzed regioselective “ligation” of azides and terminal alkynes. *Angewandte Chemie - International Edition*, 41(14), 2596–2599. [https://doi.org/10.1002/1521-3773\(20020715\)41:14<2596::AID-ANIE2596>3.0.CO;2-4](https://doi.org/10.1002/1521-3773(20020715)41:14<2596::AID-ANIE2596>3.0.CO;2-4)
- Rowland, S. P., & Howley, P. S. (1988). Hydrogen bonding on accessible surfaces of cellulose from various sources and relationship to order within crystalline regions. *Journal of Polymer Science Part A: Polymer Chemistry*, 26(7), 1769–1778. <https://doi.org/10.1002/POLA.1988.080260708>
- Saini, J. K., Saini, R., & Tewari, L. (2015). Lignocellulosic agriculture wastes as biomass feedstocks for second-generation bioethanol production: concepts and recent developments. *3 Biotech*, 5(4), 337–353. <https://doi.org/10.1007/S13205-014-0246-5/TABLES/8>

- San Clemente, H., & Jamet, E. (2015). WallProtDB, a database resource for plant cell wall proteomics. *Plant Methods*, *11*(1), 1–7. <https://doi.org/10.1186/S13007-015-0045-Y/FIGURES/4>
- Santos, R. B., Capanema, E. A., Balakshin, M. Y., Chang, H. M., & Jameel, H. (2012). Lignin structural variation in hardwood species. *Journal of Agricultural and Food Chemistry*, *60*(19), 4923–4930. https://doi.org/10.1021/JF301276A/ASSET/IMAGES/LARGE/JF-2012-01276A_0003.JPEG
- Saxon, E., & Bertozzi, C. R. (2000). Cell Surface Engineering by a Modified Staudinger Reaction. *Science*, *287*(5460), 2007–2010. <https://doi.org/10.1126/SCIENCE.287.5460.2007>
- Saxon, E., Luchansky, S. J., Hang, H. C., Yu, C., Lee, S. C., & Bertozzi, C. R. (2002). Investigating cellular metabolism of synthetic azidosugars with the Staudinger ligation. *Journal of the American Chemical Society*, *124*(50), 14893–14902. https://doi.org/10.1021/JA027748X/SUPPL_FILE/JA027748X-2_S1.PDF
- Scheller, H. V., & Ulvskov, P. (2010). Hemicelluloses. *Annual Review of Plant Biology*. <https://doi.org/10.1146/annurev-arplant-042809-112315>
- Schuetz, M., Benske, A., Smith, R. A., Watanabe, Y., Tobimatsu, Y., Ralph, J., Demura, T., Ellis, B., & Samuels, A. L. (2014). Laccases Direct Lignification in the Discrete Secondary Cell Wall Domains of Protoxylem. *Plant Physiology*, *166*(2), 798–807. <https://doi.org/10.1104/PP.114.245597>
- Seifert, G. J., & Roberts, K. (2007). The Biology of Arabinogalactan Proteins. *Annual Review of Plant Biology*, *58*, 137-161 <https://doi.org/10.1146/annurev.arplant.58.032806.103801>
- Shigeto, J., Kiyonaga, Y., Fujita, K., Kondo, R., & Tsutsumi, Y. (2013). Putative cationic cell-wall-bound peroxidase homologues in *Arabidopsis*, AtPrx2, AtPrx25, and AtPrx71, are involved in lignification. *Journal of Agricultural and Food Chemistry*, *61*(16), 3781–3788. <https://doi.org/10.1021/JF400426G>
- Showalter, A. M., Keppler, B., Lichtenberg, J., Gu, D., & Welch, L. R. (2010). A bioinformatics approach to the identification, classification, and analysis of hydroxyproline-rich glycoproteins. *Plant Physiology*, *153*(2), 485–513. <https://doi.org/10.1104/PP.110.156554>

Simon, C., Lion, C., Spriet, C., Baldacci-Cresp, F., Hawkins, S., & Biot, C. (2018). One, Two, Three: a bioorthogonal triple labelling strategy for studying the dynamics of plant cell wall formation in vivo. *Angewandte Chemie - International Edition*, 57(51), 16665-16671

<https://doi.org/10.1002/anie.201808493>

Smith-Moritz, A. M., Chern, M., Lao, J., Sze-To, W. H., Heazlewood, J. L., Ronald, P. C., & Vega-Sánchez, M. E. (2011). Combining multivariate analysis and monosaccharide composition modeling to identify plant cell wall variations by Fourier Transform Near Infrared spectroscopy. *Plant Methods*, 7(1), 1–13. <https://doi.org/10.1186/1746-4811-7-26/FIGURES/3>

Staudinger, H., & Meyer, J. (1919). New organic compounds of phosphorus. III. Phosphinemethylene derivatives and phosphinimines. *Helvetica Chimica Acta*.

Sulis, D. B., & Wang, J. P. (2020). Regulation of lignin biosynthesis by post-translational protein modifications. *Frontiers in Plant Science*, 11. <https://doi.org/10.3389/FPLS.2020.00914>

Taylor, J. G., Owen, T. P., Koonce, L. T., & Haigler, C. H. (1992). Dispersed lignin in tracheary elements treated with cellulose synthesis inhibitors provides evidence that molecules of the secondary cell wall mediate wall patterning. *The Plant Journal*, 2(6), 959–970. <https://doi.org/10.1111/J.1365-313X.1992.00959.X>

Taylor, N. G., Howells, R. M., Huttly, A. K., Vickers, K., & Turner, S. R. (2003). Interactions among three distinct CesA proteins essential for cellulose synthesis. *Proceedings of the National Academy of Sciences of the United States of America*, 100(3), 1450–1455. <https://doi.org/10.1073/PNAS.0337628100/ASSET/F92E9920-A982-4682-AFDF-4738F7828BD3/ASSETS/GRAPHIC/PQ0337628005.JPEG>

Taylor, N. G., Scheible, W. R., Cutler, S., Somerville, C. R., & Turner, S. R. (1999). The *irregular xylem3* locus of *Arabidopsis* encodes a cellulose synthase required for secondary cell wall synthesis. *The Plant Cell*, 11(5), 769–779. <https://doi.org/10.1105/TPC.11.5.769>

Terashima, N., Ko, C., Matsushita, Y., & Westermarck, U. (2016). Monolignol glucosides as intermediate compounds in lignin biosynthesis. Revisiting the cell wall lignification and new ¹³C-tracer experiments with *Ginkgo biloba* and *Magnolia liliiflora*. *Holzforschung*, 70(9), 801–810. https://doi.org/10.1515/HF-2015-0224/ASSET/GRAPHIC/J_HF-2015-0224_FIG_005.JPG

- Terrett, O. M., & Dupree, P. (2019). Covalent interactions between lignin and hemicelluloses in plant secondary cell walls. *Current Opinion in Biotechnology*, 56, 97–104. <https://doi.org/10.1016/J.COPBIO.2018.10.010>
- Tobimatsu, Y., & Schuetz, M. (2019). Lignin polymerization: how do plants manage the chemistry so well? In *Current Opinion in Biotechnology*, 56, 75–81. <https://doi.org/10.1016/j.copbio.2018.10.001>
- Tobimatsu, Y., Wouwer, D. Van De, Allen, E., Kumpf, R., Vanholme, B., Boerjan, W., & Ralph, J. (2014). A click chemistry strategy for visualization of plant cell wall lignification. *Chemical Communications*. <https://doi.org/10.1039/c4cc04692g>
- Tolivia, D., & Tolivia, J. (1987). Fasga: A new polychromatic method for simultaneous and differential staining of plant tissues. *Journal of Microscopy*, 148(1), 113–117. <https://doi.org/10.1111/J.1365-2818.1987.TB02859.X>
- Tsien, R. Y. (1998). The green fluorescent protein. In *Annual Review of Biochemistry* (Vol. 67, pp. 509–544). Annual Reviews 4139 El Camino Way, P.O. Box 10139, Palo Alto, CA 94303-0139, USA. <https://doi.org/10.1146/annurev.biochem.67.1.509>
- Tsuji, Y., Chen, F., Yasuda, S., & Fukushima, K. (2004). The Behavior of Deuterium-Labeled Monolignol and Monolignol Glucosides in Lignin Biosynthesis in Angiosperms. *Journal of Agricultural and Food Chemistry*, 52(1), 131–134. <https://doi.org/10.1021/JF034817Y/ASSET/IMAGES/MEDIUM/JF034817YN00001.GIF>
- Tsuyama, T., Kawai, R., Shitan, N., Matoh, T., Sugiyama, J., Yoshinaga, A., Takabe, K., Fujita, M., & Yazaki, K. (2013). Proton-dependent coniferin transport, a common major transport event in differentiating xylem tissue of woody plants. *Plant Physiology*, 162(2), 918–926. <https://doi.org/10.1104/PP.113.214957>
- Umezawa, T. (2018). Lignin modification in planta for valorization. *Phytochemistry Reviews*, 17(6), 1305–1327. <https://doi.org/10.1007/S11101-017-9545-X/FIGURES/4>
- Vaahtera, L., Schulz, J., & Hamann, T. (2019). Cell wall integrity maintenance during plant development and interaction with the environment. *Nature Plants*, 5, 924–932. <https://doi.org/10.1038/s41477-019-0502-0>
- Väisänen, E., Takahashi, J., Obudulu, O., Bygdell, J., Karhunen, P., Blokhina, O., Laitinen, T.,

- Teeri, T. H., Wingsle, G., Fagerstedt, K. V., & Kärkönen, A. (2020). Hunting monoglignol transporters: membrane proteomics and biochemical transport assays with membrane vesicles of Norway spruce. *Journal of Experimental Botany*, *71*(20), 6379–6395. <https://doi.org/10.1093/JXB/ERAA368>
- Van der Hoorn, R. A. L. (2008). Plant Proteases: From Phenotypes to Molecular Mechanisms. *Annual Review of Plant Biology*, *59*, 191–223. <https://doi.org/10.1146/annurev.arplant.59.032607.092835>
- Vanholme, R., De Meester, B., Ralph, J., & Boerjan, W. (2019). Lignin biosynthesis and its integration into metabolism. In *Current Opinion in Biotechnology*. <https://doi.org/10.1016/j.copbio.2019.02.018>
- Vanholme, R., Demedts, B., Morreel, K., Ralph, J., & Boerjan, W. (2010). Lignin Biosynthesis and Structure. *Plant Physiology*, *153*(3), 895–905. <https://doi.org/10.1104/pp.110.155119>
- Vasile, C., & Baican, M. (2023). Lignins as Promising Renewable Biopolymers and Bioactive Compounds for High-Performance Materials. *Polymers*, *15*(15), 3177. <https://doi.org/10.3390/POLYM15153177>
- Vermaas, J. V., Dixon, R. A., Chen, F., Mansfield, S. D., Boerjan, W., Ralph, J., Crowley, M. F., & Beckham, G. T. (2019). Passive membrane transport of lignin-related compounds. *Proceedings of the National Academy of Sciences of the United States of America*, *116*(46), 23117–23123. https://doi.org/10.1073/PNAS.1904643116/SUPPL_FILE/PNAS.1904643116.SD01.XLS
- Voiniciuc, C. (2022). Modern mannan: a hemicellulose’s journey. *New Phytologist*, *234*(4), 1175–1184. <https://doi.org/10.1111/NPH.18091>
- Wang, J. P., Chuang, L., Loziuk, P. L., Chen, H., Lin, Y. C., Shi, R., Qu, G. Z., Muddiman, D. C., Sederoff, R. R., & Chiang, V. L. (2015). Phosphorylation is an on/off switch for 5-hydroxyconiferaldehyde O-methyltransferase activity in poplar monoglignol biosynthesis. *Proceedings of the National Academy of Sciences of the United States of America*, *112*(27), 8481–8486. https://doi.org/10.1073/PNAS.1510473112/SUPPL_FILE/PNAS.1510473112.SD01.XLSX
- Wang, T., McFarlane, H. E., & Persson, S. (2016). The impact of abiotic factors on cellulose

- synthesis. *Journal of Experimental Botany*, 67(2), 543–552. <https://doi.org/10.1093/jxb/erv488>
- Wang, Y., Chantreau, M., Sibout, R., & Hawkins, S. (2013). Plant cell wall lignification and monolignol metabolism. *Frontiers in Plant Science*, 4. <https://doi.org/10.3389/fpls.2013.00220>
- Wenger, J., Haas, V., & Stern, T. (2020). Why Can We Make Anything from Lignin Except Money? Towards a Broader Economic Perspective in Lignin Research. *Current Forestry Reports*, 6(4), 294–308. <https://doi.org/10.1007/S40725-020-00126-3/FIGURES/3>
- Wiley, J. H., & Atalla, R. H. (1987). Band assignments in the raman spectra of celluloses. *Carbohydrate Research*, 160(C), 113–129. [https://doi.org/10.1016/0008-6215\(87\)80306-3](https://doi.org/10.1016/0008-6215(87)80306-3)
- Wilson, J. R., & Hatfield, R. D. (1997). Structural and chemical changes of cell wall types during stem development: consequences for fibre degradation by rumen microflora. *Australian Journal of Agricultural Research*, 48(2), 165–180. <https://doi.org/10.1071/A96051>
- Wittig, G., & Krebs, A. (1961). Zur Existenz niedergliedriger Cycloalkine, I. *Chemische Berichte*, 94(12), 3260–3275. <https://doi.org/10.1002/CBER.19610941213>
- Xie, D., Ma, L., Šamaj, J., & Xu, C. (2011). Immunohistochemical analysis of cell wall hydroxyproline-rich glycoproteins in the roots of resistant and susceptible wax gourd cultivars in response to *Fusarium oxysporum* f. sp. *Benincasae* infection and fusaric acid treatment. *Plant Cell Reports*, 30(8), 1555–1569. <https://doi.org/10.1007/S00299-011-1069-Z/TABLES/2>
- Xie, M., Zhang, J., Tschaplinski, T. J., Tuskan, G. A., Chen, J. G., & Muchero, W. (2018). Regulation of lignin biosynthesis and its role in growth-defense tradeoffs. *Frontiers in Plant Science*, 9, 407961. <https://doi.org/10.3389/FPLS.2018.01427/BIBTEX>
- Xu, F., Zhong, X. C., Sun, R. C., & Lu, Q. (2006). Anatomy, ultrastructure and lignin distribution in cell wall of *Caragana Korshinskii*. *Industrial Crops and Products*, 24(2), 186–193. <https://doi.org/10.1016/J.INDCROP.2006.04.002>
- Yamaguchi, M., Goué, N., Igarashi, H., Ohtani, M., Nakano, Y., Mortimer, J. C., Nishikubo, N., Kubo, M., Katayama, Y., Kakegawa, K., Dupree, P., & Demura, T. (2010).

VASCULAR-RELATED NAC-DOMAIN6 and VASCULAR-RELATED NAC-DOMAIN7 effectively induce transdifferentiation into xylem vessel elements under control of an induction System. *Plant Physiology*, 153(3), 906–914. <https://doi.org/10.1104/PP.110.154013>

Yamashita, D., Kimura, S., Wada, M., & Takabe, K. (2016). Improved Mäule color reaction provides more detailed information on syringyl lignin distribution in hardwood. *Journal of Wood Science*, 62(2), 131–137. <https://doi.org/10.1007/S10086-016-1536-9/FIGURES/9>

Yeats, T. H., & Rose, J. K. C. (2013). The formation and function of plant cuticles. *Plant Physiology*, 163(1), 5–20. <https://doi.org/10.1104/pp.113.222737>

Yi Chou, E., Schuetz, M., Hoffmann, N., Watanabe, Y., Sibout, R., & Samuels, A. L. (2018). Distribution, mobility, and anchoring of lignin-related oxidative enzymes in Arabidopsis secondary cell walls. *Journal of Experimental Botany*, 69(8), 1849–1859. <https://doi.org/10.1093/JXB/ERY067>

Zhang, J., Campbell, R. E., Ting, A. Y., & Tsien, R. Y. (2002). Creating new fluorescent probes for cell biology. *Nature Reviews Molecular Cell Biology* 3:12, 3(12), 906–918. <https://doi.org/10.1038/NRM976>

Zhao, Q., Nakashima, J., Chen, F., Yin, Y., Fu, C., Yun, J., Shao, H., Wang, X., Wang, Z. Y., & Dixon, R. A. (2013). LACCASE is necessary and nonredundant with peroxidase for lignin polymerization during vascular development in Arabidopsis. *The Plant Cell*, 25(10), 3976–3987. <https://doi.org/10.1105/TPC.113.117770>

Zhao, Z., Shen, Y., Hu, F., & Min, W. (2017). Applications of vibrational tags in biological imaging by Raman microscopy. *The Analyst*, 142(21), 4018. <https://doi.org/10.1039/C7AN01001J>

Zhong, R., & Ye, Z. H. (2009). Transcriptional regulation of lignin biosynthesis. *Plant Signaling & Behavior*, 4(11), 1028. <https://doi.org/10.4161/PSB.4.11.9875>